



---

CORSO DI DOTTORATO DI RICERCA IN

---

CICLO DEL CORSO DI DOTTORATO

---

Titolo della tesi

---

Nome e Cognome del dottorando

---

firma

---

Docente Guida/Tutor: Prof.

---

firma

---

Coordinatore: Prof.

---

firma



# Vector Boson Fusion channel for Axion Like Particles detection at Belle II: Phase Space Theory and Collider Phenomenology

Università degli Studi di Roma Tre  
Dottorato di Ricerca in Fisica (XXXV cycle)

**Francesca Acanfora**

ID number 58577

Advisor  
Prof. Roberto Franceschini

Co-Advisor  
Prof. Diego Redigolo

Academic Year 2021/2022

Thesis not yet defended

---

**Vector Boson Fusion channel for Axion Like Particles detection at Belle II: Phase Space Theory and Collider Phenomenology**

PhD thesis. Roma Tre University of Rome

© 2023 Francesca Acanfora. All rights reserved

This thesis has been typeset by L<sup>A</sup>T<sub>E</sub>X and the Sapthesis class.

Author's email: francesc.acanfora@uniroma3.it

*Grazie alla mia famiglia, nulla sarebbe stato possibile senza di voi.*  
*Grazie Giovanni: ormai è chiaro che senza di te non voglio fare più un passo.*  
*Grazie ai miei supervisor, avete reso possibile una crescita che perfino io non posso*  
*permettermi di ignorare grazie alla vostra costante guida gentile.*  
*Grazie don Claudio, in questa tesi c'è anche il tuo (Vostro) zampino!*  
*Grazie alle amiche di Porta Nevia, senza di voi sarei impazzita!*  
*Grazie Alessio, in questa vita o nella prossima riceverai merito di aver lavorato con*  
*me per tre anni.*  
*Grazie Marco, senza di te Via della Vasca Navale sarebbe implosa.*



## Abstract

In this dissertation I study the Vector Boson Fusion (VBF) of two photons into an Axion Like Particle (ALP) both under the theoretical and phenomenological point of view. Axion Like Particles are receiving special attention in the last decades since they can provide viable solutions to many areas of Physics (Dark Matter [1–4], the strong CP problem [5–8], the over-efficient cooling of some stars, the transparency of the Universe to very high-energy  $\gamma$ -rays, the 3.55 keV line from Andromeda and galaxy clusters). Axion Like Particles [9,10] coupled to fermions, photons, gluons, W and Z bosons have been investigated. In this dissertation I will consider an ALP coupled to photons only.

Different kinds of experiments are working on closing the ALP phase space, like helioscopes [11,12], haloscopes [13], but also colliders [14]. Specifically, Belle II is an interesting facility in this sense due to its high luminosity. The state of the art on Belle II sensitivity to ALPs is limited to the ALP-strahlung channel  $e^+e^- \rightarrow a\gamma$ , both in the case of visible or invisible ALP (i.e. respectively the ALP does or does not decay to visible photons within the detector). This is because the VBF ( $e^+e^- \rightarrow e^+e^-a$ ) is believed to be negligible. Nonetheless, the  $t$  channel proves valuable both in the Higgs discovery and at future colliders, where high Centre of Mass energies will suppress the  $s$  channels with respect to the  $t$  channels. This pushed us to study the VBF cross section distributions so to have a grasp of the physical configurations making the VBF more important than the ALP-strahlung. The first part of this work is devoted to cross section distributions computation. The  $2 \rightarrow 3$  scattering required us to recover the Gram Determinant formalism, to overcome the difficulties that rapidly emerge when one tries and use polar coordinates: not only through Gram Determinants I could recover some original, non constant matrix element cross section distributions, but also I could provide a personal contribution to a thorough characterisation of the phase space of a generic scattering in a Lorentz invariant, highly symmetric fashion. I could then apply this knowledge to phenomenological considerations, both in the visible and invisible ALP decay. As to the  $e^+e^- \rightarrow e^+e^-a, a \rightarrow \gamma\gamma$  case, I designed an optimised set of events selections and obtained that with the current Belle II lepton polar angle acceptance the VBF can compete with the ALP-strahlung only at very high or very small ALP masses. However, if that acceptance was increased, the VBF would overcome the ALP-strahlung sensitivity by an order of magnitude. Lastly, I studied the photon fusion production of an Axion Like Particle coupled to dark matter proposing a nearly background-free search in the  $e^+e^- +$  invisible channel. This search leverages dedicated kinematic variables, whose behaviour and performance I test under a simplified, yet realistic, treatment of detector effects. I found that at the Belle II experiment the VBF has the potential to be as sensitive as mono- $\gamma$  for all the ALP mass range that can be probed by Belle II and can significantly improve the bounds expected for O(GeV) ALP mass. This demonstrates that new Dark Matter searches based on high signal purity channels can give comparable or better bounds than searches based on more traditional large-background final states.



# Contents

<b>1</b>	<b>Introduction</b>	<b>1</b>
1.1	What is the strong CP problem . . . . .	1
1.2	Dynamical solution to the strong CP problem . . . . .	2
1.3	Axion effective Lagrangian . . . . .	3
1.4	UV completions of the axion effective Lagrangian . . . . .	4
1.5	Axion-Like Particles . . . . .	5
1.6	ALP experimental facilities . . . . .	7
1.7	The many body phase space . . . . .	8
<b>I</b>	<b>Gram determinants</b>	<b>13</b>
<b>2</b>	<b>Gram Determinants motivation</b>	<b>15</b>
2.1	The pseudoscalar matrix element . . . . .	15
2.2	Ignoring the spin . . . . .	16
2.3	Failure of polar coordinates integration . . . . .	17
2.3.1	$M_e \rightarrow 0$ limit . . . . .	19
<b>3</b>	<b>Gram Determinants are the language of Scattering Amplitudes</b>	<b>23</b>
3.1	Definitions and properties of Gram matrices . . . . .	23
3.2	Geometrical meaning of GDs . . . . .	26
3.3	From polar coordinates to Lorentz invariant variables . . . . .	29
3.4	Null Gram determinants define the boundary of the physical region of the phase space . . . . .	30
3.4.1	2, 3, 4 bodies . . . . .	30
3.4.2	In general . . . . .	33
<b>4</b>	<b>Constraints on Mandelstam variables from GDs</b>	<b>35</b>
4.1	A $2 \rightarrow 2$ scattering invitation . . . . .	35
4.2	Working out the $2 \rightarrow 3$ case . . . . .	39
4.2.1	Generalized Mandelstam variables . . . . .	40
4.2.2	Understanding the phase space as parabolas . . . . .	41
4.3	Byers and Yang . . . . .	50
4.4	Slow ALP: $2 \rightarrow 3$ degenerates to $2 \rightarrow 2$ . . . . .	53
4.4.1	Heavy ALP . . . . .	55
4.4.2	Scattering reduction in Gram terminology . . . . .	57

<b>5</b>	<b>2 → 3 cross section and distributions</b>	<b>59</b>
5.1	Gram Phase Space density and how to integrate on it . . . . .	59
5.2	$\frac{d^2\sigma_t}{dt_2 ds_1}$ . . . . .	63
5.3	$\frac{d^2\sigma_s}{du_1 ds_2}$ . . . . .	67
5.4	Comparison between $s$ and $t$ total cross section . . . . .	70
<b>6</b>	<b>Integrand symmetries: how to avoid computing all of the cross section distribution</b>	<b>73</b>
6.1	Combinatorics . . . . .	73
6.1.1	Lepton swaps and distributions . . . . .	76
6.2	Other distributions . . . . .	77
<b>7</b>	<b><math>\frac{d^2\sigma_t}{dt_1 dt_2}</math></b>	<b>79</b>
7.1	The $s_1$ integration . . . . .	79
7.2	Results and remarks . . . . .	84
7.3	Peripherality classes . . . . .	87
<b>8</b>	<b>Massive photons and Scalar Equivalent Photon Approximation</b>	<b>93</b>
8.1	Massless lepton and massive photon . . . . .	93
8.2	Equivalent Photon Approximation . . . . .	94
8.3	The VBF has final $e^\pm$ anisotropic angular distribution . . . . .	95
8.4	100 years of EPA . . . . .	99
8.5	SEPA, EPA in all scalar theory . . . . .	105
8.5.1	SEPA from electron-proton collision . . . . .	105
8.5.2	SEPA: results . . . . .	107
8.6	Comparison of SSM VS SEPA cross section . . . . .	111
<b>II</b>	<b>Phenomenology</b>	<b>115</b>
<b>9</b>	<b>ALP @ Belle II state of the art</b>	<b>119</b>
9.1	Basics of Belle II . . . . .	119
9.2	ALP-strahlung . . . . .	121
9.2.1	Helicity angles . . . . .	123
9.3	MG5_aMC@NLO generation . . . . .	124
9.3.1	Resolving photons . . . . .	125
9.3.2	The dataset . . . . .	126
9.3.3	Reach . . . . .	126
<b>10</b>	<b>Visible reach: Belle II sensitivity to <math>e^-e^+ \rightarrow e^-e^+a, a \rightarrow \gamma\gamma</math></b>	<b>129</b>
10.1	Belle III: what $e^\pm$ acceptance to choose? . . . . .	129
10.2	Event selection . . . . .	131
10.3	Reach . . . . .	133
<b>11</b>	<b>Invisible reach: Belle II sensitivity to <math>e^-e^+ \rightarrow e^-e^+a, a \rightarrow</math> invisible</b>	<b>137</b>
11.1	Collider effects ask for original selections . . . . .	138
11.2	QED background . . . . .	143

11.2.1	Boundaries of the forbidden region from its circumscribed rectangle . . . . .	144
11.3	Simultaneous missing mass and rapidity minimization: analysis by categories for $n \lesssim 10$ invisible photons . . . . .	146
11.3.1	$n_H = 1$ . . . . .	146
11.3.2	Two hard photons in the same cone . . . . .	148
11.3.3	Two hard photons in different cones . . . . .	148
11.3.4	Larger $n$ rectangles have smaller $\bar{\mathcal{P}}_{\text{inv}}^{(n)}$ . . . . .	149
11.4	Many hard photons, the generic case . . . . .	150
11.4.1	Unconstrained missing mass minimisation . . . . .	152
11.4.2	Constrained missing mass minimisation . . . . .	153
11.5	Allowing for one soft photon onto boundaries . . . . .	155
11.6	Background from $\tau\tau$ . . . . .	156
11.7	Cuts and regimes . . . . .	161
11.7.1	Cuts used in the small mass analysis . . . . .	162
11.7.2	Cuts in the high mass analysis . . . . .	164
<b>12</b>	<b>Conclusions</b> . . . . .	<b>169</b>
<b>Appendices</b>		<b>171</b>
A	Shortcuts . . . . .	171
B	Acronyms . . . . .	171
C	Polar coordinates . . . . .	171
D	Belle II parameters . . . . .	172
E	The $2 \rightarrow 3$ scattering . . . . .	173
E.1	Dimensionality of frequently occurring quantities . . . . .	175
F	Gram determinants and Levi-Civita symbols . . . . .	175
F.1	From the product of two Levi-Civita symbols to the determinant of a matrix of metric tensors . . . . .	175
F.2	Matrix element in terms of GDs . . . . .	177
G	Special functions . . . . .	178
H	Cross sections from theories with or without spins . . . . .	179
I	Proof of eq. (4.48) . . . . .	180
J	Allowed permutations in the $e^+e^- \rightarrow e^+e^-a$ process . . . . .	181
K	$\mathcal{G}_{12}$ roots ordering . . . . .	183
L	$\frac{d^2\sigma_t}{dt_1 dt_2}$ gallery . . . . .	184
M	VBF selections efficiency . . . . .	189
M.1	Significance with systematics at Belle II . . . . .	190
M.2	Belle II bg efficiencies . . . . .	191
M.3	Belle II sig efficiencies . . . . .	192
N	The smearing algorithm . . . . .	192
O	Python simulation of forbidden region to 3 invisible photons . . . . .	193
P	Long Lived ALP . . . . .	193
<b>Bibliography</b>		<b>197</b>



# Chapter 1

## Introduction

The SM proved to be the best tool at our hand to describe Particle Physics. Still, we have the luck to live a historical moment in which from multiple directions this picture may be broken. We expect it, for example, thanks to the hierarchy problem [15], the DM problem [1–4], the strong CP problem [5, 6, 16, 17] and many others. The ideal BSM theory solves more than one of these issues at once. In the last decades many models were proposed [18–21], of which some aged better than others. Often BSM solutions propose some spontaneously broken symmetry [22], like the majoron [23] or the familon [24]. Axion-Like Particles (ALPs) are among the most fortunate in the category: they are the natural evolution of the axion, a pseudo Nambu-Goldstone bosons originally born to wash away the strong CP problem; soon it was also realised that at the same time the axion could be a good DM candidate [25–27]. Their compelling theoretical motivation and the possibility to detect them at currently running colliders compelled us to dedicate this dissertation to ALPs. It is then useful to dedicate the following sections to recalling some basic notions of axion and ALPs theory. For broader reviews please refer to [8, 28], for example.

### 1.1 What is the strong CP problem

CP is not a SM symmetry, as we can see it is violated in the electroweak sector through the  $\delta$  phase in the CKM matrix [29]. If CP is violated somewhere in the SM, we have no reason to believe that it should be conserved in some other interactions, so if there is another place where we expect CP to be broken, it should be. For example, this place may be the QCD  $\bar{\theta}$  term. Let us define it. Consider the QCD lagrangian

$$\mathcal{L}_{\text{QCD}} = \sum_q \bar{q} \left( i\not{D} - m_q e^{i\theta_q} \right) q - \frac{1}{4} G^{a\mu\nu} G_{\mu\nu}^a + \theta \frac{g_s^2}{32\pi^2} G^{a\mu\nu} \tilde{G}_{\mu\nu}^a. \quad (1.1)$$

where in general we define the dual as

$$\tilde{F}^{\mu\nu} = \frac{1}{2} \epsilon^{\mu\nu\rho\sigma} F_{\rho\sigma}. \quad (1.2)$$

Pretend there only is one quark and perform the global chiral transformation

$$q \rightarrow e^{i\gamma_5\alpha}q. \quad (1.3)$$

Correspondingly the axial current is not conserved:

$$J_\mu^5 = \bar{\psi}\gamma_\mu\gamma_5\psi, \quad (1.4)$$

$$\partial^\mu J_\mu^5 = 2m_q\bar{q}i\gamma_5q + \frac{g_s^2}{16\pi^2}G\tilde{G}. \quad (1.5)$$

Now  $\theta_q$  shifts under the quark chiral rotation as  $\theta_q \rightarrow \theta_q + 2\alpha$  while  $\theta$  shifts like  $\theta \rightarrow \theta - 2\alpha$ . This is due to the path integral measure being non invariant under eq. (1.3) [30]. Then we can only observe  $\bar{\theta} = \theta + \theta_q$ . With more than one quark

$$\bar{\theta} = \theta + \arg \det Y_U Y_D, \quad (1.6)$$

where  $Y_{U,D}$  are up and down Yukawa matrices. Now the most sensitive observable induced by  $\bar{\theta}$  is the Neutron Electric Dipole Moment (NEDM)  $d_n$  [31]. The corresponding operator is

$$-d_n \frac{i}{2} \bar{n} \sigma_{\mu\nu} \gamma_5 n F^{\mu\nu}. \quad (1.7)$$

In chiral perturbation theory one would see that the NEDM comes from a loop neutron-pion interaction [31]. Then we can make up an idea on  $d_n$  from these considerations: it must come from an EM loop ( $\frac{e}{16\pi^2}$  factor in eq. (1.8)); it has dimension 5 so there must be a  $1/m_n$  factor; we must pick the CP odd term ( $\frac{m_q e^{i\bar{\theta}}}{m_n}$  factor in eq. (1.8)). The operator will have the form

$$\mathcal{L} \sim \frac{e}{16\pi^2} \frac{m_q e^{i\bar{\theta}}}{m_n} \frac{1}{m_n} \bar{n} \sigma_{\mu\nu} \gamma_5 n F^{\mu\nu}, \quad (1.8)$$

from which

$$\bar{\theta} \lesssim 10^{-10} \quad (1.9)$$

(see for example [32] for NEDM experimntal measurement). The smallness of  $\bar{\theta}$  is the strong CP problem.

## 1.2 Dynamical solution to the strong CP problem

One can either take the smallness of  $\bar{\theta}$  as an accident of life or find a motivation for it. The anthropic principle will not help in this case. One solution may be that  $\bar{\theta} = 0$  is dynamically reached as it represents the minimum of some quantity. Specifically, consider a new spin 0 field  $a$  having the following interactions

$$\mathcal{L}_a = \frac{1}{2} (\partial_\mu a)^2 + \mathcal{L}(\partial_\mu a, \psi) + \frac{g_s^2}{32\pi^2} \frac{a}{f_a} G\tilde{G}, \quad (1.10)$$

with a quasi shift symmetry  $a \rightarrow a + \kappa f_a$ .  $f_a$  is analogous to the pion decay constant while  $\kappa$  can be used to remove the  $\bar{\theta}$  term, because this shift transforms the action like

$$S \rightarrow S + \frac{\kappa}{32\pi^2} \int d^4x G\tilde{G}. \quad (1.11)$$

Peccei and Quinn [5, 16] proposed a UV completion for this kind of non renormalizable theory, a  $U(1)_{\text{PQ}}$  global symmetry, spontaneously broken and anomalous under QCD. Weinberg and Wilczek [6, 17] realised that the symmetry breaking produces a pseudo-Goldstone boson  $a$ , the axion.

Let us remark here that the fact that the PQ symmetry is supposed to be global is an issue. In fact it should to be preserved to a great degree of accuracy in order for the axion VEV to be relaxed to zero. Also, it is believed that quantum gravity forbids global symmetries because global charges would not be conserved by some non perturbative effects (evaporating black holes). This issue is known as the PQ quality problem [33–35]. To avoid it, PQ symmetry could arise as an accidental symmetry as a consequence of fundamental principles, like for example gauge and Lorentz invariance, so that it would be impossible to write down PQ violating effective operators up to dimension 10 (so to preserve the NEDM smallness, see [28] for the estimate). Alternatively, one may conceive a model with small  $f_a$ . Astrophysical constraints ruled out this possibility, unless one upgrades the axion to be an ALP, i.e. one disentangles  $m_a$  from  $f_a$ .

### 1.3 Axion effective Lagrangian

The axion effective lagrangian is

$$\mathcal{L}_a = \frac{1}{2} (\partial_\mu a)^2 + \frac{a}{f_a} \frac{g_s^2}{32\pi^2} G\tilde{G} + \frac{1}{4} g_{a\gamma}^0 a F\tilde{F} + \frac{\partial_\mu a}{2f_a} \bar{q} c_q^0 \gamma^\mu \gamma_5 q - \bar{q}_L M_q q_R + \text{h.c.} . \quad (1.12)$$

Sometimes the axion-photon coupling  $g_{a\gamma}^0$  is expressed in a model dependent way. To see how, let  $J_\mu^{\text{PQ}}$  be the current associated with PQ symmetry and parametrize its anomaly as

$$\partial^\mu J_\mu^{\text{PQ}} = \frac{g_s^2 N}{16\pi^2} G\tilde{G} + \frac{e^2 E}{16\pi^2} F\tilde{F}, \quad (1.13)$$

where  $N$  and  $E$  are respectively the QCD and EM anomaly coefficients. From eq. (1.13) the axion-photon coupling can be written as

$$g_{a\gamma}^0 = \frac{\alpha}{2\pi f_a} \frac{E}{N}. \quad (1.14)$$

In eq. (1.12) the axion-gluon-gluon term can be eliminated by the field-dependent axial transformation of the quark fields

$$q \rightarrow e^{i\gamma_5 \frac{a}{2f_a} Q_a} q, \quad (1.15)$$

where  $Q_a$  is a matrix acting on the quark fields with trace 1. Chiral Perturbation Theory can be used to derive the axion potential and the axion mass [36, 37]

$$\begin{aligned} V(a, \pi^0) &= -m_\pi^2 f_\pi^2 \sqrt{1 - \frac{4m_u m_d}{(m_u + m_d)^2} \sin^2\left(\frac{a}{2f_a}\right)} \cos\left(\frac{\pi^0}{f_\pi} - \phi_a\right), \\ \tan \phi_a &= \frac{m_u - m_d}{m_u + m_d} \tan\left(\frac{a}{2f_a}\right). \end{aligned} \quad (1.16)$$

It corresponds to  $Q_a = \frac{1}{2}\text{diag}(1, 1)$  and has minimum in  $(a, \pi^0) = (0, 0)$ .

## 1.4 UV completions of the axion effective Lagrangian

UV completions of the axion effective Lagrangian can be divided in two classes: models of the Dine-Fischler-Srednicki-Zhitnitsky (DFSZ) type [38, 39] and models of the Kim-Shifman-Vainshtein-Zakharov (KSVZ) type [40, 41]. One crucial difference is that for the former SM particles are charged under the PQ symmetry so that the couplings between the axion and the SM fermions acquire a contribution proportional to the quarks and leptons PQ charges. In KSVZ models SM fermions and the electroweak Higgs fields do not carry PQ charges, the axion-electron coupling vanishes at leading order, and the leading contribution to the axion-nucleon and axion-pion couplings only depends on the  $G\tilde{G}$  term.

More specifically, the KSVZ model proposes a vector-like fermion  $Q$  with (3,1,0) SM charges  $SU(3) \times SU(2)_L \times U(1)_Y$  and a SM singlet  $\Phi \sim (1, 1, 0)$ . Their interaction

$$\mathcal{L}_{\text{KSVZ}} = |\partial_\mu \Phi|^2 + \bar{Q} i \not{D} Q - \left( y_Q \bar{Q}_L Q_R \Phi + \text{h.c.} \right) - V(\Phi), \quad (1.17)$$

with potential

$$V(\Phi) = \lambda_\Phi \left( |\Phi|^2 - \frac{v_a^2}{2} \right)^2. \quad (1.18)$$

The  $U(1)_{\text{PQ}}$  symmetry is

$$\Phi \rightarrow e^{i\alpha} \Phi, \quad Q_L \rightarrow e^{i\alpha/2} Q_L, \quad Q_R \rightarrow e^{-i\alpha/2} Q_R \quad (1.19)$$

and the axion is  $\Phi$  Goldstone mode.

In this model the  $E/N$  parameter is 0 as there is no EM anomaly.

The DFSZ model BSM content consists of two Higgs doublets  $H_{u,d}$  and a complex scalar field  $\Phi$  with charges

$$H_u \sim \left(1, 2, -\frac{1}{2}\right), \quad H_d \sim \left(1, 2, \frac{1}{2}\right), \quad \Phi \sim (1, 1, 0). \quad (1.20)$$

The potential is made of all the moduli terms allowed by gauge invariance plus a non-hermitian operator  $\lambda H_u H_d \Phi^{\dagger 2}$ . The latter is responsible for the explicit breaking

$$U(1)_{H_u} \times U(1)_{H_d} \times U(1)_\Phi \rightarrow U(1)_Y \times U(1)_{\text{PQ}} \quad (1.21)$$

DFSZ models can have two variants of Yukawa couplings. The first species or  $d$ -type is

$$\mathcal{L}_{\text{DFSZ-I}}^Y = -Y_U \bar{q}_L u_R H_u - Y_D \bar{q}_L d_R H_d - Y_E \bar{\ell}_L e_R H_d + \text{h.c.} \quad (1.22)$$

and has  $E/N = 8/3$ . The second species or  $u$ -type is

$$\mathcal{L}_{\text{DFSZ-II}}^Y = -Y_U \bar{q}_L u_R H_u - Y_D \bar{q}_L d_R H_d - Y_E \bar{\ell}_L e_R \tilde{H}_u + \text{h.c.} \quad (1.23)$$

and has  $E/N = 2/3$ .

Each of the  $H_u$ ,  $H_d$  and  $\Phi$  get a VEV ( $v_u$ ,  $v_d$  and  $v_\Phi$  respectively) and a phase. The axion is a superposition of these phases and its VEV will be

$$v_a^2 = v_\Phi^2 + v^2 (\sin 2\beta)^2, \quad (1.24)$$

where  $v$  is the usual Higgs VEV (246 GeV) and  $\sin \beta := v_u/v$ .

Beyond the basic KSVZ and DFSZ models, other BSM completions featuring an axion were proposed, enhancing or suppressing some of the effective lagrangian couplings.

## 1.5 Axion-Like Particles

An Axion-Like Particle is a particle having the same effective Lagrangian as an axion but whose couplings are not correlated to each other so that this BSM Particle allowed phase space can become wider, which is crucial considered that the PQ axion is very constrained by data [42]. This overcomes the fact that models of QCD axions like those described in section 1.4 have a rather strict relation between the axion mass and  $f_a$ . Such a configuration is largely motivated in the literature in many directions: ALPs are viable DM candidates [43–46] and, in some configurations, can solve the strong CP problem too. ALPs with masses below the MeV scale can affect the Big Bang Nucleosynthesis [47], the evolution of stars and the Cosmic Microwave Background; they may explain the transparency of the Universe to very high-energy  $\gamma$ -rays [48], the over-efficient cooling of certain classes of stars [49] and the unidentified 3.55 keV line from Andromeda and galaxy clusters [9, 50].

But Also ALPs are an ingredient of many BSM theories. For example in String Theory Axion Like Particles emerge from compactification [51, 52]; or in Supersymmetric Theories, whose R-axion gathered great attention in the past years: it is the pseudo Nambu-Goldstone boson of the R-symmetry breaking in low-energy supersymmetry. The relation between R-symmetry and broken supersymmetry is not straightforward [53]: generically, there is broken supersymmetry if and only if there is an R-symmetry. But for building realistic models, an unbroken R-symmetry is problematic because it forbids Majorana gaugino masses. Having an exact, but spontaneously broken R-symmetry is also problematic, as it leads to a light R-axion (though including gravity can help). Finally explicitly breaking the R-symmetry means that we should live in a metastable state. Specifically, in [54] it is remarked that the existence of an R symmetry is a necessary condition for supersymmetry breaking; a spontaneously broken R symmetry is a sufficient condition provided

two conditions are satisfied in turn: genericity and calculability. By genericity the authors mean that the effective Lagrangian is a generic Lagrangian consistent with the symmetries of the theory; calculability means that the low energy theory can be described by a supersymmetric Wess-Zumino effective Lagrangian without gauge fields. Therefore [54] show that, since genericity is not a feature of supersymmetric theories, even when nonperturbative renormalization is included, the R symmetry can in many cases be explicitly broken without restoring supersymmetry and so the axion can be given an acceptably large mass. Actually in [55] the authors argue that R symmetry should be explicitly broken because the cosmological constant can (and should) be cancelled by adding a constant term to the superpotential. This constant explicitly breaks any continuous R symmetry, and gives mass to the R axion. [55] found that in visible-sector models with supersymmetry breaking scale greater than  $10^5$  GeV, the axion is sufficiently heavy to evade astrophysical constraints. In nonrenormalizable hidden-sector models, the axion mass is of order the electroweak scale and can lead to cosmological difficulties. In renormalizable hidden-sector models, the axion mass is quite large, of order  $10^7$  GeV. Such an axion is cosmologically safe although, in an inflationary scenario, it can be a new source of gravitinos. If the reheat temperature after inflation is too high, the large gravitino abundance affects the successful predictions for the light elements.

The R-axion can have a direct impact on phenomenology, as argued by [56]: the authors discuss a limit of the NMSSM where a light axion is present in the Higgs spectrum. It appears as a result of an approximate global  $U(1)_R$  symmetry of the scalar potential, which is spontaneously broken. The mass of such an axion can be lighter than half the SM-like Higgs boson mass, implying that the axion-Higgs coupling could modify the SM-like Higgs boson collider signatures.

Recently model-independent constraints on the R-axion decay constant for R-axion masses in the GeV-TeV (colliders) ballpark were derived in [57], leaving open the possibility for R-axion to be the first measured sign of SUSY.

The possibility of detecting ALPs at collider has been intensely investigated in these years [58–64]: traditional searches for Axion-like particles (ALPs) span orders of magnitude in ALP interaction strength but have to focus on the low mass region; in [58] the authors show how present and future colliders are able to cover the low mass region and extend the sensitivity to larger masses until the TeV range, highlighting the fact that future colliders will be able to close a region of the parameter space which would be inaccessible to, for example, helioscopes and existing beam dump experiments. A specific example of an ALP whose mass may be within the colliders reach is a theory having the ALP as a member of a composite Higgs sector [65, 66]. In these models,  $m_a^2 \sim \frac{y_f \Lambda^3}{16\pi^2 f}$ , where  $y_f$  is the Yukawa coupling of a fermion and  $\Lambda$  is the scale of heavier states in the theory. With  $f$  and  $\Lambda$  around the electroweak-TeV scale, the mass of the ALP can be anywhere in the sub-GeV to the multi-TeV region. In this mass range, ALPs are largely irrelevant for astrophysics and cosmology, but they can have a number of interesting implications for particle physics. For example, ALPs have been considered as an explanation for the anomalous magnetic moment of the muon [62, 67, 68] or for exotic resonances in nuclear transitions [69]. Moreover, it has been pointed out that ALPs may play a crucial role in electroweak symmetry breaking and the solution of the hierarchy

problem [70] via the so-called relaxion mechanism [71].

This justifies our decision to study ALPs at Belle II, providing the advantage of its great luminosity. In order to reproduce (and complete) the results from [72], we first of all need to consider their very same Lagrangian (refer to [73] for a precise treatment of each coupling up to two loop order):

$$\mathcal{L} = \frac{1}{2}\partial^\mu a\partial_\mu a - \frac{1}{2}m_a^2 a^2 - \frac{c_B}{4f_a} a B^{\mu\nu} \tilde{B}_{\mu\nu} - \frac{c_W}{4f_a} a W^{i,\mu\nu} \tilde{W}_{\mu\nu}^i, \quad (1.25)$$

Here an Axion-Like Particle is coupled to electroweak gauge bosons, as arises quite naturally in string models [52]. Couplings to fermions or gluons are not considered. This restriction is well-motivated in models where the interactions between ALPs and the SM arise from new heavy fermions that do not carry colour charge. The reason we are interested in ALPs that do not couple to gluons and fermions is that such interactions typically lead to flavour-changing processes which are tightly constrained by searches for rare decays [44, 63]. A coupling to the Higgs boson too is excluded as, while operators in eq. (1.25) have dimension 5, vertices with ALPs and Higgs have dimension 6 and including them would not change much the present results [64].

After EW symmetry breaking

$$\mathcal{L} \supset -\frac{g_{a\gamma\gamma}}{4} a F_{\mu\nu} \tilde{F}^{\mu\nu} - \frac{g_{a\gamma Z}}{4} a F_{\mu\nu} \tilde{Z}^{\mu\nu} - \frac{g_{aZZ}}{4} a Z_{\mu\nu} \tilde{Z}^{\mu\nu} - \frac{g_{aWW}}{4} a W_{\mu\nu} \tilde{W}^{\mu\nu}, \quad (1.26)$$

$$g_{a\gamma\gamma} = \frac{c_B \cos^2 \theta_W + c_W \sin^2 \theta_W}{f_a}, \quad g_{a\gamma Z} = \frac{\sin 2\theta_W (c_W - c_B)}{f_a}. \quad (1.27)$$

For this dissertation we will stick to  $g_{a\gamma\gamma} \neq 0$ ,  $g_{a\gamma Z} = 0$ , which is simply obtained by choosing  $c_B = c_W$ .  $g_{aZZ}$  and  $g_{aWW}$  will not play a role at Belle II: with a Centre of Mass energy  $\sqrt{s} = 10.58$  GeV,  $Z$  and  $W$  production are suppressed.

## 1.6 ALP experimental facilities

ALP detection facilities are all around the world. Among them ABRACADABRA [74], HAYSTAC [75], CASPEr [76], MADMAX [77], QUAX [78], are some examples of detectors of ALPs as DM in the galactic halo; Baby IAXO [79] and IAXO [12], CAST [80], XENON1T [81] look for axions from the Sun; DESY ALPS II [82] is built for lab detection.

The idea of haloscopes is due to Sikivie [83]: he computes the axion density assuming that they make up the DM galactic halo and provides an estimate of the photon-axion conversion cross section in the presence of an inhomogeneous magnetic field. He proposes to use a variable frequency cavity so that it can be tuned to the energy of Milky Way axions.

Detectors looking for axions from the Sun are called Helioscopes: (taking into account the light bending from the atmosphere) they point to our star and convert the (hypothesized) solar axion flux into light by the means of a magnetic field, exploiting the fact that, if axions exist, Maxwell equations would be modified as, for example, in [84] (see [85] for a recent generalization).

ALP lab detection are somewhat similar: instead of considering axions from the Sun, they use a high power laser and convey it inside a production cavity having a magnetic field, which should excite photon-ALP conversion. The so produced flux of photons and ALPs travels towards a barrier, which is able to stop the former but not the latter. Therefore, in the subsequent regeneration cavity (having again a magnetic field) ALPs can convert back to photons. If at the end of the chain any photon is detected, it can only be because ALPs converted back to photons (assuming ideally 0 background).

## 1.7 The many body phase space

Now that we explained why ALPs are such a relevant particle to hunt for and that colliders may be a privileged place for hunting them, we can introduce some interesting aspects of the collider search itself. At a lepton collider the most important channels to see the ALP are an ALP-strahlung (see fig. 1.1c)

$$e^+e^- \rightarrow \gamma a, \quad (1.28)$$

or a Vector-Boson Fusion (VBF, see figs. 1.1a and 1.1b)

$$e^+e^- \rightarrow e^+e^-a. \quad (1.29)$$

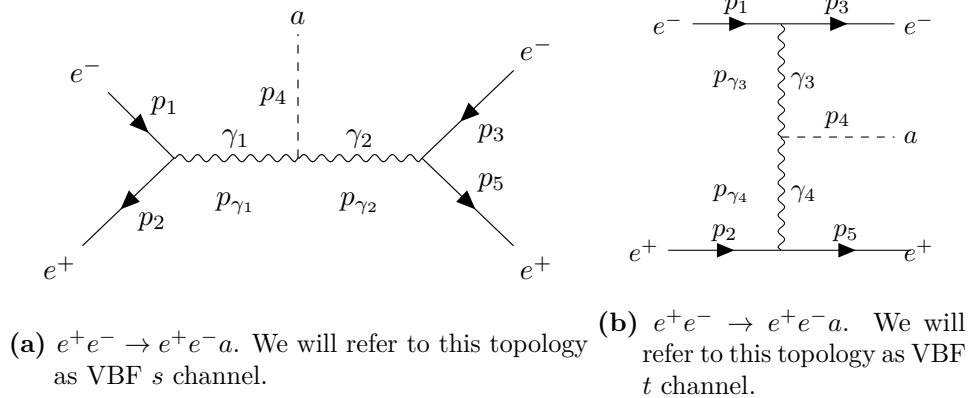


Figure 1.1. ALP channels at Belle II.

Our interest in the VBF is not merely academic: if on the one hand it may look like it can be discarded at Belle II as collider acceptance can highly suppress it, on the other hand it proved to be worth looking at, for example, in the Higgs discovery; even more, it is receiving persistent attention for the future accelerators construction [86,87], as future high energy machines will see the  $s$  channels more and more suppressed with respect to the  $t$  channels.

We will embed this search at SuperKEKB. The sensitivity of its detector is reported in [72] (see section 9.1 for more details on Belle II and section 9.2 for its ALP sensitivity state of the art). Dolan et al. neglect the VBF as it is claimed that the ALP-strahlung is way more important. We asked ourselves: is it really so? A quick inspection of the VBF scattering amplitude shows that if  $e^\pm$  were massless and collinear to the beam, the cross section would diverge (we show this step by step in section 2.3.1). Although electrons are not massless nor they can be detected when flying close to the beampipe, VBF can overcome the ALP-strahlung. Our first task has been to analytically determine how this happens. The aforementioned divergence made our analytic attempts complicated. The solution we found relies in Gram Determinants (GDs): the first part of this dissertation (part I) is devoted to them. That they solve this kind of problems was known almost since the bubble chambers times. We can trace back the history of the use of the phase space properties for discovery back to Dalitz work [88]. He wanted to characterise the  $J^P$  of the  $K^+$  from the  $K^+ \rightarrow \pi^+\pi^-\pi^+$  decay. Similar processes have only two degrees of freedom, that can be expressed in a Lorentz invariant form, for example, as invariant masses of two couples of final state particles. Basing on the population of a two dimensional plot of such variables,  $J^P$  could be predicted. Dalitz was working in a non relativistic frame, but soon Fabri [89] improved his work by implementing relativistic corrections.

The need for a mathematical grasp on the  $1 \rightarrow n$  decay phase space was soon fulfilled by Byers and Yang: in [90] they provide the phase space region and density via the Gram Determinants language. However a  $1 \rightarrow n$  decay has  $3n - 7$  degrees of freedom and dealing with a  $(3n - 7)$ -dimensional phase space density may be cumbersome. Therefore it is still worth to specialise to some  $n$  and study some phenomenologically relevant phase space distributions. This is the case of [91], that considers  $n = 4$ . Phase space distributions are provided for trivial matrix elements, emphasising how symmetry can help us transform some distributions into some others. Nyborg et al. also extend the validity of their results to  $2 \rightarrow 4$  scatterings with special resonances. Another specialization of [90] is due to Morrow [92], studying the  $2 \rightarrow 3$  scattering as a generalization of Kibble's treatment. He implicitly provides 2 dimensional distributions of the phase space (neglecting the matrix element). Kajantie and Lindblom [93] start from Morrow's work and add to it the explicit analytic form of 1 and 2 dimensional phase space distributions.

Finally, what Byers and Yang express formally for the  $1 \rightarrow n$  generic decay is made explicit by Poon: in [94] the author derives all the determinantal relations which are necessary for expressing the  $1 \rightarrow n$  phase space boundary.

The picture that emerges is that scattering phase spaces and their distributions are dense of information. If a scattering includes a BSM particle, model independent kinematic features can be used to recover the new particle mass. The first quantities that have been exploited in this sense are one dimensional kinematic features, namely

edges and endpoints in invariant masses distributions [95–100]. However [101] show that multi-dimensional features can be way more effective: the authors perform a likelihood analysis exploiting the integrable divergence on the phase space boundary<sup>1</sup> of many-body processes and compare it to a quality of fit analysis of classical edges and endpoints of squared masses distributions. They obtain a great improvement on the latter in two directions: via multi-dimensional analysis one can determine not only NP mass differences but also the overall scale of masses; moreover it is viable in case of low signal statistics too, which can likely be the case of BSM Physics. Another direction for exploiting the dimension 4 Symmetric Gram Determinant<sup>2</sup>  $\Delta_4$  is found in [102]: they realise that the phase space boundary is both an accumulation surface for events thanks to the integrable divergence and a sharp limit beyond which signal events can not be found any more. To use these informations it is necessary to study the fully derivative phase space, whose technical complication is overcome by the means of Voronoi Tassellations. The  $\Delta_4$  variable can itself be a Lorentz invariant function to inspect as a discovery variable at colliders, as proposed by [103].

This dissertation adds some new results on top of the  $1 \rightarrow n$  phase space study tradition because we consider non trivial matrix elements and we provide explicit analytic cross section distributions. The necessity of such an improvement is blatant as pure phase space knowledge may not be enough for BSM discovery. For the sake of clarity we focus on the simplest matrix element (pure propagators) but we could show that there is no problem in handling more complicated cases. At the same time we could verify that there is a large ensemble of configurations for which pure propagators matrix elements is as good as the full matrix element, showing that our improvement over the state of the art is also sufficient. On top of that, it is worth noticing that the  $\Delta_4$  variable got re-discovered having in mind some specific decay chains that may be useful for SUSY discovery. This dissertation introduces two new topologies to the discussion, specifically realised here in figs. 1.1a and 1.1b. This opens the possibility for many BSM models to be discovered thanks to Gram Determinants.

In sight of this, in chapter 2 I explain why Gram Determinants are the best tool to use in a  $2 \rightarrow 3$  scattering when the massless particles approximation is unviable; in chapter 3 I introduce the formalism and show that a generic scattering phase space volume can be easily expressed in terms of Gram Determinants inequalities. In chapter 4 I resume the Lorentz invariant expression of a  $2 \rightarrow 2$  scattering phase space and proceed to extend the same reasoning to the  $2 \rightarrow 3$  process. Some crucial Gram Determinants features are proved in this chapter, for example: the cross section integration domain is expressed by the means of the higher order possible GD (principal GD or PGD); successive integrations of the scattering amplitude are performed on regions expressed by lower order GDs; if the exact phase space is expressed via the PGD, lower order GDs can approximate it. I finally provide the analytic computations we were seeking: chapters 5 to 7 collect the most important, as well as original results of this part. In chapter 5 I derive some basic cross sections and distributions; in chapter 6 I highlight some

---

<sup>1</sup>We will show it in section 5.1.

<sup>2</sup>See chapter 3 for definition and properties

symmetries of the problem, by virtue of which I will be able to derive many distributions from the previously computed ones, without further calculations; lastly chapter 7 is devoted to the most complicated, yet most important distribution, that with respect to the final electron and final positron deflection angles. All these results serve us to justify two alternative computations: in chapter 8 we propose an approach similar to that used for the Higgs by Altarelli, Mele and Pitolli [104], and go through the history and application of the Equivalent Photon Approximation.

Once the VBF cross section is completely under control under the analytic point of view, we can proceed to the Phenomenology of this process. In part II we consider two cases: the ALP decays into photons within the detector (chapter 10), or the ALP does not decay into photons within the detector (chapter 11). If for the former, visible case we can already prove (fig. 10.5) that the VBF must be taken into account at Belle II as a viable channel for discovery, for the latter, invisible search we manage to produce a better sensitivity than the ALP-strahlung state of the art by the means of an elegant, original selection whose idea was inspired by our previous, analytic studies.



Part I

**Gram determinants**



## Chapter 2

# Gram Determinants motivation

In this chapter I motivate the use of Gram Determinants for the computation of our Vector Boson Fusion cross section: I will show you that this is not an academic *caprice*, some overshooting technology or an unnecessary complication by demonstrating the failure of any other technique we could think of to tackle our problem down (section 2.3). Neglecting the spin of the scattering particles is of great help but still asks for GDs to be employed (section 2.2). A possible further simplification may come from neglecting the electron mass as one may think that it is negligible with respect to Belle II Centre of Mass energy:

$$\sqrt{s} = 10.58 \text{ GeV} \gg M_e = 511 \text{ keV}. \quad (2.1)$$

In section 2.3 we demonstrate what troubles  $M_e \neq 0$  brings in. We will show that both the  $\frac{M_e}{\sqrt{s}} \rightarrow 0$  limit (section 2.3.1) and a more refined Laurent expansion around  $\frac{M_e}{\sqrt{s}} = 0$  diverge.

### 2.1 The pseudoscalar matrix element

I will show you how the pseudoscalar nature of the ALPs makes our matrix element difficult to deal with and propose to ignore the spin of all particles for the moment.

The s and t channel matrix elements for figs. 1.1a and 1.1b are respectively

$$\mathcal{M}_s = -e^2 g_{a\gamma\gamma} \epsilon^{\mu\nu\rho\sigma} p_4^\sigma (p_3 + p_5)^\rho \frac{[\bar{v}_{r_2}(p_2)\gamma^\mu u_{r_1}(p_1)][\bar{u}_{r_3}(p_3)\gamma^\nu v_{r_4}(p_4)]}{s(p_3 + p_5)^2}, \quad (2.2)$$

$$\mathcal{M}_t = -e^2 g_{a\gamma\gamma} \epsilon^{\mu\nu\rho\sigma} p_4^\sigma (p_2 - p_5)^\rho \frac{[\bar{u}_{r_3}(p_3)\gamma^\mu u_{r_1}(p_1)][\bar{v}_{r_2}(p_2)\gamma^\nu v_{r_4}(p_4)]}{(p_1 - p_3)^2(p_2 - p_5)^2}, \quad (2.3)$$

where we named fourmomenta as in fig. 1.1 and followed the notation of [105] for spinors. The polarization of the fourmomentum  $p_i$  is  $r_i$ . We need to compute the scattering amplitude squared modulus and sum over all polarizations  $r_i, i \in \{1, 2, 3, 5\}$ :

$$|\mathcal{M}|^2 = \sum_{r_1} \cdots \sum_{r_5} |\mathcal{M}_s + \mathcal{M}_t|^2 = \sum_{r_i} (|\mathcal{M}_s|^2 + |\mathcal{M}_t|^2 + \mathcal{M}_{\text{int}}), \quad (2.4)$$

$$\mathcal{M}_{\text{int}} := \mathcal{M}_s \mathcal{M}_t^* + \mathcal{M}_s^* \mathcal{M}_t. \quad (2.5)$$

We defined  $\mathcal{M}_{\text{int}}$  the interference term. In all  $|\mathcal{M}_s|^2, |\mathcal{M}_t|^2, \mathcal{M}_{\text{int}}$ , after the polarization sum we will end with a contraction of two Levi-Civita Symbols with metric tensors and fourmomenta. For example, from [106], the two Levi-Civita Symbols will provide a determinant

$$\epsilon^{\alpha_1 \alpha_2 \alpha_3 \alpha_4} \epsilon^{\beta_1 \beta_2 \beta_3 \beta_4} = - \begin{vmatrix} g^{\alpha_1 \beta_1} & \cdots & g^{\alpha_4 \beta_1} \\ \vdots & & \vdots \\ g^{\alpha_1 \beta_4} & \cdots & g^{\alpha_4 \beta_4} \end{vmatrix}. \quad (2.6)$$

We decided to decouple the difficulties coming from the phase space integration from those due to the verbosity of a matrix element built as in eq. (2.6). In next section I will explain that this can be achieved by firstly ignoring all the spins in the theory, so to be able to solve any kind of physically meaningful theory secondly.

## 2.2 Ignoring the spin

The pseudoscalar nature of the ALP makes the matrix element non trivial. Let us get rid of it by considering a much simpler theory, that we will call Scalar Standard Model (SSM). At this stage one can not tell how far from the physical results we are stepping. For the impatient, section 7.3 provides some motivation of the goodness of this simplification. This will allow us to first address the issues caused by the potential divergences of the propagators, leaving the difficulty of integrating the full matrix element to a second step. The method that we propose for solving the first, more compelling problem, will prove viable even with more complicated matrix elements. In fact I was successful in integrating the matrix element from the theory in eq. (1.25) and compare the simplified VS the full result. I point the reader to appendix H for the results.

I now list SSM rules for a 1+3 dimensional theory<sup>1</sup>:

- Every SM particle is sent to a scalar neutral particle having the same mass.
- We will not bother with inventing new names, as it will be straightforward to understand to what theory we will be referring to.
- SSM only has one type of propagator: whatever virtual particle with fourmomentum  $p$  and mass  $m$  propagates like  $\frac{1}{p^2 - m^2}$ .
- All fields have mass dimension 1.
- All the Feynman rules of non-scalar particles are reduced to just couplings.

<sup>1</sup>The formalism I will introduce in these chapters can be generalised to arbitrary space and time dimensions but, having phenomenological applications as objective, I will stick to 1+3.

- Couplings do deserve a new name as they remarkably change their mass dimension. They will be named after the particles that enter the vertex. For example, if a vertex has two photons and one ALP, we will call it  $c_{a\gamma\gamma}$ , and so on (particles order is unimportant).
- Since each vertex must have dimension 4, the coupling:

$$[c_{\text{vertex}}] = 4 - n - 2m, \quad (2.7)$$

with  $n$  the number of fields in the vertex and  $2m$  the number of derivatives. It is an even number as derivatives can only contract among themselves in order to give the vertex a Lorentz scalar nature.

### 2.3 Failure of polar coordinates integration

Let us see why Gram Determinants are so necessary for carrying out a helpful analytic computation. As an example, we will write down  $|\mathcal{M}_t|^2$  in polar coordinates within the SSM we just introduced and try to solve the cross section integration. We will quickly get to integrations that can only be carried out numerically.

Some notation:

- Except when differently stated, we will consider to be in the CoM frame, whose energy is  $\sqrt{s}$ .
- Initial fourmomenta are

$$p_1 = \frac{1}{2\sqrt{s}} \left( s + m_1^2 - m_2^2, 0, 0, \lambda(s, m_1^2, m_2^2) \right) \xrightarrow{m_1, m_2 \rightarrow M_e} \left( \frac{\sqrt{s}}{2}, 0, 0, \sqrt{\frac{s}{4} - M_e^2} \right), \quad (2.8)$$

$$p_2 = \frac{1}{2\sqrt{s}} \left( s - m_1^2 + m_2^2, 0, 0, -\lambda(s, m_1^2, m_2^2) \right) \xrightarrow{m_1, m_2 \rightarrow M_e} \left( \frac{\sqrt{s}}{2}, 0, 0, -\sqrt{\frac{s}{4} - M_e^2} \right) \quad (2.9)$$

- $m_i$  is the mass of the  $i$ th particle. For the sake of generality we will use the  $m_i$  and specialise to the case  $m_i = M_e \forall i \neq 4, m_4 = M_a$  when we will deal with specific aspects of our scattering.
- $E_i, \theta_i, \phi_i$  are the energy, polar angle, azimuthal angle of the  $i$ th particle.
- $c_i, s_i$  are the cosine and sine of the  $i$ th particle polar angle respectively.
- $c_{ij}$  is the cosine between the  $i$ th and  $j$ th particle.
- $c_i^\phi, s_i^\phi$  are the cosine and sine of the  $i$ th particle azimuthal angle respectively.

Following the above method, the matrix element modulo squared is

$$|\mathcal{M}_t|_{\text{SSM}}^2 = \left( \frac{c_{ee\gamma}^2 c_{\gamma aa}}{\mathcal{P}} \right)^2, \quad (2.10)$$

$$\begin{aligned} \mathcal{P} := & \left( m_1^2 + m_3^2 - \sqrt{s}E_3 + \sqrt{s - 4m_1^2} \sqrt{E_3^2 - m_3^2} c_3 \right)^2 \\ & \cdot \left( m_2^2 + m_5^2 - \sqrt{s}E_5 - \sqrt{s - 4m_2^2} \sqrt{E_5^2 - m_5^2} c_5 \right)^2, \end{aligned} \quad (2.11)$$

The total cross section is

$$\sigma = \int \frac{d^3 p_3}{2E_3} \frac{d^3 p_4}{2E_4} \frac{d^3 p_5}{2E_5} \delta^{(4)}(p_1 + p_2 - p_3 - p_4 - p_5) \frac{\sigma_0}{\mathcal{P}}, \quad (2.12)$$

with

$$\sigma_0 = \frac{|c_{ee\gamma}|^4 |c_{a\gamma\gamma}|^2}{(2\pi)^5 \sqrt{\lambda_{\text{in}}}}, \quad \lambda_{\text{in}} := \lambda(s, m_1^2, m_2^2). \quad (2.13)$$

Let us integrate  $p_4$  away with the Dirac  $\delta$

$$\begin{aligned} \int \frac{d^3 p_4}{2E_4} \frac{\delta^{(4)}(p_1 + p_2 - p_3 - p_4 - p_5)}{\mathcal{P}} &= \\ \int d^4 p_4 \delta(p_4^2 - m_4^2) \frac{\delta^{(4)}(p_1 + p_2 - p_3 - p_4 - p_5)}{\mathcal{P}} &=: \frac{\delta(f)}{\mathcal{P}_4}, \end{aligned} \quad (2.14)$$

where I defined  $\mathcal{P}_4$  the  $\mathcal{P}$  from eq. (2.11) in which I substitute  $p_4 \rightarrow p_1 + p_2 - p_3 - p_5$ :

$$\mathcal{P}_4 := \mathcal{P}(p_4 \rightarrow p_1 + p_2 - p_3 - p_5), \quad (2.15)$$

and the Dirac  $\delta$  argument to be the function

$$\begin{aligned} f := & (p_1 + p_2 - p_3 - p_5)^2 - m_4^2 \\ & = s - 2\sqrt{s}(E_3 + E_5) + m_3^2 + m_5^2 + 2(E_3 E_5 - |\vec{p}_3| |\vec{p}_5| c_{35}) - m_4^2. \end{aligned} \quad (2.16)$$

Express the  $p_3$  and  $p_5$  integrations in terms of polar coordinates. First notice that we have the freedom to rotate the system around the  $z$  axis in order to always annihilate the azimuthal angle of  $\vec{p}_5$ . The  $d\phi_5$  is integrated away and amounts to a  $2\pi$  factor. Let us then update

$$\sigma_0 = \frac{|c_{ee\gamma}|^4 |c_{a\gamma\gamma}|^2}{(2\pi)^4 \sqrt{\lambda(s, m_1^2, m_2^2)}}. \quad (2.17)$$

Name the remaining polar coordinates integrations as  $d\phi_3 d\mu_P$ :

$$d\mu_P := \frac{|\vec{p}_5|^2 d|\vec{p}_5| |\vec{p}_3|^2 d|\vec{p}_3| d\cos\theta_3 d\cos\theta_5}{2E_3 2E_5}. \quad (2.18)$$

The cross section becomes

$$\sigma = \sigma_0 \int d\mu_P d\phi_3 \frac{\delta(f(E_3, E_5, c_3, c_5, \phi_3))}{\mathcal{P}_4}. \quad (2.19)$$

We now list the strategies we thought about for solving this integral. Due to the Dirac  $\delta$ , it is equivalent to searching for a way of solving eq. (2.16) that does not spawn too much of a monstrous integrand:

1. Solve  $f = 0$  as a function of  $E_3$  (or, symmetrically,  $E_5$ ). The complexity is twofold:
  - (a) The presence of both  $E_3$  and  $|\vec{p}_3| = \sqrt{E_3^2 - M_e^2}$  leads to a two branch solution. For some values of  $(E_5, c_3, c_5, \phi_3)$  we are meant to select the first and for some other the second.
  - (b) When the integrand is evaluated onto any one of the branches, its dependence on  $(E_5, c_3, c_5, \phi_3)$  becomes so complicated that there are no tabulated integrals for solving our problem (cf. [107]).
2. An attempt with  $c_3$  (or, symmetrically,  $c_5$ ) goes the same way as the energy attempt, as the Dirac  $\delta$  argument depends on  $c_{35}$  which is a function of both  $c_3$  and  $\sqrt{1 - c_3^2}$ .
3. Solve  $f = 0$  for  $\phi_3$ . This looks easy as  $f$  is linear in  $c_{35}$ , hence in  $c_3^\phi$ , but brings with itself a non trivial Dirac  $\delta$  Jacobian. Say that  $f = 0$  if  $\phi_3 = \bar{\phi}$ , then

$$\sigma = \sigma_0 \int d\mu_P \frac{1}{\mathcal{P}_4} \frac{1}{\left| \frac{df}{d\phi_3} \right|_{\phi_3 = \bar{\phi}}}. \quad (2.20)$$

Again there are no tabulated integrals for next integrations.

The above attempts show that polar coordinates integration is a path that leads us very soon to numerical calculation as the only option.

All the complications listed above come from the presence of  $M_e$ . Since

$$\epsilon := \frac{M_e}{\sqrt{s}} \ll 1, \quad (2.21)$$

one may think to work in the approximation  $\epsilon = 0$ . This is next section task.

### 2.3.1 $M_e \rightarrow 0$ limit

In the  $M_e \rightarrow 0$  limit the cross section integration would be almost trivial:

$$\begin{aligned} \sigma(\epsilon = 0) &= \sigma_0 \int d\mu_P d\phi_3 \frac{\delta(s - 2E_5\sqrt{s} - 2E_3(\sqrt{s} - E_5(1 - c_{35})))}{(sE_3E_5(1 - c_3)(1 + c_5))^2} \\ &= 2\pi\sigma_0 \int dE_5 dc_3 dc_5 \frac{1}{(s(1 - c_3)(1 + c_5))^2 E_5 (s - 2E_5\sqrt{s} - M_a^2)}. \end{aligned} \quad (2.22)$$

Here the Dirac  $\delta$  argument is linear in the energies hence there are no double branches, plus there are tabulated solutions to all of the integrals, but the result is blossoming with divergences! Precisely on  $c_3 \rightarrow 1, c_5 \rightarrow -1$  and  $E_5 \rightarrow 0$ , to which we will be referring to the VBF poles.

One may think to put a cutoff on them. This is the simplest way to pursue when you are working at a collider, since generally you get cutoffs by construction, literally, as detectors in general will miss too soft particles or particles along the beam pipe. For example, assume that in the CoM frame all particles have both energies and polar angles bounded from above <sup>2</sup> and from below:

$$E_i^* \in [E_l, E_h], \quad E_l \gg M_e \quad c_i^* \in [c_l, c_h], \quad c_l > -1, c_h < 1. \quad (2.23)$$

The exact cross section in this case will be:

$$\begin{aligned} \sigma(\epsilon = 0) \Big|_{\text{cutoff}} &= 2\pi\sigma_0 \int_{E_l}^{E_h} dE_5 \int_{c_l}^{c_h} dc_3 \int_{c_l}^{c_h} dc_5 \frac{1}{(s(1-c_3)(1+c_4))^2 E_5 (s - 2E_5\sqrt{s} - M_a^2)} \\ &= \frac{2\pi\sigma_0}{s^2(s - M_a^2)} \frac{(c_h - c_l)^2}{(c_h^2 - 1)(c_l^2 - 1)} \log \left( \frac{E_l}{E_h} \frac{s - 2E_h\sqrt{s} - M_a^2}{s - 2E_l\sqrt{s} - M_a^2} \right), \end{aligned} \quad (2.24)$$

which is plotted in fig. 2.1

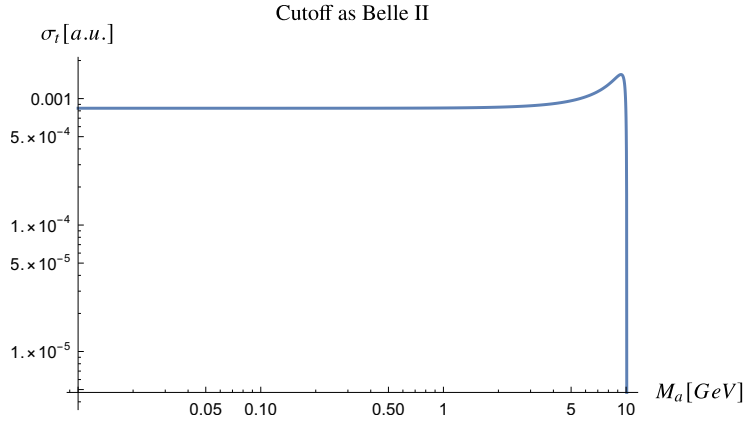


**Figure 2.1.** Cross section of the t channel of the scattering  $e^+e^- \rightarrow e^+e^-a$  in the scalar theory when energies and angles have a cutoff. Belle II parameters have been used, check for them in appendix D. Couplings have been set to 1.

But this is not what we wanted to do! In the introduction we agreed to look for some tools allowing us to thoroughly study this cross section to demonstrate that

<sup>2</sup>Instrumentation may not introduce an upper bound on single energies. Nonetheless, consider a  $2 \rightarrow n$  scattering with at least some visible particles in the final state. At a collider this means that they will have at least some lower bounds on energy and lower and upper bounds on the polar angle. If one has to inject a minimal energy in some particles, the others will not have access to the maximal energy they may reach in an unbounded phase space. This explains the energy upper bound  $E_h$  in eq. (2.23).

there exists an improved angular coverage of the detector such that VBF can be seen at Belle II on equal footing as the ALP-strahlung. You may argue: take eq. (2.24) and tune your cutoffs until you reach your goal, ideally using  $M_e$  itself as a cutoff. A similar strategy lacks the mathematical rigour that is needed in such a delicate situation in several directions. To be more explicit, the strategy would be using eq. (2.24) (i.e. taking  $M_e = 0$  everywhere within the cross section integral), but instead of eq. (2.23) one should use

$$\begin{aligned} 0 \leq E_l(M_e) \leq E_{3,5}^* \leq E_h(M_e) \leq \frac{\sqrt{s}}{2}, \\ -1 \leq c_l(M_e) \leq c_{3,5}^* \leq c_h(M_e) \leq 1. \end{aligned} \quad (2.25)$$

First, in these inequalities the = signs are not viable. As long as  $M_e \neq 0$  the  $2 \rightarrow 3$  phase space is such that the VBF poles are excluded. On the contrary, in eq. (2.24) we would get

$$\begin{aligned} \lim_{\epsilon \rightarrow 0} (p_1 - p_3)^2 \Big|_{c_3=1} &= \lim_{\epsilon \rightarrow 0} 2M_e^2 - E_3 \sqrt{s} + \sqrt{E_3^2 - M_e^2} \sqrt{s - 4M_e^2} \\ &= 0 \quad \forall E_3, \end{aligned} \quad (2.26)$$

$$\lim_{\epsilon \rightarrow 0} (p_1 - p_3)^2 \Big|_{E_3=M_e} = \lim_{\epsilon \rightarrow 0} M_e(2M_e - \sqrt{s}) = 0 \quad \forall c_3. \quad (2.27)$$

$(p_1 - p_3)^2 = 0$  can only happen on  $M_e \rightarrow 0$ . In fact, in  $p_1$  rest frame the electron energy is  $E_3^{(p_1)}$  and

$$(p_1 - p_3)^2 = 2M_e^2 - 2M_e E_3^{(p_1)}, \quad (2.28)$$

which annihilates iff  $p_3$  is still too. Therefore in the CoM frame we would have identical  $p_1$  and  $p_3$ . But this is not possible as

$$\max E_3 = \frac{s - M_a^2 - 2M_e M_a}{2\sqrt{s}} < \frac{\sqrt{s}}{2} \quad \forall M_a > 0. \quad (2.29)$$

This proves why  $M_e \neq 0$  avoids divergences in eq. (2.19) and concludes our demonstration that we can not allow for equalities in eq. (2.25). Still, the smallest  $(p_1 - p_3)^2$  is realized when  $E_3$  and  $c_3$  are the biggest in the CoM frame. This will be the most important region of our phase space.

I can give you at least three reason why inequalities too in eq. (2.25) would lead us to the wrong result.

First of all, the only way to correctly find  $E_{l,h}(M_e)$  and  $c_{l,h}(M_e)$  is solving the full  $2 \rightarrow 3$  phase space, which is exactly what we are trying to avoid to do in polar coordinates.

Second, in eq. (2.24) the only small quantity that was put to 0 is  $M_e$  but nothing holds other quantities to be even smaller, like  $M_a$  or  $\sqrt{s} - M_a$ . To properly treat these configurations we should dedicate a series expansion to each case: what should have been a simplifying shortcut is splitting down in too many alleys.

Third,  $E_3 \sim \max E_3, c_3 \sim 1, E_5 \sim \max E_5, c_5 \sim -1$  is exactly the region where the

matrix element is maximised. Cutting away even narrow slices of the phase space in that region can produce an error that can be bigger than the cross section estimate itself.

A more careful way of proceeding may be performing a Laurent expansion of the cross section. To expand  $\sigma_t(\epsilon)$  around some point  $x$  (we will take  $x = 0$ ), there needs to exist an annulus (donut) around  $x$  in which  $\sigma_t(\epsilon)$  is holomorphic<sup>3</sup>. This is our case. Within the annulus take a Jordan curve (plane, simple, closed curve, i.e. it does not intersect itself) and call it  $\gamma$ . The series will be

$$\sigma_t = \sum_{k=-\infty}^{\infty} a_k (\epsilon - x)^k, \quad (2.30)$$

$$a_k = \frac{1}{2\pi i} \oint_{\gamma} \frac{\sigma_t(z)}{(z-x)^{k+1}} dz. \quad (2.31)$$

Pick your favourite representation of the Dirac  $\delta$  as a limit of a series of analytic functions

$$\int dx \delta(f(x)) = \int dx \lim_{n \rightarrow \infty} \mathcal{D}_n(f(x)) = \lim_{n \rightarrow \infty} \int dx \mathcal{D}_n(f(x)), \quad (2.32)$$

so that eq. (2.19) becomes

$$\sigma_t = \sum_{k=-\infty}^{\infty} (\epsilon - x)^k \frac{1}{2\pi i} \oint_{\gamma} dz \frac{\sigma_0}{(z-x)^{k+1}} \lim_{n \rightarrow \infty} \int d\mu_P d\phi_3 \frac{\mathcal{D}_n}{\mathcal{P}_4}. \quad (2.33)$$

Consider

$$\sigma_t = \lim_{n \rightarrow \infty} \sigma_0 \int d\mu_P d\phi_3 \left( \frac{1}{2\pi i} \sum_{k=-\infty}^{\infty} (\epsilon - x)^k \oint_{\gamma} \frac{dz}{(z-x)^{k+1}} \frac{\mathcal{D}_n}{\mathcal{P}_4} \right). \quad (2.34)$$

If the integration swaps I operated with respect to eq. (2.33) are not allowed, the Laurent series is not viable *ab initio*, so let me assume they are allowed. This means we are now integrating over  $d\mu_P, d\phi_3$  the Laurent series I highlighted in brackets. I introduced the analytic expression of the Dirac  $\delta$  so that now we can advocate the residue theorem onto the holomorphic function  $\frac{\mathcal{D}_n}{\mathcal{P}_4}$ . The  $k = 0$  case corresponds to evaluating the integrand onto  $\epsilon = 0$ , hence to eq. (2.22). We already showed it diverges. Plus, its divergence can not be cured by any other series term as they will be proportional to a different  $\epsilon$  power.

---

<sup>3</sup>Since we work in  $\mathbb{R}$ , this is equivalent to analytic.

## Chapter 3

# Gram Determinants are the language of Scattering Amplitudes

We are hopefully now convinced of the necessity of introducing some new technology to analytically recover the cross section of the process

$$e^+e^- \rightarrow e^+e^- a. \quad (3.1)$$

Our difficulties come from the fact that a scattering amplitude is expressed in terms of fourmomenta scalar products. These are complicated functions of polar coordinates as they are expressed in terms of both  $E_i$  and  $|\vec{p}_i| = \sqrt{E_i^2 - m_i^2}$ , both  $c_i$  and  $\sqrt{1 - c_i^2}$ . No series expansion can absorb this complexity away. But what if we gave up on expressing scattering amplitudes in polar coordinates and simply use scalar products as our new variables? The following sections are devoted to this task. We build the necessary common ground of definitions and properties in section 3.1. In section 3.3 I provide a dictionary for going from polar coordinates to GDs. In section 3.4 I demonstrate one of the most important results of the GDs technique: the phase space boundary is the locus where the Principal Gram Determinant is 0 (cf. definition 4).

### 3.1 Definitions and properties of Gram matrices

In this section I will list all the properties and definitions that I will use later. The reader may also skip this section and come back to it whenever she needs to. A recent reference for most of these properties is appendix C from [108]. A more complete but older reference is appendix A from [109].

**Definition 1** (Gram Matrix).

Consider a vector space and two sets of elements in this space,  $\{p_1, \dots, p_n\}$  and  $\{q_1, \dots, q_n\}$ . For our purposes, let the  $p_i, q_i$  be fourmomenta and the vector space multiplication be the Minkowskian product. Define the  $n \times n$  Gram Matrix

$$M \left( \begin{array}{c} \{p_1, \dots, p_n\} \\ \{q_1, \dots, q_n\} \end{array} \right) = \begin{pmatrix} p_1 \cdot q_1 & \dots & p_1 \cdot q_n \\ \vdots & & \vdots \\ p_n \cdot q_1 & \dots & p_n \cdot q_n \end{pmatrix}. \quad (3.2)$$

□

**Definition 2** (Gram Determinants (GDs)).

A GD is the determinant of a Gram Matrix:

$$G \left( \begin{array}{c} \{p_1, \dots, p_n\} \\ \{q_1, \dots, q_n\} \end{array} \right) = \det M \left( \begin{array}{c} \{p_1, \dots, p_n\} \\ \{q_1, \dots, q_n\} \end{array} \right) \quad (3.3)$$

□

**Definition 3** (Symmetric Gram Determinant.).

The symmetric Gram Determinant (sGD) is a GD whose two entries are the same.

$$\Delta_n(\{p_1, \dots, p_n\}) = G \left( \begin{array}{c} \{p_1, \dots, p_n\} \\ \{p_1, \dots, p_n\} \end{array} \right). \quad (3.4)$$

Call  $n$  the dimension of  $\Delta_n$

□

**Lemma 1** (Invariance under argument ordering).

The order of the two GD arguments is irrelevant because of the invariance of the determinant of a matrix under exchange of its rows or columns.

$$G \left( \begin{array}{c} \{p_1, \dots, p_i, p_{i+1}, \dots, p_n\} \\ \{q_1, \dots, q_n\} \end{array} \right) = G \left( \begin{array}{c} \{p_1, \dots, p_{i+1}, p_i, \dots, p_n\} \\ \{q_1, \dots, q_n\} \end{array} \right), \quad (3.5)$$

$$G \left( \begin{array}{c} \{p_1, \dots, p_n\} \\ \{q_1, \dots, q_i, q_{i+1}, \dots, q_n\} \end{array} \right) = G \left( \begin{array}{c} \{p_1, \dots, p_n\} \\ \{q_1, \dots, q_{i+1}, q_i, \dots, q_n\} \end{array} \right). \quad (3.6)$$

□

**Lemma 2** (Invariance on the order of the arguments).

The order of the arguments of a GD is irrelevant because a matrix determinant is invariant under matrix transposition.

$$G \left( \begin{array}{c} \{p_i\}_{i=1}^n \\ \{q_i\}_{i=1}^n \end{array} \right) = G \left( \begin{array}{c} \{q_i\}_{i=1}^n \\ \{p_i\}_{i=1}^n \end{array} \right). \quad (3.7)$$

□

**Lemma 3** (One momentum deformation).

If any of the elements of any GD argument is multiplied by a scalar  $\lambda$  of the vector space, the whole GD is rescaled by the same scalar:

$$G \left( \begin{array}{c} \{p_1, \dots, \lambda p_i, \dots, p_n\} \\ \{q_1, \dots, q_n\} \end{array} \right) = \lambda G \left( \begin{array}{c} \{p_1, \dots, p_i, \dots, p_n\} \\ \{q_1, \dots, q_n\} \end{array} \right), \quad (3.8)$$

$$G \left( \begin{array}{c} \{p_1, \dots, p_n\} \\ \{q_1, \dots, \lambda q_i, \dots, q_n\} \end{array} \right) = \lambda G \left( \begin{array}{c} \{p_1, \dots, p_i, \dots, p_n\} \\ \{q_1, \dots, q_n\} \end{array} \right), \quad (3.9)$$

because  $G$  is the det of a matrix whose whole row (eq. (3.8)) or column (eq. (3.9)) is rescaled.

□

**Lemma 4** (Invariance under linear combination of arguments elements).

A GD is left invariant if any of its arguments is replaced by the same set in which one entry is traded for a linear superposition of its elements:

$$\begin{aligned} G \left( \begin{array}{c} \{p_1, \dots, p_i, \dots, p_k, \dots, p_n\} \\ \{q_1, \dots, q_j, \dots, q_l, \dots, q_n\} \end{array} \right) &= G \left( \begin{array}{c} \{p_1, \dots, p_i + \alpha p_k, \dots, p_k, \dots, p_n\} \\ \{q_1, \dots, q_j, \dots, q_l, \dots, q_n\} \end{array} \right) \\ &= G \left( \begin{array}{c} \{p_1, \dots, p_n\} \\ \{q_1, \dots, q_j + \beta q_l, \dots, q_l, \dots, q_n\} \end{array} \right). \end{aligned} \quad (3.10)$$

This is due to the invariance of the determinant of a matrix under linear superposition of its rows or columns.

□

**Lemma 5** (GDs and Levi-Civita symbols).

GDs can be expressed in terms of products of Levi-Civita symbols with fourmomenta and viceversa. Therefore eq. (2.6) can be reframed in terms of GDs. See appendix F.

□

**Definition 4** (Principal Gram Determinant (PGD)).

Given a set of linearly dependent fourmomenta, the PGD is the symmetric GD computed onto (any expression of) the largest set of independent fourmomenta.

□

**Lemma 6** (PGD of a scattering).

In an  $n \rightarrow N - n$  process the PGD is a symmetric GD computed onto whatever subset of fourmomenta of dimension  $N - 1$ . This is due to lemma 4.

□

### 3.2 Geometrical meaning of GDs

GDs have a deep geometrical meaning. The reader may have already met them without even knowing. In this section I show you how. At school we learned that matrix determinants can be associated to the volume of a hyper-rectangle (remark 1). I generalise this fact by introducing Cayley determinants, an object that mathematicians use to compute the volume of, so to say,  $n$  dimensional triangles (simplexes). Finally I state the equivalence among GDs and Cayley determinants and proceed to specialise to low dimensional cases, namely the infamous triangular  $\lambda$  and its older brother, the tetrahedral or kinematic  $\mathcal{G}$  (its name is enough for suggesting you we will use it later). In particular  $\Delta_2(p_1, p_2)$  is related to the area of a triangle whose sides are functions of  $p_1^2, p_2^2$  and  $p_1 \cdot p_2$  (see corollary 1),  $\Delta_3(p_1, p_2, p_3)$  to the volume of a tetrahedron whose sides depend on  $p_i \cdot p_j$ ,  $i, j \in \{1, 2, 3\}$  (see theorem 2).

**Remark 1** (Determinants of an  $n \times n$  matrix  $M$  and volume of a parallelepiped in  $\mathbb{R}^n$ ).

Consider an  $n \times n$  diagonal matrix  $M_D$ . You can see its eigenvalues as the sides of a hyper-rectangle in  $n$  dimensions and its determinant as its volume. If you transform

$$M_D \rightarrow M = A \cdot M_D \cdot A^{-1}, \quad (3.11)$$

with  $A$  an invertible  $n \times n$  matrix, the determinant is unchanged. However the columns of  $M_D$  were orthogonal vectors while those of  $M$  are not. This means that the corresponding parallelepiped is no longer rectangle. Still, the determinant of an  $n \times n$  matrix is the volume of a hyper-rectangle with one vertex in the origin and all other vertices pointed by the matrix columns.

□

But we can do more than just rectangles:

**Definition 5** (Cayley determinants).

Cayley determinants are a way of expressing the area of a simplex<sup>1</sup>. Suppose to have  $n + 1$  points in  $\mathbb{R}^k$  with  $k \geq n$ . They define an  $n$ -dimensional simplex. Call  $V_n$  its volume and  $d_{ij}$  the distance among the  $i^{\text{th}}$  and the  $j^{\text{th}}$  point. Build the following matrix  $M_n$ :

$$M_{n-1} = \begin{pmatrix} 0 & 1 & 1 & \dots & 1 \\ 1 & 0 & d_{12} & \dots & d_{1n} \\ & & \vdots & & \\ 1 & d_{1n} & d_{2n} & \dots & 0 \end{pmatrix}. \quad (3.12)$$

Then

$$V_n^2 = (-1)^{n+1} \frac{\det M_n}{\Gamma(n+1)^2 2^n}. \quad (3.13)$$

---

<sup>1</sup>A  $k$ -simplex is a  $k$ -dimensional polytope, i.e. a geometric object with flat faces. In other words, given  $k + 1$  vertices, the  $k$ -simplex is their smallest convex envelope.

□

Gram and Cayley determinants can be equivalently used, we only need a rule for expressing the  $d_{ij}$  in eq. (3.12). For this purpose let me define:

**Definition 6** ( $m$ -particle invariant masses).

$$s_{ijk\dots} := (p_i + p_j + p_k + \dots)^2. \quad (3.14)$$

Ingoing and outgoing particles have opposite signs.

□

From this we derive the following lemma

**Lemma 7** (Relation between the  $n$ -dimensional Cayley volume and the  $\Delta_n$ ).

There is a 1 to 1 correspondence between  $\Delta_n$  and the Cayley determinant built as in definition 5 with

$$\Delta_n(p_1, \dots, p_n) = \Gamma(n+1)^2 V_n^2(d_{ij}) \quad (3.15)$$

if sides are chosen like

$$d_{ij} = s_{i,(i+1),(i+2),\dots,(j-1)} = \left( \sum_{k=i}^{j-1} p_k \right)^2, \quad i \in [1, n], j \in [2, n+1]. \quad (3.16)$$

Signs are as in definition 6.

□

We will not prove lemma 7 but one can easily check it for  $n = 1$  (trivially true) and for  $n = 2$ . On one hand

$$\Delta_2 = \begin{vmatrix} m_1^2 & p_1 \cdot p_2 \\ p_1 \cdot p_2 & m_2^2 \end{vmatrix} = (m_1 m_2)^2 - (p_1 \cdot p_2)^2. \quad (3.17)$$

On the other hand, using eq. (3.16),

$$V_2^2 = -\frac{1}{16} \begin{vmatrix} 0 & 1 & 1 & 1 \\ 1 & 0 & m_1^2 & s_{12} \\ 1 & m_1^2 & 0 & m_2^2 \\ 1 & s_{12} & m_2^2 & 0 \end{vmatrix} = \frac{(m_1 m_2)^2 - (p_1 \cdot p_2)^2}{4}, \quad (3.18)$$

which satisfies lemma 7.

The first non trivial simplex is the triangle. Correspondingly we define an ubiquitous function of particle physics:

**Definition 7** (Triangular  $\lambda$ ).

$$\lambda(x, y, z) = (x - y - z)^2 - 4yz, \quad (3.19)$$

Equation (3.19) is fully symmetric under all  $x, y, z$  permutations.

□

The reason for it to be called triangular can be found in the following theorem:

**Theorem 1** (The triangular  $\lambda$  is the area of a triangle).

From the Hero theorem  $\frac{\sqrt{-\lambda(x^2, y^2, z^2)}}{4}$  is the area of the triangle of sides  $x, y, z$ .

□

**Corollary 1** ( $\Delta_2$  is the area of a triangle).

$$4\Delta_2(p_1, p_2)^2 = -\lambda(x, y, z), \quad (3.20)$$

$$x := m_1^4 + (p_1 \cdot p_2)^2, \quad (3.21)$$

$$y := (p_1 \cdot p_2)^2 + m_2^4, \quad (3.22)$$

$$z := (m_1^2 - (p_1 \cdot p_2))^2 + (m_2^2 - (p_1 \cdot p_2))^2. \quad (3.23)$$

□

Following the same philosophy, the next simplex is the tetrahedron:

**Definition 8** (Kinematic  $\mathcal{G}$ ).

$$\mathcal{G}(x, y, z, u, v, w) := \begin{vmatrix} 0 & 1 & 1 & 1 & 1 \\ 1 & 0 & u & y & v \\ 1 & u & 0 & w & x \\ 1 & y & w & 0 & z \\ 1 & v & x & z & 0 \end{vmatrix}. \quad (3.24)$$

□

**Theorem 2** (The tetrahedral  $\mathcal{G}$  and  $\Delta_3$  are the area of a tetrahedron).

There is a 1 to 1 correspondence between  $\Delta_3$  and  $\mathcal{G}$ :

$$\Delta_3(p_1, p_2, p_3) = -\frac{1}{2}\mathcal{G}((p_1 + p_2)^2, (p_1 - p_3)^2, (p_1 + p_2 - p_3)^2, m_1^2, m_2^2, m_3^2). \quad (3.25)$$

Consequently  $\Delta_3$  is the area of the tetrahedron whose vertices are

$$v_1 = (0, 0, 0), \quad (3.26)$$

$$v_2 = (0, 0, u), \quad (3.27)$$

$$v_3 = y(\sin \theta_y, 0, \cos \theta_y), \quad (3.28)$$

$$v_4 = v(\sin \theta_v \cos \phi, \sin \theta_v \sin \phi, \cos \theta_v), \quad (3.29)$$

with  $(\theta_y, \theta_v, \phi)$  solutions of

$$\|v_2 - v_3\| = w, \quad (3.30)$$

$$\|v_2 - v_4\| = x, \quad (3.31)$$

$$\|v_3 - v_4\| = z. \quad (3.32)$$

□

### 3.3 From polar coordinates to Lorentz invariant variables

**Lemma 8** (Transformation of polar coordinates to sGDs).

Let  $p_i$  have mass  $m_i$ , energy  $E_i$ , polar angle  $\theta_i$  and azimuthal angle  $\phi_i$ . There is a non bijective relation among the  $(m_i, E_i, \theta_i, \phi_i)$  and the  $\Delta_1, \Delta_2, \Delta_3, \Delta_4$  having  $p_i$  among their arguments. Consider a set of fourmomenta  $\{p_i\}_{i=1}^n$  in 4 dimensions and go to  $p_0$  rest frame. Then

$$m_i = \sqrt{\Delta_1(p_i)}, \quad (3.33)$$

$$|\vec{p}_i| = \frac{\sqrt{-\Delta_2(p_0, p_i)}}{m_0}, \quad (3.34)$$

$$|\sin \theta_{ij}| = m_0 \sqrt{\frac{\Delta_3(p_0, p_i, p_j)}{\Delta_2(p_0, p_i) \Delta_2(p_0, p_j)}}, \quad (3.35)$$

$$|\sin \phi_{(ij);(ik)}| = \left[ \frac{\Delta_4(p_0, p_i, p_j, p_k) \Delta_2(p_0, p_i)}{\Delta_3(p_0, p_i, p_j) \Delta_3(p_0, p_i, p_k)} \right]^{1/2}. \quad (3.36)$$

This can be seen either from direct computation or found in appendix A of [109], for example. In eq. (3.35) we refer to the angle between  $p_i$  and  $p_j$ . For example, if  $p_i$  is along your  $z$  axis,  $\theta_{ij}$  is the polar angle of  $p_j$ . In eq. (3.36) we refer to the angle between two planes, whose directories are respectively  $(p_i, p_j)$  and  $(p_i, p_k)$ . For example, if  $p_i$  is along the  $z$  axis and  $p_j$  is along the  $x$  axis,  $\phi_{(ij);(ik)}$  is the azimuthal angle of  $p_k$ .

□

**Theorem 3** (Signs and bounds).

Given the lemma 8 and the fact that

$$m_i, |\vec{p}_i|, |\sin \theta_{ij}|, |\sin \phi_{(ij);(ik)}| \in \mathbb{R}^+ \quad \forall i, j, \quad (3.37)$$

the following are true:

$$\Delta_1(p_i) \geq 0, \quad (3.38a)$$

$$\Delta_2(p_0, p_i) \leq 0, \quad (3.38b)$$

$$\Delta_3(p_0, p_i, p_j) \geq 0, \quad (3.38c)$$

$$\Delta_4(p_0, p_i, p_j, p_k) \leq 0. \quad (3.38d)$$

□

**Corollary 2.**

Equations (3.35) and (3.36) have the right domain for a  $|\sin|$ . In fact

$$m_0^2 \Delta_3(p_0, p_i, p_j) - \Delta_2(p_0, p_i) \Delta_2(p_0, p_j) = -(p_0 \cdot p_1 p_0 \cdot p_2 - m_0^2 p_1 \cdot p_2)^2, \quad (3.39)$$

from which it follows that

$$0 \leq m_0 \sqrt{\frac{\Delta_3(p_0, p_i, p_j)}{\Delta_2(p_0, p_i) \Delta_2(p_0, p_j)}} \leq 1, \quad (3.40)$$

and

$$\begin{aligned} & \Delta_4(p_0, p_i, p_j, p_k) \Delta_2(p_0, p_i) - \Delta_3(p_0, p_i, p_j) \Delta_3(p_0, p_i, p_k) = \\ & - [m_0^2 (p_1 \cdot p_2 p_1 \cdot p_3 - m_1^2 p_2 \cdot p_3) + m_1^2 p_0 \cdot p_2 p_0 \cdot p_3 + \\ & p_0 \cdot p_1 (-p_0 \cdot p_3 p_1 \cdot p_2 - p_0 \cdot p_2 p_1 \cdot p_3 + p_0 \cdot p_1 p_2 \cdot p_3)]^2, \end{aligned} \quad (3.41)$$

from which it follows that

$$0 \leq \left[ \frac{\Delta_4(p_0, p_i, p_j, p_k) \Delta_2(p_0, p_i)}{\Delta_3(p_0, p_i, p_j) \Delta_3(p_0, p_i, p_k)} \right]^{1/2} \leq 1. \quad (3.42)$$

□

**Corollary 3** (Boosted coordinates).

All of the above are identically valid in the rest frame of any other fourmomentum  $p_i$  modulo relabelling.

□

### 3.4 Null Gram determinants define the boundary of the physical region of the phase space

In the previous section I showed how to perform a change of variables from polar coordinates to Lorentz invariant quantities. But how do we express the Phase Space boundary? Where should the cross section integration be held? Starting from the easiest 2 bodies case to the most generic configuration, I will show that the Phase Space boundary is the locus of the nodes of the Principal Gram Determinant of the scattering (section 3.4.1). This is why GDs are the most natural way of expressing a scattering Phase Space.

#### 3.4.1 2, 3, 4 bodies

Consider the fourmomenta  $p_a$  and  $p_b$  and go to the rest frame of the former; call  $\vec{\beta}$  the velocity of  $p_b$  in this frame and  $\gamma$  its associated Lorentz factor. Then we specialize eq. (3.17) to

$$\Delta_2(p_a, p_b) = -m_a m_b \gamma^2 \beta^2 = 0 \text{ if } \beta = 0. \quad (3.43)$$

This means  $\vec{p}_a, \vec{p}_b$  define a 0-dimensional simplex (a **point**).

Consider now the process  $p_1 \rightarrow p_2 + p_3$ . Threemomenta are arranged along the sides of a triangle because  $\vec{p}_1 = \vec{p}_2 + \vec{p}_3$ . Go to the reference frame in which one momentum is at rest, for example  $p_1$  (in this problem indices are irrelevant,  $1 \leftrightarrow 2 \leftrightarrow 3$ ). This point must belong to the boundary of the physical region because  $\vec{0}$  is the minimum allowed to the  $\vec{p}_i$ . Then  $|\vec{p}_2 + \vec{p}_3| = 0$  too, i.e. the velocities  $\vec{\beta}_2$  and  $\vec{\beta}_3$  are collinear and the triangle degenerated into a segment. We can state the following theorem:

**Theorem 4** (Degenerate triangle and maximal energies).

In the process  $p_1 \rightarrow p_2 + p_3$ ,  $|\vec{p}_2|$  is maximal when  $|\vec{p}_1| = 0$ .

□

Let us prove theorem 4. In  $p_1$  rest frame (that we will call CoM and indicate with a \*)  $|\vec{p}_1^*| = 0$  and  $|\vec{p}_2^*|$  and  $|\vec{p}_3^*|$  are

$$|\vec{p}_2^*| = |\vec{p}_3^*| = \frac{\sqrt{\lambda_0}}{2m_1} =: p, \quad (3.44)$$

see fig. 3.1. I defined

$$\lambda_0 := \lambda(m_1^2, m_2^2, m_3^2) \quad (3.45)$$

I want to show that if I perform a boost of Lorentz parameter  $\beta$  to a new rest frame, the modulus of  $\vec{p}_2$  will be the biggest if the boost has an angle  $\theta = 0$  with respect to  $\vec{p}_2$ , i.e. if the boost is parallel to  $\vec{p}_2$ , regardless from  $\beta$ . The new  $p_2$  is a function of  $\beta$  and  $\theta$ :

$$2m_1\sqrt{1-\beta^2}p_2 = \left( \Sigma + \beta \cos \theta \sqrt{\lambda_0}, \sin \theta \sqrt{\lambda_0} \sqrt{1-\beta^2}, 0, \beta \Sigma + \cos \theta \sqrt{\lambda_0} \right) \quad (3.46)$$

with  $\Sigma := m_1^2 + m_2^2 - m_3^2$ . The derivative of  $|\vec{p}_2|$  with respect to  $\theta$  is

$$\frac{d|\vec{p}_2|}{d\theta} = -\frac{p \beta \sin \theta}{m_1(1-\beta^2)} \left[ m_1^2 \left( 1 + 2\beta \cos \theta \frac{p}{m_1} \right) + m_2^2 - m_3^2 \right] \leq 0 \quad \forall \theta \in [0, \pi], \quad \forall \beta \in [0, 1], \quad (3.47)$$

because  $m_1 > m_2 + m_3$ . Equation (3.47) vanishes onto  $\beta = 0$ , corresponding to making no boost, when the square bracket is 0, corresponding to two unacceptable solutions on which  $p_2^0 = 0 < m_2$ , and onto  $\theta = 0$ . This proves our statement. Let us remark that this demonstration only depends on the fact that  $\vec{p}_{1,2,3}$  form a triangle. Let's check the corresponding GD in  $p_1$  rest frame. Let  $\theta_{23}$  be the angle between  $\vec{p}_2$  and  $\vec{p}_3$ . Then

$$\Delta_3(p_1, p_2, p_3) = (m_1 |\vec{p}_2| |\vec{p}_3| \sin \theta_{23})^2 = 0 \quad \text{if} \quad \sin \theta_{23} = 0. \quad (3.48)$$

This indicates **aligned** velocities.

Consider now the process  $p_1 + p_2 \rightarrow p_3 + p_4$ . threemomenta are arranged along the sides of a tetrahedron, see fig. 3.2. Call  $\tau_{ij}$  the triangular face containing the

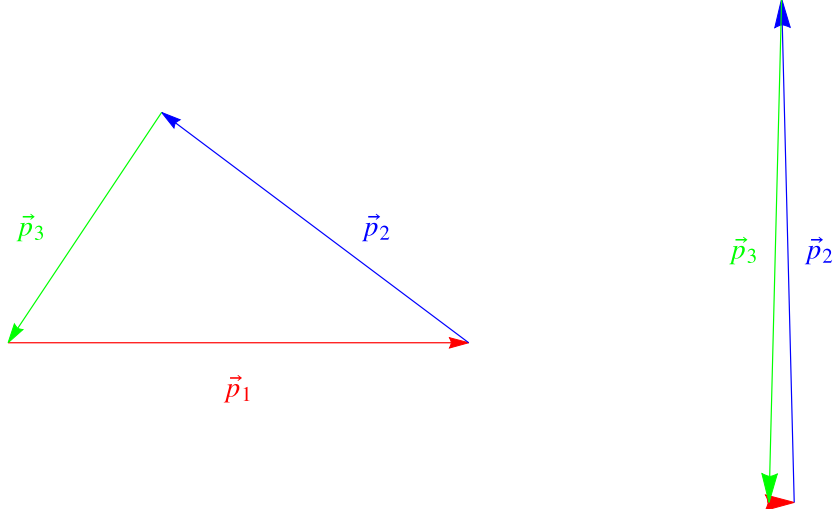


**Figure 3.1.** Graphic representation of the threemomenta  $\vec{p}_{1,2,3}$  satisfying  $\vec{p}_1 - \vec{p}_2 - \vec{p}_3 = \vec{0}$ . On the left we are in a generic frame. On the right we are in  $p_1$  rest frame (a small  $\vec{p}_1$  magnitude is left for visualisation purpose).

threemomenta  $\vec{p}_{i,j}$ , the third follows.

Go to  $p_1$  rest frame. The tetrahedron degenerates into a triangle,  $\tau_{23}$  collapsed onto  $\tau_{34}$ ,  $\tau_{14}$  becomes a segment. All other threemomenta are maximised with respect to  $\vec{p}_1$ , as from theorem 4.  $\vec{\beta}_2$ ,  $\vec{\beta}_3$  and  $\vec{\beta}_4$  are **coplanar** (they live in the  $\tau_{23} \equiv \tau_{34}$  plane).

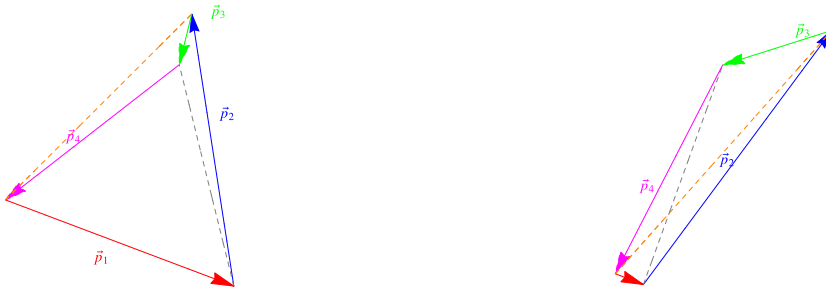


**Figure 3.2.** Graphic representation of the threemomenta  $\vec{p}_{1,2,3,4}$  satisfying  $\vec{p}_1 + \vec{p}_2 = \vec{p}_3 + \vec{p}_4$ . On the left we are in a generic frame. On the right we are in  $p_1$  rest frame. A small  $\vec{p}_1$  magnitude is left for visualisation purpose. The dashed sides do not correspond to any fourmomentum: the orange one corresponds to the sum  $\vec{p}_1 + \vec{p}_2$  (or equivalently  $\vec{p}_3 + \vec{p}_4$ ), the grey one simply closes the tetrahedron.

Correspondingly, let us go in  $p_1$  rest frame and assume none of the fourmomenta is aligned with the other; as above, take  $\theta_{ab}$  the angle among  $\vec{p}_a$  and  $\vec{p}_b$ ; define  $\phi$  the angle among the planes generated by the couples  $(\vec{p}_2, \vec{p}_3)$  and  $(\vec{p}_2, \vec{p}_4)$ , then

$$\Delta_4(p_1, p_2, p_3, p_4) = -(m_1 |\vec{p}_2| |\vec{p}_3| |\vec{p}_4| \sin \theta_{23} \sin \theta_{24} \sin \phi)^2 = 0 \text{ if } \phi = 0. \quad (3.49)$$

This is the definition of **coplanarity** of  $\vec{p}_2, \vec{p}_3, \vec{p}_4$ .

### 3.4.2 In general

I now proceed to generalize what we saw for 2, 3 and 4 particles for a generic process with some initial and some final state particles. I will follow the demonstration in section 3.2.1 from [110]. The idea is that I can pick whatever subset of particles and go to the subset rest frame. This is an extremal configuration, in the sense that it belongs to the phase space boundary. Exploiting the fact that the system is at rest, I will be able to write down a system of equations involving the particles fourmomenta. The system is solved non trivially when the Principal Gram Determinant of the scattering vanishes.

**Theorem 5** (Symmetric Gram Determinants are null when there is a linear dependence among its arguments.).

Consider a scattering with  $n$  initial state particles  $\{p_i\}_{i=1}^n$  and  $m$  final state particles  $\{p_j\}_{j=n+1}^N$ ,  $n + m = N$ :

$$p_1 + \cdots + p_n \rightarrow p_{n+1} + \cdots + p_N. \quad (3.50)$$

Fourmomentum conservation looks like

$$\sum_{i=1}^n p_i = \sum_{j=n+1}^N p_j. \quad (3.51)$$

To write simpler sums let us write an equivalent process with all initial state particles

$$q_1 + \cdots + q_N \rightarrow 0, \quad (3.52)$$

where

$$q_i := \begin{cases} p_i & \text{if } 1 \leq i \leq n, \\ -p_i & \text{if } n < i \leq N. \end{cases} \quad (3.53)$$

Among the  $q_i$ , pick a group of  $k$  fourmomenta and say they make up the system  $\mathcal{S}$ ; go to its rest frame, where the fourmomentum of  $\mathcal{S}$  is  $q_{\mathcal{S}} = (M_{\mathcal{S}}, \vec{0})$ . Then

$$\sum_{i \notin \mathcal{S}} q_i + \sum_{i \in \mathcal{S}} q_i = \sum_{i \notin \mathcal{S}} q_i + q_{\mathcal{S}} = (0, \vec{0}), \quad (3.54)$$

which is specifically true for the time component

$$\sum_{i \notin \mathcal{S}} q_i^0 = -M_{\mathcal{S}}. \quad (3.55)$$

Let's rewrite the unity as

$$1 = -\frac{1}{M_S} \sum_{i \notin \mathcal{S}} q_i^0, \quad (3.56)$$

and use it in eq. (3.54):

$$\sum_{i \notin \mathcal{S}} q_i = \left( \frac{1}{M_S} \sum_{i \notin \mathcal{S}} q_i^0 \right) q_S. \quad (3.57)$$

We can rewrite eq. (3.57) as a linear combination of all the  $q_i$  by using again that  $\sum_{i \in \mathcal{S}} q_i = q_S$ :

$$\sum_{i=1}^N \lambda_i q_i = 0, \quad (3.58)$$

$$\lambda_i = \begin{cases} 1 & \text{if } i \notin \mathcal{S}, \\ -\frac{1}{M_S} \sum_{i \notin \mathcal{S}} q_i^0 & \text{if } i \in \mathcal{S}. \end{cases} \quad (3.59)$$

Now if  $\sum_{i=1}^N \lambda_i q_i = 0$ , then also  $q_i \cdot \sum_{i=1}^N \lambda_i q_i = 0$  for whatever  $i$ . We can collect many of these equations in the system:

$$\begin{cases} q_1 \cdot \sum_{i=1}^N \lambda_i q_i = 0, \\ \dots, \\ q_{N-1} \cdot \sum_{i=1}^N \lambda_i q_i = 0. \end{cases} \quad (3.60)$$

I stopped at  $N-1$  because the equation for  $q_N$  can be recovered from fourmomentum conservation. The determinant of the system for the unknowns  $\lambda_i$  is exactly the Principal Gram Determinant of the scattering. The solution for the system is non trivial if the PGD is 0.

This concludes our demonstration of the fact that null Gram Determinants define the boundary of the Phase Space region.

□

## Chapter 4

# Constraints on Mandelstam variables from GDs

Up to now we showed how GDs are the natural functions for defining a scattering (or decay) phase space. Mandelstam variables are the natural quantities in which those functions are expressed, in fact most textbooks (see [105, 111] for example) discuss the  $2 \rightarrow 2$  scattering and the  $1 \rightarrow 3$  decay in terms of  $s, t$  and  $u$  (see eq. (4.1)). I will use the  $2 \rightarrow 2$  scattering as a familiar invitation (section 4.1) in preparation for the  $2 \rightarrow 3$  case, analysed in section 4.2. Differently from the  $2 \rightarrow 2$  one, the  $2 \rightarrow 3$  phase space has the problem that it is described by 4 variables, thus we can not directly visualize our conjectures on it. On top of that, a plethora of GDs up to  $\Delta_4$  have to be satisfied. However in section 4.2.2 I demonstrate that we can provide a way easier, rougher approximation of the phase space by limiting ourselves to a system of  $\Delta_m$ ,  $m < 4$ . Improving to larger  $m$  provides a Phase Space volume which is fully contained within the former (corollary 5). This property stems from theorem 7, on which we will be basing all of the computations we will perform in next chapter, as it is fundamental for solving the cross section distributions integrals.

In section 4.3 I show that what was found in sections 4.1 and 4.2 has a deep mathematical origin by retracing Byers and Yang [90]  $2 \rightarrow n$  generic phase space characterisation.

The last section is meant to show a relationship between the  $2 \rightarrow 3$  and the  $2 \rightarrow 2$  scattering, as I will point out one kinematic configuration reducing the former into the latter, the resting ALP case. The reason of my attention to this case will be clear in next section.

My main sources for this chapter have been [109, 110].

### 4.1 A $2 \rightarrow 2$ scattering invitation

In this section we work out eq. (3.38) for a  $2 \rightarrow 2$  scattering  $p_1 + p_2 \rightarrow p_3 + p_4$ . It is standard to define the Mandelstam variables as

$$\begin{aligned} s &= (p_1 + p_2)^2, \\ t &= (p_2 - p_4)^2, \\ u &= (p_1 - p_4)^2. \end{aligned} \tag{4.1}$$

$(i, j)$	Bound
$(1, 2) \equiv (3, 4)$	$s \leq (m_1 - m_2)^2 \cup s \geq (m_1 + m_2)^2$
$(1, 3)$	$t \leq (m_1 - m_3)^2 \cup t \geq (m_1 + m_3)^2$
$(1, 4)$	$u \leq (m_1 - m_4)^2 \cup u \geq (m_1 + m_4)^2$
$(2, 3)$	$u \leq (m_2 - m_3)^2 \cup u \geq (m_2 + m_3)^2$
$(2, 4)$	$t \leq (m_2 - m_4)^2 \cup t \geq (m_2 + m_4)^2$
$(1 + 2, 3) \equiv (3 + 4, 3) \equiv (3, 4) \equiv (1 + 2, 4)$	$s \leq (m_3 - m_4)^2 \cup s \geq (m_3 + m_4)^2$

**Table 4.1.** On the left column the couple of fourmomenta entering in  $\Delta_2(p_i, p_j)$ . On the right column the bounds on  $s, t$  or  $u$  coming from  $\Delta_2(p_i, p_j) \leq 0$ .

From fourmomentum conservation it follows that

$$s + t + u = m_1^2 + m_2^2 + m_3^2 + m_4^2 =: k. \quad (4.2)$$

In each row of table 4.1 we list the effect of imposing  $\Delta_2(p_i, p_j) \leq 0$ .

The Principal Gram Determinant for a  $2 \rightarrow 2$  scattering is  $\Delta_3$ , equivalently  $\mathcal{G}(s, t, m_4^2, m_1^2, m_2^2, m_3^2)$ , or simply  $\mathcal{G}$ .  $\mathcal{G} \geq 0$  defines the scattering phase space,  $\mathcal{G} = 0$  is its boundary. It is also called Kibble curve

$$-2\mathcal{G} = stu - (\alpha s + \beta t + \gamma u) = 0, \quad (4.3)$$

with

$$k\alpha := (m_1^2 m_2^2 - m_3^2 m_4^2)(m_1^2 + m_2^2 - m_3^2 - m_4^2), \quad (4.4)$$

$$k\beta := (m_1^2 m_3^2 - m_2^2 m_4^2)(m_1^2 + m_3^2 - m_2^2 - m_4^2), \quad (4.5)$$

$$k\gamma := (m_1^2 m_4^2 - m_2^2 m_3^2)(m_1^2 + m_4^2 - m_2^2 - m_3^2). \quad (4.6)$$

where  $k$  is defined in eq. (4.2). The Kibble curve and its tangents are represented in fig. 4.1, that we split in 2 only to better depict the many tangents. You can see that the area identified by  $\mathcal{G} \geq 0$  in the  $(s, t)$  plane is a disconnected union of four convex regions. Three of them correspond to the  $2 \rightarrow 2$  scattering and one to the  $1 \rightarrow 3$  decay. The latter is finite, while the former are only limited by two tangents. Each of them correspond to the  $s, t$  or  $u$  channel. The  $s$  region is located in the  $s \geq (m_1 + m_2)^2$ ,  $t \leq (m_1 - m_3)^2$  portion of the  $(s, t)$  plane; the horizontal line  $t = 0$  is an asymptote to this region in the  $s \rightarrow \infty$  limit. The  $t$  region has  $t \geq (m_1 + m_3)^2$ ,  $s \leq (m_1 - m_2)^2$  and the vertical line  $s = 0$  is an asymptote for the  $t \rightarrow \infty$  limit. However the Kibble curve intersects the lines  $s = 0, t = 0, u = 0$  before approaching them at infinity, hence their envelope is not made of these lines but of some other parallel to them. We now derive them.

The system

$$\begin{cases} \mathcal{G} = 0 \\ s + t + u = k \end{cases} \quad (4.7)$$

(i.e. eqs. (4.2) and (4.3)) is solved, for example, by

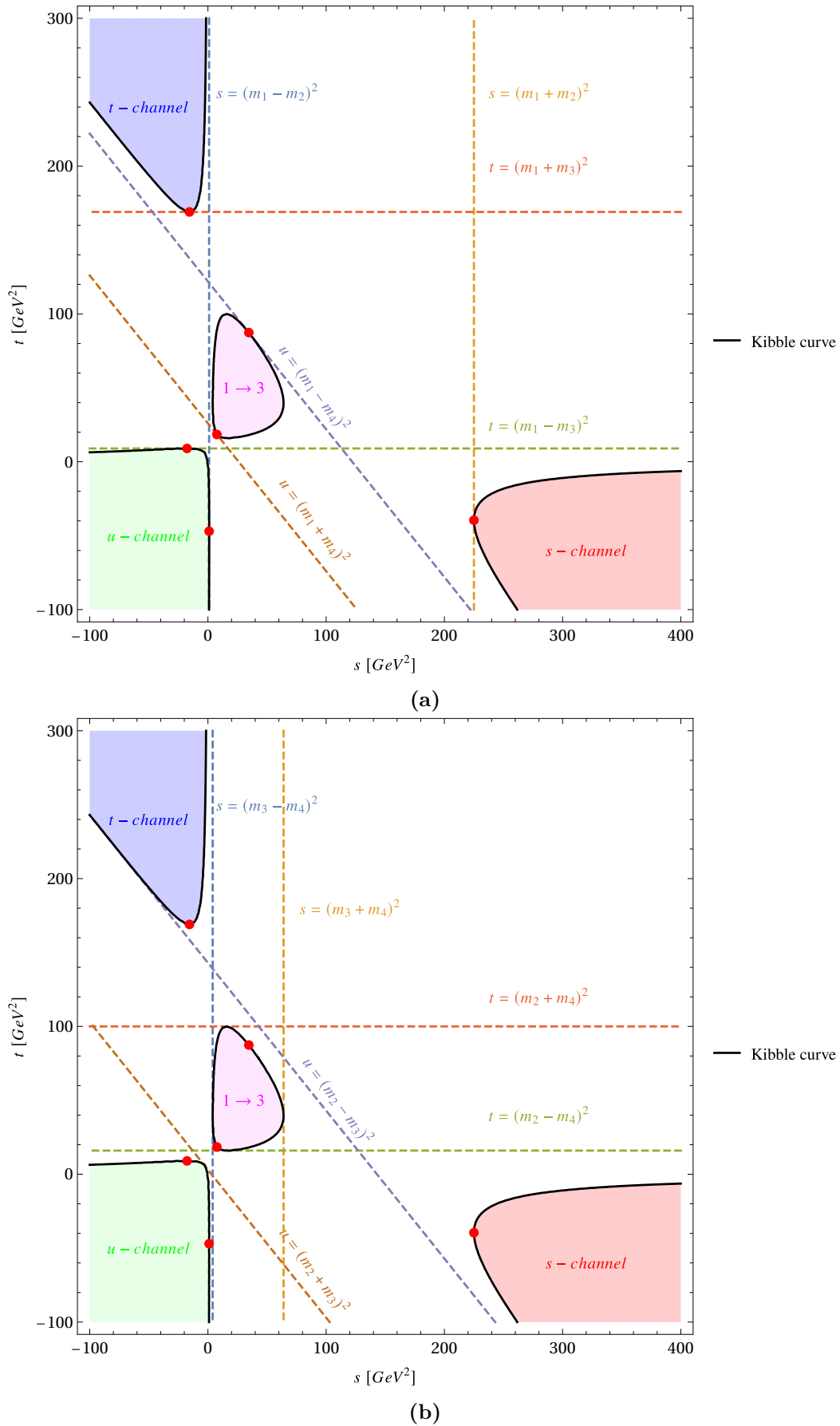


**Figure 4.1.** Example of Kibble curve for the mass choice  $m_1 = 8, m_2 = 7, m_3 = 5, m_4 = 3$  a.u. For simplicity we split the asymptotes in two pictures, so that they can be seen more clearly, while the red, blue and green area and the Kibble curve are the same between the panels. Red dots are tangency points.

$$\begin{cases} t = t(s) \\ u = k - s - t(s) \end{cases} \quad (4.8)$$

$t(s)$  is the Kibble curve. To find its tangents we can explicitly find  $t(s)$  and solve  $\frac{dt(s)}{ds} = 0$ . An easier way is recovering  $\frac{d\mathcal{G}}{ds}$  from  $\frac{d\mathcal{G}}{ds}$ :

$$\frac{d\mathcal{G}}{ds} = \frac{\partial\mathcal{G}}{\partial s} + \frac{\partial\mathcal{G}}{\partial t} \frac{dt}{ds} + \frac{\partial\mathcal{G}}{\partial u} \frac{du}{ds} = 0; \quad (4.9)$$

explicitly

$$\frac{\partial\mathcal{G}}{\partial s} = tu - \alpha, \quad (4.10)$$

$$\frac{\partial\mathcal{G}}{\partial t} = su - \beta, \quad (4.11)$$

$$\frac{\partial\mathcal{G}}{\partial u} = st - \gamma, \quad (4.12)$$

$$\frac{du}{ds} = -1 - \frac{dt}{ds}. \quad (4.13)$$

$$(4.14)$$

By plugging the latter into eq. (4.9)

$$\frac{d\mathcal{G}}{ds} = tu - \alpha + (su - \beta) \frac{dt}{ds} - (st - \gamma) \left(1 + \frac{dt}{ds}\right) = 0, \quad (4.15)$$

which is solved for

$$\frac{dt}{ds} = -\frac{st - \gamma - tu + \alpha}{st - \gamma - su + \beta}. \quad (4.16)$$

Equation (4.16) is 0 while satisfying  $\mathcal{G} = 0$ ,  $s + t + u = k$  onto

$$t = (m_1 \pm m_3)^2, (m_2 \pm m_4)^2. \quad (4.17)$$

Repeat the same reasoning for finding all other tangents:

Tangent parallel to plane	Solutions
$s = 0$	$s = (m_1 \pm m_2)^2, \quad s = (m_3 \pm m_4)^2$
$t = 0$	$t = (m_1 \pm m_3)^2, \quad t = (m_2 \pm m_4)^2$
$u = 0$	$u = (m_1 \pm m_4)^2, \quad u = (m_2 \pm m_3)^2$

Let us now state some properties that will be useful in the more complicated case of the  $2 \rightarrow 3$  scattering.

Constraints on Mandelstam variables coming from  $\Delta_2 \leq 0$  are planes in the  $(s, t, u)$  space; the constraint from the Principal Gram Determinant is more complicated.

The growing  $u$  direction is from the bottom left to the upper right corner. Hence, when all bounds from table 4.1 are respected, the central blob is not included in the  $2 \rightarrow 2$  scattering phase space; instead, it is the  $1 \rightarrow 3$  decay domain. The other 3 regions correspond to the  $s$ ,  $t$  or  $u$  channel, respectively counter-clockwise from the

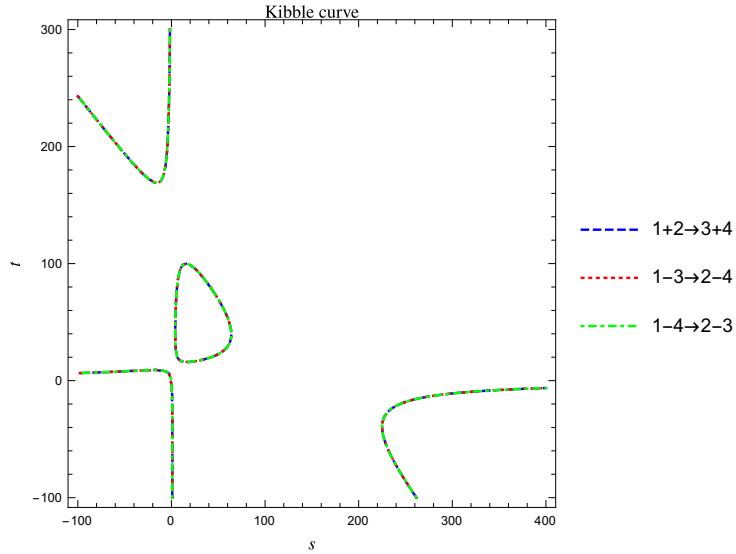


**Figure 4.2.** In all the three curves the mass choice is that of fig. 4.1. The blue dashed line is the Kibble curve from eq. (4.3); the red, dotted line is eq. (4.3) to which we applied the  $s - t$  rotation (eq. (4.18)); the green, dot-dashed line is eq. (4.3) to which we applied the  $s - u$  rotation (eq. (4.19)). This plot demonstrates how the curve is rotated into itself. Therefore we identify the bottom right disconnected area as the  $s$  channel, the top area as the  $t$  channel and the bottom left area as the  $u$  channel.

bottom right corner. This means that every channel only picks one branch at a time of all the branches that are in table 4.1.

The  $s$  region can be rotated into the  $t$  one by plugging into the Kibble curve

$$s \leftrightarrow t \wedge m_2 \leftrightarrow m_3; \quad (4.18)$$

$s$  is rotated into  $u$  via

$$s \leftrightarrow u \wedge m_2 \leftrightarrow m_4; \quad (4.19)$$

$t$  is rotated into  $u$  via

$$t \leftrightarrow u \wedge m_3 \leftrightarrow m_4. \quad (4.20)$$

You can see these symmetries in action in fig. 4.2. On this base we can state that we can restrict to one channel and work out all other possibilities through symmetry. That's exactly what we will do in next section.

## 4.2 Working out the $2 \rightarrow 3$ case

In this section I finally demonstrate the convenience of GDs for expressing the  $2 \rightarrow 3$  scattering or  $1 \rightarrow 4$  decay phase space  $\mathcal{P}_5$ , hence ultimately for computing cross sections and their distributions. The validity of such demonstration comes from

many directions. Firstly, in section 5.1 I will derive the analytic form of  $\mathcal{P}_5$  in the new set of variables:

$$\frac{\theta(-\Delta_4)}{\sqrt{-\Delta_4}}, \quad (4.21)$$

which is integrably divergent;  $\Delta_4$  is the Principal Gram Determinant of this problem. It is inclusive of the Phase Space density  $\frac{1}{\sqrt{-\Delta_4}}$  and the Phase Space region definition  $\theta(-\Delta_4)$ . We will see that from it many other  $\Delta_{2,3}$  constraints will spawn. Equation (4.21) is manifestly more convenient than

$$\frac{|\vec{p}_3|^2}{E_3} \frac{|\vec{p}_5|^2}{E_5} \delta(s - 2\sqrt{s}(E_3 + E_5) + m_3^2 + m_5^2 + 2(E_3 E_5 - |\vec{p}_3||\vec{p}_5|c_{35}) - m_4^2), \quad (4.22)$$

in polar coordinates. Not only it is simpler and all of the cross section distributions correspond to tabulated integrals, but also it diverges exactly where the  $2 \rightarrow 3$  scattering is degenerate, i.e.  $\Delta_4 = 0$ . This easily points to the most frequent kinematic configurations. This formalism has also proven efficient in MC generators to speed up simulation.

In this section we define the Generalised Mandelstam variables (section 4.2.1) and deepen some considerations (section 4.2.2) already given in the previous section, which will be the foundation for performing the integrations of next chapter.

### 4.2.1 Generalized Mandelstam variables

In section 2.3 we saw that 5 particles subject to fourmomentum conservation can be described by 5 degrees of freedom that are the Mandelstam  $s$  plus 4 real numbers to be chosen to our liking. For the 4 variables we can use the **Generalized Mandelstam variables** (gMvs):

$$s, s_1, s_2, t_1, t_2. \quad (4.23)$$

They simply correspond to fourmomenta scalar products  $p_{ij} = p_i \cdot p_j$ . In fact from now on we adopt the convention

**Convention 1** (The  $2 \rightarrow 3$  scattering).

$$p_1 + p_2 \rightarrow p_3 + p_4 + p_5, \quad (4.24)$$

$$p_i^2 = m_i^2, \quad (4.25)$$

$$\vec{m} := (m_1, m_2, m_3, m_4, m_5), \quad (4.26)$$

□

from which follow the definition

**Definition 9** (Generalized Mandelstam Variables).

$$\begin{aligned} s &:= (p_1 + p_2)^2, & t_1 &:= (p_1 - p_3)^2, \\ s_1 &:= (p_3 + p_4)^2, & t_2 &:= (p_2 - p_5)^2. \\ s_2 &:= (p_4 + p_5)^2, \end{aligned} \quad (4.27)$$

□

Sometimes some auxiliary variables will be handy:

**Definition 10** (Auxiliary variables).

$$\begin{aligned} u_1 &:= (p_3 + p_5)^2, & u_4 &:= (p_2 - p_4)^2, \\ u_2 &:= (p_1 - p_5)^2, & u_5 &:= (p_1 - p_4)^2. \\ u_3 &:= (p_2 - p_3)^2, \end{aligned} \quad (4.28)$$

□

See appendix E for conversion among scalar products, gMvs and auxiliary variables. In these variables and using SSM eqs. (2.2) and (2.3) become

$$\mathcal{M}_s \rightarrow \frac{1}{su_1}, \quad \mathcal{M}_t \rightarrow \frac{1}{t_1 t_2}. \quad (4.29)$$

### 4.2.2 Understanding the phase space as parabolas

The first (and last) non trivial phase space that we study at school is the 1 → 3 decay. You may remember that a useful tool for its characterization are Dalitz plots. They represent the allowed phase space to two invariant masses. For example if we consider 3 fourmomenta  $p_{3,4,5}$ , a Dalitz plot is depicted in terms of  $m_{34}^2 := (p_3 + p_4)^2$  and  $m_{45}^2 := (p_4 + p_5)^2$ . Generally they are used for resonance hunting. At an experiment one can draw a point in the  $(m_{34}^2, m_{45}^2)$  for each event. If some vertical or horizontal band is more populated than others, there may be a resonance. If one expresses gMvs in terms of  $s, m_{34}^2, m_{45}^2$  and asks for  $\Delta_s(p_3, p_4, p_5) \geq 0$  one obtains the corresponding Dalitz plot, i.e., Dalitz plots are nothing more than the physical areas allowed to GDs, see fig. 4.3.

We are going to describe some less trivial phase space in a very similar way. If in the previous example we dealt with  $\Delta_3$ , let us upgrade now to  $\Delta_4$ , the Principal Gram Determinant of a 2 → 3 scattering:

$$\Delta_4 = \begin{vmatrix} m_1^2 & \frac{1}{2}(-m_1^2 - m_2^2 + s) & \frac{1}{2}(m_1^2 + m_3^2 - t_1) & \frac{1}{2}(-m_2^2 + s - s_1 + t_2) \\ \frac{1}{2}(-m_1^2 - m_2^2 + s) & m_2^2 & \frac{1}{2}(-m_1^2 + s - s_2 + t_1) & \frac{1}{2}(m_2^2 + m_5^2 - t_2) \\ \frac{1}{2}(m_1^2 + m_3^2 - t_1) & \frac{1}{2}(-m_1^2 + s - s_2 + t_1) & m_3^2 & \frac{1}{2}(m_4^2 + s - s_1 - s_2) \\ \frac{1}{2}(-m_2^2 + s - s_1 + t_2) & \frac{1}{2}(m_2^2 + m_5^2 - t_2) & \frac{1}{2}(m_4^2 + s - s_1 - s_2) & m_5^2 \end{vmatrix}. \quad (4.30)$$

A determinant of a  $4 \times 4$  matrix expressed in terms of 5 gMvs can hardly look palatable. Even graphic representation is put to the test. That is why in the following subsection we will provide some  $\Delta_n$  properties, leading us to conclude that the study of the boundaries coming from imposing  $\Delta_2(p_i, p_j) \leq 0$ ,  $i, j \in 1, 2, 3, 4, 5$  can be a Phase Space approximation to be content with.

In section 4.1 we saw that this kind of bounds leads to many branches and that we can rotate one into the other. In section 4.2.2 we give a more formal demonstration of the fact that we can limit ourselves to a specific branch selection and provide one.

We proceed to show some Gram Determinants properties that are responsible of the Phase Space shape. Equation (4.30) shows that

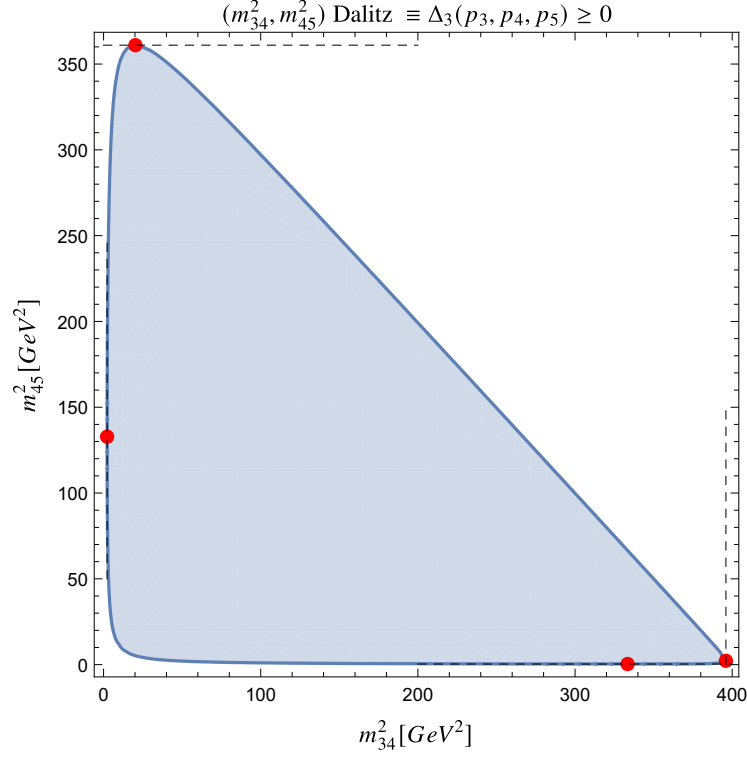


**Figure 4.3.**  $(m_{34}^2, m_{45}^2)$  Dalitz plot. Onto red dots the tangent (grey dashed lines) are either horizontal or vertical.

**Theorem 6** (GDs as parabolas).

Gram Determinants of order  $n$  are multivariate polynomials of the generalised Mandelstam variables of the same order. In each of its monomial every variable has either order 0,1 or 2 and must recover the mass dimension of  $2n$ . Hence GDs can always be viewed as parabolas in one gMv whose coefficients may depend on other gMvs.

□

For example, consider  $\Delta_3(p_1, p_2, p_3)$  and collect  $s$ :

$$\begin{aligned}
\Delta_3(p_1, p_2, p_3) = & -\frac{s^2 t_1}{4} \\
& + \frac{s}{4} \left[ s_2(m_1^2 - m_3^2 + t_1) + (m_1^2 + m_2^2 + m_3^2)t_1 + m_2^2(m_3^2 - m_1^2) - t_1^2 \right] \\
& + \frac{1}{4} \left\{ -m_1^2 s_2^2 + s_2[(m_1^2 - m_2^2)t_1 - m_1^4 + m_1^2(m_2^2 + m_3^2) + m_2^2 m_3^2] \right. \\
& \left. - m_3^2[(m_1^2 - m_2^2)t_1 + m_2^2(-m_1^2 + m_2^2 + m_3^2)] \right\}.
\end{aligned} \tag{4.31}$$

Analogously for  $t_1$ :

$$\begin{aligned}
\Delta_3(p_1, p_2, p_3) = & -\frac{st_1^2}{4} \\
& + \frac{t_1}{4} \left[ s(m_1^2 + m_2^2 + m_3^2 + s_2) + (m_1^2 - m_2^2)(s_2 - m_3^2) - s^2 \right] \\
& + \frac{1}{4} \{ s(m_1^2 - m_3^2)(s_2 - m_2^2) - m_1^2 s_2^2 + s_2[-m_1^4 + m_1^2(m_2^2 + m_3^2) + m_2^2 m_3^2] \\
& - m_2^2 m_3^2(-m_1^2 + m_2^2 + m_3^2) \}.
\end{aligned} \tag{4.32}$$

Theorem 6 looks to confirm the difficulty of GDs, however, from dimensional analysis:

**Corollary 4** (Dimensions constraints).

The mass dimension of a  $\Delta_n$  is

$$[\Delta_n] = n[s] = 2n. \tag{4.33}$$

Call  $c_2^{(x)}$  the  $x^2$  coefficient in a GD of order  $n$ , for  $x \in \{s, s_1, s_2, t_1, t_2\}$ . Then

$$[c_2^{(x)} x^2] = [\Delta_n] = 2n = [c_2^{(x)}] + [x^2] = [c_2^{(x)}] + 4, \tag{4.34}$$

from which

$$[c_2^{(x)}] = 2n - 4 \tag{4.35}$$

It follows that the solution to  $(-1)^{n+1} \Delta_n \geq 0$  has dimension  $2n - 4$  in the space  $(s, s_1, s_2, t_1, t_2)$ . For example, the  $\Delta_2$ s give hyperplanar constraints (the tangents to the Kibble curve in section 4.1).

□

The reason why I said that we can be content on the  $\Delta_2$  is because in general conditions on lower dimensional GDs are contained in the conditions for higher dimensional  $\Delta_n$ . Therefore if one wants  $(-1)^{n+1} \Delta_n \geq 0$  one also needs to satisfy all of the due  $(-1)^{m+1} \Delta_m \geq 0$ , for  $m < n$ . Specifically, in eq. (4.21) I anticipated that for  $\mathcal{P}_5$  we will only need to ask for  $\Delta_4 \leq 0$ . We are saying that with  $\Delta_4 \leq 0$  also come all the constraints on smaller degree GDs.

If this is true, then

**Corollary 5** (Constraints on higher order  $\Delta_n$  carve out a smaller phase space).

Consider a set of  $n + 1$  fourmomenta  $\{p_i\}_{i=1}^{n+1}$  with  $\sum_{i=1}^{n+1} p_i = 0$ . Its Principal Gram Determinant is  $\Delta_n$ ,  $\mathcal{R}_n$  is the region defined by

$$(-1)^{n+1} \Delta_n(\{p_i\}_{i=1}^n) \geq 0, \tag{4.36}$$

and  $\mathcal{R}_{n-1}$  is the region defined as the intersection of all possible  $\Delta_{n-1}$  you can build on the fourmomenta set:

$$\bigcap_{k \in \{1, \dots, n\}} [(-1)^n \Delta_{n-1}(\{p_i\}_{i=1}^n \setminus \{p_k\}) \geq 0]. \tag{4.37}$$

From corollary 4,  $\mathcal{R}_{n-1}$  defines a bigger volume than  $\mathcal{R}_n$ . The latter gives a better approximation<sup>1</sup> of the Phase Space than the former.

□

In fig. 4.4 you can see an example of corollary 5 for our case of interest, the  $2 \rightarrow 3$  scattering. In this case  $n = 4$ ; on the left panel you can see  $\mathcal{R}_3$  appearing bigger than  $\mathcal{R}_4$ , on the right panel. This can be seen even more clearly in fig. 4.5, where I selected from fig. 4.4 the slice  $s_2 = 250 \text{ GeV}^2$ . Notice how beautifully  $\mathcal{R}_4$  is entirely contained within  $\mathcal{R}_3$ , being at most tangent to it in some points.

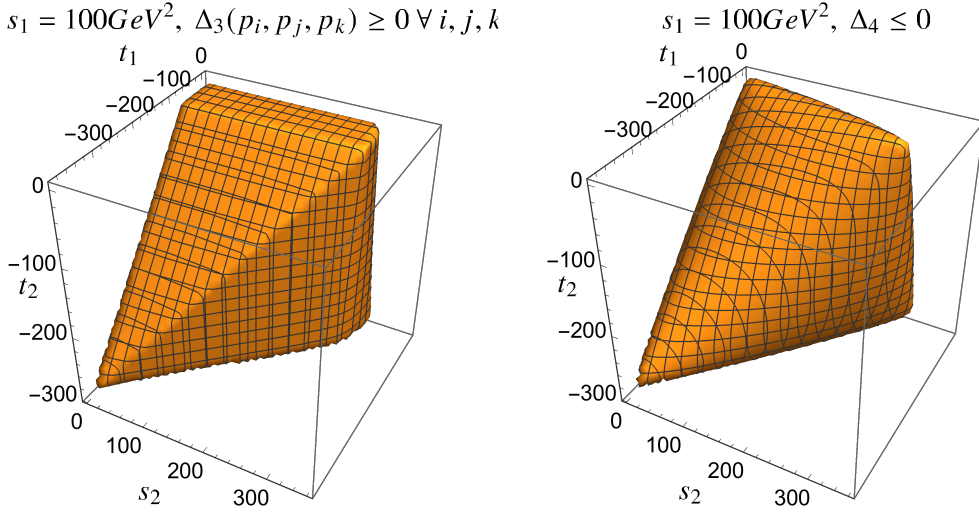


**Figure 4.4.** Comparison of the constraints coming from  $\Delta_3(p_i, p_j, p_k) \geq 0$ ,  $i, j, k \in \{1, 2, 3, 4, 5\}$  (left) and  $\Delta_4 \leq 0$  in a  $2 \rightarrow 3$  scattering having  $s = 400 \text{ GeV}^2$ ,  $s_1 = 100 \text{ GeV}^2$ ,  $m_1 = 3 \text{ GeV}$ ,  $m_2 = 2 \text{ GeV}$ ,  $m_3 = 1 \text{ GeV}$ ,  $m_4 = 0.5 \text{ GeV}$ ,  $m_5 = 0.1 \text{ GeV}$ .

Let us prove corollary 5. We will follow these steps: we consider a generic  $\Delta_n$ ,  $n > 2$ ; as Kajantie and Lindblom state in [93], we remark that, via lemma 4, we can choose one scalar product  $p_l \cdot p_m$ ,  $l \neq m$  and make it appear only in two symmetric positions of  $M_n$ . But then

$$\Delta_n = a_2(p_l \cdot p_m)^2 + a_1(p_l \cdot p_m) + a_0 = 0 \quad (4.38)$$

is solved onto some special roots requiring for two  $\Delta_{n-1}$  to have the proper sign. The demonstration being valid for any  $n$  allows us to repeat it equally onto these

<sup>1</sup>As a consequence, we also understand why sometimes we hear that a process with fewer bodies in the final state is expected to have a bigger cross section than one with more:

**Corollary 6** (Fewer bodies means bigger Phase Space).

Consider a  $n_i \rightarrow n_f$  process and a second process equal to the previous one but with an extra particle  $X$  in the final state of mass  $m_X \geq 0$ , so that all the shared particles have the same mass. Regardless of  $m_X$ , from corollary 5 we deduce that the second process has a smaller or equal Phase Space than the first one.

□

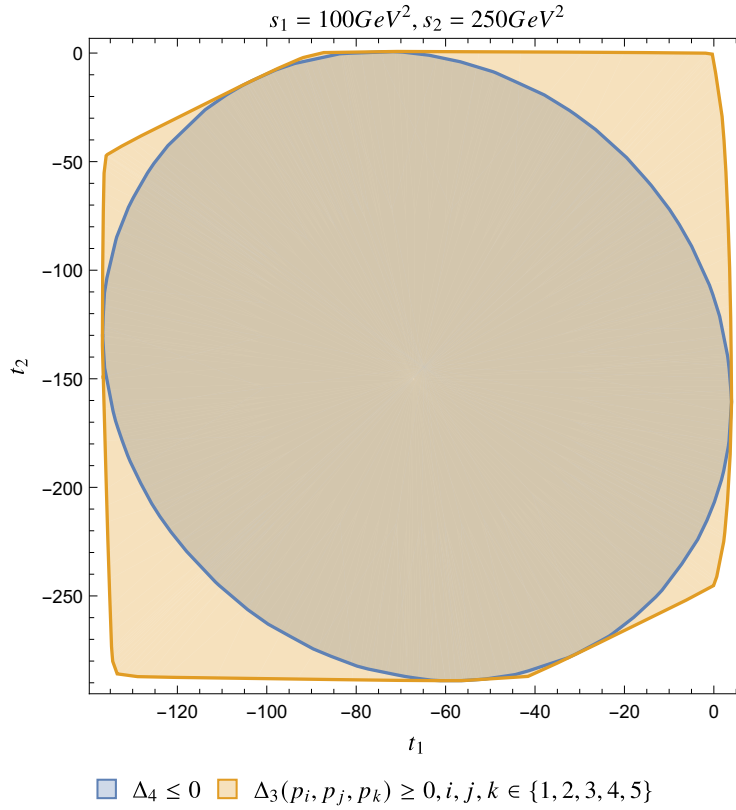


**Figure 4.5.** Same as fig. 4.4, but I asked for  $s_2 = 250 \text{ GeV}^2$ .  $\mathcal{R}_4$  is entirely contained within  $\mathcal{R}_3$ , being at most tangent to it in some points (see text for definitions).

new  $\Delta_{n-1}$  down to the  $\Delta_1$ .

For this proof we will need some terminology:

**Convention 2** (Matrix elements and minors naming).

Let

- $A$  be a generic  $n \times n$  symmetric matrix.
- $a_i^j$  be the element at the  $i^{\text{th}}$  row and the  $j^{\text{th}}$  column.
- $A_{i_1, \dots, i_k}^{j_1, \dots, j_z}$  be the minor obtained by erasing the rows  $(i_1, \dots, i_k)$  and the columns  $(j_1, \dots, j_z)$  from  $A$ .
- In our particular case  $A$  is the Gram Matrix  $M_n$  and we want to express it as a parabola as if  $p_l \cdot p_m, l \neq m$  was the independent variable and all other scalar products were parameters.
- In our proof there will be many sums. All of them are carried on indices among 1 and  $n$ . If as a sum limit we indicate, for example,  $r \neq l$ , we mean that we sum on  $\{1, n\} \setminus \{l\}$ .

□

For this proof we will use the Laplace expansion. Along the  $i^{\text{th}}$  row.

$$\det A = \sum_{j=1}^n (-1)^{i+j} a_i^j A_l^j. \quad (4.39)$$

The Laplace expansion can be used twice. Pick two distinct rows  $i, k$  and define

$$\det A = \sum_{j=1}^n \sum_{r \neq j} (-1)^{i+j+\phi(i,k)+\phi(j,r)} a_i^j a_k^r A_{l,\neq k}^{j,r}. \quad (4.40)$$

where  $\phi$  is needed to account for columns and rows cancellations. Here I provide one of its many possible definitions:

$$\phi(a, b) = \begin{cases} b & \text{if } b < a, \\ b - 1 & \text{if } a < b, \\ \text{error value} & \text{if } a = b. \end{cases} \quad (4.41)$$

Through eq. (4.40) it is easy to express  $\Delta_n$  as a parabola in  $x = p_l \cdot p_m$ :

**Corollary 7** ( $a_{lm}$  collection).

$$\begin{aligned} \det A = & -a_l^m a_m^l A_{l,\neq l}^{r^h,l} \\ & + \left[ a_l^m \sum_{k \neq l} (-1)^{l+k+\phi(l,m)+\phi(m,k)} a_m^k A_{l,\neq h}^{r^h,k} + a_m^l \sum_{j \neq m} (-1)^{m+j+\phi(l,m)+\phi(j,l)} a_l^j A_{l,\neq h}^{j,l} \right] \\ & + \sum_{j \neq m} \sum_{k \neq j,l} (-1)^{l+j+m+k+\phi(l,m)+\phi(j,k)} a_l^j a_m^k A_{l,\neq h}^{j,k}. \end{aligned} \quad (4.42)$$

□

Now in the first term in eq. (4.42) we erased both the  $l$ th row and column and both the  $m$ th row and column. Applying eq. (4.42) to our computation means that  $A$  is a Gram Matrix of fourmomenta  $(p_1, \dots, p_4)$  and  $A_{l,\neq h}^{r^h,l}$  is a symmetric Gram Determinant in which you erased the  $l$ th and the  $m$ th fourmomentum.

With now provide some notation in order to identify each  $a_{0,1,2}$  from eq. (4.38) with the terms from eq. (4.42).

**Definition 11** (GD with erased entries).

Start from a set of independent fourmomenta  $\{p_i\}_{i=1}^n$  and its associated  $\Delta_n$ .  $\Delta_{n-k}^{(i_1, \dots, i_k)}$  is  $\Delta_n$  in which we eliminated the fourmomenta with indices<sup>2</sup>  $i_1, \dots, i_k$ . For example in the  $2 \rightarrow 3$  scattering we will use  $\Delta_4(p_1, p_2, p_3, p_5)$ .  $\Delta^{(l)}$  is  $\Delta_3(p_2, p_3, p_5)$ ,  $\Delta^{(\underline{2}, \underline{5})} = \Delta_2(p_1, p_3)$ . In what follows we will be omitting the GD dimension when it will be obvious.

□

<sup>2</sup>This is not to be confused with the fourmomentum in the position  $i_1, \dots, i_k$ : a definition based on positions would have been meaningless given the GD symmetry under entries permutation.

From the first row of eq. (4.42), the  $a_{lm}^2$  coefficient in eq. (4.42) is  $-\Delta^{(l\eta)}$ .

The term in square brackets in eq. (4.42) is made of two symmetric terms. For example in the first one we compute the  $a_i^m$  cofactor as if  $a_m^l$  was 0 and viceversa. Let us name this cofactor  $V_{lm0}$ .

Finally the last term in eq. (4.42) is like computing the full GD with  $a_l^m = a_m^l = 0$ . In conclusion

**Theorem 7** (Kajantie and Lindblom trick).

Consider an  $n \times n$  Gram Matrix  $M$  and let

$$\Delta = a(M_{lm})^2 + bM_{lm} + c = a(M_{lm} - x_-)(M_{lm} - x_+). \quad (4.43)$$

with  $M_{lm} = M_{ml} = p_l \cdot p_m$ . You can show that

$$a = -\Delta^{(l\eta)} = -\Delta^{(ml)}, \quad (4.44)$$

$$b = \frac{V_{lm0}}{2} = \frac{V_{ml0}}{2}, \quad (4.45)$$

$$c = \Delta_n|_{x=0}, \quad (4.46)$$

$$(4.47)$$

and that the  $x_{\pm}$  from eq. (4.43) are

$$x_{\pm} = \frac{V_{lm0} \pm \sqrt{\Delta^{(l)}\Delta^{(\eta)}}}{\Delta^{(l\eta)}}. \quad (4.48)$$

□

Kajantie and Lindblom state the latter for a generic  $n$  without demonstrating it nor pointing to any reference for it. Nonetheless in my opinion it is non trivial to show that eq. (4.48) corresponds to  $\frac{-b \pm \sqrt{b^2 - 4ac}}{2a}$  with  $a, b, c$  from eqs. (4.44) to (4.46). I provide my tentative proof by induction in appendix I, while welcoming any pointer from the reader to anything more elegant.

In conclusion, for  $x_{\pm}$  to be real we need  $\Delta^{(l)}\Delta^{(\eta)} \geq 0$ , i.e.  $\Delta^{(l)}$  and  $\Delta^{(\eta)} \geq 0$  must have the same sign. The sign can be recovered from theorem 3. This concludes our proof.

### Branch selection

In this section we will focus on bounds coming from all possible  $\Delta_2$ s. Practically we will inscribe the physical region for a 2 → 3 process into a hyperbox in the  $(s_1, s_2, t_1, t_2)$  space<sup>3</sup> so that it will be clear that the process is bounded from all sides. Consequently all possible divergences of cross sections may only come from the matrix element diverging somewhere on the physical region.

<sup>3</sup>See definition 9 for the Generalised Madelstam variables definition.

Consider

$$\Delta_2(p_1, p_2) \leq 0 \rightarrow s \geq (m_1 + m_2)^2 \cup s \leq (m_1 - m_2)^2. \quad (4.49)$$

Since all  $\Delta_2(p_i, p_j)$  need to be  $\leq 0$ , instead of performing computations every time, we may also permute the indices of the fourmomenta (and those of the masses with them). In this way we can generalise to

$$(p_i \pm p_j)^2 \geq (m_i + m_j)^2 \cup (p_i \pm p_j)^2 \leq (m_i - m_j)^2. \quad (4.50)$$

Of the two branches we must pick

$$\begin{cases} (p_i + p_j)^2 \geq (m_i + m_j)^2, \\ (p_i - p_j)^2 \leq (m_i - m_j)^2, \end{cases} \quad (4.51)$$

if we want

$$p_i \cdot p_j = E_i E_j - \cos \theta_{ij} |\vec{p}_i| |\vec{p}_j| \geq 0, \quad (4.52)$$

which is the case since  $E_i \geq |\vec{p}_i| \geq 0$  and  $\cos \theta_{ij} \leq 1$ . Notice how choosing eq. (4.52) is the same thing of choosing the  $s$  branch in the Kibble curve in fig. 4.2.

We finally provide two more constraints to complete the gMvs hyperbox:  $\Delta_2(p_1 + p_2, p_3) \leq 0$  is solved by  $\{s_2 \leq (\sqrt{s} - m_3)^2\} \cup \{s_2 \geq (\sqrt{s} + m_3)^2\}$ . Since we know that  $s_2 \leq s$  we can only accept the solution  $s_2 \leq (\sqrt{s} - m_3)^2$ . Same reasoning for  $\Delta_2(p_1 + p_2, p_5) \leq 0 \rightarrow s_1 \leq (\sqrt{s} - m_5)^2$ . These last two bounds are generally valid for whatever scattering. Consider in fact  $p_{i,j}$  two final state fourmomenta and name  $P = (P^0, \vec{P})$  the sum of all initial state fourmomenta. Go to the frame in which all the remaining final fourmomenta are at rest

$$\sum_{k \neq i,j} p_k = (M, \vec{0}). \quad (4.53)$$

Then

$$(p_i + p_j)^2 = \left( P - \sum_{k \neq i,j} p_k \right)^2 = (\sqrt{s} - M)^2 - 2M(P^0 - \sqrt{s}) \leq (\sqrt{s} - M)^2. \quad (4.54)$$

The last inequality is valid since  $P^0 \geq \sqrt{s}$ , as  $P^2 = (P^0)^2 - \vec{P}^2 = s \geq 0$ . Let us summarise this result in

**Theorem 8** (Further bound on  $s$ -like variables).

In a  $n \rightarrow m$  process, let the initial state invariant mass be  $\sqrt{s}$ , take  $i, j$  in the final state and let the invariant mass of all other final particles be  $M$ . Then

$$(p_i + p_j)^2 \leq (\sqrt{s} - M)^2. \quad (4.55)$$

□

Something similar can be said for  $t$ -type variables. We provide for simplicity a demonstration for a  $2 \rightarrow 3$  process. Consider

$$u_2 = (p_1 - p_5)^2 = (p_2 - p_3 - p_4)^2 = m_2^2 + s_1 - 2p_2 \cdot (p_3 + p_4). \quad (4.56)$$

$p_2 \cdot (p_3 + p_4)$  is biggest if  $p_5 = (0, \vec{0})$ , but then  $p_3 + p_4 = p_1 + p_2$ . From this we can derive the following theorem

**Theorem 9** (Further bounds on  $t$ -like variables).

Consider a  $2 \rightarrow 3$  scattering and define generalised Mandelstam variables as in definition 9. We can show that the following bounds hold:

$$\begin{aligned} t_1 &> m_1^2 + s_2 - s, & u_3 &> m_2^2 + s_2 - s, \\ t_2 &> m_2^2 + s_1 - s, & u_4 &> m_2^2 + u_1 - s, \\ u_2 &> m_1^2 + s_1 - s, & u_5 &> m_1^2 + u_1 - s. \end{aligned} \quad (4.57)$$

□

To wrap up we collect here all the useful bounds for the gMVs when the positive branch for  $s$  is chosen:

**Theorem 10** (gMVs are bounded from above and from below).

$$(m_3 + m_4)^2 \leq s_1 \leq (\sqrt{s} - m_5)^2, \quad (4.58a)$$

$$(m_4 + m_5)^2 \leq s_2 \leq (\sqrt{s} - m_3)^2, \quad (4.58b)$$

$$m_1^2 + s_2 - s < t_1 \leq (m_1 - m_3)^2, \quad (4.58c)$$

$$m_2^2 + s_1 - s < t_2 \leq (m_2 - m_5)^2. \quad (4.58d)$$

□

Let's specify eq. (4.58) to the  $e^+e^- \rightarrow e^+e^-a$  case:

**Corollary 8** (Hyperbox of the VBF).

$$(M_e + M_a)^2 \leq s_1 \leq (\sqrt{s} - M_e)^2, \quad (4.59a)$$

$$(M_e + M_a)^2 \leq s_2 \leq (\sqrt{s} - M_e)^2, \quad (4.59b)$$

$$M_e^2 + s_2 - s < t_1 \leq 0, \quad (4.59c)$$

$$M_e^2 + s_1 - s < t_2 \leq 0. \quad (4.59d)$$

□

Notice how for  $M_a \rightarrow \max M_a = \sqrt{s} - 2M_e$  the allowed interval for  $s_{1,2}$  shrinks down to 0 and final leptons energies tend to their masses in the CoM frame, i.e. leptons tend to stay at rest.

### 4.3 Byers and Yang

Results of the previous sections are special cases of Byers and Yang mathematical description of scattering and decays phase spaces [90]. In this section I will walk in their footsteps in a more pictorial, physicists friendly way, as it will be helpful to better understand the  $2 \rightarrow 3$  scattering.

They base their beautiful review on the space  $\mathcal{S}_n$  of all the scalar products (definition 13) of the considered process (Assumption 1) and associate a Gram Matrix to each point of said space. Many remarks can be made on these real matrices, especially on their eigenvalues. The sign of the eigenvalues of these matrices can be used to classify subspaces of the entire space. The key question one can pose on  $\mathcal{S}_n$  is: is there a transformation that can make me continuously go from one point of  $\mathcal{S}_n$  to another? The answer is: it depends (theorem 14). If we want to stick to the physical case (1+3 dimensional space, theorem 13), we need to remember that to transform from forward to backward time-like fourmomenta there is no continuous transformation. This causes the 1+3 phase space to break down in pieces (theorem 15), that Byers and Yang analyse. They finally provide the GD phase space boundary theorem and their Kibble curve derivation.

**Assumption 1** (Positive masses).

We will consider  $1 \rightarrow n$  decays or  $2 \rightarrow n$  scatterings with non-zero masses:

$$m_i \neq 0 \quad \forall i = 1, \dots, n. \quad (4.60)$$

□

**Definition 12** (Generalised Minkowskian space  $D_{ab}$  and Generalised Minkowskian Metric  $\eta^{(ab)}$ ).

In a generalised  $d$  dimensional space  $D_{ab}$  we pick  $a$  dimensions to be time dimensions and  $b$  to be space,  $a + b = d$ . In particular  $D_{13}$  is the physical Minkowskian space  $\mathbb{M}_4$ . Correspondingly, the usual mostly negative Minkowskian metric is expressed in terms of the block matrices

$$\eta^{(ab)} := \begin{pmatrix} \mathbb{1}_a & 0 \\ 0 & -\mathbb{1}_b \end{pmatrix}, \quad (4.61)$$

where  $\mathbb{1}_d$  indicates a unit  $d \times d$  matrix.

□

**Definition 13** (Scalar product space  $\mathcal{S}_n$ ).

$\mathcal{S}_n$  is the space of all scalar products one can make with  $n$  fourmomenta. To each point in  $\mathcal{S}_n$  corresponds a Gram Matrix and a Gram Determinant.

□

**Definition 14** (Scalar product space region  $r_{a_- a_+}$ ).

Let  $M_n$  be a generic Gram Matrix of dimension  $n$ . Its ordered eigenvalues are  $\{\lambda_i\}_{i=1}^n \in \mathbb{R}$ . We say  $M_n$  belongs to the region  $r_{a_- a_+}$  if the number of  $M_n$  positive eigenvalues is  $a_+$  and the number of negative eigenvalues is  $a_-$ . We can define the number of null eigenvalues as  $a_0 = n - a_- - a_+$ .

□

**Corollary 9** (Regions and independent fourmomenta).

If  $M_n \in r_{a_- a_+}$  then exactly  $a_- + a_+$  fourmomenta are independent, in fact the other ones give null eigenvalues.

□

**Theorem 11** (Space and time dimension of an  $M_n$  realization: from  $r_{a_- a_+}$  to fourmomenta).

If  $M_n \in r_{a_- a_+}$  there exists a physical configuration of  $n$  fourmomenta in dimension  $D_{a_- a_+}$  making up  $M_n$ , of which only  $a_- + a_+$  are independent. Differently stated, there is a realization for  $M_n$ .  $a_-$  is the smallest possible space dimension,  $a_+$  is the smallest time dimension, meaning that it is always possible to embed the realization in a bigger space but there is no transformation that can be operated to make some space or time dimension redundant.

□

**Theorem 12** (From fourmomenta to  $r_{a_- a_+}$ ).

The converse is true: if  $n$  fourmomenta live in  $D_{a_- a_+}$  and  $a_- + a_+$  of them are independent, then the matrix  $M_n$  made from those fourmomenta lives in  $r_{a_- a_+}$ .

□

**Theorem 13** ( $D_{13}$ ).

In  $D_{13}$  (Minkowski) we can only have  $a_+ = 0, 1$ . Since

$$\text{tr } M_n = \sum_i m_i^2 > 0, \quad (4.62)$$

there must at least be one positive eigenvalue, hence  $a_+ = 1$ . This is because the trace of a matrix is the sum of its eigenvalues, therefore, if all the eigenvalues were negative, there would be no way to make the trace positive.

The possible regions of  $f_n$  in  $D_{13}$  are

$$r_{13}, r_{12}, r_{11}, r_{10}. \quad (4.63)$$

□

**Theorem 14** (If  $a_+ > 1$ ,  $r_{a_- a_+}$  is connected).

Starting from a set of vectors I can always perform a continuous deformation leaving the number of independent fourmomenta and the length of the fourmomenta unchanged.

□

**Theorem 15** (If  $a_+ = 1$ ,  $r_{a_- a_+}$  is made of  $2^{n-1}$  connected regions).

This is because there is no way of continuously transform from forward to backward time-like fourmomenta and vice-versa. However an overall sign will not change  $M_n$  hence the regions are  $2^{n-1}$ .

□

Let us now stick to the  $a_+ = 1$  case and consider a  $1 \rightarrow n$  decay, so that all final fourmomenta are forward timelike. There exists a region  $r_{1b}^0$  with all positive scalar products, exactly the one that we carved out in section 4.2.2.

**Definition 15** (Byers and Yang GDs).

Given a set of  $n$  fourmomenta  $\{p_i\}_{i=1}^n$ , the GDs à la Byers and Yang are

$$\delta_m = \sum_{\vec{p}} \Delta_m(\vec{p}), \quad (4.64)$$

where  $\Delta_m$  follows definition 2 and we summed over all possible subset  $\vec{p}$  of size  $m$  of the set  $\{p_i\}_{i=1}^n$ .

□

**Theorem 16** (Phase Space boundary).

A necessary and sufficient condition for a point of  $\mathcal{S}_n$  to be in  $r_{1s}$  is

$$(-1)^{n+1} \delta_n \begin{cases} \geq 0 & \text{if } n \leq s + 1, \\ = 0 & \text{if } n > s + 1. \end{cases} \quad (4.65)$$

$$(4.66)$$

The sufficiency can be proved as follows. Let us write down the characteristic polynomial of  $M_n$  as a function of  $\lambda$ :

$$\lambda^{n-s-1}(\lambda^{s+1} - \delta_1 \lambda^s - \dots - \delta_{s+1}) = 0, \quad (4.67)$$

where we stopped at  $\delta_{s+1}$  thanks to eq. (4.66). But then  $M_n$  has  $n - s - 1$  null eigenvalues. Moreover the term in brackets has only 1 change of sign henceforth there only is 1 positive eigenvalue.

For the necessity we need to assume that  $M_s$  is in  $r_{1s}$  and recover eqs. (4.65) and (4.66). Equation (4.66) is easy because null eigenvalues will make all minors of dimension bigger than  $s+1$  null. As for eq. (4.65), it is proven via linear independence and masses positivity.

□

Specifically in 3 spatial dimensions eqs. (4.65) and (4.66) reduce to the discussed Kibble problem.

$\Delta_3 = 0$  is an algebraic surface  $S$  of degree 3, i.e. it is a cubic surface in  $s, t, u$ . It has 4 conical points. A conical point of a surface is a point  $M$  such that there exists a cone with vertex  $M$  tangent at  $M$  to the surface. They are

$$\begin{aligned} C_0 &: (x, y, z) = (m_2 m_3, m_3 m_1, m_1 m_2), \\ C_1 &: (x, y, z) = (m_2 m_3, -m_3 m_1, -m_1 m_2), \\ C_2 &: (x, y, z) = (-m_2 m_3, m_3 m_1, -m_1 m_2), \\ C_3 &: (x, y, z) = (-m_2 m_3, -m_3 m_1, m_1 m_2). \end{aligned} \quad (4.68)$$

$S$  is made by a central piece  $S_0$  and 4 horns  $H_{0,1,2,3}$  stemming out of the respective  $C_i$ .  $S_0$  is a closed surface contained in the parallelepiped whose vertices are

$$(\pm m_2 m_2, \pm m_3 m_1, \pm m_1 m_2). \quad (4.69)$$

What are the possible regions? In principle all  $r_{ab}$  combinations with  $a + b = 3$  are possible, however some are not allowed by theorem 13. They are

- $r_{30}$ , the inside of  $S_0$ .
- $r_{20}$ , the surface of  $S_0$ ,  $C_i$  excluded.
- $r_{21}$ , the region outside  $S_0$  and outside the horns.

Instead the allowed ones are

- $r_{12}$ , the inside of the horns.
- $r_{11}$ , the surfaces of the horns,  $C_i$  excluded.
- $r_{10}$ , the  $C_i$ .

The Kibble curve is obtained by intersecting the  $H_0$  horn with the plane coming from

$$s + t + u = k. \quad (4.70)$$

These properties can be generalised to  $1 \rightarrow n$  decays and  $2 \rightarrow n$  scatterings.

## 4.4 Slow ALP: $2 \rightarrow 3$ degenerates to $2 \rightarrow 2$

In section 4.3 we saw that in  $1 + 3$  dimensions a set of  $n$  fourmomenta has an associated space that can be divided in discontinuous regions; some of them do allow for a physical representation of a scattering. Each of the latter have a different number of space dimensions, from 3 to 0. Fewer space dimensions means that some fourmomenta are a linear combination of some other. In this section I will explore the case in which the ALP fourmomentum is a linear combination of the initial ones  $p_{1,2}$ , implying that in the CoM the ALP is at rest. This is not just an academic exercise as in the next sections (sections 7.2 and 8.5.2) I will derive that the ALP at rest case is maximising for our matrix element.

Assume that in the CoM let  $E_4$  live in the tiny slice:

$$E_4 \in m_4[1, 1 + \nu], \quad \nu \ll 1. \quad (4.71)$$

Let us define the cross section computed under this assumption:

**Definition 16** (Restricted cross section).

Define the VBF cross section (eq. (1.29)) under the condition in eq. (4.71), i.e. when the ALP is almost at rest:

$$\sigma_\nu = \int d\vec{x} I_4(\nu), \quad (4.72)$$

where the integration variables are

$$\vec{x} = (E_3, E_5, c_3, c_4, c_5, \phi_3, \phi_4, \phi_5), \quad (4.73)$$

and

$$I_4(\nu) := \int_{m_4}^{m_4(1+\nu)} \frac{dE_4}{2E_4} \delta^{(4)}(p_1 + p_2 - p_3 - p_4 - p_5) f(\vec{x}, E_4) =: \int_{m_4}^{m_4(1+\nu)} dE_4 g(\vec{x}, E_4). \quad (4.74)$$

In eq. (4.74) we summarised the matrix element and all other coefficients in  $f(\vec{x}, E_4)$ .

□

Let us expand  $I_4(\nu)$  in series with respect to the small adimensional parameter  $\nu$ .  $I_4(0) = 0$ , so the first non 0 term in the expansion is of order  $\nu$ . To compute its coefficient we need to evaluate the first derivative with respect to  $\nu$ :

$$l := \lim_{k \rightarrow 0} \frac{I_4(\nu + k) - I_4(\nu)}{k} = \lim_{k \rightarrow 0} \frac{1}{k} \int_{m_4(1+\nu)}^{m_4(1+\nu+k)} dE_4 g(\vec{x}, E_4). \quad (4.75)$$

For the mean value theorem there exists a point  $\Lambda$  in  $[m_4(1 + \nu), m_4(1 + \nu + k)]$  such that

$$\int_{m_4(1+\nu)}^{m_4(1+\nu+k)} dE_4 g(\vec{x}, E_4) = k g(\vec{x}, \Lambda). \quad (4.76)$$

We can plug this in our limit eq. (4.75)

$$l = \lim_{k \rightarrow 0} g(\vec{x}, \Lambda) = g(\vec{x}, m_4(1 + \nu)). \quad (4.77)$$

We finally have to evaluate the derivative on 0:

$$l \xrightarrow{\nu \rightarrow 0} g(\vec{x}, m_4), \quad (4.78)$$

then

$$\sigma_\nu = \int d\vec{x} I_4(\nu) = \int d\vec{x} \left[ I_4(0) + \nu \frac{dI_4}{d\nu}(0) + \mathcal{O}(\nu^2) \right] = \int d\vec{x} \left[ 0 + \nu g(\vec{x}, m_4) + \mathcal{O}(\nu^2) \right] \quad (4.79)$$

When  $E_4 = m_4$  the fourth particle is at rest; no polar or azimuthal angle can be defined for  $\vec{p}_4 = 0$ , then angular integrations in eq. (4.72) amount to  $4\pi$ . The problem becomes planar and  $\phi_{3,5}$  can be rotated away. Finally

$$\begin{aligned} \sigma_\nu &= 0 \\ &+ 16\pi^3 \int dE_3 dE_5 dc_3 dc_5 \delta(\sqrt{s} - E_3 - m_4 - E_5) \delta^{(3)}(\vec{p}_3 + \vec{p}_5) f(\vec{x}, m_4) \\ &+ \mathcal{O}(\nu^2) \end{aligned} \quad (4.80)$$

In summary

**Theorem 17** (At rest ALP cross section expansion and Byers-Yang regions).

In  $e^+e^- \rightarrow e^+e^-a$ , the ALP can either move or be at rest in the CoM. The moving ALP configuration belongs to the Byers and Yang  $r_{13}$  region. In the  $r_{12}$ ,  $r_{11}$  and  $r_{10}$  regions the ALP is at rest. We can put them in relation with the the VBF cross section series expansion with respect to the ALP three-momentum:

- The 0<sup>th</sup> order expansion is 0.  $E_4 = m_4$  is a physical configuration but weights 0 into the cross section integral because it happens on a 0 measure volume.
- The first order expansion gives back exactly a 2 body scattering. This is telling us that if we refine sufficiently our precision in order to see things as small as  $\nu$ , we will see a fourth particle at rest while the dynamics of the others can correctly be approximated as a  $2 \rightarrow 2$  process with a new injected energy  $s' = (\sqrt{s} - m_4)^2$ .
- If we could be even more precise we would start realizing that particle 4 is not exactly at rest but has a tiny range in which it can move. In this sense we are describing a quasi 2 body decay.

□

As long as it is sufficient to only retain the first order, the kinematics of the process is fully solved. For our case study

$$e^-(p_1)e^+(p_2) \rightarrow e^-(p_3)e^+(p_5)a(p_4) \quad (4.81)$$

we have:

- The final leptons are back to back and only one angle is relevant, since  $\theta := \theta_3 = \theta_5 - \pi$ .
- Leptons energies are fixed to

$$E_3 = E_5 = \frac{\sqrt{s} - M_a}{2}. \quad (4.82)$$

#### 4.4.1 Heavy ALP

A concrete case in which a little energy range is allowed to the ALP is when its mass is very close to its allowed maximum. From theorem 10

$$E_a = \frac{s + M_a^2 - u_1}{2\sqrt{s}}, \quad 4M_e^2 \leq u_1 \leq (\sqrt{s} - M_a)^2. \quad (4.83)$$

from which

$$\max E_a = E_a(u_1 = 4M_e^2) = \frac{s + M_a^2 - 4M_e^2}{2\sqrt{s}} \quad (4.84)$$

$$\min E_a = E_a(u_1 = (\sqrt{s} - M_a)^2) = M_a. \quad (4.85)$$

Now  $M_a \in [0, \bar{M}]$ ,  $\bar{M} = \sqrt{s} - 2M_e$  so in the limit of big  $M_a$

$$\max E_a \xrightarrow{M_a \rightarrow \bar{M}} \bar{M}, \quad \min E_a \xrightarrow{M_a \rightarrow \bar{M}} \bar{M}. \quad (4.86)$$

i.e. the minimal and maximal ALP energy coincide and collapse on the ALP mass itself. We are then justified to use an expansion of the form eq. (4.80).

We plot here the SM+ALP squared amplitude in this 2 body regime fig. 4.6) as a function of  $\cos \theta$  in order to show that for sufficiently large  $M_a$  the matrix element starts to not being dependent on  $\cos \theta$ , i.e. isotropy is achieved. We lose the anisotropy that is typical of the  $2 \rightarrow 3$  phase space (as we will see, the  $2 \rightarrow 3$  phase space is anisotropic *per se*) and downgrade to the  $2 \rightarrow 2$  scattering isotropy, in fact the  $2 \rightarrow 2$  phase space density does not depend on angular variables. Although the matrix element does depend on  $\cos \theta$ , the smallness of  $\sqrt{s} - \bar{M}$  eats this dependence up.

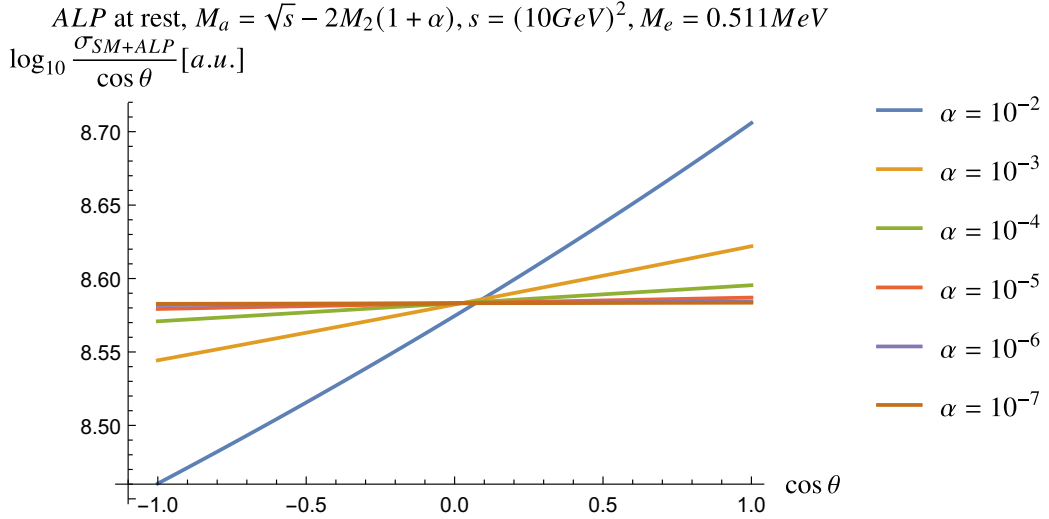


**Figure 4.6.** SM+ALP matrix element evaluated on ALP at rest in the centre of mass frame for the process eq. (4.81). There the final leptons have fixed and equal energies and are back to back.  $\theta$  is the angle between the positive  $z$  direction, aligned with the incoming electron, and the outgoing  $e^-$ . For extreme values of the ALP mass, isotropy is achieved, a signal that our process is transitioning from a  $2 \rightarrow 3$  into a  $2 \rightarrow 2$  scattering.

In order to better quantify isotropy we define the following *asymmetry functional*

**Definition 17** (Asymmetry functional).

Let  $f(\cos \theta, \vec{x})$  be a function depending on  $\cos \theta$  and whatever other variables  $\vec{x}$  and let it be monotonic in  $\cos \theta$  over the solid angle. Let  $c_{\mp}$  be the minimum and the maximum allowed  $\cos \theta$ , respectively. Asymmetry is a functional defined as

$$\mathcal{A}_f := \frac{f(c_+, \vec{x}) - f(c_-, \vec{x})}{f(c_+, \vec{x}) + f(c_-, \vec{x})}. \quad (4.87)$$

□

If  $f$  is deeply anisotropic and points to  $c_{\pm}$  we expect  $\mathcal{A}_f$  to point towards  $\pm 1$ ; if  $f$  is isotropic we expect  $\mathcal{A}_f$  to be 0. In fig. 4.7 we apply the functional  $\mathcal{A}$  to the full

matrix element evaluated on the CoM in the quasi two body approximation with the definition  $M_a = \sqrt{s} - 2(1 + \alpha)M_e$ . We see how for large  $M_a$ , hence for small  $\alpha$ , the process tends to get more and more isotropic.

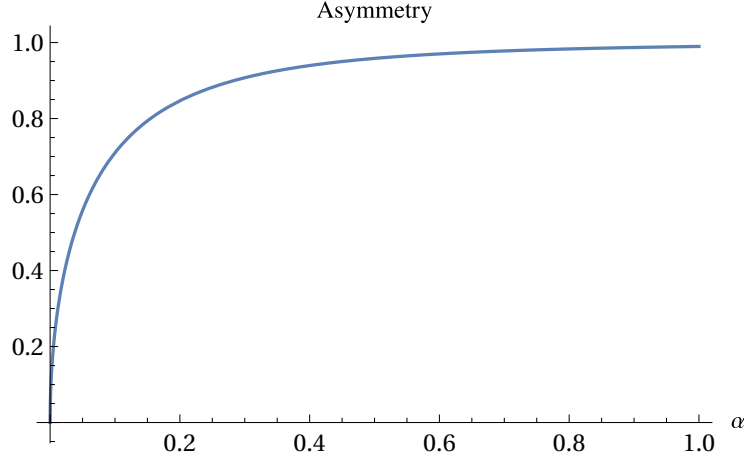


**Figure 4.7.** Asymmetry (eq. (4.87)) of the SM+ALP matrix element evaluated in the CoM in the quasi two body approximation with the definition  $M_a = \sqrt{s} - 2(1 + \alpha)M_e$ .

For our physical values  $M_e = 0.511$  MeV,  $s = 112$  GeV<sup>2</sup>, the asymmetry is less than  $\frac{1}{3}$  if  $\alpha < 0.015$ .

#### 4.4.2 Scattering reduction in Gram terminology

In this section we show how the same discussion of the previous section can be conducted within the GDs formalism. Consider the following symmetric Gram determinants defined onto eq. (4.81)

$$\left\{ \begin{array}{l} \Delta_2(p_1 + p_2, p_4) = -s|\vec{p}_4|^2 \leq 0, \end{array} \right. \quad (4.88)$$

$$\left\{ \begin{array}{l} \Delta_3(p_1 + p_2, p_1, p_4) = s(|\vec{p}_1||\vec{p}_4| \sin \theta_4)^2 \geq 0, \end{array} \right. \quad (4.89)$$

$$\left\{ \begin{array}{l} \Delta_3(p_1 + p_2, p_3, p_4) = s(|\vec{p}_3||\vec{p}_4| \sin \theta_{34})^2 \geq 0, \end{array} \right. \quad (4.90)$$

$$\left\{ \begin{array}{l} \Delta_4(p_1 + p_2, p_2, p_3, p_4) = -s(|\vec{p}_2||\vec{p}_3||\vec{p}_4| \sin \theta_{23} \sin \theta_{24} \sin \phi)^2 \leq 0. \end{array} \right. \quad (4.91)$$

In eqs. (4.88) to (4.91) we imposed the signs from eq. (3.38).

Let  $M_a$  be so large that the three-momentum

$$|\vec{p}_4| < \lambda\sqrt{s}, \quad \lambda \ll 1. \quad (4.92)$$

At  $\mathcal{O}(\lambda^0)$  all inequalities in the system are equalities in the gMvs, hence we are onto the phase space boundary. The solution to equalities in eqs. (4.88) to (4.90) is

$$\left\{ \begin{array}{l} s_1 = s_2 = M_e^2 + M_a\sqrt{s} =: s_0, \\ t_1 = t_2. \end{array} \right. \quad (4.93)$$

When this solution is plugged into the equality in eq. (4.91), it is automatically satisfied. In polar coordinates eq. (4.93) is

$$\left\{ \begin{array}{l} E_3 = E_5 = \frac{\sqrt{s} - M_a}{2}, \\ c_5 = -c_3, \end{array} \right. \quad (4.94)$$

and the energy conservation becomes  $\sqrt{s} - M_a - E_3 - E_5 = 0$ , in other words we got to a  $2 \rightarrow 2$  scattering. Anticipating the result from eq. (5.8), the cross section integral becomes

$$\begin{aligned} \sigma &= \sigma_0 \int ds_1 ds_2 dt_1 dt_2 |\mathcal{M}|^2 \frac{\theta(-\Delta_4)}{\sqrt{-\Delta_4}} \xrightarrow{\text{ALP at rest}} \\ &\sigma_0 \int dt_1 \int_{t_1-\delta}^{t_1+\delta} dt_2 \int_{s_0-\delta}^{s_0+\delta} ds_1 \int_{s_0-\delta}^{s_0+\delta} ds_2 |\mathcal{M}|^2 \frac{\theta(-\Delta_4)}{\sqrt{-\Delta_4}}, \end{aligned} \quad (4.95)$$

where

$$\delta := \frac{\lambda^2 s}{2}. \quad (4.96)$$

The  $s_2$  integration can be performed expanding <sup>4</sup> in small  $\lambda$  and small  $M_e$ , performed the  $s_1$  integration and expanded again, ending up with

$$\begin{aligned} \sigma(\text{ALP at rest}) &= \sigma_0 \frac{4s^{3/2}\lambda^4}{(\sqrt{s} - M_a)} \int dt_1 \int_{t_1-\delta}^{t_1+\delta} \left( \frac{dt_2 |\mathcal{M}|^2}{\sqrt{(t_1 - t_2)^2}} \right)_{s_1=s_2=s_0} + \mathcal{O}(\lambda^5) \\ &= \sigma_0 \frac{16\sqrt{s}\lambda^4}{(\sqrt{s} - M_a)} \log\left(\frac{\lambda}{\sqrt{2}}\right) \int dt_1 \left( |\mathcal{M}|^2 \right)_{\substack{s_1=s_2=s_0 \\ t_2=t_1}} + \mathcal{O}(\lambda^5) \end{aligned} \quad (4.97)$$

In eq. (4.97) we simply evaluated  $(s_1, s_2, t_2)$  on the middle point of the integration domain committing an error that we include in the  $\mathcal{O}(\lambda^5)$ . The fact that we end up with a  $t_1$  integration over a constant phase space means that we reduced to a  $2 \rightarrow 2$  scattering in this case too.

---

<sup>4</sup>This is proper since with an ALP at rest we can be sure the electrons are ultrarelativistic and their mass is negligible.

## Chapter 5

# 2 $\rightarrow$ 3 cross section and distributions

We left our problem of computing cross sections for the process eq. (1.29) at the eq. (2.19) promising that GDs would have helped to solve our integrals. We are now able to restart exactly from there to prove it. The strategy will be integrating over the azimuthal angle  $\phi_3$  and converting everything to GDs so that we can exploit all of the nice properties from the previous chapter. One can equivalently use  $\phi_3$  or  $\phi_5$ , keeping in mind that the fourmomentum  $p_4$  was integrated away with the Dirac  $\delta$  of fourmomentum conservation and that one of the two  $\phi_{3,5}$  can always be rotated away. The reason to integrate the chosen azimuthal angle first is because, as will be evident shortly, the Jacobian that is produced from the Dirac  $\delta$  from eq. (2.14) can be promptly expressed in terms of just a  $\Delta_4$ . If we integrated other variables with the  $\delta$  we would not obtain an equally simple Jacobian.

With this, we will compute the differential and total cross sections  $\frac{d^2\sigma_t}{dt_2 ds_1}$  and  $\frac{d\sigma_t}{dt_2}$  (section 5.2);  $\frac{d^2\sigma_s}{ds_2 du_1}$ ,  $\frac{d\sigma_s}{du_1}$  and  $\sigma_s$  (section 5.3).

We will use these computations to show that, when all of the phase space is considered, the  $s$  channel and the  $s-t$  interference can be neglected with respect to the  $t$  channel. Other distributions can be recovered by the means of the integrand symmetries, as we will show in chapter 6. Finally, we dedicate to the most important distribution,  $\frac{d^2\sigma_t}{dt_1 dt_2}$ , its own chapter (chapter 7).

### 5.1 Gram Phase Space density and how to integrate on it

We reprise our calculation of the cross section eq. (2.19) by dealing with the the Dirac  $\delta$  argument. The argument of  $\delta$ , denoted by  $f$ , is linear in  $\cos\phi_3$ , whereas the matrix element does not depend on it. Hence we can define

$$f = a \cos\phi_3 - b = 0 \text{ if } \cos\phi_3 = \frac{b}{a}, \quad (5.1)$$

from which it follows

$$\int d\phi_3 \delta(f) = \frac{1}{|a| \sqrt{1 - \left(\frac{b}{a}\right)^2}}, \quad (5.2)$$

with  $a$  and  $b$  depending on energies, masses and angles. To deal with the jacobian in eq. (5.2), we notice that the expression  $1 - \left(\frac{b}{a}\right)^2$  is  $\sin^2(\phi_3)$ , for which we can exploit eq. (3.36) and obtain

$$a^2 \left[ 1 - \left(\frac{b}{a}\right)^2 \right] = \frac{-4\Delta_4}{\lambda(s, m_1^2, m_2^2)}, \quad (5.3)$$

$\lambda$  as in definition 7.

Let us now perform a change of variables from polar coordinates to gMvs:

$$d\mu_P = ds_1 ds_2 dt_1 dt_2 |J| =: d\mu_L |J|, \quad (5.4)$$

$$|J| = \frac{1}{16\lambda(s, m_1^2, m_2^2)}, \quad (5.5)$$

where we defined  $d\mu_L$  as the volume element for the gMvs. In conclusion the 2 → 3 scattering cross section is expressed in terms of Lorentz invariant quantities as

$$\sigma_0 = \frac{|c_{ee\gamma}|^4 |c_{a\gamma\gamma}|^2}{32(2\pi)^4 f \sqrt{\lambda(s, m_1^2, m_2^2)}}, \quad (5.6)$$

$$\mathcal{D} := \frac{\theta(-\Delta_4)}{\sqrt{-\Delta_4}}, \quad (5.7)$$

$$\sigma = \sigma_0 \int d\mu_L |\mathcal{M}|^2 \mathcal{D}. \quad (5.8)$$

In the literature eq. (5.7) is often referred to as the scattering density.

Since the cross section integration was so radically transformed, I think this is a good point to stop and make a dimensionality sanity check and invite you to look it up in appendix E.1.

We now finally use what we learned in section 4.2.2, specifically I will use theorem 7 with  $s_2$  as independent variable supposing the matrix element is not depending on it. This is an assumption I can do as I am using the SSM, so that I know that the Matrix element depends at most on two gMvs. I leave dealing with more complicated Matrix elements for future work. For now it is sufficient to know that the generic integral

$$I_x^{(n)} := \int dx \frac{x^n}{\sqrt{(x-x_-)(x-x_+)}} \quad (5.9)$$

is solved to

$$I_x^{(n)} = -\frac{\sqrt{\pi}\Gamma(n+2)(x_-^{n+1} {}_2F_1(\frac{1}{2}, n+1; n+\frac{3}{2}; \frac{x_-}{x_+}) - x_+^{n+1} {}_2F_1(\frac{1}{2}, n+1; n+\frac{3}{2}; \frac{x_+}{x_-}))}{(n+1)\sqrt{x_-}\sqrt{x_+}\Gamma(n+\frac{3}{2})} \quad (5.10)$$

where my assumptions were  $n \in \mathbb{Z}$ ,  $a, x_{\pm} \in \mathbb{R}$ , simply coming from asking that  $I_x^{(n)}$  is an integration on some gMv for a physical matrix element.  ${}_2F_1$  is the hypergeometric function. I point to appendix G for the definition of special mathematical functions.

Sticking to the SSM case, let us define the  $s_2$  integration as

$$I_{s_2} := \int ds_2 \frac{\theta(-\Delta_4)}{\sqrt{-\Delta_4}}. \quad (5.11)$$

We can express  $\Delta_4$  as a polynomial in  $s_2$  and call its roots  $s_2^{\pm}$  (we will always be using this convention from now on):

$$\Delta_4 = as_2^2 + bs_2 + c = a(s_2 - s_2^-)(s_2 - s_2^+). \quad (5.12)$$

By using eq. (4.48) we can deduce that

$$\begin{aligned} b^2 - 4ac &= 64\Delta_3^{(\beta)} \Delta_3^{(\beta)} = 64\Delta_3(p_1, p_2 - p_5, p_5)\Delta_3(p_1, p_2 - p_5, p_3) \\ &= 4\mathcal{G}_1(s, t_2, s_1, m_2^2, m_1^2 m_5^2)\mathcal{G}_2(t_1, s_1, t_2, m_3^2, m_1^2, m_4^2). \end{aligned} \quad (5.13)$$

For this we deduce that further integration will take place in the region identified by  $\mathcal{G}_{1,2} \leq 0$ . Equation (5.8) becomes

$$\sigma = \sigma_0 \int ds_1 dt_1 dt_2 \theta(-\mathcal{G}_1)\theta(-\mathcal{G}_2)I_{s_2}. \quad (5.14)$$

$\mathcal{G}_{1,2}$  will be crucial in the following sections hence we explicitly write them

$$\mathcal{G}_1 = \frac{M_e^2 s_1^2}{2} - s_1 \left( \frac{s t_2}{2} + M_e^4 \right) + \frac{1}{2}(M_e^6 - 3M_e^2 s t_2 + s t_2(s + t_2)), \quad (5.15)$$

$$\begin{aligned} \mathcal{G}_2 &= \frac{t_1 s_1^2}{2} - \frac{1}{2}s_1(M_a^2 + 2M_e^2 + t_2 - t_1) \\ &+ \frac{1}{2}(M_a^4 M_e^2 + M_e^4 t_1 + M_e^2 t_2(t_2 - t_1) + M_a^2(t_1 t_2 - M_e^2(t_1 + 2t_2))). \end{aligned} \quad (5.16)$$

As to the actual integration, using eq. (5.12) we can restate the integration to the support of the  $\theta$  function between  $s_-$  and  $s_+$

$$\begin{aligned}
I_{s_2} &:= \int_{s_2^-}^{s_2^+} \frac{ds_2}{\sqrt{-\Delta_4}} = \frac{-i}{\sqrt{a}} \left[ \log \left( 2\sqrt{-\Delta_4} - i \frac{2as_2 + b}{\sqrt{a}} \right) \right]_{s_2^-}^{s_2^+} \\
&= \frac{-i}{\sqrt{a}} \left[ \log \left( -i \frac{\sqrt{b^2 - 4ac}}{\sqrt{a}} \right) - \log \left( i \frac{\sqrt{b^2 - 4ac}}{\sqrt{a}} \right) \right] \\
&= \frac{-i}{\sqrt{a}} \left[ \log(-1) + \log \left( i \frac{\sqrt{b^2 - 4ac}}{\sqrt{a}} \right) - \log \left( i \frac{\sqrt{b^2 - 4ac}}{\sqrt{a}} \right) \right] \\
&= \frac{\pi}{\sqrt{a}}.
\end{aligned} \tag{5.17}$$

This result is obtained with Mathematica and is found tabulated in [107]. It only depends on  $a$ , the reason being the following. Consider a generic function  $g(x, y)$  and integrate it as follows

$$\mathcal{I} = \int dx g(x - x_1, x - x_2). \tag{5.18}$$

Perform the change of variable (conformal transformation)

$$z := \frac{x - x_1}{\alpha}, \quad \alpha := x_2 - x_1. \tag{5.19}$$

Then

$$\mathcal{I} = \int \alpha dz g(\alpha z, \alpha(z - 1)). \tag{5.20}$$

If

$$g(\alpha x, \beta y) = g_1(\alpha)g_2(\beta)g(x, y), \tag{5.21}$$

the integration becomes

$$\mathcal{I} = \alpha g_1(\alpha) g_2(\alpha) \int dz g(z, z - 1), \tag{5.22}$$

which does not depend on  $x_{1,2}$  separately but only on  $x_2 - x_1 = \alpha$  and only depends on  $\alpha$  multiplicatively. In eq. (5.11) we are lucky because

$$g(x, y) \rightarrow \frac{1}{\sqrt{xy}}, \tag{5.23}$$

$$g_{1,2}(\alpha) = \alpha^{-1/2}, \tag{5.24}$$

for which  $\alpha g_1(\alpha)g_2(\alpha) = 1$ . In conclusion in eq. (5.17) we only have to recover  $a$ . As from theorem 7:

$$a = \frac{\lambda(s_1, t_2, m_1^2)}{16}. \tag{5.25}$$

A concrete example of matrix element not depending on  $s_2$  is that of the  $t$  channel, for which  $\mathcal{M}_t = \frac{1}{t_1^2 t_2^2}$ . Using eqs. (5.14) and (5.17), the total cross section reads

$$\sigma_t = \sigma_0 \pi \int \frac{dt_1 dt_2 ds_1}{t_1^2 t_2^2} \frac{\theta(-\mathcal{G}_1)\theta(-\mathcal{G}_2)}{\sqrt{\lambda(s_1, t_2, m_1^2)}}. \quad (5.26)$$

## 5.2 $\frac{d^2\sigma_t}{dt_2 ds_1}$

Let us continue the computation we started in eq. (5.26) and integrate  $t_1$  away, so to obtain a fully analytical expression for  $\frac{d^2\sigma_t}{dt_2 ds_1}$  of the  $t$ - channel. First of all let us focus on the integration domain. Only  $\mathcal{G}_2$  depends on  $t_1$ , so the integration domain is given by

$$\mathcal{G}_2 = \frac{s_1^2}{2}(t_1 - t_1^-)(t_1 - t_1^+) \leq 0, \quad (5.27)$$

realised onto

$$t_1^- \leq t_1 \leq t_1^+ < 0. \quad (5.28)$$

In eq. (5.27) I used eq. (5.16) as a polynomial in  $t_1$  with roots  $t_1^\pm$ :

$$2s_1 t_1^\pm = s_1 t_2 - s_1^2 + M_a^2(s_1 - t_2) + M_e^2(M_a^2 + 2s_1 + t_2) - M_e^4 \pm \sqrt{\lambda(s_1, M_e^2, M_a^2)\lambda(s_1, t_2, M_e^2)}. \quad (5.29)$$

Notice how eq. (5.29) respects the form predicted in theorem 7. Moreover  $t_1^+ = 0$  if  $t_2 = M_a^2$ , which is impossible since  $t_2 \leq 0$  always. Therefore the dangerous  $t_1 = 0$  subspace is always excluded. The subspace  $t_2 = 0$  is excluded too for symmetry. At this point the double cross section distribution domain must satisfy both

$$\mathcal{G}_1 = \frac{M_e^2}{2}(s_1 - s_1^-)(s_1 - s_1^+) \leq 0 \quad (5.30)$$

and the constraints coming from eq. (5.29):

$$\begin{cases} s_1^+ \leq (M_e + M_a)^2 \leq s_1 \leq s_1^- \leq (\sqrt{s} - M_e)^2, \\ \min t_2 \leq t_2 \leq \max t_2, \end{cases} \quad (5.31)$$

with

$$\min t_2 = (M_e + M_a)^2 + M_e^2 - \frac{s + (M_e + M_a)^2 - M_e^2}{2} + \frac{\sqrt{\lambda_{\text{in}}\lambda(s, (M_a + M_e)^2, M_e^2)}}{2s}, \quad (5.32)$$

$$\max t_2 = (M_e + M_a)^2 + M_e^2 - \frac{s + (M_e + M_a)^2 - M_e^2}{2} - \frac{\sqrt{\lambda_{\text{in}}\lambda(s, (M_a + M_e)^2, M_e^2)}}{2s}. \quad (5.33)$$

The results are in agreement with ref. [93] (we remind that in this case  $\lambda_{\text{in}} = \lambda(s, M_e^2, M_e^2)$ ). The value of  $\min t_{1,2}$  in eqs. (5.32) and (5.33) may have been guessed already in our polar coordinates epoch, in fact:

$$\max E_{3,5} = \frac{s - 2M_a M_e - M_a^2}{2\sqrt{s}}, \quad (5.34)$$

$$\max t_1(E_3, c_3) = t_1(\max E_3, 1), \quad (5.35)$$

$$\max t_2(E_5, c_5) = t_1(\max E_5, -1) = \max t_1. \quad (5.36)$$

$$(5.37)$$

This concludes our domain considerations. The  $t_1$  integration is even easier:

$$\begin{aligned} \sigma_t &= \sigma_0 \pi \int \frac{dt_2 ds_1}{t_2^2} \frac{\theta(-\mathcal{G}_1)}{\sqrt{\lambda(s_1, t_2, m_1^2)}} \int \frac{dt_1}{t_1^2} \theta(-\mathcal{G}_2) \\ &=: \frac{\sigma_0 \pi}{M_e^2} \int dt_2 ds_1 \theta(-\mathcal{G}_1) \rho(s_1, t_2, M_a, M_e), \end{aligned} \quad (5.38)$$

with

$$\rho(s_1, t_2) := \frac{\sqrt{\lambda(s_1, M_a^2, M_e^2)}}{t_2^2 (t_2 - M_a^2)^2}. \quad (5.39)$$

It is useful to study this double differential cross section, particularly the phase space areas making it maximal so to deduce the most relevant kinematic configurations. When evaluated on the physical domain,  $\frac{d^2\sigma_t}{dt_2 ds_1}$  is an always positive function and its gradient is always strictly positive

$$\frac{d\rho}{ds_1} = \frac{M_a^2 + M_e^2 - s_1}{\lambda(s_1, M_a^2, M_e^2)(M_a^2 - t_2)^2(-t_2)^2}, \quad (5.40)$$

$$\frac{d\rho}{dt_2} = \frac{2(M_a^2 - 2t_2)}{(M_a^2 - t_2)^3(-t_2)^3}. \quad (5.41)$$

No physical point make the gradient 0, therefore the absolute maximum of  $\rho$  is to be searched for onto the boundary of the function domain. The problem is made more complicated by the fact that this boundary depends on the function variables themselves. In fact one may think to go and sit onto the maximum value for  $s_1$ , which actually maximizes the function, but it depends on  $t_2$ . If we try and evaluate  $\frac{d^2\sigma_t}{dt_2 ds_1}$  on  $s_1 = s_1^-$  and  $t_2 = \max t_2$  we get 0 because by construction  $s_1^-(t_2 = \max t_2) = (M_e + M_a)^2$  and  $\lambda(s_1 = (M_e + M_a)^2, M_a^2, M_e^2) = 0$ . We should maximize  $\rho(s_1^-, t_2)$  but it is a complicated task. We can however sketch an idea of the position of the maximum by looking at some plots; to give a general picture we show some density plots for different values of the ALP mass (fig. 5.1):

Let us now focus on the region where the maximum is attained and provide plots for  $\rho(s_1^-, t_2)$  (fig. 5.3). Maximising  $\rho(s_1^-, t_2)$  is complicated so we limit ourselves to show in fig. 5.2 that the maximum exists for all  $M_a$  and is close but not onto the phase space boundary, as  $\frac{d\rho(s_1^-, t_2)}{dt_2}$  changes sign around  $\max t_2$ . This was to be expected since in the small  $|t_2|$  subspace the integrand is affected by two competing factors, the matrix element maximisation and the phase space closure.

Say  $\rho(s_1^-, t_2)$  is maximal at some  $t_2 = \bar{t}_2 \simeq \min t_2 \simeq 0$ . We can exploit this smallness and, instead of maximising the full function, we can maximise its expansion in small

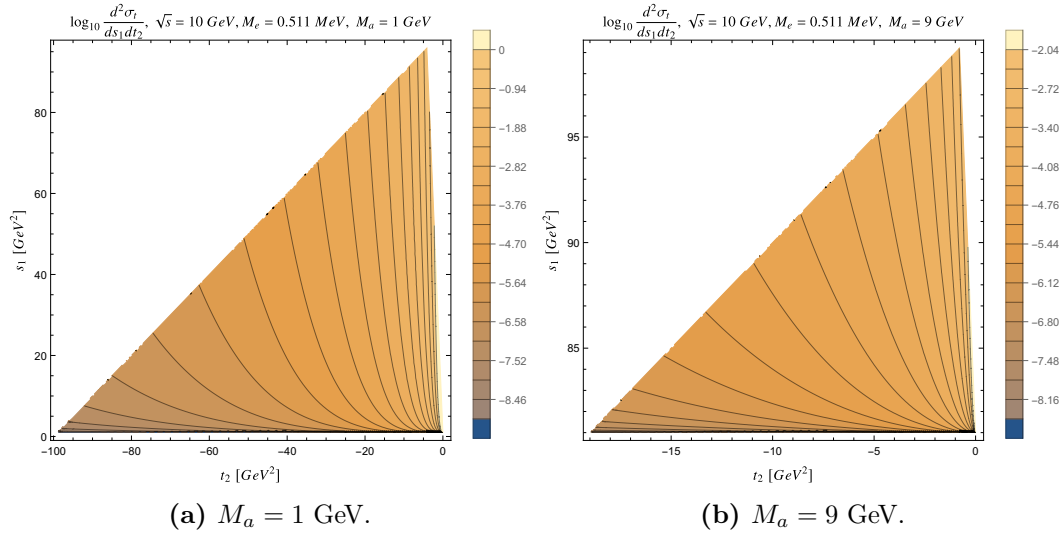


**Figure 5.1.**  $\frac{d^2\sigma_t}{dt_2 ds_1}$  for two values of the ALP mass.

$\frac{t_2}{s}$  and small  $\frac{M_e}{\sqrt{s}}$ . The position of the expansion maximum is denoted by  $\tilde{t}_2$  and gives the following satisfactory approximation of  $\bar{t}_2$ :

$$\tilde{t}_2 = \frac{M_e^2}{4s(s - M_a^2)} (9s^2 - 8M_a^2 s - 4M_a^4 - (3s - 2M_a^2) \sqrt{9s^2 - 4M_a^2 s + 4M_a^4}) \simeq \bar{t}_2. \quad (5.42)$$

The goodness of  $\tilde{t}_2$  and its proximity to  $\min t_2$  can be appreciated in figs. 5.2 and 5.3. In conclusion  $\frac{d^2\sigma_t}{dt_2 ds_1}$  is maximal for  $s_1$  very close to its minimum  $(M_a + M_e)^2$  and  $t_2$  very close to its maximum. For  $s_1$  to be minimal we need the ALP and the electron to have the same velocity. In fact, go to the rest frame of  $p_3$  and let  $\vec{\beta}_4$  and  $\gamma_4$  be the ALP velocity and Lorentz factor respectively. Then

$$s_1 = (p_3 + p_4)^2 = m_3^2 + m_4^2 + 2m_3 m_4 \gamma_4 \geq (m_3 + m_4)^2. \quad (5.43)$$

The minimum is attained when ALP and electron have the same velocity. In particular if in the CoM they are both at rest, then  $E_5^*$  is maximal.

Minimal  $t_2$  can be attained onto maximal  $E_5$  and  $\cos\theta_5 \rightarrow -1$ . In fact, in the rest frame of  $p_2$ , with  $\vec{\beta}_5$  and  $\gamma_5$  the final positron velocity and Lorentz factor respectively,

$$t_2 = (p_2 - p_5)^2 = m_2^2 + m_5^2 - 2m_2 m_5 \gamma_5 \leq (m_2 - m_5)^2. \quad (5.44)$$

The maximum is attained when initial and final positron have same velocity. Since their masses are the same, the whole 4momenta will be equal.

We may finally integrate  $s_1$  away so to obtain a single differential cross section. It is remarkable that the GD formalism allows us to compute a distribution that in

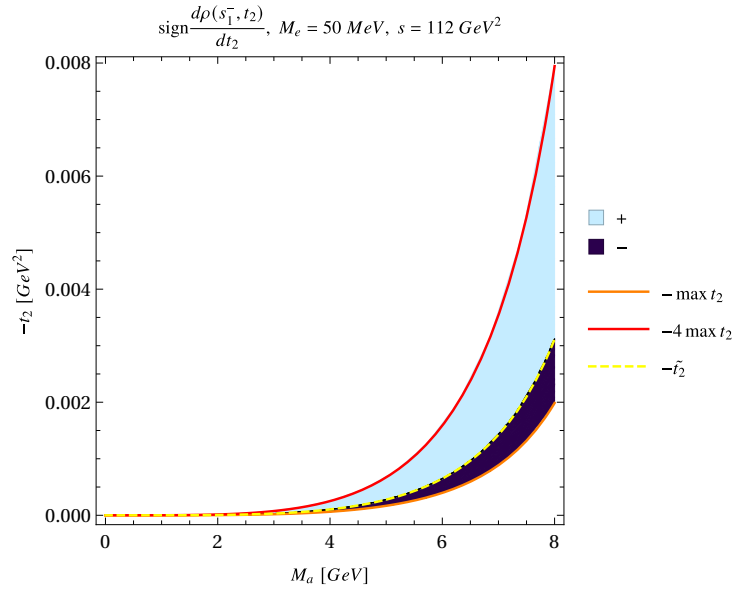


**Figure 5.2.** Sign of the derivative  $\frac{d\rho(s_1^-, t_2)}{dt_2}$  near to the  $t_2$  phase space closure. To make a clearer picture I used  $M_e = 50 \text{ MeV}$  and  $-t_2$  instead of  $t_2$ . The red and orange solid lines are respectively  $-4 \max t_2$  and  $-\max t_2$  ( $\max t_2$  can be read in eq. (5.33).) I chose this slice of the  $t_2$  phase space next to its closure to point to the region in which  $\frac{d\rho(s_1^-, t_2)}{dt_2}$  changes sign (everywhere else it is positive). The yellow dashed line plots eq. (5.42). We can appreciate how precisely it follows the boundary among the + light blue region and the - dark blue region.

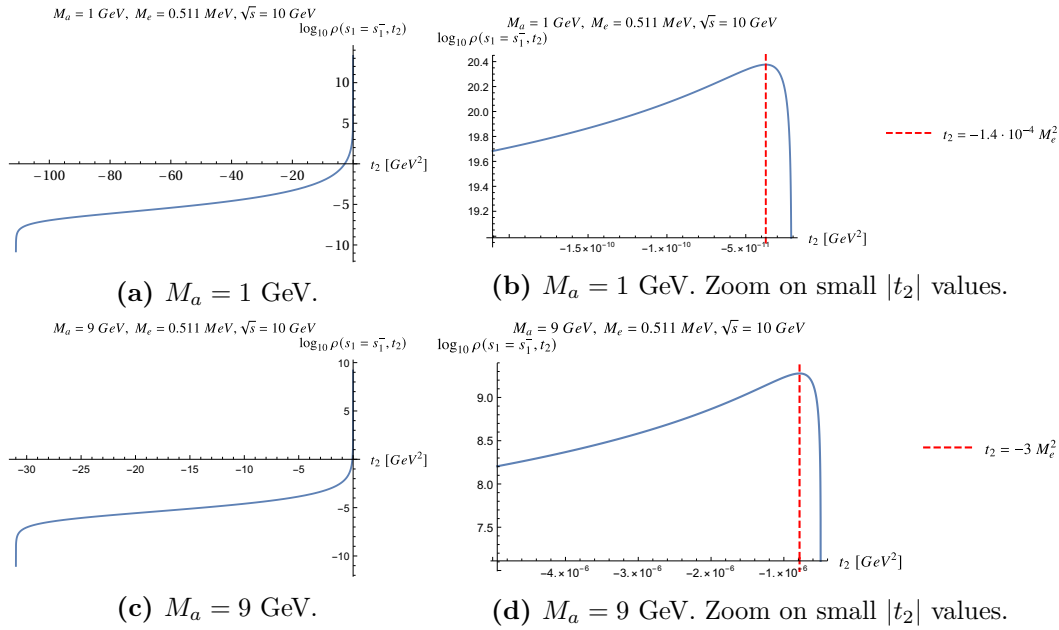


**Figure 5.3.** In all panels the solid blue line is  $\rho(s_1 = s_1^-, t_2)$ . We show it for two values of the ALP mass: both in the small ( $M_a = 1$  GeV) or big ( $M_a = 9$  GeV) ALP mass case, the fully derivative cross section evaluated onto the boundary for the  $s$ -like variable  $s_1$  exhibit a maximum very close to the closure of the  $t_2$  phase space. The red dashed lines point to our estimate of the position of the maximum. You can see it plotted in fig. 5.2 or in formulas in eq. (5.42). Notice its proximity to the smallest allowed  $|t_2|$ .

general is not easy to recover analytically and yet is notably useful at experiments. We obtain

$$\begin{aligned} \frac{d\sigma_t}{dt_2} = & \frac{\sigma_0 \pi}{M_e^2} \frac{1}{t_2^2 (t_2 - M_a^2)^2} \left[ \frac{1}{2} \sqrt{\lambda(s_1^-, M_a^2, M_e^2)} (s_1^- - (M_a^2 + M_e^2)) \right. \\ & \left. - 2(M_a M_e)^2 \log \left( \frac{\sqrt{\lambda(s_1^-, M_a^2, M_e^2)} + s_1^- - (M_a^2 + M_e^2)}{2M_a M_e} \right) \right]. \end{aligned} \quad (5.45)$$

Since the  $s_1$  integration was performed on the interval  $[(M_a + M_e)^2, s_1^-]$ , there is no  $s_1^+$  in eq. (5.45).

### 5.3 $\frac{d^2\sigma_s}{du_1 ds_2}$

In this section I provide an example of  $s$  channel computation that will be useful for comparison with respect to the  $t$  channel. We will follow the same path of the previous section. I remind that the matrix element is  $|\mathcal{M}_s|^2 = \frac{1}{s^2 u_1^2}$  and that  $s_1$  and  $u_1$  are related by eq. (E.12), so that  $ds_1 = du_1$ . Then

$$\sigma_s = \sigma_0 \int \frac{ds_2 du_1 dt_1 dt_2}{s^2 u_1^2} \frac{\theta(-\Delta_4)}{\sqrt{-\Delta_4}}. \quad (5.46)$$

We use again theorem 7 with independent variable  $t_2$  in position, (2, 4), (4, 2) of the gram matrix  $M_4(p_1 + p_2, p_2, p_3, p_5)$ . Using also eq. (5.17)

$$\int_{t_2^-}^{t_2^+} \frac{dt_2}{\sqrt{-\Delta_4}} = \frac{4\pi}{\sqrt{\lambda(s, s_2, m_3^2)}}. \quad (5.47)$$

Then

$$\sigma_s = 4\sigma_0\pi \int \frac{ds_2 du_1 dt_1}{s^2 u_1^2} \frac{\theta(-\mathcal{G}_1)\theta(-\mathcal{G}_2)}{\sqrt{\lambda(s, s_2, m_3^2)}}, \quad (5.48)$$

with

$$\mathcal{G}_1 := \mathcal{G}(s, t_1, s_2, m_1^2, m_2^2, m_3^2), \quad (5.49)$$

$$\mathcal{G}_2 := \mathcal{G}(u_1, s_2, m_5^2, s, m_4^2, m_3^2). \quad (5.50)$$

Proceeding with the  $t_1$  integration, the inequality:

$$\mathcal{G}_1 = \frac{s}{2}(t_1 - t_1^-)(t_1 - t_1^+) \leq 0 \quad (5.51)$$

is solved by

$$t_1^- \leq t_1 \leq t_1^+. \quad (5.52)$$

Then

$$\begin{aligned} \sigma_s &= 4\sigma_0\pi \int \frac{ds_2 du_1}{s^2 u_1^2} \frac{\theta(-\mathcal{G}_2)}{\sqrt{\lambda(s, s_2, m_3^2)}} \int_{t_1^-}^{t_1^+} dt_1 \\ &= 4\sigma_0\pi \int \frac{ds_2 du_1}{s^2 u_1^2} \frac{\theta(-\mathcal{G}_2)}{\sqrt{\lambda(s, s_2, m_3^2)}} \frac{\sqrt{\lambda(s, m_1^2, m_2^2)}\sqrt{\lambda(s, s_2, m_3^2)}}{s} \theta(\lambda(s, s_2, m_3^2)) \\ &= \sigma_0\pi \sqrt{\lambda_{\text{in}}} \int \frac{ds_2 du_1}{s^3 u_1^2} \theta(-\mathcal{G}_2) \theta(\lambda(s, s_2, m_3^2)), \end{aligned} \quad (5.53)$$

where I remind the  $\lambda_{\text{in}}$  definition in eq. (2.13).

In this case too we may keep going and integrate over  $s_2$  so to recover a single derivative cross section distribution. Where does the  $s_2$  integration take place? Due to the masses of our problem, it is always verified that if  $\mathcal{G}_2 \leq 0$  then also  $\lambda(s, s_2, m_3^2) \geq 0$ , therefore, with our usual notation,

$$\mathcal{G}_2 \leq 0 \text{ if } s_2^- \leq s_2 \leq s_2^+. \quad (5.54)$$

The double cross section distribution  $\frac{d^2\sigma_s}{ds_2 du_1}$  from eq. (5.53) does not depend on  $s_2$  so we only have to integrate  $\theta(-\mathcal{G}_2)$  away:

$$\int ds_2 \theta(-\mathcal{G}_2) = \theta(\Lambda(u_1))(s_2^+ - s_2^-) = \theta(\Lambda(u_1)) \frac{\sqrt{\Lambda(u_1)}}{u_1^2}, \quad (5.55)$$

where I defined

$$\Lambda(u_1) := \lambda(u_1, m_3^2, m_5^2) \lambda(u_1, s, m_4^2). \quad (5.56)$$

In conclusion

$$\frac{d\sigma_s}{du_1} = \frac{4\sigma_0\pi}{s^3 u_1^2} \sqrt{\lambda_{\text{in}} \Lambda(u_1)} \theta(\Lambda(u_1)). \quad (5.57)$$

It is possible to analytically integrate eq. (5.57), here is how.  $\Lambda(u_1)$  is the product of two parabolas in  $u_1$ . At least in our specific problem, their roots are ordered. Call  $y_{1,2}$  the roots of  $\lambda(u_1, m_3^2, m_5^2)$  and  $y_{3,4}$  the roots of  $\lambda(u_1, s, m_4^2)$  as polynomials in  $u_1$

$$\lambda(u_1, m_3^2, m_5^2) = 0 \text{ if } u_1 = y_{1,2}; \quad \lambda(u_1, s, m_4^2) = 0 \text{ if } u_1 = y_{3,4}. \quad (5.58)$$

The following chain of inequalities is true

$$0 \leq (m_3 - m_5)^2 = y_1 \leq y_2 \leq y_3 \leq y_4 \leq s, \quad y_4 = (\sqrt{s} + m_4)^2 \neq 0. \quad (5.59)$$

To integrate eq. (5.57) we need to satisfy  $\Lambda(u_1) \geq 0$ , which is true onto  $y_2 \leq u_1 \leq y_3$ , therefore the integration extrema are  $y_{2,3}$ . We may exploit that  $y_4 \neq 0$  and divide  $u_1$  and all the  $y_i$  by  $y_4$ , so to rewrite the integral in an easier way:

$$\sigma_s \propto y_4 \int_{x_2}^{x_3} \frac{\sqrt{x-x_1} \sqrt{x-x_2} \sqrt{x-x_3} \sqrt{x-1}}{x^2} dx. \quad (5.60)$$

with  $\frac{u_1}{y_4} =: x$  and  $x_i := \frac{y_i}{y_4}$ . At this point I suggest you use Mathematica [112]. I copy here the result for a case that is of interest for us,  $y_1 = 0$ :

$$\begin{aligned} \sigma_s(x_1 = 0) &= \frac{4\sigma_0\pi\sqrt{\lambda_i}}{s^3} \left\{ \frac{3r_{42}}{r_{31}} (r_{31}E(\kappa) + K(\kappa)) + \right. \\ &\left. + \frac{r_{43}^2}{r_{32}} \left[ 2r_{42}F(\alpha, \kappa^{-1}) + \Sigma \cdot \Pi(x_3, \alpha, \kappa^{-1}) \right] \right\}, \end{aligned} \quad (5.61)$$

where I defined

$$r_{ij} := \sqrt{x_i - x_j}, \quad i > j, \quad (5.62)$$

$$\kappa := \frac{x_3 - x_2}{x_3(1 - x_2)}, \quad (5.63)$$

$$\Sigma = \frac{y_1 + y_2 + y_3 + y_4}{y_4} \rightarrow 1 + x_2 + x_3, \quad (5.64)$$

$$\alpha := i \operatorname{arcsinh}(\sqrt{\kappa}). \quad (5.65)$$

$E$  and  $\Pi$  are incomplete elliptic integrals respectively of the second and third kind while  $K$  is the complete integral of the first kind (see appendix G for their definitions).

## 5.4 Comparison between $s$ and $t$ total cross section

Let us now plot<sup>1</sup>  $\frac{d\sigma_s}{du_1}$  (eq. (5.57)) and  $\frac{d\sigma_t}{dt_2}$  (eq. (6.16)), for physical values  $M_e = 0.511$  MeV,  $\sqrt{s} = 10$  GeV and different values of  $M_a$ , fig. 5.4. These picture together with the previous section demonstrate that  $\frac{d\sigma_s}{du_1}$  is maximized around the minimal allowed  $u_1$ , which occurs when the two final leptons have the same velocity and the ALP is back to back with the leptonic system.  $\frac{d\sigma_t}{dt_2}$  is maximized around the minimal allowed  $t_2$ , which occurs when the positrons have the same velocity, i.e. the final positron stayed aligned to the initial one.

But more remarkably we notice that the  $t$  channel is way bigger than the  $s$  channel. This characteristic is shared by both a theory with and without spins and is due to the fact that the  $t$  channel can be twice as divergent as the  $s$  channel due to it propagators. In fig. 5.5 I numerically prove it by integrating the two cross sections and inspect their ratio. We can conclude that  $s$  channel and interference are negligible with respect to the  $t$  channel for all possible  $M_a$  values.

---

<sup>1</sup>In fig. 5.4 the distributions are given in arbitrary units due to the fact that we are setting  $\sigma_0 = 1$ . We can do it as when all  $2\pi$  factors and all couplings are taken into account,  $\frac{d\sigma_s}{du_1}$  and  $\frac{d\sigma_t}{dt_2}$  are rescaled by the same quantity.

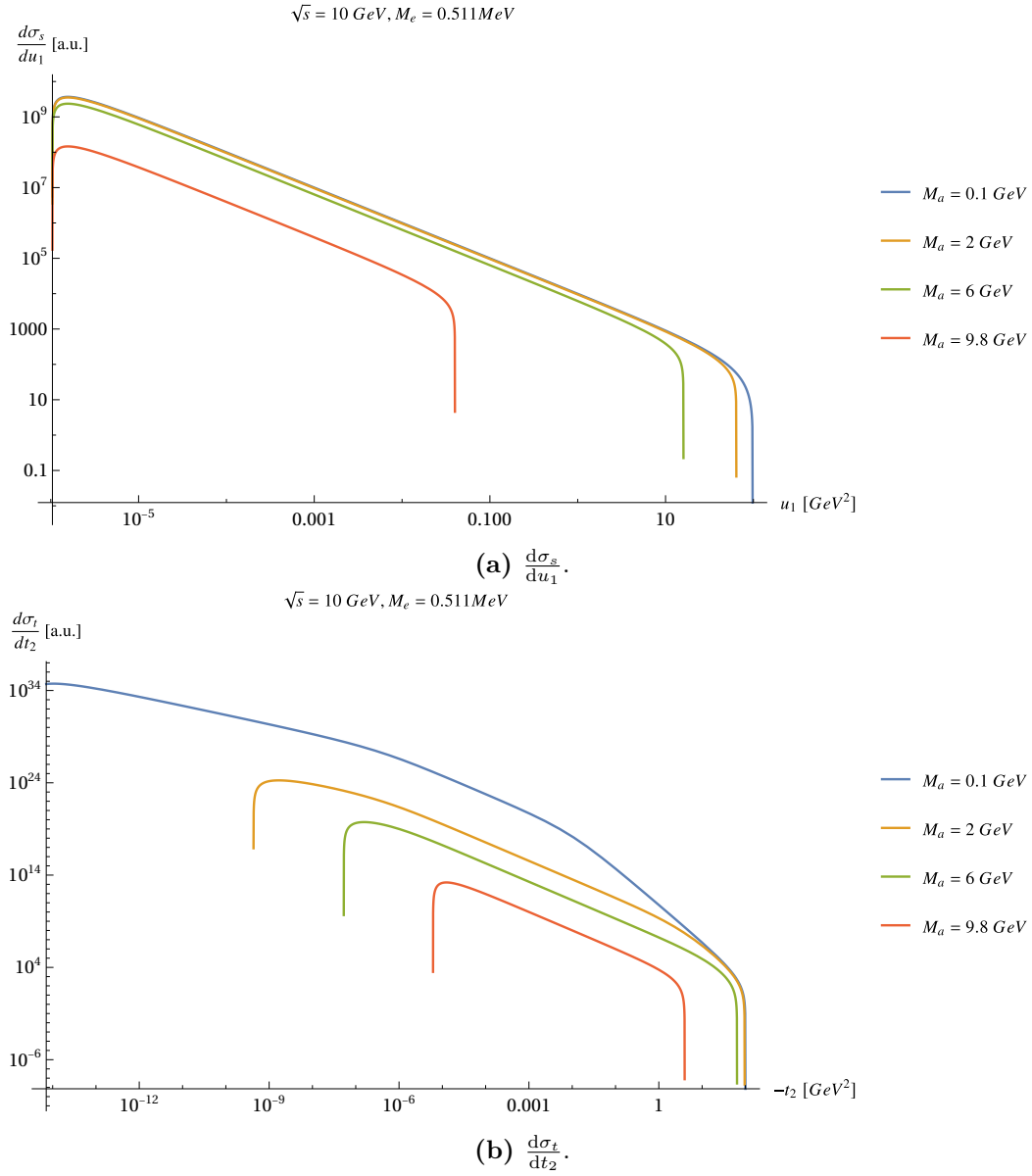


**Figure 5.4.**  $s$  and  $t$  channel distributions with respect to one relevant gMv for different values of the ALP mass.

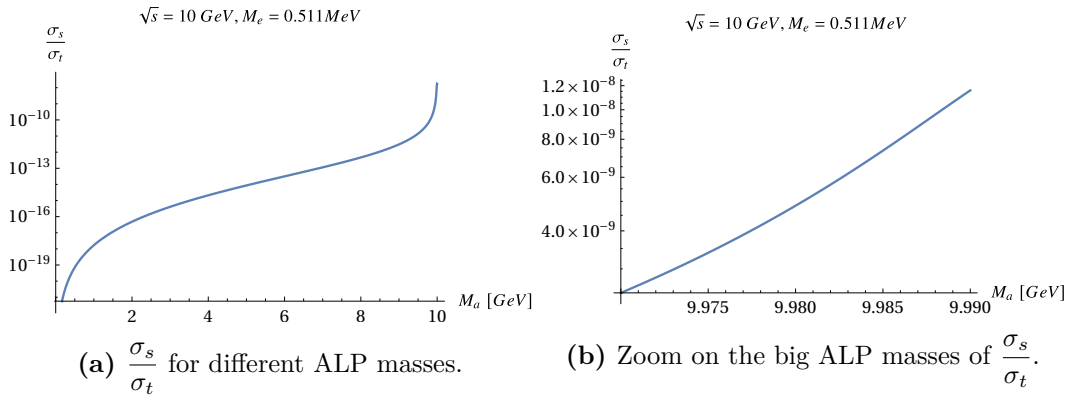


**Figure 5.5.** Comparison of total cross sections for  $t$  and  $s$  channel.

## Chapter 6

# Integrand symmetries: how to avoid computing all of the cross section distribution

It is worth analysing the symmetries of the  $2 \rightarrow 3$  scattering integration problem: firstly, because thanks to them we can divide cross section distributions in families and only compute one family element for all; secondly because it will demonstrate the goodness of the GD language choice, as it helps making the symmetries manifest. In section 6.1 we make all the necessary symmetry remarks of our process, among which the most important results are that the scattering density eq. (5.7) is maximally symmetric (i.e. invariant under any fourmomenta permutations), and that in general the matrix element may break many symmetries of the density but our particular (SM+ALP) matrix element has a charge conjugation symmetry that allows us to get many cross section distributions without extra calculation effort. In fact in section 6.2 we provide  $\frac{d\sigma_t}{dt_1}$ ,  $\frac{d^2\sigma_s}{ds_1 dt_1}$  and  $\frac{d^2\sigma_s}{ds_1 ds_2}$ , deriving them from symmetry. The reader that trusts our symmetries derivation can skip the more formal initial sections and directly go to section 6.2.

### 6.1 Combinatorics

Let us first agree on some convention and terminology:

**Definition 18** (Base strings).

Call the starting ordered string  $\mathcal{S}_0 := (1, 2, 3, 4, 5)$  and the corresponding ordered set of gMvs  $\mathcal{M}(\mathcal{S}_0) := (s, s_1, s_2, t_1, t_2, u_1, u_2, u_3, u_4, u_5)$ . In  $\mathcal{M}(\mathcal{S}_0)$  we call  $(s, s_1, s_2, t_1, t_2)$  the straight or fundamental substring and  $(u_1, u_2, u_3, u_4, u_5)$  the auxiliary, secondary or derived substring.

□

**Definition 19** (Permutation among strings).

Call  $\sigma_i^j$  the permutation sending the string  $\mathcal{S}_i$  into the string  $\mathcal{S}_j$  :

$$\sigma_i^j \mathcal{S}_i = \mathcal{S}_j, \tag{6.1}$$

$$\sigma_i^j \mathcal{M}(\mathcal{S}_i) = \mathcal{M}(\mathcal{S}_j). \tag{6.2}$$

The position of the string index is not important (we will always place it on the bottom) while the position of the permutation indices is relevant. We remark that

$$\sigma_j^i = (\sigma_i^j)^{-1}. \tag{6.3}$$

Also notice that permuting fourmomenta also implies permuting masses.

□

**Lemma 9.**

There are  $5! = 120$  possible orderings of  $\mathcal{S}_0$  i.e. there are 120 permutations  $\sigma_0^i$ .

□

**Lemma 10.**

To respect the fourmomentum conservation  $p_1 + p_2 = p_3 + p_4 + p_5$ , every time an initial fourmomentum is sent into a final fourmomentum and vice versa, change the sign of the fourmomentum. If all elements of a  $\sigma_0^i$  are multiplied by  $-1$  we agree that it gives the same  $\mathcal{M}(\mathcal{S}_i)$ .

□

**Theorem 18.**

The composition of permutations is indicated by the symbol  $\circ$ . The pair  $(\{\sigma_i^j, i, j \in [0, 119]\}, \circ)$  forms the group  $\mathfrak{p}$ .

□

The Phase Space as expressed in eq. (5.8) has a beautiful symmetry:

**Theorem 19** (Symmetric Phase Space).

The Phase Space density eq. (5.7)  $\frac{\theta(-\Delta_4)}{\sqrt{-\Delta_4}}$  is invariant under whatever permutation we may perform on fourmomenta as it only depends on the Principal Gram determinant. This means that the phase space is sent into itself under all permutations one can perform on 4 momenta.

□

You may argue that performing integrations may spoil this symmetry. This is not completely true, in fact we can make the following statement on the relation that exists between boundaries:

**Corollary 10** (Symmetry-related gMvs have related integration boundaries).  
From theorem 6, the Principal Gram Determinant is a parabola in some gMv  $x$

$$\Delta_n(\mathcal{S}_i) = a_2x^2 + a_1x + a_0 = a_2(x - x_-)(x - x_+). \quad (6.4)$$

( $x$  is the scalar product of a couple of fourmomenta). All the parabolas coefficients depend on all other gMvs and parameters (such as masses). Due to its maximal symmetry, the PGD does not change under any  $\sigma_i^j$  permutation, but the  $a_i$  and  $x$  do:  $a_i \rightarrow a'_i, x \rightarrow x'$ , i.e.

$$\Delta_n(\mathcal{S}_i) = \Delta_n(\sigma_i^j \mathcal{S}_i) = a'_2(x')^2 + a'_1x' + a'_0 = a'_2(x' - x'_-)(x' - x'_+). \quad (6.5)$$

Since the  $a'_i$  can be recovered from the  $a_i$  by implementing  $\mathcal{S}_i \rightarrow \sigma_i^j \mathcal{S}_i$ , and from the fact that  $x'_\pm$  are functions of the  $a'_i$ , the transformed parabola nodes  $x'_\pm$  too can be recovered from the original ones  $x_\pm$  through symmetry. In conclusion, the integration will have an identical functional form, modulo permutations.

□

This concludes our considerations on the integration density (and with it, the integration domain) symmetry. To complete the analysis of the cross section integrand eq. (5.8) we shall now consider the Lorentz invariant volume element  $d\mu_L = ds_1 ds_2 dt_1 dt_2$  and the matrix element  $|\mathcal{M}(\vec{\mu}_L, s, \vec{m})|^2$ . We can state:

**Lemma 11.**

$d\mu_L |\mathcal{M}(\vec{\mu}_L, s, \vec{m})|^2$  must be independent of all relabellings sending  $\vec{\mu}_L$  into itself and leaving  $s$  and  $\vec{m}$  invariant, as I should always be able to rename my integration variables.

□

In general we must stick to permutations sending the ordered string  $\vec{m}$  into itself. In fact consider a process with  $m_1 = 0, m_2 \neq 0$  and  $|\mathcal{M}|^2$  having some dependence on  $m_2$  like  $\frac{1}{m_2}$ . Therefore a permutation exchanging  $1 \leftrightarrow 2$  is forbidden. Nevertheless the process may be sufficiently symmetrical to allow a greater number of permutations. This is the case when some of the masses are equal or amplitudes do not depend on some gMv or some parameter.

**Corollary 11** (Symmetries of Standard Model cross section).

In the (SM+ALP) the  $e^+e^- \rightarrow e^+e^-a$  process the matrix element depends on all the 5 fundamental gMvs, but all masses are equal except  $M_a$ . Then, whatever the matrix element is, the cross section integrand is symmetric under all permutations sending  $p_4$  in  $p_4$  and  $s$  in  $s$ . We say these permutations pivot in  $p_4$ .

□

**Theorem 20** (Symmetries of Scalar Standard Model cross section).

In the simplified case of the scalar theory we also get the matrix element to be independent of all masses and of some invariants, see eq. (4.29). We can allow all permutations pivoting on 4. Call  $\mathfrak{p}_4$  this subgroup of  $\mathfrak{p}$  and mark all corresponding Mandelstam strings with a superscript  $\mathcal{S}_i^4, i \in [0, 23]$ . You can look up at the complete subgroup  $\mathcal{S}_i^4$  in appendix J.

□

### 6.1.1 Lepton swaps and distributions

Permutations pivoting in 4, sending  $s$  in  $s$  and exchanging final leptons are  $(1, 2, 5, 4, 3)$  and  $(2, 1, 5, 4, 3)$ . These two permutations imply a mass swap that is forbidden in principle and is allowed only if the elements of the swapped couple have the same mass. In our case all leptons have the same mass and we are safe. The said permutations are acceptable for the scalar theory but are not for the theory with spins. Precisely, the  $s$  channel is symmetric under both of them, while the  $t$  channel will not allow a vertex with incoming electron and outgoing positron and photon, as the first permutation would require. The only viable one is  $(2, 1, 5, 4, 3)$ , which is nothing more than charge conjugation. This had to be expected as electric charge does not play any role<sup>1</sup> in  $e^+e^- \rightarrow e^+e^-a$ . The corresponding Mandelstam strings is (LS=Lepton Swap)

$$\mathcal{M}(\mathcal{S}_{\text{LS}}) := (s, s_2, s_1, t_2, t_1, u_1, u_3, u_2, u_5, u_4). \quad (6.6)$$

Every time we will consider cross section distributions sending  $\mathcal{M}(\mathcal{S}_0)$  into  $\mathcal{M}(\mathcal{S}_{\text{LP}})$  we will be looking at the same process as in fig. 1.1 with swapped leptons.

We now show that out of all possible 1 and 2 dimensional cross section distributions it is sufficient to compute only few thanks to LS symmetry:

**Theorem 21** (LS symmetry and distribution equivalence).

1.  $\frac{d^2\sigma_x}{ds_1 ds_2}$  is a symmetric function of  $s_1$  and  $s_2$  for each  $x = s, t$ , int.
2.  $\frac{d^2\sigma_x}{dt_1 dt_2}$  is a symmetric function of  $t_1$  and  $t_2$  for each  $x = s, t$ , int.
3. With the same notation  $\frac{d\sigma_x}{ds_1}$  ( $\frac{d\sigma_x}{dt_1}$ ) has the same functional form of  $\frac{d\sigma_x}{ds_2}$  ( $\frac{d\sigma_x}{dt_2}$ ) in the sense that if the former is a function depending on  $s_1(t_1)$ , the latter is the same function depending on  $s_2(t_2)$ . It is exactly the same function because all masses are sent in themselves.
4.  $\frac{d^2\sigma_x}{ds_1 dt_1}$  ( $\frac{d^2\sigma_x}{ds_1 dt_2}$ ) has the same functional form of  $\frac{d^2\sigma_x}{ds_2 dt_2}$  ( $\frac{d^2\sigma_x}{ds_2 dt_1}$ ).

□

We will only prove the straight points, those in parenthesis can be easily deduced from them. Consider the most generic LS invariant matrix element, ideally depending on all of the gMVs  $|\mathcal{M}_x|^2(s_1, s_2, t_1, t_2)$ . The cross section is

$$\sigma_x \propto \int ds_1 ds_2 \int dt_1 dt_2 |\mathcal{M}_x|^2(s_1, s_2, t_1, t_2) \frac{\theta(-\Delta_4)}{\sqrt{-\Delta_4}} =: \int ds_1 ds_2 f_1(s_1, s_2). \quad (6.7)$$

---

<sup>1</sup>In the sense that each particle could have had whatever charge as long as electric charge conservation was respected.

Perform a change of variables names

$$\sigma_x \propto \int ds_1 ds_2 \int dt_1 dt_2 |\mathcal{M}_x|^2(s_2, s_1, t_2, t_1) \frac{\theta(-\Delta_4)}{\sqrt{-\Delta_4}} =: \int ds_1 ds_2 f_2(s_1, s_2), \quad (6.8)$$

but since the whole integrand is LS invariant

$$f_1(s_1, s_2) = f_1(s_2, s_1) \equiv f_2(s_1, s_2) = f_2(s_2, s_1). \quad (6.9)$$

Also

$$F_1(s_2) := \int ds_1 f_1(s_1, s_2) = \int ds_1 f_1(s_2, s_1) = \int ds_2 f_1(s_1, s_2), \quad (6.10)$$

$$F_2(s_1) := \int ds_2 f_2(s_1, s_2) = F_1(s_1). \quad (6.11)$$

The first equality in eq. (6.10) comes from  $f_1$  symmetry, the second one is a change of variables names. The equality in eq. (6.11) comes from the  $f_1, f_2$  equivalence. This concludes our proof.

It is easy to show that some of the above symmetries can be transposed to the polar coordinate language too as it is sufficient to show that the change of variables from gMvs to polar variables produces a symmetric jacobian. For example the jacobian bringing from  $(s_1, s_2)$  to  $(E_3, E_5)$  is a constant, or

$$|J((s_2, t_1) \rightarrow (E_3, c_3))| = 2\sqrt{s} \sqrt{s - M_e^2} \sqrt{E_3^2 - M_e^2}, \quad (6.12)$$

$$|J((s_1, t_2) \rightarrow (E_5, c_5))| = 2\sqrt{s} \sqrt{s - M_e^2} \sqrt{E_5^2 - M_e^2}, \quad (6.13)$$

which are transformed one into the other via  $E_3 \leftrightarrow E_5$ .

## 6.2 Other distributions

In light of the LS symmetry that we proved in section 6.1.1 we will not provide the full computation for  $\frac{d\sigma_t}{dt_1}$  or for  $\frac{d^2\sigma_t}{dt_1 ds_2}$ . The reader who wants to try will find that every step of these integrals can be recovered from the very same steps made for  $\frac{d\sigma_t}{dt_2}$ . Only two differences will be encountered: first

$$\mathcal{G}_1 \rightarrow \mathcal{G}_3 := \mathcal{G}(s, t_1, s_2, M_e^2, M_e^2, M_e^2), \quad (6.14)$$

$$\mathcal{G}_2 \rightarrow \mathcal{G}_4 := \mathcal{G}(t_2, s_2, t_1, M_e^2, M_e^2, M_e^2). \quad (6.15)$$

Second,  $\frac{d^2\sigma_t}{dt_1 ds_2}$  still prefers the s-like variable to be close to its minimum and the t-like variable to be close to its maximum, which happens onto  $\cos\theta_3 \sim 1$ .

$$\begin{aligned} \frac{d\sigma_t}{dt_1} = & \frac{\sigma_0\pi^2}{4M_e^2\sqrt{\lambda_i}} \frac{1}{t_1^2(t_1 - M_a^2)^2} \left[ \frac{1}{2} \sqrt{\lambda(s_2^-, M_a^2, M_e^2)} (s_2^- - (M_a^2 + M_e^2)) \right. \\ & \left. - 2(M_a M_e)^2 \log \left( \frac{\sqrt{\lambda(s_2^-, M_a^2, M_e^2)} + s_2^- - (M_a^2 + M_e^2)}{2M_a M_e} \right) \right], \end{aligned} \quad (6.16)$$

$$\frac{d^2\sigma_s}{ds_1 dt_2} = \left[ \frac{\pi}{s M_e (M_a^2 - s)} \right]^2 \frac{\sigma_0}{\sqrt{\lambda_i}} \sqrt{\lambda(s_2, M_e^2, M_a^2)} \theta(-\mathcal{G}_1), \quad (6.17)$$

$$\frac{d^2\sigma_s}{ds_1 ds_2} = \frac{\sigma_0\pi^2\theta(\Delta_3^{(2)})}{16s^3(2M_e^2 + M_a^2 + s - s_1 - s_2)^2}. \quad (6.18)$$

Equation (6.18) is  $s_1 \leftrightarrow s_2$  symmetric as predicted.

## Chapter 7

$$\frac{d^2\sigma_t}{dt_1 dt_2}$$

$\frac{d^2\sigma_t}{dt_1 dt_2}$  is the most difficult distribution as in this case the kinematic functions are entangled in a complicated way. However not only we can solve it,  $\frac{d^2\sigma_t}{dt_1 dt_2}$  also is the distribution from which we can learn the most about this  $t$  channel. In fact in this chapter I will first characterize the  $(t_1, t_2)$  phase space (section 7.1); I will demonstrate that it gets tremendously close to the matrix element poles but keeps them outside of its boundaries and finally compute the actual distribution (section 7.2); with these results, I will show that most of the time the product of the vector fusion (the ALP) will prefer to stay at rest (section 7.2). I will then reflect upon the fact that all what we found applies much more generally as it only comes from  $\sqrt{s} \gg M_e$  (section 7.3).

### 7.1 The $s_1$ integration

We can start this computation from eq. (5.26) (i.e. from  $\frac{d^3\sigma_t}{ds_1 dt_1 dt_2}$ ) and integrate  $s_1$  away:

$$\int ds_1 \theta(-\mathcal{G}_1) \theta(-\mathcal{G}_2) = \int_{f(t_1, t_2)}^{g(t_1, t_2)} ds_1. \quad (7.1)$$

Our job is finding the extrema  $f$  and  $g$ .

Start from visualizing what the two Heaviside thetas require (fig. 7.1). To be inside the physical region, a point in the space  $(s_1, t_1, t_2)$  must satisfy both  $\mathcal{G}_{1,2} \leq 0$ .  $\mathcal{G}_{1,2}$  depend on  $s_1, t_1$  and  $t_2$  and each of them lives on a segment, then the domain of definition of  $\mathcal{G}_{1,2}$  is a convex volume in the  $(s_1, t_2, t_1)$  space, i.e. there is a parallelepiped in which the solving volume is inscribed.

$\mathcal{G}_1$  (eq. (5.15)) is a convex parabola in  $s_1$  (the  $s_1^2$  coefficient is  $\frac{M_e^2}{2}$ ). This means that there is a convex set of points  $\mathcal{V}_1$  in the  $(s_1, t_2)$  space where  $\mathcal{G}_1 \leq 0$ . The equality  $\mathcal{G}_1 = 0$  can only be achieved on the boundary  $\partial\mathcal{V}_1$ , but the converse is not true, i.e. not every point of the boundary has  $\mathcal{G}_1 = 0$  as it may come from some other constraint coming from the  $\Delta_2$ s. This happens when the zeros of  $\mathcal{G}_1$  fall outside the physical region. Still,  $\partial\mathcal{V}_1$  is a 1D continuous curve, see fig. 7.2.

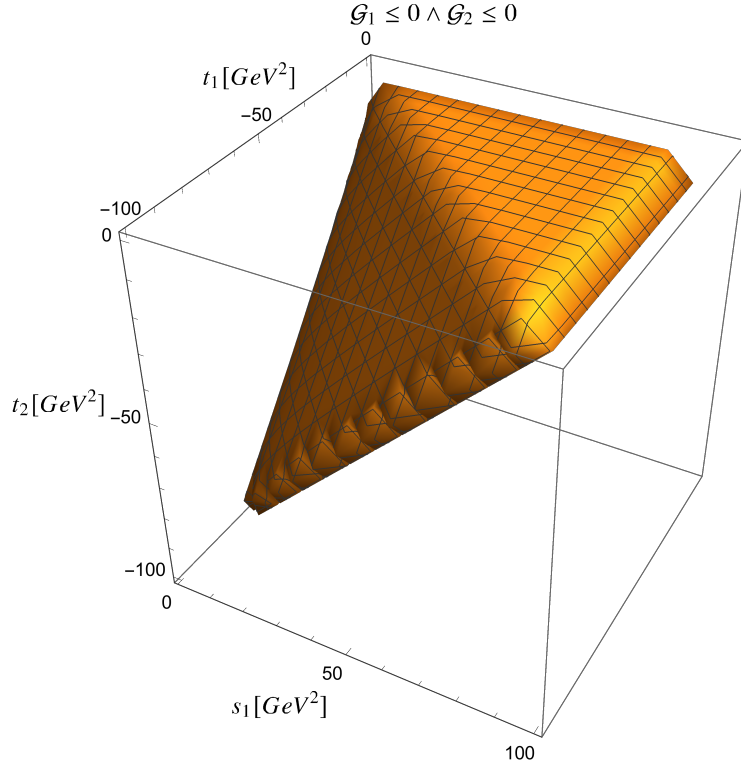


**Figure 7.1.**  $(s_1, t_1, t_2)$  phase space.

$\mathcal{G}_2$  (eq. (5.16)) is a convex parabola in  $t_1$  (the  $t_1^2$  coefficient is  $\frac{s_1}{2}$ ). Then there is a convex set of points  $\mathcal{V}_2$  in the  $(s_1, t_2, t_1)$  space where  $\mathcal{G}_2 \leq 0$ . The border of this volume  $\partial\mathcal{V}_2$  is defined by the physical roots of  $\mathcal{G}_2 = 0$  and the boundaries on  $s_1, t_1$  and  $t_2$ .  $\partial\mathcal{V}_2$  is a convex 2D surface in the 3D  $(s_1, t_2, t_1)$  space, see fig. 7.3.

Since we want both  $\mathcal{G}_1 \leq 0$  and  $\mathcal{G}_2 \leq 0$  at the same time, we will only retain the intersection  $\mathcal{V} := \mathcal{V}_1 \cap \mathcal{V}_2$ . Notice how if  $\mathcal{V} = \emptyset$  our process is unphysical. In appendix K I use a cartoon representation of  $\mathcal{G}_{1,2}$  and their roots so that it is easier to visualise in which cases the two kinematic functions can be 0 at the same time. We evince that the boundary is to be found onto

$$\begin{cases} \mathcal{G}_1 = 0, \\ \mathcal{G}_2 = 0. \end{cases} \quad (7.2)$$

i.e. when  $\mathcal{G}_1$  and  $\mathcal{G}_2$  share roots. Since  $\mathcal{V}_1$  and  $\mathcal{V}_2$  are convex,  $\mathcal{V}$  is convex.  $\mathcal{V}$  is a volume in the 3D  $(s_1, t_2, t_1)$  space. Depending on the shape of  $\mathcal{V}_1$  and  $\mathcal{V}_2$ , the border of  $\mathcal{V}$  is the union of subsets of the borders of the parent sets.  $\partial\mathcal{V}$  is a 2D curve in the 3D  $(s_1, t_2, t_1)$  space. To find the  $s_1$  integration extrema and the  $(t_1, t_2)$  phase space boundary, consider fig. 7.1 and imagine to scan it from left to right with a plane  $s_1 = s_0$ . On this plane you will see a convex shape. The union of all these shapes is the  $(t_1, t_2)$  phase space  $\mathcal{V}_t$ . Its boundary  $\partial\mathcal{V}_t$  is a 1D curve. All these formal remarks are helpful because even when things will get computationally hard we will always know everything we need for our purposes.

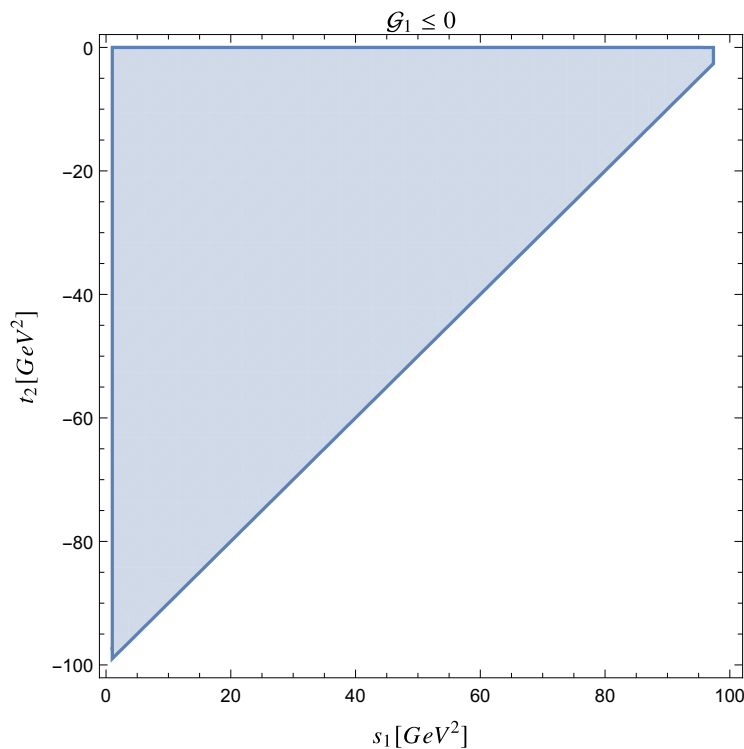


**Figure 7.2.** The blue area is the area allowed to  $s_1$  and  $t_2$  when we impose  $\mathcal{G}_1 \leq 0$ .

Let us work out  $\partial\mathcal{V}_t$ . Kajantie and Lindblom ([93]) do it for a generic case but can not provide a generic curve for  $\partial\mathcal{V}_t$  since it heavily depends on the masses of the  $2 \rightarrow 3$  scattering. They only manage to recover some salient loci of the curve and then proceed to specialise to simple configurations. We extend the treatment of [93] as we do not put any of the scattering masses to 0, but take all of them to be  $M_e$  except  $m_4$ , that is the ALP mass. This allows us to explicitly derive  $\partial\mathcal{V}_t$  as a function of  $t_2$ .

Call  $s_{1i}^\pm$  the roots of  $\mathcal{G}_i$  when solved for  $s_1$ . Explicitly

$$s_{11}^\pm = \frac{2M_e^4 + st_2 \pm \sqrt{\lambda(s, M_e^2, M_e^2)\lambda(t_2, M_e^2, M_e^2)}}{2M_e^2}, \quad (7.3)$$

$$s_{12}^\pm = \frac{M_a^2 t_1 + 2M_e^2 t_1 - t_1^2 t_2 \pm \sqrt{\lambda(s, M_e^2, M_e^2)\lambda(t_1, t_2, M_a^2)}}{2t_1}. \quad (7.4)$$

We need to check whether  $s_{1i}^\pm$  fall inside the physical domain of definition of  $s_1$ . On the boundary at least one of the following is satisfied:

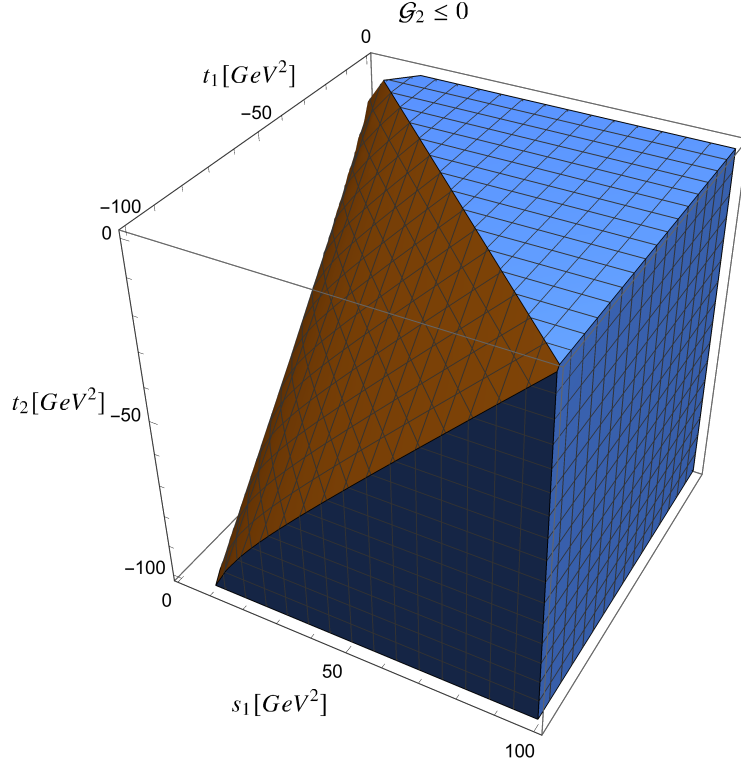


**Figure 7.3.** Volume allowed to  $(s_1, t_1, t_2)$  when we impose  $\mathcal{G}_2 \leq 0$ .

$$s_{11}^+ = s_{12}^-, \quad (7.5)$$

$$s_{11}^- = s_{12}^+, \quad (7.6)$$

$$t_1 = \max t_1 = (m_1 - m_3)^2, \quad (7.7)$$

$$t_2 = \max t_2 = (m_2 - m_5)^2, \quad (7.8)$$

$$\lambda(t_1, t_2, m_4^2) = 0. \quad (7.9)$$

Equation (7.9) would need at least one between  $t_1$  and  $t_2$  to be positive, which is unphysical. Equations (7.7) and (7.8) is just what we would like to avoid. They can be discarded easily for our scattering as, if you plug  $t_{1,2} = 0$  in eq. (7.2), you get

$$\mathcal{G}_1(t_2 = 0) = \frac{M_e^2}{2}(s_1 - M_e^2)^2, \quad (7.10)$$

$$\mathcal{G}_2(t_1 = 0) = \frac{M_e^2}{2}(t_2 - M_a^2)^2. \quad (7.11)$$

The solutions of both are non physical and this is enough for excluding eqs. (7.7) and (7.8). Then for each  $t_2$  either eq. (7.5) or eq. (7.6) must be true. Since our set of masses is particularly easy we can decide which. Let us begin this task by just inspecting  $\mathcal{G}_{1,2}$  as parabolas in  $s_1$ :

$$\mathcal{G}_1 = \frac{M_e^2 s_1^2}{2} - s_1 \left( \frac{st_2}{2} + M_e^4 \right) + \frac{1}{2} (M_e^6 - 3M_e^2 st_2 + st_2(s + t_2)), \quad (7.12)$$

$$\begin{aligned} \mathcal{G}_2 &= \frac{t_1 s_1^2}{2} - \frac{1}{2} s_1 (M_a^2 + 2M_e^2 + t_2 - t_1) \\ &+ \frac{1}{2} (M_a^4 M_e^2 + M_e^4 t_1 + M_e^2 t_2 (t_2 - t_1) + M_a^2 (t_1 t_2 - M_e^2 (t_1 + 2t_2))). \end{aligned} \quad (7.13)$$

The  $s_1^2$  and  $s_1$  coefficients in  $\mathcal{G}_1$  are positive while the shift is negative. We can already tell that it will have only one real positive root. About  $\mathcal{G}_2$ , instead, we can only tell the  $s_1^2$  coefficient is negative, hence there may be 0, 1 or 2 acceptable roots. If there are 0, the process is unphysical. If there are 1 or 2 the process is physical but the least work would be done if only 1 root is acceptable. We can show that this is luckily our case since not even the verge of the parabola is allowed in the Phase Space. In fact if you solve  $\frac{d\mathcal{G}_2}{ds_2} = 0$  and plug the solution in  $\mathcal{G}_2$ , you can never satisfy  $\mathcal{G}_2 \leq 0$ . We conclude that there is only one physical root for  $\mathcal{G}_1$  and one physical root for  $\mathcal{G}_2$ , but at this stage we don't know which. Nonetheless, we discovered that only one between eqs. (7.5) and (7.6) can be true. We may decide which root is acceptable even by looking at them at some specific point being particularly easy for us. Also, expanding in small  $\frac{M_e}{\sqrt{s}} =: \epsilon$  can not affect the reasoning above. The two expanded  $\mathcal{G}_1 = 0$  solutions are

$$s_{11}^- = s + t_2 + \mathcal{O}(\epsilon^2), \quad (7.14)$$

$$s_{11}^+ = \epsilon^{-2} t_2 - s - t_2 + \mathcal{O}(\epsilon^2). \quad (7.15)$$

Since  $s_{11}^+$  is always negative, we will keep  $s_{11}^+$ .

For excess of zeal we will check  $s_{12}^\pm$  too; we will adopt a different strategy and expand on the line  $t_2 = t_1(1 + \epsilon)$  which we are sure belongs to the physical region:

$$s_{12}^\pm = \frac{M_a^2}{2} + M_e^2 \pm \frac{\sqrt{4M_e^2 - t_1} \sqrt{M_a^4 - 4M_a^2 t_1}}{2\sqrt{-t_1}} + \mathcal{O}(\epsilon). \quad (7.16)$$

The fact that we can only retain  $s_{12}^+$  gives us the second confirmation that we must discard eq. (7.5) and retain eq. (7.6).  $t_2$  will live on a segment and, for each  $t_2$ ,  $t_1$  will be bounded from above and from below:  $t_1^{\min}(t_2) \leq t_1 \leq t_1^{\max}(t_2)$ .  $t_1^{\min}$  and  $t_1^{\max}$  are the two branches of the solution to  $s_{11}^- = s_{12}^+$ , a quadratic equation in  $t_1$ .

Finally, for each  $t_1$  and  $t_2$ , in order to perform the  $s_1$  integration we need to establish the biggest among  $s_{11}^-$  and  $s_{12}^+$ . Since  $s_{11}^-$  is everywhere concave and  $s_{12}^+$  is everywhere convex in  $t_2$  and they intersect on the domain boundary, inside the physical region

$$s_{11}^- \geq s_{12}^+. \quad (7.17)$$

See fig. 7.4 for an example.

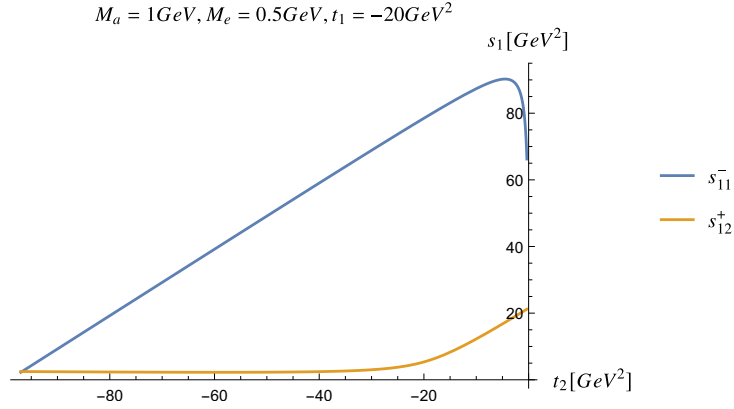


**Figure 7.4.**  $s_{11}^-$  is everywhere concave and  $s_{12}^+$  is everywhere convex in  $t_1$  and they intersect on the domain boundary, therefore, inside the physical region,  $s_{11}^- \geq s_{12}^+$ . Here we give a specific realization with  $s = 100 \text{ GeV}^2$ ,  $M_a = 1 \text{ GeV}$ ,  $M_e = 0.5 \text{ GeV}$ ,  $t_1 = -20 \text{ GeV}^2$ .

## 7.2 Results and remarks

In conclusion, for matrix elements  $|\mathcal{M}(t_1, t_2)|^2$  not depending on  $s_1$  and  $s_2$

$$\frac{d\sigma}{dt_1 dt_2} \propto \frac{\sigma_0 |\mathcal{M}(t_1, t_2)|^2 \pi^2}{4\sqrt{\lambda(s, m_1^2, m_2^2)}} \ln \left( \frac{s_{11}^- - t_2 - m_1^2 + \sqrt{\lambda(s_{11}^-, t_2, m_1^2)}}{s_{12}^+ - t_2 - m_1^2 + \sqrt{\lambda(s_{12}^+, t_2, m_1^2)}} \right), \quad (7.18)$$

where  $s_{11}^-$  and  $s_{12}^+$  are defined in eqs. (7.3) and (7.4). Equation (7.18) may look somewhat obscure; to convince ourselves of its symmetry under  $t_1 \leftrightarrow t_2$  we provide here the 0<sup>th</sup> order expansion in  $M_e$  of the argument of the logarithm, clearly LS symmetric:

$$\frac{-2t_1 t_2}{s(t_1 + t_2 - M_a^2 + \sqrt{\lambda(t_1, t_2, M_a^2)}}. \quad (7.19)$$

All properties listed in this section are plotted in fig. 7.5, where the magenta contour is  $\partial\mathcal{V}_t$ . Specifically we can see that  $\mathcal{V}_t$  is convex, that  $\mathcal{V}_t$  is continuous and symmetric under  $t_1 - t_2$  exchange, and is enclosed among its vertical tangents  $t_1 = \min, \max t_1$ , as in eqs. (5.32) and (5.33), and its horizontal tangents  $t_2 = \min, \max t_2$ . That eqs. (5.32) and (5.33) are minima and maxima to  $t_2$  comes from the fact that they were obtained from  $\mathcal{G}_1$  roots when we were studying  $\frac{d^2\sigma_t}{ds_1 dt_2}$ , the same  $\mathcal{G}_1$  we have here; that they are minima and maxima to  $t_1$  comes from symmetry. We provide here their series expansion in

$\frac{M_e}{\sqrt{s}}$ :

$$\max t_1 = \max t_2 = -\frac{M_a^4 M_e^2}{s(s - M_a^2)} \left( 1 + \mathcal{O}\left(\frac{M_e^4}{s^2}\right) \right), \quad (7.20)$$

$$t_2^T = t_1^T = (-M_a M_e + M_e^2) \left( 1 + \mathcal{O}\left(\frac{M_e^3}{s^{3/2}}\right) \right). \quad (7.21)$$

Lastly, from the zoomed fig. 7.6 you can appreciate what we stated without proof in section 2.3.1, i.e. that the Phase Space is such that the divergences of the  $e^+e^- \rightarrow e^+e^-a$  scattering lies at its feet. The fact that the  $t$  channel can approach the divergence so closely but is protected from it as it does not belong to the phase space, makes the cross section bigger than that of the  $s$  channel. Vice versa, applying constraints on final particles can cut away the phase space regions close to the divergences, thus reducing the cross section. Specifically, asking for the final leptons to overcome an energy threshold and not to fly close to the beam pipe has this precise effect: the red upper right corner in fig. .5, appendix L, i.e. the  $(t_1, t_2)$  region with the biggest  $\frac{d^2\sigma_t}{dt_1 dt_2}$ , would be cut away. Notice that the same cut would have a marginal effect on the  $s$  channel. As is clear from fig. 5.4a a selection killing the  $s$  channel is imposing a minimal final leptons angular distance, which would make  $u_1$  big and lose the  $\frac{d\sigma_s}{du_1}$  maximum.

We can analytically find  $t_2^T$ , the  $t_2$  point at which  $t_1$  is minimal, compute the tangent to the Phase Space boundary in  $t_2^T$ , and numerically verify that it is horizontal (since doing it analytically is too complicated), as depicted in fig. 7.6. By symmetry we recover  $t_1^T$ , the  $t_1$  point at which  $t_2$  is minimal.

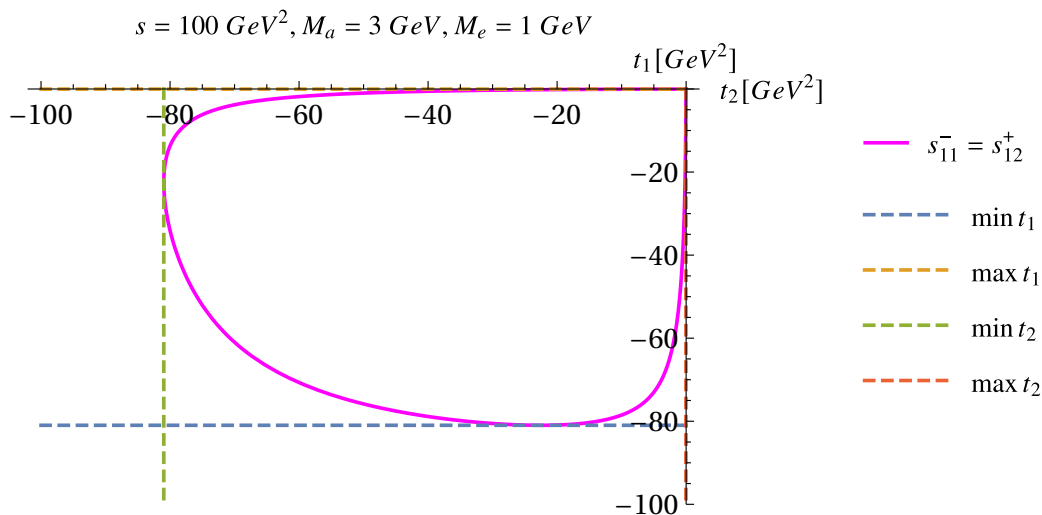


**Figure 7.5.** The magenta solid curve is the Phase Space boundary of the  $(t_1, t_2)$  cross section distribution. Dashed curves are vertical and horizontal tangents. They delimit the minimum and the maximum allowed to  $t_{1,2}$ . For the clarity of the picture we chose  $s = 100 \text{ GeV}^2, M_a = 3 \text{ GeV}, M_e = 1 \text{ GeV}$ .

Now that we know everything about the Phase Space boundary, we can take a look at the cross section distribution itself. Equation (7.18) is expressed for a generic matrix element that does not depend on  $s_{1,2}$ . Hence we can take a look both at the pure phase space (constant matrix element; we indicate its integrated cross section as  $\Phi$ ) and at our SSM theory ( $\mathcal{M} \rightarrow \frac{1}{t_1 t_2}$ ). We devote appendix L to this purpose. All of figs. .4 to .11 depict some  $t_1 \leftrightarrow t_2$  symmetric, strongly anisotropic  $\frac{d^2\sigma_t}{dt_1 dt_2}$  and  $\frac{d^2\Phi}{dt_1 dt_2}$ . The difference among them is that  $\mathcal{M} \rightarrow \frac{1}{t_1 t_2}$  pulls the distribution maximum towards small  $|t_{1,2}|$  and towards the boundary, while  $\frac{d^2\Phi}{dt_1 dt_2}$  attains its maximum

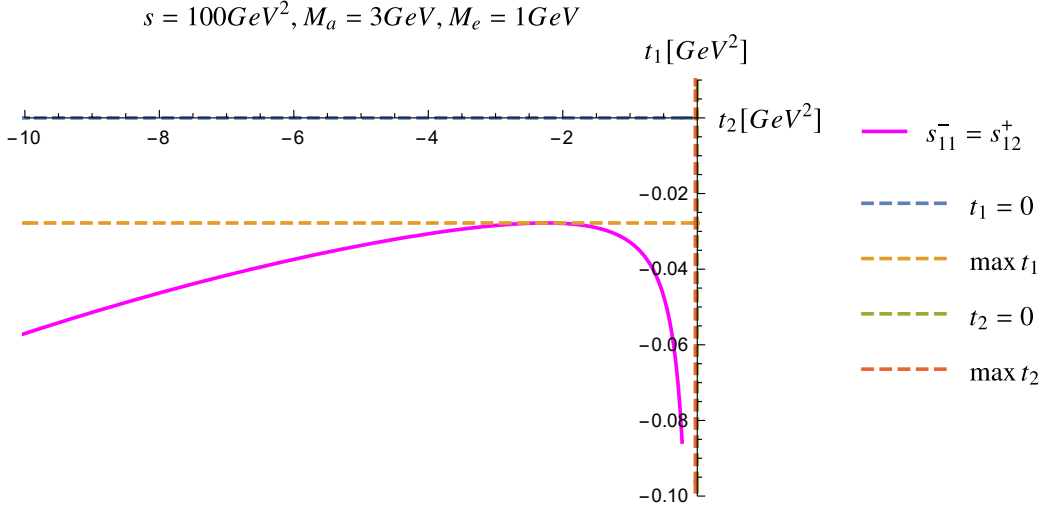


**Figure 7.6.** Zoom of fig. 7.5 that shows how the  $t_1 = 0$  blue dashed line is kept outside the Phase Space boundary, the solid magenta line. Here distances are magnified by our choice of  $M_e$  (same as fig. 7.5) for the clarity of the picture but the physical case has them much closer (see eq. (7.20)). Notice the big difference in magnitude among  $t_1$  and  $t_2$  onto the tangency point, in accord with eqs. (7.20) and (7.21).

within the physical region.

Let us be more specific on the kinematic configuration of the VBF maximising region. The  $(t_1, t_2)$  PS boundary  $\partial\mathcal{V}_t$  is symmetric under  $t_1 \leftrightarrow t_2$ . The cross section maximizing region lies close to the corner of the quadrant. Here the distance from the origin of the  $(t_1, t_2)$  plane is minimized.  $\partial\mathcal{V}_t$  is closest to the  $(0, 0)$  point onto its intersection with the quadrant bisector. The intersection point has coordinates  $(\bar{t}_1, \bar{t}_2)$  with  $\bar{t}_1 = \bar{t}_2$ . In that point the slope of the tangent to  $\partial\mathcal{V}_t$  is -1, i.e. it is orthogonal to the bisector. I have two proofs of these statements:

1. In the limiting case  $M_e = 0$  the  $(0, 0)$  corner is included in  $\partial\mathcal{V}_t$  and the matrix element diverges hence  $\bar{t}_1 = \bar{t}_2 = 0$ . Since  $\partial\mathcal{V}_t$  is continuous in  $M_e$ , by slightly modifying  $M_e$  the  $(\bar{t}_1, \bar{t}_2)$  must still be the closest point to the origin.
2.  $\partial\mathcal{V}_t$  is made by two branches, functions of  $t_2$ . They meet onto  $t_2 = \min t_2$  and  $t_2 = \max t_2$ , i.e. where the tangent is vertical. Let us start from  $\min t_2$  and cycle all around  $\partial\mathcal{V}_t$ . On the first branch, i.e. from  $\min t_2$  to  $\max t_2$ , the tangent is horizontal only once. On the second branch, i.e. from  $\max t_2$  to  $\min t_2$ , it is the same. Then one branch is concave and the other one is convex. On one branch the slope of the tangent starts from  $+\infty$ , has a node and sinks down to  $-\infty$ , then the other branch starts and the slope meets  $-\infty, 0, +\infty$  in this order. This means that each branch has slope -1 only once. Since you can plug  $(\bar{t}_1, \bar{t}_2)$  in  $\partial\mathcal{V}_t$  and verify the slope is -1 there,  $(\bar{t}_1, \bar{t}_2)$  is the only point with slope -1 on the branch it belongs to.

What kinematic configuration corresponds to the boundary upper corner point  $(\bar{t}_1, \bar{t}_2)$ ? In the centre of mass frame consider the usual process fig. 1.1b and let the fourmomentum  $p_i$  have velocity  $\vec{\beta}_i$  and Lorentz factor  $\gamma_i$  for  $i \in [1, 5]$ . Define

$$\vec{\beta}_1 = -\vec{\beta}_2 =: \vec{\beta}, \quad \gamma_1 = \gamma_2 =: \gamma. \quad (7.22)$$

Then we can rewrite  $t_{1,2}$  as

$$t_1 = (p_1 - p_3)^2 = 2M_e^2[1 - \gamma\gamma_3(1 - \vec{\beta} \cdot \vec{\beta}_3)], \quad (7.23a)$$

$$t_2 = (p_2 - p_5)^2 = 2M_e^2[1 - \gamma\gamma_5(1 + \vec{\beta} \cdot \vec{\beta}_5)]. \quad (7.23b)$$

Equation (7.23a) is equal to eq. (7.23b) if  $\vec{\beta}_3 = -\vec{\beta}_5 =: \vec{\beta}_f$  (hence  $\gamma_3 = \gamma_5 =: \gamma_f$ ). Then the fourmomentum conservation is solved for

$$\gamma_f = \frac{\sqrt{s} - M_a}{2M_e}, \quad (7.24a)$$

$$\vec{\beta}_4 = 0. \quad (7.24b)$$

The ALP is at rest, initial leptons are back to back along the  $z$  axis, final leptons have equal energy and are back to back along an axis of polar angle  $\theta$ :

$$t_1 = t_2 = 2M_e^2[1 - \gamma\gamma_f(1 - \beta\beta_f \cos \theta)], \quad (7.25)$$

$$s_1 = s_2 = M_e^2 + M_a\sqrt{s}. \quad (7.26)$$

Equation (7.25) is minimized onto  $\theta = 0$ ; thus we find

$$\bar{t}_1 = \bar{t}_2 = 2M_e^2[1 - \gamma\gamma_f(1 - \beta\beta_f)]. \quad (7.27)$$

In fig. 7.7 we show that  $|\bar{t}_1|$  is much smaller than all s-like Mandelstam variables  $s, s_1, s_2$  for whatever  $M_a$ . The same can not be said for  $s_1$ : for  $s_1$  to be less than some  $\epsilon_a s$  we will need  $M_a < \frac{\epsilon_a s - M_e^2}{\sqrt{s}}$ .

### 7.3 Peripherality classes

All that I stated in the previous section comes from requiring that  $s$  is much bigger than some of the scattering masses. In fact a matrix element numerator is a polynomial  $\mathcal{P}_n$  in the scalar products (masses included) of order  $n \geq 0$ .  $n$  depends on the vertices of the interaction. A matrix element denominator comes from propagators and is a polynomial of order  $m \geq 1$ ,  $m$  depending on the number of virtual particles in the process.

**Definition 20** (Scalar products and matrix elements).

Define scalar products as

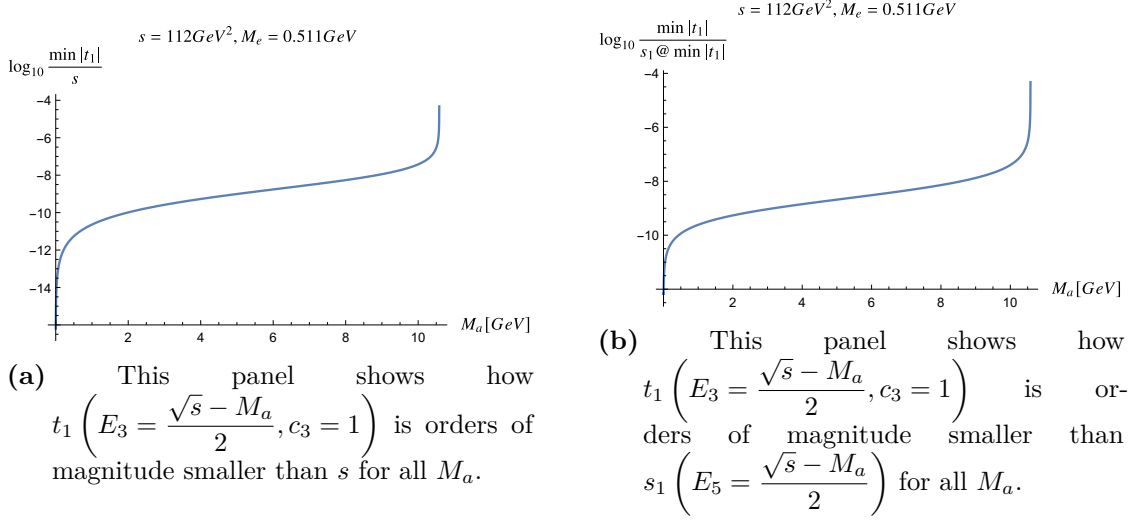


**Figure 7.7.** In the text I derived that the VBF maximising configuration has the ALP at rest, the leptons energies  $E_{3,5} = \frac{\sqrt{s} - M_a}{2}$ , the cosine of the electron polar angle  $c_3 = 1$  and the cosine of the positron polar angle  $c_5 = 1$ . In this picture I show that this configuration makes  $t_{1,2}$  much smaller than all  $s$ -like variables ( $s, s_1, s_2$ ) for all  $M_a$  values. On the left panel I plot  $s^{-1}t_1 \left( E_3 = \frac{\sqrt{s} - M_a}{2}, c_3 = 1 \right)$ , i.e. the ratio between the minimum  $|t_1|$  and the CoM energy. On the right panel I plot  $t_1 \left( E_3 = \frac{\sqrt{s} - M_a}{2}, c_3 = 1 \right) s_1^{-1} \left( E_5 = \frac{\sqrt{s} - M_a}{2} \right)$ , i.e. the ratio between  $t_1$  and  $s_1$  both in VBF maximising configuration.

$$p_i^2 = m_i^2, \quad (7.28)$$

$$p_{\text{in}}^2 := (p_1 + p_2)^2 = s \quad (7.29)$$

$$\vec{m} := (\sqrt{s}, m_1, \dots, m_n) \quad (7.30)$$

$$(p_i + p_j)^2 =: s_{ij}, \quad (7.31)$$

$$(p_i - p_j)^2 =: t_{ij}. \quad (7.32)$$

Propagators of particles of different spin contribute with a numerator that we will implicitly include in the overall matrix element numerator and a denominator which is that of propagating scalar particles. If the propagating particle has fourmomentum  $q$  and mass  $m_p$  we define

$$\frac{1}{Q(q, m_p)} := \frac{1}{q^2 - m_p^2}. \quad (7.33)$$

Finally define two different matrix elements:

$$\mathcal{M}_1 = \frac{\mathcal{P}_{n_1}^1(\vec{m}, s_{ij}, t_{ij})}{\mathcal{D}_1}, \quad \mathcal{D}_1 = \mathcal{Q}(p_1 - p_3, m_p) \prod_{(ij) \in \sigma_1} \mathcal{Q}(p_i + p_j, m_p^{ij}) \quad (7.34)$$

$$\mathcal{M}_2 = \frac{\mathcal{P}_{n_2}^2(\vec{m}, s_{ij}, t_{ij})}{\mathcal{D}_2}, \quad \mathcal{D}_2 = \prod_{(ij) \in \sigma_2} \mathcal{Q}(p_i + p_j, m_p^{ij}) \quad (7.35)$$

with  $m_p^{ij}$  the mass of the propagating particle in the  $i, j$  line. In particular, without loss of generality, we chose  $\mathcal{D}_1$  to be the product of  $t_{13}$  and some  $s$ -like variables belonging to a set  $\sigma_1$  and  $\mathcal{D}_2$  to be the product of some  $s$ -like variables belonging to a set  $\sigma_2$ .

□

Consider now  $m_p \ll \sqrt{s}$ .  $t_{ij}$  can be small if both

$$\frac{m_{i,j}}{\sqrt{s}} := \epsilon x_{i,j}, \quad 0 < \epsilon \ll 1, \quad 0 \leq x_{i,j} \leq 1. \quad (7.36)$$

Then

$$\min |t_{ij}| \sim \epsilon^2 \text{ GeV}^2, \quad (7.37)$$

so  $\mathcal{Q}(p_1 - p_3, m_p)$  can be small if  $\frac{m_{1,3,p}}{\sqrt{s}} \ll 1$ . Consequently

**Theorem 22** (*t dominance and spin blindness*).

Consider a scattering respecting definition 20. In  $\mathcal{M}_1$  (eq. (7.34)) the denominator  $\mathcal{D}_1$  is proportional to  $\mathcal{Q}(p_1 - p_3, m_p) = t_{13} - m_p^2$  (see eq. (7.32) for the  $t_{13}$  definition). If  $m_p \ll \sqrt{s}$  and whose fourmomentum is  $p_1 - p_3$ . The corresponding propagator is

$$\sim \frac{\text{spin dependent numerator}}{t_{13}}. \quad (7.38)$$

Then the following are true

$$\lim_{\substack{E_3 \rightarrow \max E_3 \\ c_3 \rightarrow 1}} \left( \frac{\mathcal{P}_{n_1}^1(\vec{m}, s_{ij}, t_{ij})}{t_{13} \prod_{(ij) \in \sigma_1} \mathcal{Q}(p_i + p_j, m_p^{ij})} - \frac{\mathcal{P}_{n_1}^1(\vec{m}, 0, 0)}{t_{13} \prod_{(ij) \in \sigma_1} \mathcal{Q}(p_i + p_j, m_p^{ij})} \right) = 0, \quad (7.39)$$

$$\lim_{\substack{E_3 \rightarrow \max E_3 \\ c_3 \rightarrow 1}} \left( \frac{\mathcal{P}_{n_1}^1(\vec{m}, s_{ij}, t_{ij})}{t_{13} \prod_{(ij) \in \sigma_1} \mathcal{Q}(p_i + p_j, m_p^{ij})} - \frac{\mathcal{P}_{n_2}^2(\vec{m}, s_{ij}, t_{ij})}{\prod_{(ij) \in \sigma_2} \mathcal{Q}(p_i + p_j, m_p^{ij})} \right) = \infty. \quad (7.40)$$

□

Theorem 22 means two things:

1. From eq. (7.39), every time in a full Phase Space scattering there are very small masses, you make a small error if you trade a  $t$ - channel topology of some theory for the same topology in SSM, i.e. you go spin-blind. Since at sufficiently high energies all the masses of a scattering can be neglected, a given process may follow any field theory, we will not be able to tell the theory apart by looking at the cross section only.
2. From eq. (7.40), every time in a full Phase Space scattering there are topologies whose propagators can be very small and topologies whose propagators can not, you can neglect the latter. The higher the number of propagators that can go to 0, the more the topology is important for the total cross section.

Theorem 22 is a very strong result because in full generality it provides two very powerful simplifications: topology hierarchy and spin blindness. Specifically to our computation, they close the circle to our reasoning: in the introduction (chapter 1), we pointed out that the authors of [72] were neglecting the VBF and asked ourselves when this can be a valid approximation? Theorem 22 concludes our demonstration that in many cases this is not so and in part II we will prove it in under the phenomenological point of view too.

Another solved point is the goodness of SSM: in section 2.2 we proposed spin blindness as a simplification for a complicated problem. We proved now that this is not that bad of an approximation as one may have suspected. It is true that up to now we dealt with limits i.e. we evaluated the fully derivative cross section in one very specific direction.

Although this is the maximising direction, it has a 0 measure over the full Phase Space hence one could argue we basically proved nothing. Therefore let us improve theorem 22 and study the spin blindness region  $\mathcal{R}_{\text{SB}}$  VS the matrix element maximizing phase space region  $\mathcal{R}_{\text{max}}$ . With fixed  $\vec{m}$ , I reiterate that the spin blind region is that in which the matrix element numerator can be reduced to a constant, which is what happens if all the particles of the theory had spin 0; the maximising region is that in which the full theory matrix element (and, as a consequence, the spin blind theory too) is maximal. We will stick to the  $e^+e^- \rightarrow e^+e^-a$  process.

We already know we have to consider a still ALP to hope to make all gMVs small at once. Plus, we need  $M_a$  too to be small if we want  $s_{1,2} < \epsilon_a s$  for some small positive  $\epsilon_a \ll 1$  (see eq. (7.26)). As to  $t_{1,2}$ , consider eq. (7.25): there is a  $\tau \in [0, 1]$  such that if  $|t_{1,2}| < -\tau s$  there is no other kinematic configuration that can make the matrix element bigger. This happens when  $\theta < \theta(\tau)$ . This inequality spans the maximising region. In fig. 7.8 we give the acceptable region for  $\cos\theta$  when  $(\epsilon_a, \tau) = (0.2, 0.1)$  and  $(0.1, 0.05)$ : we can see that  $|t_{1,2}|$  should be small is a shared requirement of  $\mathcal{R}_{\text{max}}$  (cyan area) and  $\mathcal{R}_{\text{SB}}$  (magenta area), but in the case of  $\mathcal{R}_{\text{max}}$  we can get up to  $M_a = \sqrt{s} - 2M_e$ . See how more and more values of the angle become acceptable as  $M_a$  gets bigger: although the minimal  $|t_{1,2}|$  is still achieved at  $\theta = 0$ , we start seeing in the final state that the leptons can deflect more and more from their mother's direction of flight as  $M_a$  approaches  $\sqrt{s} - 2M_e$ . This is perfectly aligned with the asymmetry argument we were making in section 8.3. Lastly, notice how smaller both regions become when  $\epsilon_a$  and  $\tau$  are smaller. Theorem 22 corresponds to  $\tau, \epsilon_a \rightarrow 0$ .

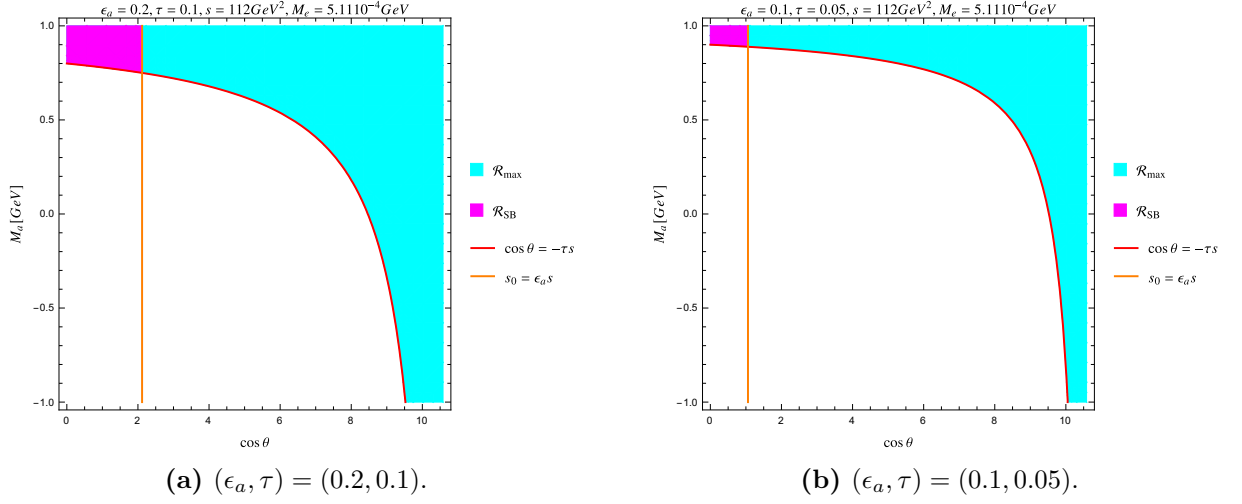


**Figure 7.8.** In these plots we depict the area in which spin blindness is achieved for the VBF ( $\mathcal{R}_{\text{SB}}$ , magenta) and the area in which the matrix element is maximised ( $\mathcal{R}_{\text{max}}$ , cyan, see text for details). For both we consider a still ALP, the former corresponding to  $|t_1| = |t_2| \leq \tau s \wedge s_1 = s_2 \leq \epsilon_a s$ , the latter simply to  $|t_1| = |t_2| < \tau s$ . The red line satisfies  $|t_1| = |t_2| = \tau s$ , the orange line  $s_1 = s_2 \leq \epsilon_a s$ .

To wrap up, in  $\mathcal{R}_{\text{max}}$  it is sufficient for  $t_1$  and  $t_2$  to be small. This is achieved when the ALP has a small velocity  $|\vec{\beta}| \sim 0$  and the final leptons fly close to the beam pipe; in  $\mathcal{R}_{\text{SB}}$  there is the extra requirement that  $M_a$  is small with respect to  $\sqrt{s}$ . The smallness of  $t_1$ ,  $t_2$ ,  $(1 - c_3)$  and  $(1 + c_5)$  can be controlled by two parameters  $\epsilon_a$  and  $\tau$ . The closer  $\epsilon_a$  and  $\tau$  come to 0, the smaller  $\mathcal{R}_{\text{max}}$  and  $\mathcal{R}_{\text{SB}}$  become.



## Chapter 8

# Massive photons and Scalar Equivalent Photon Approximation

In the last chapter of part I we want to explore the viability of two alternative strategies: the massive photon way (section 8.1) and the Equivalent Photon Approximation (section 8.2). In the following two sections we not only show that they actually are viable, but they also work as a counter-proof of the results we already explained. Let us remark that they could not be used a priori since we did not have a way to demonstrate their viability while being agnostic of the full computation.

### 8.1 Massless lepton and massive photon

In [104] (from now on AMP), Altarelli, Mele and Pitolli studied a very similar process to ours, a Higgs production from a  $2 \rightarrow 3$  scattering. The differences between this paper and our attempt are:

1. They consider the Higgs, a scalar, rather than the ALP, a pseudoscalar, making their matrix element different from ours. Nonetheless we showed that the spin blind approximation works very well for our problem, so we can still borrow some of their results.
2. AMP take  $M_e = 0$ . This means that in their phase space the point  $t_{1,2} = 0$  can be reached, while we stay safely away from it.
3. Their virtual particles have a non negligible mass  $M_V$ . This means that their propagators are of the form  $\frac{1}{t_{1,2} - M_V^2}$  rather than  $\frac{1}{t_{1,2}}$ . Then, even when  $t_{1,2} = 0$ , they never reach any divergence, as it happens in the VBF. This means that it is everywhere safe for them to neglect  $M_e$  while we have to keep it.

We propose to consider  $M_e = 0$  and give the photon a mock mass  $m_\gamma$  so that in our SSM we can follow AMP's path. Two  $m_\gamma$  candidates stand out,  $|\bar{t}_1|$  (eq. (7.27)) and  $\min |t_1|$  (eq. (7.20)). I will pick

$$m_\gamma^2 \equiv |\bar{t}_1| \tag{8.1}$$

for three main reasons: the region with largest cross section is around  $\bar{t}_1$  rather than  $\max t_1$ ;  $\bar{t}_1$  is easily analytically given; for this masses choice  $|\bar{t}_1|$  and  $\min |t_1|$  are generally very similar, so that this choice will not have great numerical impact. With this, the SSM VBF amplitude would be

$$|\mathcal{M}|_{m_\gamma}^2 = \left( \frac{1}{(t_1 - m_\gamma^2)^2} \frac{1}{(t_2 - m_\gamma^2)^2} \right)_{M_e=0}^2. \quad (8.2)$$

We can now repeat the very same steps of AMP. First, we name fourmomenta like

$$p_1 + p_2 \rightarrow p_{e^-} + p_{e^+} + p_a. \quad (8.3)$$

Go to the reference frame with back to back final leptons. The fourmomentum conservation is easily integrated away here against  $\vec{p}_{e^-}$  (final electron three-momentum) and  $E_{e^+}$  (final positron energy) or *vice versa*. Express all scalar products in terms of  $p_{1,2} \cdot p_a$ . These are Lorentz invariants that only depend on the ALP. We can evaluate them later. Now we are left with a polar and an azimuthal integration to perform over the whole solid angle of the positron. The azimuthal integration is of the form

$$\frac{1}{(\cos \phi + a)^2}. \quad (8.4)$$

Thanks to  $m_\gamma \neq 0$  we know this integration is safe from singularities as  $a > 1$ . If instead we wanted to expand in small  $m_\gamma$  at this point, we would impair its function to avoid singularities.

With the same spirit we proceed to the polar integration (over  $c_3 = \cos$  of the  $e^-$  polar angle), which has the form

$$\frac{n_1 c_3 + n_0}{(d_5 c_3 + d_4)^2 (d_2 c_3^2 + d_1 c_3 + d_0)^{3/2}}. \quad (8.5)$$

with  $n_i, d_i$  some coefficients. These integrals can be computed but are very verbose. However, knowing it may be divergent, we may take a look at the lowest order in the  $m_\gamma$  expansion:

$$\frac{d^2 \sigma_{m_\gamma}}{dE_a d \cos \theta_a} \propto \frac{4\pi^2 m_\gamma^2}{s^{3/2} \sin^4 \theta_a^2 E_a (E_a^2 - M_a^2)} \quad (8.6)$$

Since we expanded in  $m_\gamma$  we obviously got a fake divergence at  $E_a = M_a$ . Had we performed the full computation we would have had a finite peak around  $E_a \simeq M_a$ . Still this is instrumental to support our claim that the ALP is preferably produced at rest.

In conclusion, we showed that with the due care one can use the AMP method at least to get a flavour of the cross section distribution with respect to the fusion product fourmomentum for a finite VBF process.

## 8.2 Equivalent Photon Approximation

Up to now we tried to solve our  $e^+e^- \rightarrow e^+e^-a$  problem by ignoring the spin of all particles in the process and through the GD formalism. This was very effective,

in fact we were able to study many cross section distributions. On this basis we can decide whether our process is eligible for another, simplifying strategy, that of the Equivalent Photon Approximation (EPA). The EPA is a good approximation every time in a process there is an electron emitting photons in a way that does not change much nor its energy or its direction. In what follows we will see that a relevant effort during these years has been put in the quantification of this *not change much*. In the previous section we showed that this may be our case as our scattering is enhanced exactly on such points ( $t_1 \sim 0, t_2 \sim 0$ ) in general. But does this statement hold regardless from the scattering parameters? Yes, in most cases: we devote section 8.3 to show that the EPA will not be viable only for

$$M_a > \sqrt{s} - 2(1 + 7.5 \cdot 10^{-3})M_e, \quad (8.7)$$

as for too heavy ALP masses the  $2 \rightarrow 3$  scattering loses a necessary EPA condition, the kinematic preference for non deviating final leptons. We then proceed to recap what EPA is section 8.4 and apply it to our fully scalar theory section 8.5, recovering what we dubbed SEPA (Scalar Equivalent Photon Approximation). We finally proceed to use SEPA on our scattering.

### 8.3 The VBF has final $e^\pm$ anisotropic angular distribution

At the end of corollary 8 we showed how the phase space shrinks down in the limit of the ALP mass approaching the whole energy injected in the scattering. In section 4.4 we showed that this leads to a quasi two body process, implying the matrix element and then the cross section to go isotropic in the final leptons emission. We give here a gallery (fig. 8.1) to show that the behaviour of  $\frac{d^2\sigma_t}{ds_1 dt_2}$  under these conditions is exactly how we predicted in section 4.4, i.e. strongly peaked on  $c_5 \sim -1$ , meaning that the final positron is not deviating from the initial one. In fig. 8.1 I converted from gMvs to polar coordinates and fixed the final  $e^+$  energy to some constant values. From fig. 8.1a to fig. 8.1d I pick some increasing  $M_a$  values, consequently the biggest allowed  $E_5$  decreases. We can see that the  $c_5 \sim -1$  preference is more and more evident when big  $E_5$  are allowed. We need to go up to  $M_a = \sqrt{s} - (2 + 10^{-3})M_e$  to completely wash the anisotropy away.

In fig. 8.2 we provide a plot of the asymmetry of  $\frac{d^2\sigma_t}{dE_5 dc_5}$  in the sense of definition 17. We used the convenient parametrizations

**Definition 21** ( $\alpha$  and  $x$  parametrization).

$$M_a = \sqrt{s} - 2(1 + \alpha)M_e, \alpha \geq 0 \quad (8.8)$$

$$E_5 = x(\max E_5 - M_e) + M_e, x \in [0, 1], \quad (8.9)$$

so that  $x$  linearly interpolates between the positron minimal and maximal energy. Remember that the maximal allowed  $M_a$  is attained on  $\alpha = 0$  and is  $\bar{M} = \sqrt{s} - 2M_e$ .

□

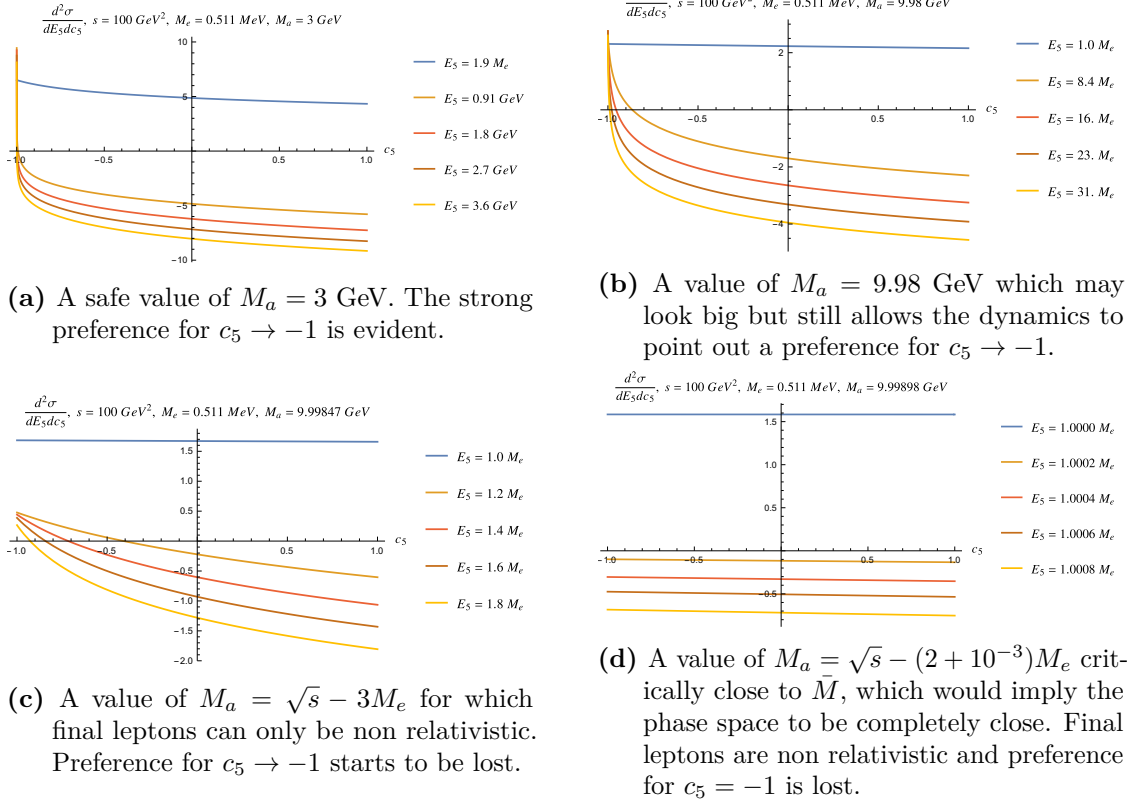


**Figure 8.1.**  $\log_{10} \left( \frac{d^2 \sigma_t}{dE_5 dc_5} \right)$  evaluated on  $s = 100$  GeV<sup>2</sup>,  $M_e = 0.511$  MeV and different values of  $M_a$ . In each subfigure we provide 6 curves of constant positron energy, from the smallest (it should be equal to the electron mass but it will be something slightly bigger, due to the machine precision) to max  $E_5$ .

We remind that an asymmetry pointing to 1 corresponds to a function of  $\cos \theta$  that is much bigger on  $\theta = 0$  than on  $\theta = \pi$ ; an asymmetry pointing to  $-1$  corresponds to a function that is much bigger on  $\theta = \pi$  than on  $\theta = 0$ ; an asymmetry pointing to 0 corresponds to a function that is equal on  $\theta = 0$  and  $\theta = \pi$ . Then all quadrants of fig. 8.2 contribute to demonstrate that isotropy can be achieved only for ALP mass very close to  $\bar{M}$  or the lepton energy very similar to  $M_e$ . The very small energy case is depicted in fig. 8.2, in which we plot the ratio

$$\omega(M_a) := \frac{\frac{d^2 \sigma_t}{dE_5 dc_5}(E_5 = E^*)}{\frac{d^2 \sigma_t}{dE_5 dc_5}(E_5 = E^*, c_5 = 0)}, \quad (8.10)$$

where

$$E^* = (1 + 10^{-3})M_e. \quad (8.11)$$

We may ask for what value of  $\alpha$  we can be sure that all curves from  $x = 0$  to  $x = 1$  will have an asymmetry inside the interval  $[-\frac{1}{3}, 0]$ . We find numerically  $\alpha = 7.5 \cdot 10^{-3}$ .

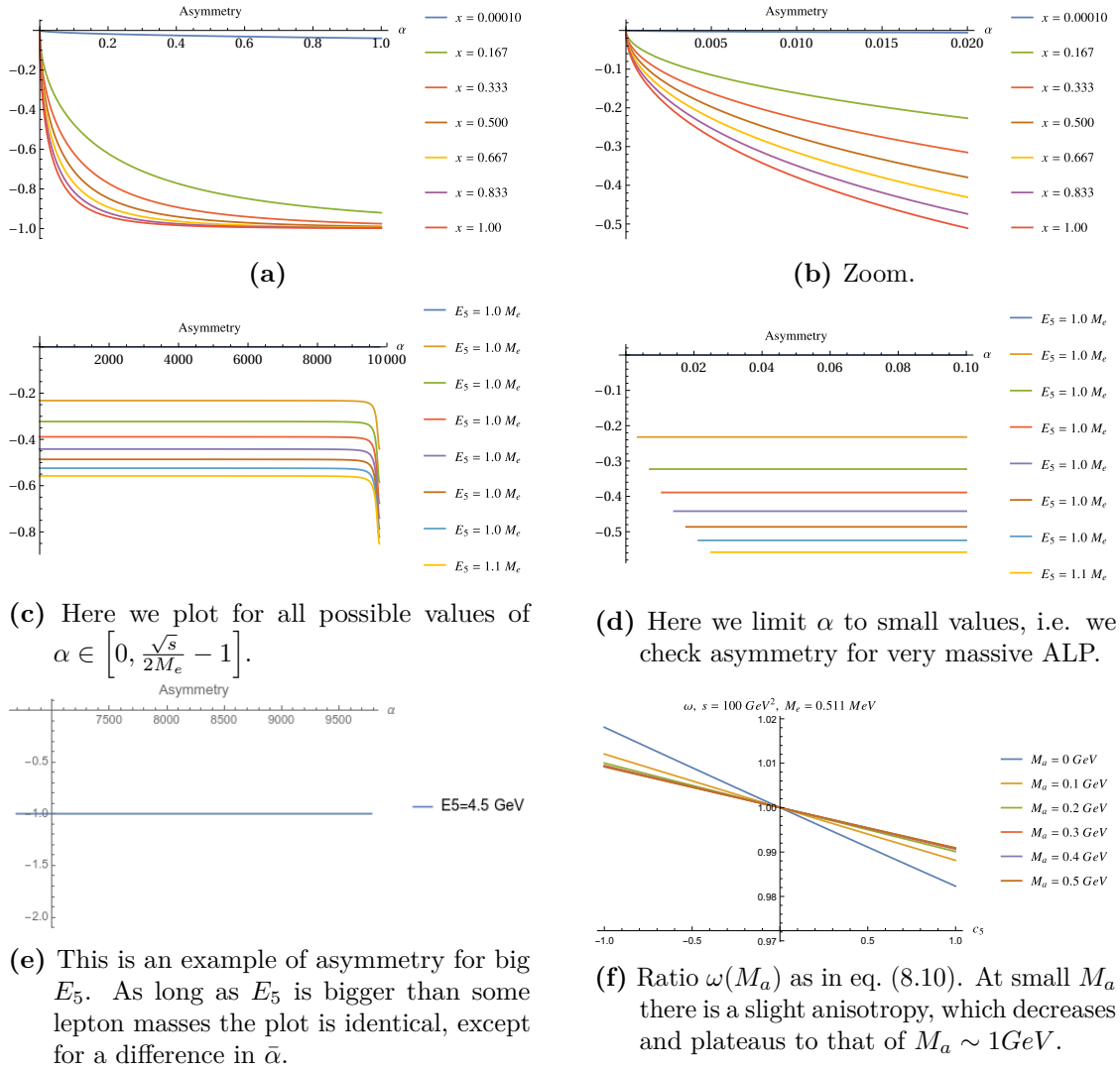


**Figure 8.2.** Asymmetry of  $\frac{d^2\sigma_t}{dE_5 dc_5}$  (see text for details).

### Collinearity is lost beyond the critical $\alpha$

In definition 17 compute the anisotropy functional on  $f = \frac{d^2\sigma_t}{dE_5 dc_5} \vec{x} = E_5$  with respect to the positron cosine of polar angle. Take a sufficiently large  $M_a$  that the positron is always non relativistic. Specifically, if we want  $\beta_5 < 0.3$  in all the phase space, we must consider  $\alpha < 0.024$ . Using

$$\epsilon = \frac{M_e}{\sqrt{s}}, \quad (8.12)$$

$$E_5 = \frac{1}{\sqrt{1 - \beta_5^2}} \sqrt{s} \epsilon, \quad (8.13)$$

We can expand  $f$  in small  $\epsilon$  and small  $\beta_5$ . At lowest order the asymmetry is a straight line in  $\beta_5$ :

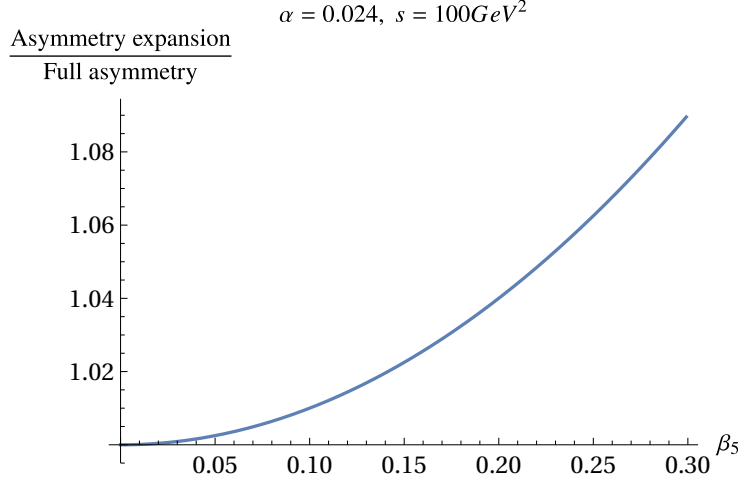


**Figure 8.3.** We consider the asymmetry of the function  $\frac{d^2\sigma_t}{dE_5dc_5}$  when  $E_5 = \frac{1}{\sqrt{1-\beta_5^2}}M_e$  and  $M_a$  such that  $\beta_5$  is at most 0.3. We show the ratio of the linearization  $\mathcal{A}_f^0$  as in eq. (8.14) over the full function.

$$\mathcal{A}_f = \mathcal{A}_f^0 + \mathcal{O}(\beta_5^3) = -2\beta_5(1 + 3\epsilon + \mathcal{O}(\epsilon^2)) + \mathcal{O}(\beta_5^3). \quad (8.14)$$

As one could expect, being the asymmetry a dimensionless quantity that we express in terms of adimensionalized parameters, we have no dependence on  $s$ . Moreover, once we ask for  $M_a$  to be sufficiently small, when we limit ourselves to the biggest contributions to  $\mathcal{A}_f^0$  we can see that we also loose dependence on  $\alpha$ , i.e. on  $M_a$ . The only thing on which  $\mathcal{A}_f^0$  keeps some sensitivity is  $\epsilon$ . In fig. 8.3 we go to the worst case scenario, when  $\alpha$  is the biggest allowed, in order to have an always non relativistic final lepton, and compare the linear part of eq. (8.14) with the full  $\mathcal{A}_f$ . The result is that when we linearize the asymmetry as a function of the velocity we make at most an 8% error.

### k-asymmetry

Suppose your detector is unable to cover the whole solid angle, i.e. the closest polar angle to the beam axis that can be reached,  $\bar{\theta}$ , is such that  $\cos \bar{\theta} = k$ ,  $k \in [0, 1]$ . The  $k$ -asymmetry is defined as

$$\mathcal{A}_f^k := \frac{f(k, \vec{x}) - f(-k, \vec{x})}{f(k, \vec{x}) + f(-k, \vec{x})}. \quad (8.15)$$

Compute  $a(k)$ , the  $k$ -asymmetry on  $\frac{d^2\sigma_t}{dE_5dc_5}$  with  $E_5 = \max E_5$ . Its small  $\alpha$  expansion is

$$a(k) \simeq -\frac{4k}{1 - 3\epsilon + 2\epsilon^2} \sqrt{\alpha(1 - \epsilon - 4\epsilon^2 + 4\epsilon^3)} + \mathcal{O}(\alpha), \quad (8.16)$$

where we also used  $\epsilon = \frac{M_e}{\sqrt{s}}$ . We solve the previous equation for  $\alpha$  and plot it for the usual physical values and  $k = 1$  (fig. 8.4). We elected  $|a| = \frac{1}{3}$  as the limiting value

below which we consider the EPA approximation à la Budnev [113] as a very bad estimate of the cross section. Then all  $\alpha$ s below the blue line should not be used in this sense.

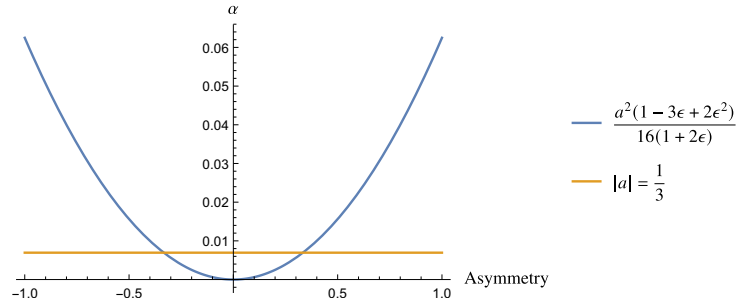


**Figure 8.4.** The blue curve solves eq. (8.16) for  $\alpha$  as a function of the  $k$ -asymmetry. Here we used  $k = 1$ . The yellow curve is the first  $|a|$  for which the asymmetry is less than  $\frac{1}{3}$ . We took this to be the threshold below which the EPA will not be a viable approximation.

## 8.4 100 years of EPA

The Equivalent Photon Approximation is such a widely spread tool that common use MC generators like MadGraph have a dedicated function for it. Sometimes a scattering can be so complicated and long to compute that approximating them is the only way we have of telling something about it. But these are exactly the cases in which it is vital to know whether the approximation was allowed or not. This is the purpose of the following sections. Despite being so common, I was not able to find a rigorous treatment of the EPA in textbooks (for example [111]). Therefore I will now browse the literature milestones of EPA.

We can trace back the Equivalent Photons Approximation origins to 1924 [114]. Fermi was investigating about the excitation and ionization of an atom due to solicitation from electronic bombardment. We know that shining light onto an atom can ionize it if the photon's energy is sufficiently large. However a similar effect can be obtained by a moving electron too, as it produces an electric field varying in time. As we will see below, its Fourier decomposition is equivalent to the decomposition of a photon's field.

To retrace Fermi's step we first need to introduce his formalism:

**Definition 22.**

Consider a moving particle  $\Pi$  of charge  $\epsilon$ . We want the spectral distribution at the point  $P$  of the photon created by the motion. Following fig. 8.5:

- Let  $\vec{v}$  be the velocity of  $\Pi$ , directed along the  $x$  axis.
- Call  $y$  the axis orthogonal to  $\vec{v}$ .
- $b$  is the minimal distance from  $\Pi$  to  $P$ .

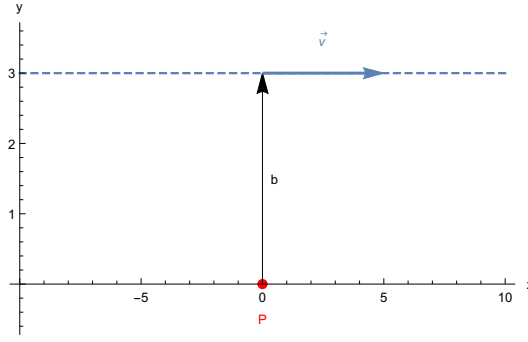


**Figure 8.5.** A particle  $\Pi$  moves parallel to the  $x$  axis with velocity  $\vec{v}$ . The minimal distance with the red point  $P$  is  $b$ .

- Call  $t$  the time and make it start when  $\Pi$  is at distance  $b$  from  $P$  ( $t = 0$ ).

□

Look at the particle after some time  $t$ : the longitudinal and transverse component of the electric field in  $P$  are

$$E_x = \frac{\epsilon v t}{(b^2 + v^2 t^2)^{3/2}}, \quad (8.17)$$

$$E_y = \frac{\epsilon b}{(b^2 + v^2 t^2)^{3/2}}. \quad (8.18)$$

The discrete Fourier transform with periodicity  $T$  is

$$E_x = \sum_{n=0}^{\infty} a_n \sin\left(2\pi n \frac{t}{T}\right), \quad a_n = \frac{2\epsilon v}{T} \int_{-\frac{T}{2}}^{\frac{T}{2}} dt \frac{t \sin\left(2\pi n \frac{t}{T}\right)}{\sqrt{(b^2 + v^2 t^2)^{3/2}}}, \quad (8.19)$$

$$E_y = \sum_{n=0}^{\infty} b_n \cos\left(2\pi n \frac{t}{T}\right), \quad b_n = \frac{2\epsilon b}{T} \int_{-\frac{T}{2}}^{\frac{T}{2}} dt \frac{\cos\left(2\pi n \frac{t}{T}\right)}{\sqrt{(b^2 + v^2 t^2)^{3/2}}}. \quad (8.20)$$

Notice how  $E_x$  only gets sin decomposition as it is odd in  $t$  while  $E_y$  only gets cos contributions as it is even.

We say that Fermi first introduced the EPA idea because he noticed that  $E_x$  is the electrical field of a light wave with intensity  $\frac{c}{4\pi} \frac{a_n^2}{2}$  and frequency  $\nu = \frac{n}{T}$ .

Another semiclassical remark comes from [115]. In chapter 73, Landau and Lifschits compute that an ultrarelativistic charge of velocity  $\vec{v}$  and acceleration  $\vec{w}$  emits radiation preferably parallel to its direction of flight. What they do is considering the electric field  $\vec{E}$  generated by the moving particle and look at a position traced by

$$\vec{R} = \hat{n}R, \quad \|\hat{n}\| = 1. \quad (8.21)$$

If you make  $R$  large, you can be contempt with a first dipole approximation

$$\vec{E} = \frac{e}{c^2 R} \frac{\hat{n} \times \left[ \left( \hat{n} - \frac{\vec{v}}{c} \right) \times \vec{w} \right]}{\left( 1 - \frac{\hat{n} \cdot \vec{v}}{c} \right)^3}. \quad (8.22)$$

Then the intensity of the radiation in the solid angle  $do$  is

$$dI = \frac{c}{4\pi} \vec{E}^2 R^2 do. \quad (8.23)$$

$\vec{E}^2$  is maximised when  $1 - \frac{\hat{n} \cdot \vec{v}}{c}$  is minimal i.e. when  $\hat{n}$  and  $\vec{v}$  are aligned. There is a cone around the direction of flight of aperture  $\sim \sqrt{1 - \frac{v^2}{c^2}}$  in which most of the radiation is contained.

Soon the EPA was used in QFT too for the approximate calculation of Feynman diagrams for the collision of fast charged particles. The first results can be traced back to [116,117], whose treatment stops at the leading order in  $\alpha_{EM}$ . For example we can consider an inelastic electron scattering off a proton, as depicted in fig. 8.6.

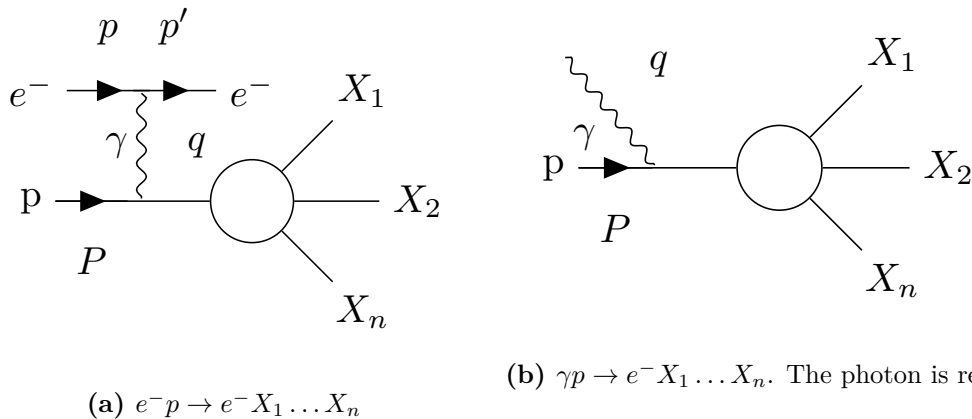


**Figure 8.6.** An electron flies by proton and interacts with it via a virtual photon. This virtual photon breaks the proton in many product particles  $X_i$ :  $e^- p \rightarrow e^- X_1 \dots X_n$ . Figure 8.6a depicts the full process, fig. 8.6b depicts its Equivalent Photon Approximation.

In general, EPA treats virtual photons as real. This means that the QFT requirement for EPA are:

- The transverse polarization contribution to the cross section is negligible.
- The photon is mainly on the mass shell.

Let the photon fourmomentum be  $q$  and let there be a cutoff  $\Lambda$  such that for all  $|q^2| < \Lambda^2$  the EPA is a good approximation.  $\Lambda$  is process dependent.

More specifically, let us follow Weizsäcker-Williams computation. Following fourmomenta naming as in fig. 8.6, the  $e^-p$  cross section is

$$d\sigma_{ep} = \frac{4\pi\alpha_{\text{EM}}}{4\Phi} (M^*)^\nu M^\mu \frac{\rho^{\mu\nu}}{(-q^2)} d\phi. \quad (8.24)$$

Let me explain what each element of eq. (8.24) mean:

- Final phase space

$$d\phi = d\Gamma \frac{d^3p'}{2E'(2\pi)^3} (2\pi)^4 \delta(p + P - p' - k). \quad (8.25)$$

- $M^\mu$  = virtual photo-absorption amplitude averaging over initial spin states and summing over the final ones.
- $\rho^{\mu\nu}$  = non normalized density matrix of the virtual photon produced by an  $e^-$ :

$$\begin{aligned} \rho^{\mu\nu} &= \frac{1}{2(-q^2)} \text{tr} \left[ (\not{p} + M_e) \gamma^\mu (\not{p}' + M_e) \gamma^\nu \right] \\ &= - \left( g^{\mu\nu} - \frac{q^\mu q^\nu}{q^2} \right) - \frac{(2p - q)^\mu (2p - q)^\nu}{q^2}. \end{aligned} \quad (8.26)$$

- $\Phi = \sqrt{(p \cdot P)^2 - p^2 P^2}$  = incoming flux.

The number of photons with a given polarization in a given element  $d^3p' = d^3q$  of the phase space volume is proportional to

$$\rho^{\mu\nu} \frac{d^3q}{q^2}. \quad (8.27)$$

From the optical theorem

$$W^{\mu\nu} = \frac{1}{2} \int M^{*\nu} M^\mu (2\pi)^4 \delta(q + P - k) d\Gamma \quad (8.28)$$

is the absorptive part of the  $\gamma p$ -forward amplitude. The integrated cross section becomes

$$\sigma_{ep} = \frac{\pi\alpha_{\text{EM}}}{\Phi(-q^2)} W^{\mu\nu} \rho^{\mu\nu} \frac{d^3q}{(2\pi)^3 E'}. \quad (8.29)$$

I now show how the product  $W^{\mu\nu} \rho^{\mu\nu}$  can be decomposed in a transverse and a scalar part. For gauge invariance

$$q^\mu W^{\mu\nu} = q^\nu W^{\mu\nu} = 0. \quad (8.30)$$

Plus, it can only be written in terms of  $g^{\mu\nu}$ ,  $q^\mu$ ,  $P^\mu$ , hence it has the form

$$W^{\mu\nu} = R^{\mu\nu} W_T(q^2, q \cdot P) + Q^\mu Q^\nu W_S(q^2, q \cdot P). \quad (8.31)$$

In writing eq. (8.31) we recurred to the photon polarizations properties.  $Q$  is a unit norm ( $Q^2 = 1$ ), orthogonal to  $q$  ( $q \cdot Q = 0$ ) fourmomentum defined as

$$Q := \frac{\sqrt{-q^2}}{\Phi} \left( P - q \frac{q \cdot P}{q^2} \right). \quad (8.32)$$

$R^{\mu\nu}$  is the transverse tensor of  $q, P$  in the following sense: given two fourmomenta  $q$  and  $p$  one can always define a transverse tensor  $R^{\mu\nu}(q, p)$  respecting the property

$$q^\mu R^{\mu\nu}(q, p) = p^\mu R^{\mu\nu}(q, p) = 0. \quad (8.33)$$

It then follows that

1.  $r_\perp^\mu := r^\mu R^{\mu\nu}(q, p)$  is such that  $r_\perp \cdot q = r_\perp \cdot p = 0$  for whatever  $r$
- 2.

$$r_\perp \cdot f_\perp = (R^{\mu\nu}(q, p)r^\nu) \cdot (R^{\mu\nu}(q, p)f^\nu) = -r^\mu R^{\mu\nu}(q, p)f^\nu = -f^\mu R^{\mu\nu}(q, p)r^\nu \quad (8.34)$$

In our case we choose  $R^{\mu\nu}(q, P)$ . It can be related to the virtual photon polarizations  $\varepsilon^\mu(a)$ ,  $a = 0, \pm 1$  with  $a = 0$  the scalar polarization and  $a = \pm 1$  the transverse ones. Assume the photon is colliding onto another particle of fourmomentum  $P$  and go to the  $(q, P)$  CoM frame, so that  $\vec{q} = -\vec{P}$ . Then

$$\varepsilon^0(\pm) = 0, \quad (8.35)$$

$$\vec{\varepsilon}(\pm) \cdot \vec{q} = \vec{\varepsilon}(\pm) \cdot \vec{P} = 0, \quad (8.36)$$

which means that they form a basis for a subspace orthogonal to the fourmomenta  $q$  and  $P$ . But then

$$\varepsilon^{*\mu}(+) \varepsilon^\nu(+) + \varepsilon^{*\mu}(-) \varepsilon^\nu(-) = R^{\mu\nu}(q, P). \quad (8.37)$$

Similarly,  $Q$  is proportional to  $\varepsilon(0)$ . This is why we say

$$W_{T(S)} = 2\Phi\sigma_{T(S)}, \quad (8.38)$$

with  $\sigma_{T(S)}$  the transverse (scalar) photon absorption cross section. Now the transverse part of eq. (8.29) is

$$\rho^{\mu\nu} R^{\mu\nu} =: 2\rho^{++} = \frac{(2p \cdot P - q \cdot P)^2}{\Phi^2} + 1 + \frac{4M_e^2}{q^2}; \quad (8.39)$$

the scalar part is

$$\rho^{\mu\nu} Q^\mu Q^\nu =: \rho^{00} = 2\rho^{++} - \frac{4M_e^2}{q^2} - 2. \quad (8.40)$$

In the small  $|q^2|$  limit

$$\lim_{q^2 \rightarrow 0} 2Q^\mu Q^\nu \Phi \sigma_S = \lim_{q^2 \rightarrow 0} \frac{-2\sigma_S |q \cdot P| q^\mu q^\nu}{q^2} \quad (8.41)$$

Since  $W^{\mu\nu}$  must be regular in  $q^2 \rightarrow 0$ , we must impose  $\sigma_S \sim q^2$  at least. If  $\sigma_T$  did not decrease with  $q^2 \rightarrow 0$  it would mean that  $\sigma_T$  is a good approximation of the whole cross section and the EPA is viable but this is not always the case. For the  $ep$  process the small  $|q^2|$  domain gives the main contribution to the cross section: onto  $|q^2| \ll \omega^2$ ,

$$2\rho^{++} = \frac{(2\mathcal{E} - \omega)^2}{\omega^2} + 1 + \frac{4M_e^2}{q^2}, \quad (8.42)$$

with

**Definition 23**  $(\omega, \mathcal{E})$ .

$$\omega := \frac{q \cdot P}{m_P}, \quad \mathcal{E} := \frac{p \cdot P}{m_P}. \quad (8.43)$$

□

As long as  $|q^2| \ll \omega^2, \Lambda^2$  holds, the EPA is viable, and we can trade the matrix element from fig. 8.6a with that from fig. 8.6b with a real photon times a probability density function:

$$\begin{aligned} d\sigma_{ep} &= \sigma_\gamma(\omega) dn(\omega, q^2), \\ dn &= \frac{\alpha}{2\pi\mathcal{E}^2} \rho^{++} \omega d\omega \frac{d(-q^2)}{|q^2|} = \frac{\alpha}{4\pi\mathcal{E}^2} \left[ \frac{(2\mathcal{E} - \omega)^2}{\omega^2 - q^2} + 1 + \frac{4M_e^2}{q^2} \right] \frac{\omega d\omega d(-q^2)}{|q^2|}. \end{aligned} \quad (8.44)$$

The accuracy of the approximation is  $\frac{|q^2|}{\Lambda^2}$ . We can finally integrate over  $q^2$

$$\begin{aligned} \int_{q_{\min}^2}^{q_{\max}^2} dn(\omega, q^2) &= N(\omega) d\omega / \omega, \\ N(\omega) &= \frac{\alpha}{\pi} \left[ \left( 1 - \frac{\omega}{\mathcal{E}} + \frac{\omega^2}{2\mathcal{E}^2} \right) \ln \frac{q_{\max}^2}{q_{\min}^2} - \left( 1 - \frac{\omega}{2\mathcal{E}} \right)^2 \ln \frac{\omega^2 + q_{\max}^2}{\omega^2 + q_{\min}^2} - \frac{M_e^2 \omega^2}{\mathcal{E}^2 q_{\min}^2} \left( 1 - \frac{q_{\min}^2}{q_{\max}^2} \right) \right], \end{aligned} \quad (8.45)$$

with

$$q_{\min}^2 = \frac{M_e^2 \omega^2}{\mathcal{E}(\mathcal{E} - \omega)} \left[ 1 + \mathcal{O} \left( \frac{M_e^2}{(\mathcal{E} - \omega)^2} \right) \right] \leq -q^2 \leq q_{\max}^2 \leq 4\mathcal{E}(\mathcal{E} - \omega). \quad (8.46)$$

$q_{\max}^2$  is either experimentally given or imposed by the cutoff  $\Lambda$ .

The last contribution to the EPA theory is [118]. Frixione et al. want to precisely characterize the  $q^2$  integration extrema. For this reason, once they get to the same point of eq. (8.44), they trade the final electron energy for

$$y := \frac{P \cdot q}{P \cdot p}, \quad (8.47)$$

which is the fraction of longitudinal fourmomentum that the photon is stripping away from the incoming  $e^-$ . Now  $q^2$  is expressed in terms of  $E'$  (final  $e^-$  energy)

and  $y$ . They define  $\theta$  as the final  $e^-$  deflection angle and, knowing that it is small in the EPA, they perform a series expansion of  $q^2$  with respect to it. In this way  $q^2$  is minimal onto  $\theta = 0$  and maximal onto the biggest allowed angle  $\theta = \theta_c$ , with  $\theta_c \ll 1$  called the critical angle. Finally they arrive to the probability density function of a photon from an electron

$$f_\gamma^{(e)}(y) = \frac{\alpha_{\text{em}}}{2\pi} \left\{ 2(1-y) \left[ \frac{M_e^2 y}{E^2(1-y)^2 \theta_c^2 + M_e^2 y^2} - \frac{1}{y} \right] + \frac{1 + (1-y)^2}{y} \log \frac{E^2(1-y)^2 \theta_c^2 + M_e^2 y^2}{M_e^2 y^2} + \mathcal{O} \left( \theta_c^2, \frac{M_e^2}{E^2} \right) \right\}. \quad (8.48)$$

with  $E$  the incoming electron energy.

## 8.5 SEPA, EPA in all scalar theory

In our fully scalar theory we can not directly use eq. (8.48) as it was recovered for a theory of fermions and vectors. We therefore proceed to compute our scalar EPA (SEPA).

### 8.5.1 SEPA from electron-proton collision

The aim of this section is recovering the probability density function of the photon inside the electron as much as was done for the SM. We will consider the mock process  $e^-(p_1)p(p_2) \rightarrow e^-(p_3)X(P)$ ,  $P = \sum_{i=1}^n p_{X_i}$ ,  $p$  being a parton inside the proton. We will write the full cross section integration and divide it in two factorizable parts, one in which the photon is produced from the electron and the other one in which the virtual photons interacts with the parton and produces the final particles  $X_i$ . The cross section is

$$\sigma_{ep} = \frac{1}{f} \int d\mu |\mathcal{M}|^2, \quad (8.49)$$

with  $f$  the scattering flux

$$f = 4|\vec{p}_{\text{in}}| \sqrt{s} \quad (8.50)$$

depending on the initial threemomentum in the CoM

$$p_1 = (E_1, \vec{p}_{\text{in}}), p_2 = (E_2, -\vec{p}_{\text{in}}). \quad (8.51)$$

$s$  is the CoM squared energy  $s := (p_1 + p_2)^2$ . The integration measure in eq. (8.49) is

$$d\mu = \frac{d^3 p_3}{(2\pi)^3 2E_3} \left( \prod_{i=1}^n \frac{d^3 p_{X_i}}{(2\pi)^3 2E_{X_i}} \right) (2\pi)^4 \delta^{(4)}(p_1 + p_2 - p_3 - P). \quad (8.52)$$

The matrix element in eq. (8.49) can be expressed as the product of two terms

$$|\mathcal{M}|^2 = |\mathcal{M}_{e\gamma}|^2 |\mathcal{M}_X|^2. \quad (8.53)$$

In our case both of the amplitudes only consist in couplings and propagators, in particular

$$|\mathcal{M}_{e\gamma}|^2 = \frac{|c_{e\gamma}|^2}{q^4}, q = p_1 - p_3. \quad (8.54)$$

We can express  $d\mu$  too in a factorised way. Let us use

$$\int_{\mathbb{R}^4} d^4P \delta^{(4)}\left(P - \sum_{i=1}^n p_{X_i}\right) = 1, \quad (8.55)$$

and rewrite  $d\mu$  as

$$d\mu = \frac{d^3p_3}{(2\pi)^3 2E_3} d^4P \delta^{(4)}\left(P - \sum_{i=1}^n p_{X_i}\right) \left(\prod_{i=1}^n \frac{d^3p_{x_i}}{(2\pi)^3 2E_{X_i}}\right) (2\pi)^4 \delta^{(4)}(p_1 + p_2 - p_3 - P) \quad (8.56)$$

We can integrate  $d^4P$  with  $\delta^{(4)}(p_1 + p_2 - p_3 - P)$ . Everywhere  $P$  is evaluated onto  $p_1 + p_2 - p_3$  so  $\delta^{(4)}\left(P - \sum_{i=1}^n p_{X_i}\right) \rightarrow \delta^{(4)}\left(p_1 + p_2 - p_3 - \sum_{i=1}^n p_{X_i}\right)$ . The latter may be integrated with whatever  $d^4p_{X_i}$ , without loss of generality  $d^4p_{X_1}$ , for example. With this eq. (8.49) becomes

$$\sigma_{ep} = \frac{1}{f} \int \frac{d^3p_3}{(2\pi)^3 2E_3} |\mathcal{M}_{e\gamma}|^2 \left(\prod_{i=2}^n \frac{d^3p_{x_i}}{(2\pi)^3 2E_{X_i}}\right) (2\pi) \delta\left((q + p_2 - \sum_{i=2}^n p_{X_i})^2 - m_{X_1}^2\right) |\mathcal{M}_X|^2. \quad (8.57)$$

Finally we can factorise the flux factor too like

$$f = f_0 f' \quad (8.58)$$

$$f' := \sqrt{(p_2 \cdot q) - p_2^2 q^2} = 2\sqrt{s} y_1 (E_2 + |\vec{p}_{\text{in}}|) \quad (8.59)$$

with  $f'$  the flux of the process  $\gamma p \rightarrow X$ ,  $\gamma$  being real.  $y_1$  is defined as in eq. (8.47). Finally the cross section is

$$\sigma_{ep} = \int \frac{1}{f_0} \frac{d^3p_3}{(2\pi)^3 2E_3} |\mathcal{M}_{e\gamma}|^2 \sigma_X, \quad (8.60)$$

with

$$\sigma_X := \frac{1}{f'} \int \left(\prod_{i=2}^n \frac{d^3p_{x_i}}{(2\pi)^3 2E_{X_i}}\right) (2\pi) \delta\left((q + p_2 - \sum_{i=2}^n p_{X_i})^2 - m_{X_1}^2\right) |\mathcal{M}_X|^2. \quad (8.61)$$

It describes the parton hadronizing into the  $\{X_i\}$  after the photon solicitation. We want to approximate  $\sigma_X$  by considering a real photon impinging onto the photon

along its same direction of motion, with opposite orientation. With all these constraints the incoming photon is completely described by its energy, i.e. by the  $y$  defined as in [118]. The explicit  $\delta$  integration was performed in order to clarify that before making the said approximations  $\sigma_X$  depends on all the 4 components of  $q$ , even with the simplest possible matrix element (SSM) as that comes from kinematics; differently stated, there is no theory such that the Equivalent Photon Approximation cease to be an approximation and becomes exact. By imposing in  $\sigma_X$  that  $q^2 = 0, \theta_{e^-} = 0$  we are making mistakes of order  $\theta_{e^-}$  and order  $q^2$ .

In eq. (8.60) The part  $\frac{1}{f_0} \frac{d^3 p_3}{(2\pi)^3 2E_3} |\mathcal{M}_{e\gamma}|^2$  is going to be treated at the same way as [118] and provide the pdf of a photon with energy fraction  $y$  inside an electron. Finally:

$$f_{\text{SEPA}}(y) = \frac{y}{16\pi^2} \left( \frac{1}{q_{\min}^2} - \frac{1}{q_{\max}^2} \right) \quad (8.62)$$

In our VBF we would like to perform the EPA on both of the virtual photons. One may doubt that this can be done by simply multiplying two photons pdfs and [113] actually warns us from the dangers of simply composing EPAs via multiplication. In fact this is viable if the transverse part of the density matrix of one virtual photon  $\rho_1^{++}$  depends only mildly on the other photon fourmomentum. Nonetheless, although I omit here the computation, I could verify that if one performs the steps we just performed for eq. (8.62) onto a generic  $e^+e^- \rightarrow e^+e^- \{X_i\}_{i=1}^n$ , one finds that SEPAs do compose via multiplication:

$$f_{\text{SEPA}^2}(y_1, y_2) = f_{\text{SEPA}}(y_1) f_{\text{SEPA}}(y_2). \quad (8.63)$$

### 8.5.2 SEPA: results

Let's compute the total cross section and the distribution with respect to the ALP momentum in the equivalent photon approximation.

#### Total cross section with double SEPA

The  $\gamma\gamma \rightarrow a$  matrix element is a constant, then the Lorentz invariant integration with respect to the ALP three-momentum simply integrates away the  $\delta$  function of the fourmomentum conservation. We are left with two integrations in  $y_{1,2} \in [0, 1]$  and the Dirac  $\delta$

$$\delta((q_1 + q_2)^2 - M_a^2) = \delta(2q_1 \cdot q_2 - M_a^2) = \delta(sy_1y_2 - M_a^2). \quad (8.64)$$

Equation (8.64) is symmetric under  $y_1 \leftrightarrow y_2$ , so the integration orders is irrelevant. Let's choose  $y_2$ . Integrating  $\delta(sy_1y_2 - M_a^2)$  with  $y_2$  gives a jacobian  $\frac{1}{y_1 s}$ , implies that everywhere  $y_2$  needs to be substituted with  $\frac{M_a^2}{sy_1}$  and constraints the remaining  $y_1$  in  $\left[ \frac{M_a^2}{s}, 1 \right]$ . In formulas

$$\begin{aligned}
\sigma_{\text{SEPA}} &= \frac{|c_{ee\gamma}|^4 |c_{\gamma\gamma a}|}{16\pi s} \int dy_1 dy_2 \left[ \frac{1}{q_{\min}(y_1)^2} - \frac{1}{q_{\max}(y_1)^2} \right] \left[ \frac{1}{q_{\min}(y_2)^2} - \frac{1}{q_{\max}(y_2)^2} \right] \delta(sy_1y_2 - M_a^2) \\
&=: \frac{|c_{ee\gamma}|^4 |c_{\gamma\gamma a}|}{16\pi s} \int_{\frac{M_a^2}{s}}^1 dy_1 \omega(y_1),
\end{aligned} \tag{8.65}$$

where

$$\omega(y_1) := \frac{s(1-y_1)^3 (sy_1 - M_a^2)^3 \theta_c^4}{(4M_e M_a)^4 \pi^3 y_1^2 ((2M_e y_1)^2 + [\theta_c \sqrt{s}(1-y_1)]^2) ((2M_e M_a)^2 + [\theta_c \sqrt{s}(1-y_1)]^2)}. \tag{8.66}$$

In eq. (8.66) we used the critical angle as defined in [118], i.e. the aperture of the cone in which the moving  $e^-$  can emit photons that can undergo an EPA within the given precision.  $\omega(y)$  can be analytically integrated but produces a long equation that we abstain from copying here. In all the following plots we will be using the full form but, to give an idea of the functional form of  $\sigma_{\text{SEPA}}$ , we provide the first non 0 term of its expansion in  $M_e$ :

$$\sigma_{\text{SEPA}} = |c_{\gamma\gamma a}|^2 |c_{ee\gamma}|^4 \frac{-M_a^4 + s^2 + 2M_a^2 s \log\left(\frac{M_a^2}{s}\right)}{4(2\pi)^3 (2M_a M_e)^4 s} + \mathcal{O}(M_e^{-3}). \tag{8.67}$$

Notice how eq. (8.67) is proportional to  $M_e^{-4}$  because  $q_{\min}^2$  is proportional to  $M_e^2$  (see eq. (8.46)), therefore the cross section in the Scalar Equivalent Photon Approximation would diverge in the limit  $M_e \rightarrow 0$ .

Even if the integrated cross section is well behaved along all the allowed domain to the ALP mass, not everywhere the conditions to use the EPA are met. From fig. 8.7 we see that the integrand  $\omega(y)$  vanishes at both ends of its domain, which shrinks and shifts to the right as  $M_a$  increases.  $\omega(y)$  grows if  $\frac{M_a^2}{s} \leq y < y_{\text{peak}}$ , attains its maximum at  $y_{\text{peak}}$  and decreases if  $y_{\text{peak}} < y \leq 1$ .  $y_{\text{peak}}$  is difficult to find analytically but can be approximated as the point  $y_{\text{peak}}^0$  such that the first non 0 order in the  $M_e$  expansion of  $\omega$  has null derivative:

$$y_{\text{peak}}^0 = \frac{2M_a^2}{M_a^2 + s}. \tag{8.68}$$

See how this result is independent on  $\theta_c$  and  $M_e$ . The same reasoning can be repeated by substituting  $y$  with its linearization

$$y = z \left( 1 - \frac{M_a^2}{s} \right) + \frac{M_a^2}{s}, \quad z \in [0, 1]. \tag{8.69}$$

With the same technique, the peak will be attained at  $z_{\text{peak}}^0 = \frac{M_a^2}{M_a^2 + s}$  which tends to  $\sim \frac{1}{2}$  as  $M_a$  goes to its maximum. This means that the peak tends to be in the

middle of the domain, i.e. that  $\omega$  goes more and more symmetric around  $z = \frac{1}{2}$ . This can also be seen if  $\omega(z)$  is expanded around big  $M_a$  and small  $M_e$  and  $\theta$ :

$$\omega \sim \frac{3\theta^4(\sqrt{s} - 2M_e - M_a)}{4M_e^3\pi^3s^3}(1-z)^3z^3, \quad (8.70)$$

which is symmetric around  $z = \frac{1}{2}$ . This behaviour may be used to determine at what ALP mass it will be preferable not to use the EPA. We know that the final electron must be ultrarelativistic, then the distribution of its energy fraction is the same as that of the photon but flipped around the vertical axis  $y = \frac{1}{2}$ . This means that we expect the  $e^-$  distribution to be peaked around 1 and the photon distribution to peak around 0.

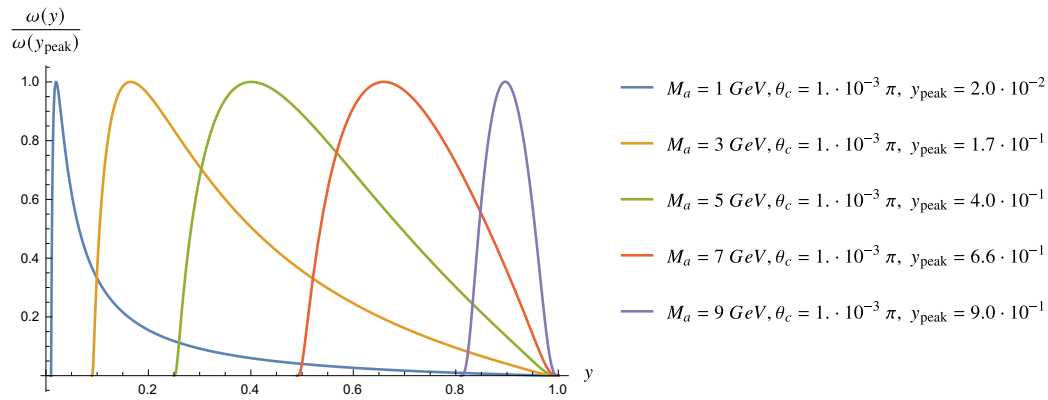


**Figure 8.7.** SEPA photon from an electron probability density function  $\omega(y)$  (eq. (8.66)) normalized by its value at its peak  $y_{\text{peak}} \sim \frac{2M_a^2}{M_a^2 + s} : \frac{\omega(y)}{\omega\left(\frac{2M_a^2}{M_a^2 + s}\right)}$ .

### Cross section distribution of ALP three-momentum magnitude with double SEPA

When both the virtual photons of the process are approximated to be real and along the beam line, the photons fourmomenta are

$$q_{1,2} = q_{1,2}^0(1, 0, 0, \pm 1) = y_{1,2} \frac{\sqrt{s}}{2}(1, 0, 0, \pm 1), \quad (8.71)$$

and the ALP fourmomentum is

$$p_a = q_1 + q_2 = \frac{\sqrt{s}}{2}(y_1 + y_2, 0, 0, y_1 - y_2) =: \frac{\sqrt{s}}{2}(\Sigma, 0, 0, \tau), \quad (8.72)$$

with

$$\Sigma := y_1 + y_2 \in [0, 2], \quad (8.73)$$

$$\tau := y_1 - y_2 \in [-1, 1]. \quad (8.74)$$

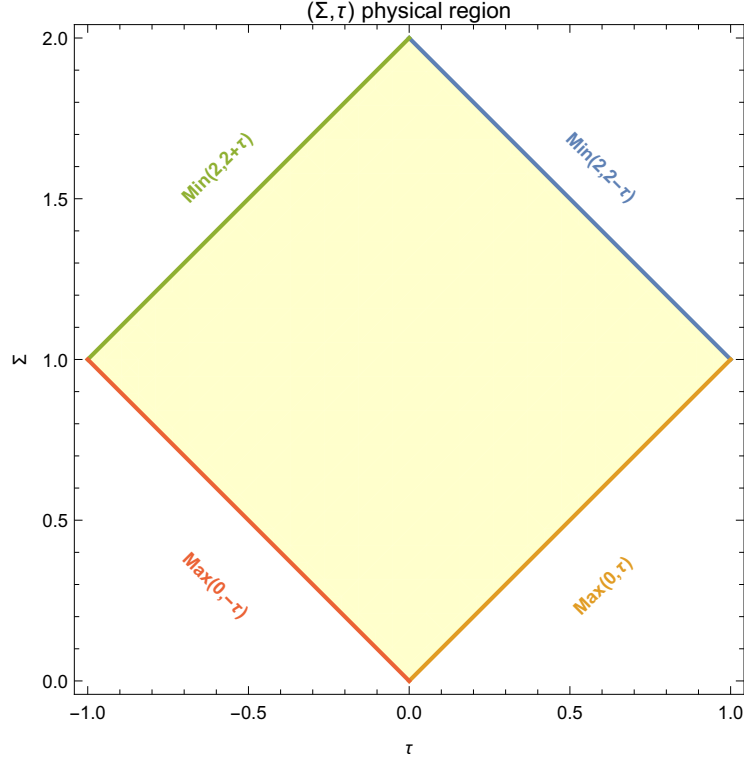


**Figure 8.8.** The yellow area represents the region allowed to  $\Sigma$  (eq. (8.73)) and  $\tau$  (eq. (8.74)), the coloured, solid lines represent the region boundary as from eq. (8.75).

The  $(\Sigma, \tau)$  domain can be further specified to

$$\begin{aligned} \max(0, -\tau) < \Sigma < \min(2, 2 - \tau), \\ \max(0, \tau) < \Sigma < \min(2, 2 + \tau), \end{aligned} \quad (8.75)$$

where the former comes from  $\Sigma = 2y_1 - \tau$  and the latter from  $\Sigma = 2y_2 + \tau$ . We depict it in fig. 8.8.

The Dirac  $\delta$  in eq. (8.64) now reads  $\delta\left(\frac{s(\tau^2 - \Sigma^2)}{4} - M_a^2\right)$ , which is solved to

$$\Sigma = \sqrt{\tau^2 + \frac{4M_a^2}{s}}, \quad \frac{M_a^2 - s}{s} \leq \tau \leq \frac{s - M_a^2}{s}. \quad (8.76)$$

We can now derive  $\frac{d\sigma_{\text{SEPA}}}{d\tau}$ , so to discover the preferred values of the ALP threemomentum. Same as before, we only show the  $M_e$  expansion

$$\begin{aligned} \frac{d\sigma_{\text{SEPA}}}{d\tau} = \frac{(-r + M_a^2 + s)^3}{256\pi^3 M_a^4 M_e^4 r} \cdot \\ \cdot \frac{1}{(-2sr + M_a^2(6s - 2r) + M_a^4 + s^2(\tau^2 + 1))} + \mathcal{O}(M_e^{-3}), \end{aligned} \quad (8.77)$$

where

$$r := \sqrt{s(4M_a^2 + s\tau^2)}. \quad (8.78)$$

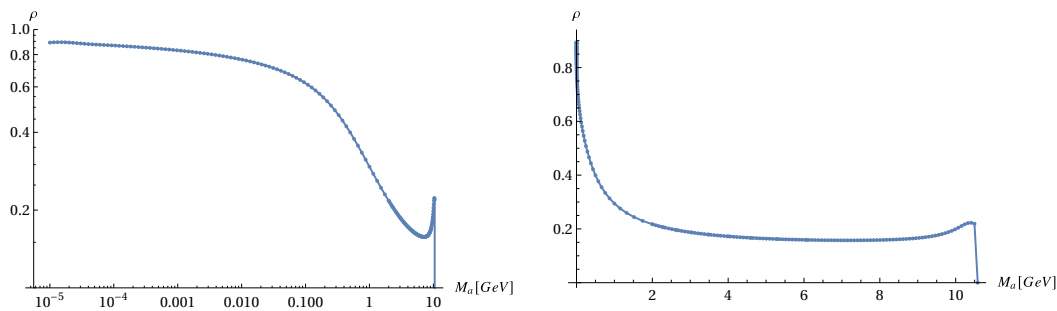


**Figure 8.9.** Log-log plot (left panel) and linear plot (right panel) of  $\rho(0.1)$  as from eq. (8.79). The fact that  $\rho \sim 1$  at small  $M_a$  demonstrates the VBF preference for the production of the pseudoscalar at rest.

Equation (8.77) is plotted in fig. 8.10: it is symmetric around its peaks at  $\tau = 0$  ( $\tau$  only appears squared in the distribution.). This means that regardless from  $M_a$ , the preferred kinematic configuration has the pseudoscalar at rest. What does change with the mass  $M_a$  is the overall magnitude: fig. 8.10a clearly shows the rapid shrinking in size when  $M_a$  increases. We can effectively compare different  $M_a$  distributions by getting rid of these magnitude effects and rescaling the distribution such that it evaluates to 1 at  $\tau = 0$ , as in fig. 8.10b. In the latter we notice that  $\frac{d\sigma_{\text{SEPA}}}{d\tau} \xrightarrow{|\tau| \rightarrow 1} 0$  either because the distribution decreases around  $|\tau| \sim 1$  or because the given  $M_a$  does not allow for  $|\tau| \sim 1$  as from eq. (8.76).

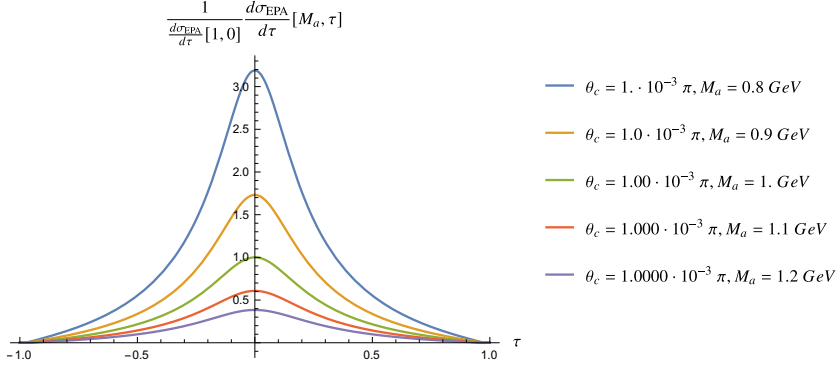
To better quantify how important the resting ALP configuration is, we define the ratio

$$\rho(x) := \frac{1}{\sigma_{\text{SEPA}}} \int_{-x\tau_0}^{x\tau_0} d\tau \frac{d\sigma_{\text{SEPA}}}{d\tau}, \quad (8.79)$$

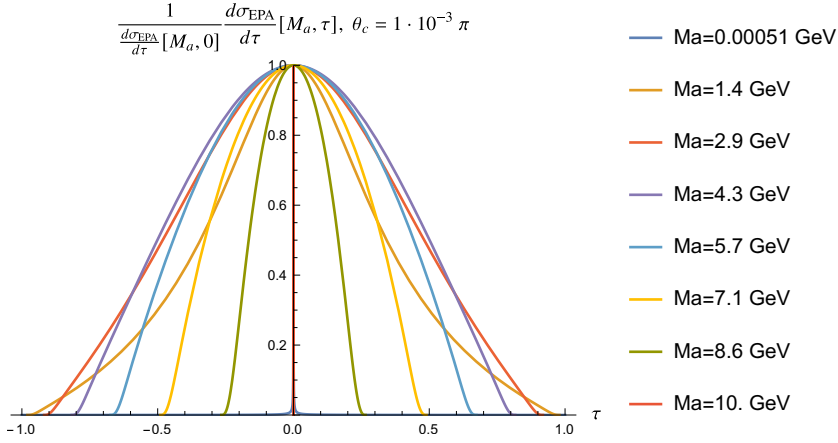
where  $\tau_0 = \frac{s-M_a^2}{s}$ ,  $x \in [0, 1]$  and plot  $\rho\left(\frac{1}{10}\right)$  in fig. 8.9. We see that at small  $M_a$  the ratio is close to 1, steadily decreases down to  $\rho \sim 0.2$  at intermediate masses, and stays constant up to  $M_a \sim 10$  GeV, where the ALP comes back to being almost at rest due to the Phase Space closure. Nonetheless, since the distribution is also flatter at larger  $M_a$ ,  $\rho(0.1)$  does not reach back to  $\sim 1$ .

## 8.6 Comparison of SSM VS SEPA cross section

Finally I provide a comparison between the integrated and approximated cross sections: figs. 8.11 and 8.12 show that, depending on the critical angle that the theory allows you, there can be a very good agreement among  $\sigma_{\text{SEPA}}$  and  $\sigma_{\text{SSM}}$  up to very high ALP masses. The bigger the  $\theta_c$  the greater the agreement with the SSM theory looks, nonetheless the approximation error increases.



(a) Here the normalization  $\mathcal{N} = \frac{d\sigma_{\text{SEPA}}}{d\tau}(M_a = 1 \text{ GeV}, \tau = 0)$ .



(b) Here the normalization  $\mathcal{N} = \frac{d\sigma_{\text{SEPA}}}{d\tau}(M_a, \tau = 0)$ .

**Figure 8.10.** Plots of normalized SEPA cross section distribution with respect to the ALP threemomentum magnitude  $(\mathcal{N}^{-1}) \frac{d\sigma_{\text{SEPA}}}{d\tau}$ . From the text,  $2|\vec{p}_a| = \sqrt{s}(y_1 - y_2)$ . We chose the critical angle in eq. (8.48) to always be  $\theta_c = 10^{-3}\pi$ .

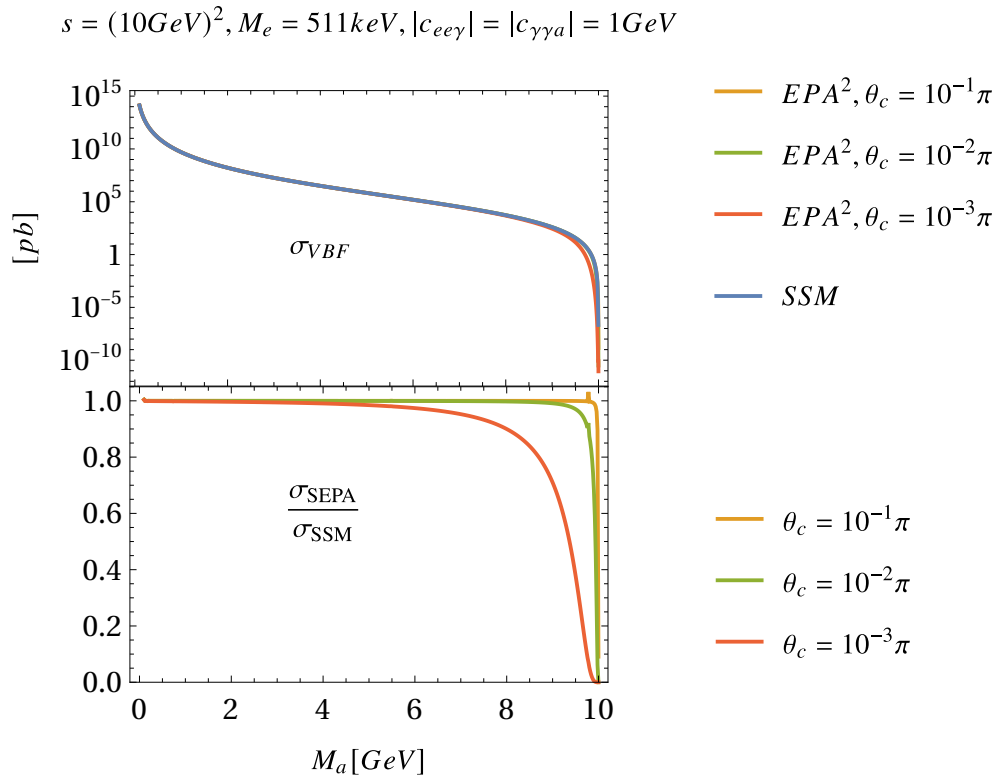


**Figure 8.11.** The top panel shows the VBF cross section in the SSM theory and with the Equivalent Photon Approximation used onto both photons of the VBF ( $EPA^2$ ). The bottom panel show the ratio between the double EPA and the SSM cross sections. In both panels we show different critical angles  $\theta_c$ .

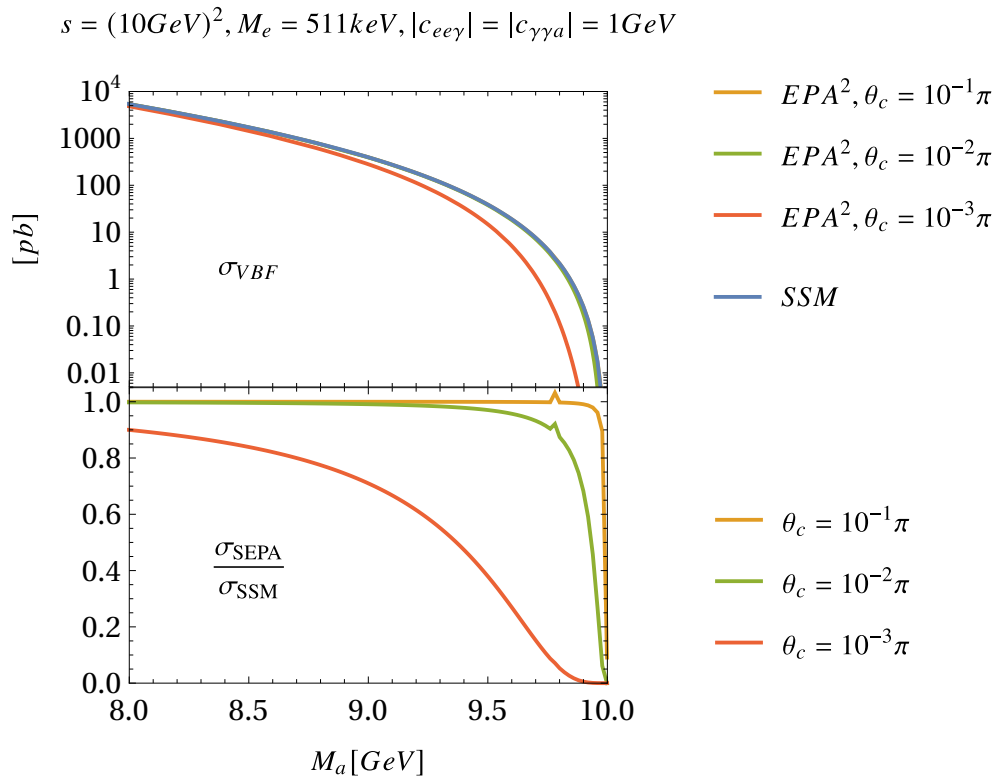


**Figure 8.12.** Zoom of fig. 8.11 that shows how larger  $M_a$  masses produce a worse EPA-SSM agreement.

Part II  
Phenomenology



The first part of this dissertation was devoted to some theoretical consideration on scattering processes. Every time we could, we tried to make as universal statements as possible, so that many generic results could be recovered. Nonetheless, we were always guided by our final purpose, that of characterising a specific  $2 \rightarrow 3$  scattering:  $e^+e^- \rightarrow e^+e^-a$ . This is the time to phenomenologically address it.

First of all, we choose Belle II as our reference collider, therefore in section 9.1 we provide in a simplistic fashion all the experiment features that serve our aim. Let me underline that all of the results that you will see do not depend on the collider we chose and can be easily transposed to other accelerators.

In chapter 9 we summarise some useful results from the literature. In chapter 1 we only suggested that the picture on ALP production [72] was not complete as the VBF was neglected. All of the following sections build up to prove that the VBF can be phenomenologically relevant. In chapter 10, but even more beautifully and strikingly in chapter 11, we show it in a phenomenological way too.



## Chapter 9

# ALP @ Belle II state of the art

### 9.1 Basics of Belle II

To simulate events at Belle II we need to know details of the collider and detector. Our principal guides will be the Physics Book [119] for some B-Physics theoretical aspects and the Technical Design Report [120] for details on the facilities.

SuperKEKB is the upgrade of KEKB and is a 3 km circumference asymmetric electron-positron collider. It is located at the High Energy Accelerator Research Organisation in Tsukuba, Japan. The beam energies were chosen such that in the collisions mainly B-mesons were produced (it is a B factory). The detector Belle could then confirm the effect of CP-violation as described by the theory of Kobayashi and Maskawa. While the LHC experiments provide a direct probe of the TeV mass scale, SuperKEKB and Belle II are devoted to high-precision measurements of rare decays and CP-violation in heavy quarks and leptons, so to provide a unique probe of New Physics at these and even higher mass scales through the effects of new particles in higher order processes. The collider high luminosity is reached thanks to the fact that the beams interact with a large crossing-angle and at the interaction point they are squeezed to nanometre-scale. It is planned to collect a  $50 \text{ ab}^{-1}$  integrated luminosity.

In the following sections we will always identify the beam pipe with the  $z$  axis, and orient it like the incoming  $e^-$ . The initial state electron has an energy of 7 GeV, the positron travels along the negative  $z$  direction with a 4 GeV energy. In total,  $\sqrt{s} = 10.583 \text{ GeV}$ , close to the  $\Upsilon(4S)$  resonance. The choice is strategic to record many boosted  $\Upsilon(4S) \rightarrow B^0 \bar{B}^0$  decays, the boost being fundamental for time-dependent CP asymmetry measurement (but irrelevant for our purposes).

For our work we are particularly interested in Belle II Electromagnetic Calorimeter (ECL). It is made of CsI crystal cells that have the shape of a truncated pyramid. Their smallest base faces the beam pipe. This face is squared and has an area of  $6 \times 6 \text{ cm}^2$ . The cell height is  $16.2 X_0$ ,  $X_0$  being the material radiation length, i.e. the mean distance over which a high-energy electron loses all but  $\frac{1}{e}$  of its energy by bremsstrahlung. The ECL is non uniform as there are some blind spots, but we will neglect them. It has a polar angle acceptance  $\theta \in [17^\circ, 150^\circ]$  in the laboratory system. For future reference

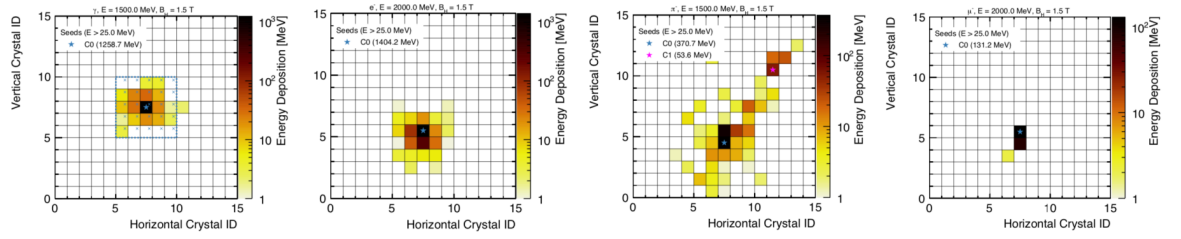


**Figure 9.1.** From left to right, impression on the ECL of a photon, an electron, a  $\pi^-$ , a muon. Picture from [122]

### 9.1.1

#### Belle II polar aperture

We define the CoM Belle II polar aperture as  $[\alpha_1, \alpha_2] = [22^\circ, 158^\circ]$ .

The crystals are triggered if the photon energy is  $E_\gamma^* > 0.25$  GeV in the CoM. Both for the visible and invisible search the detectability of electrons and photons will be crucial, so let us define

### 9.1.2

#### Visible photon or electron

A visible photon or electron has polar angle  $\theta \in [17^\circ, 150^\circ]$  and CoM energy  $E^* > 0.25$  GeV.

### 9.1.3

#### Invisible photon or electron

An invisible photon or electron has either  $\theta \notin [17^\circ, 150^\circ]$  or CoM energy  $E^* < 0.25$  GeV or both.

The ECL is used to detect neutral particles. The latter impresses some ECL cells, leaving its fingerprint on the detector. Typically, a photon excites more intensely the cell on which it impinges and less the surrounding ones; the electromagnetic shower can be enclosed in a square of 5 cells side. This signal is processed to recover precisely the position of the particle by the means of Zernike moments [121], see fig. 9.1.

Lastly, we need an estimate of the ECL energy resolution. The energy dependence of the energy resolution may be parameterized as the quadratic sum of three terms [123]:

$$\frac{\sigma_E}{E} = \sqrt{\left(\frac{a}{E^{1/4}}\right)^2 + \left(\frac{b}{E}\right)^2 + c^2}. \quad (9.1)$$

The first term, with coefficient  $a$ , is the "stochastic term", arising from fluctuations in the number of signal generating processes (together with possible additional effects such as fluctuations in the measurement of that signal). The second term, with coefficient  $b$ , is usually referred to as the noise term. It receives contributions from noise in the readout electronics and from effects such as "pile-up" (simultaneous energy deposition by uncorrelated particles). The third term is the "constant term" with coefficient  $c$ . It arises from several effects like, imperfections in calorimeter

construction, non-uniformities in signal collection, calibration errors, etc. As from [124], at Belle II

$$\frac{\sigma_E}{E} = \sqrt{\left(\frac{0.066\%}{E}\right)^2 + \left(\frac{0.81\%}{\sqrt[4]{E}}\right)^2 + (1.34\%)^2}. \quad (9.2)$$

We will assume that the error on invariant masses is the same as that on energies, neglecting the angular resolution, that we assume to be far smaller.

## 9.2 ALP-strahlung

The state of the art on ALP at Belle II is mainly due to [72]. They assume that the most important channel to see the ALP is

$$e^+e^- \rightarrow \gamma a, \quad (9.3)$$

and consider both the case in which the ALP decays in two resolvable and detectable photons,  $a \rightarrow \gamma\gamma$ , and the case in which the ALP goes undetected, for example because it had a branching ratio 1 for decaying to DM,  $\text{BR}(a \rightarrow \chi\chi)=1$ . From now on we will be calling the former case the *visible process* and the latter the *invisible one*.

Our first step was reproducing Dolan et al. visible reach. Our principal tools have been MG5\_aMC@NLO [125] and python. MG5\_aMC@NLO is a MC generator of collider events. To simulate the signal we needed to communicate the BSM lagrangian eq. (1.26) to MG5\_aMC@NLO. We wrote the ALP model in Mathematica via FeynRules [126] and produced a UFO, Universal FeynRules Output [127]. The UFO is loaded in MG5\_aMC@NLO and the visible signal

$$e^+e^- \rightarrow \gamma a, a \rightarrow \gamma\gamma \quad (9.4)$$

is simulated (see fig. 9.2). For the background (see fig. 9.3) it is sufficient to work within the SM and generate

$$e^+e^- \rightarrow 3\gamma. \quad (9.5)$$

In both cases we instruct the MC to exclude the Z boson, so to speed up the computation while discarding many irrelevant channels. Once signal and background events are produced, we analyse them with python and impose the selections that maximise the sensitivity of Belle II to ALPs.

The aim of this kind of BSM searches is computing for each  $M_a \in [0, \sqrt{s}]$  what coupling ALPs and photons  $g_{a\gamma\gamma}$  should have so that the existence of such a pseudoscalar would be excluded at a 95% CL. Differently stated, we are asking how small should  $g_{a\gamma\gamma}$  be to be hidden at Belle II in the  $2\sigma$  uncertainty of  $e^+e^- \rightarrow 3\gamma$ . This must not necessarily be true for the full phase space Belle II can probe, but we can identify some phase space regions in which we expect a small SM rate and a big BSM one. This is enforced by applying some event selections on signal and background that, ideally, suppress very few signal events while discarding most of the background. For this ALP search, for example, we can select events living in a very narrow  $M_a$  bin. In fact, despite the pseudoscalar being virtual, its width

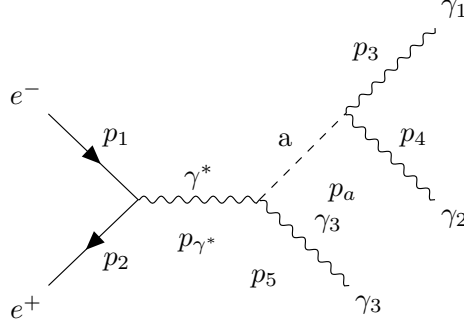


**Figure 9.2.** Feynman diagram of the BSM process  $e^+e^- \rightarrow 3\gamma$  including one intermediate ALP.

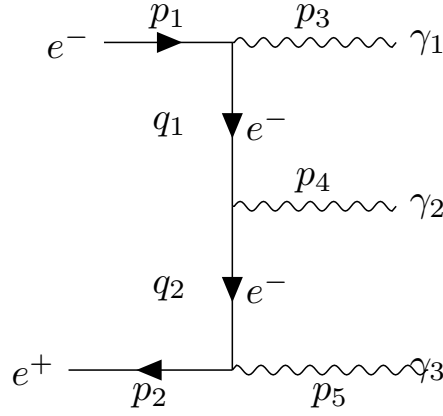


**Figure 9.3.** Feynman diagram of the SM process  $e^+e^- \rightarrow 3\gamma$ .

$$\Gamma_a = \frac{g_{a\gamma\gamma}^2 M_a^3}{64\pi} \quad (9.6)$$

is so small that within a small window we can contain most of the signal and discard a large background portion. For example, with  $g_{a\gamma\gamma} = 10^{-4} \text{ GeV}^{-1}$ ,  $M_a = 100 \text{ MeV}$ ,  $\Gamma_a = 50 \mu\text{eV}$ . We anticipate that, following [72], we will select an asymmetric window  $[-3\sigma_m, 1.5\sigma_m]$  around  $M_a$ , where  $\sigma_m$  is the energy resolution in eq. (9.2).

Another peculiarity of the ALP-strahlung is that it is a  $2 \rightarrow 2$  scattering,  $e^+e^- \rightarrow a\gamma$ , chained to an ALP decay into photons. This means that both the ALP and the photon with which it recoils have fixed energy once one assumes that the ALP is not far from its resonance

$$E_{\text{recoil}} = \frac{s - M_a^2}{2\sqrt{s}}. \quad (9.7)$$

Then we may carve a small window around some target recoil energy to identify some specific ALP mass. For this reason we say that we look into a signal bin.

Another quantity that [72] propose for an effective selection is based on helicity angles. We explain their use and definition in next section.

### 9.2.1 Helicity angles

My favourite review on why and how to use helicity angles is [128]. For our purposes it is sufficient to know that they are useful when in a generic process there are intermediate resonances. For example

#### Helicity angles

Let us elect the initial fourmomentum  $p_0$  as reference for the  $z$  axis. Consider a generic process with an intermediate resonances  $R$  decaying in two particles  $A$  and  $B$ :

$$R(p_R) \rightarrow A(p_A) + B(p_B). \quad (9.8)$$

In  $R$  rest frame we name fourmomenta  $p_i^R$ . Also define versors like threemomenta divided by their norm

$$\hat{q} := \frac{\vec{q}}{\|q\|}. \quad (9.9)$$

The cosine of the helicity polar angle of  $A$  is

$$\cos \theta_A = \hat{p}_0^R \cdot \hat{p}_A^R. \quad (9.10)$$

As long as you can distinguish the resonance decay products you know which helicity angle to compute. Instead, in the  $e^+e^- \rightarrow 3\gamma$  process we have the problem of recognising which photons come from the ALP and which one recoils with it in the  $2 \rightarrow 2$  scattering. Reference [72] finds that the best strategy changes as the ALP mass changes.

When  $M_a$  is low the suggested algorithm is:

1. Consider all the possible couples of final photons.
2. On each couple compute the invariant mass.
3. Name  $\gamma_1$  and  $\gamma_2$  the photons making the smallest invariant mass  $m_{\text{LOW}}$ . You assume  $\gamma_3$  is the recoiling photon.
4. Go to the rest frame of the  $(\gamma_1, \gamma_2)$  pair. If they are the ALP decay products, it is equivalent to take the ALP at rest. Compute the modulus of the cosine of the helicity angle of  $\gamma_1$ .

$$h_1 := |\cos \theta_1^{\text{ALP}}|. \quad (9.11)$$

Using  $\gamma_2$  provides the same result (as it is back to back with respect to  $\gamma_1$  in the ALP rest frame).

5. Select events with

$$0 \leq h_1 \leq 0.6 \wedge m_{12} \in M_a + \sigma_m[-3, +1.5]. \quad (9.12)$$

where for  $\sigma_m$  we use eq. (9.2).

When  $M_a$  is high the suggested algorithm is

1. Name the photons  $A, B, C$ .
2. Consider all the possible couples of final photons.
3. For the  $(A, B)$  couple, go to its rest frame and compute

$$h_A^{(A,B)} := |\cos \theta_A^{(A,B)}| \quad (9.13)$$

4. Repeat for the couple  $(A, C)$  and  $(B, C)$ . You should have collected  $(h_A^{(A,B)}, h_A^{(A,C)}, h_B^{(B,C)})$  (or any other equivalent trio).
5. Suppose  $h_A^{(A,B)}$  is the smallest. This makes us assume that  $A$  and  $B$  come from the ALP and  $C$  is the recoil.
6. Select events with

$$0 \leq h_A^{(A,B)} \leq 0.9 \wedge E(\gamma_C) \in \frac{s - M_a^2}{2\sqrt{s}} + \sigma_E[-3, +1.5]. \quad (9.14)$$

where for  $\sigma_E$  we use eq. (9.2).

### 9.3 MG5\_aMC@NLO generation

The signal and background simulation deserves some attention as there may be some subtleties. You want to make sure to implement all the kinematic cuts in order to reproduce the detector the best that we can. So we enforce the ECL polar angle acceptance  $\theta \in [17^\circ, 150^\circ]$  in MG5\_aMC@NLO run card with the constraint  $\eta_\gamma \in [-1.317, 1.901]$ . Notice that by default our simulator would apply symmetric cuts. The asymmetry can be obtained by the manipulation of the fortran code in the "cuts.f" file: the check on the rapidity should not be done on its absolute value but on  $\eta$  itself.

We ask for an IR cutoff on both visible photons and leptons  $E^* \geq 0.25$  GeV, which is straightforward as the simulator takes energies in the CoM frame by default.

It is necessary to ask for an angular separation among photons in order to resolve them. This deserves a little clarification.

### 9.3.1 Resolving photons

Photons must respect a minimal angular separation otherwise the particle identification algorithm will not be able to tell them apart. At this level we are not able to implement the full reconstruction that is operated at Belle II. A conservative approximation is asking that two photons are separated by a given number of cells. To reproduce the reach from [72], if we had to follow their explanation verbatim we should ask for two photons being  $n$  cells apart in the polar *and* azimuthal direction. The azimuthal dimension of every ECL cell is the same along all the barrel height and amounts to 48 mrad. Along the equatorial line whose centre is the interaction point, the polar dimension too amounts to 48 mrad. However the further we go along the  $z$  direction the smaller the polar dimension of the cell appears. The most conservative way to proceed is asking everywhere for a 48 mrad separation in both the azimuthal and the polar direction even if in a cylindrical barrel this implies asking for more and more cells to separate photons the further away we look from the interaction point. Alternatively we may think that we are dealing with a spherical detector.

Let us remark that what we would expect for a detector sensitivity is for a cluster of cells becoming blind around the ones impinged by the incoming particle. The quality of the detector determines the shape and the extension of the cluster. Schematically we may pick a circle with  $n$  cells radius. We would translate this by saying that there is an  $n$  cells distance the polar *or* azimuthal direction. We refer to this requirement as the *or cut*. Asking instead for an  $n$  cells distance the polar *and* azimuthal direction (*and cut*) implies that we should discard a whole band of equatorial cells around the impinged equator (as they may satisfy the azimuthal but not the polar requirement) and a whole band of meridian cells around the impinged meridian (as they may satisfy the polar but not the azimuthal requirement).

The *or cut* is enforced by simply asking MG5\_aMC@NLO  $\Delta R_{\gamma\gamma} > 0.048$ , where in general:

#### Pseudorapidity and Angular separation

A particle  $A$  of fourmomentum  $p_A$  has a longitudinal momentum  $p_A^L$  along a given direction  $\hat{z}$ . The pseudorapidity of  $A$  is

$$\eta(p_A) := \frac{1}{2} \log \frac{|\vec{p}_A| + |p_A^L|}{|\vec{p}_A| - |p_A^L|}. \quad (9.15)$$

Given two particles  $A$  and  $B$ , their angular separation is

$$\Delta R_{AB} = \sqrt{(\eta_A - \eta_B)^2 + (\phi_A - \phi_B)^2}, \quad (9.16)$$

with  $\phi_{A,B}$  the azimuthal angles of  $p_{A,B}$ .

For the *and cut* we need to add to the file "kin\_funcs.f" a function that calculates  $d\phi, d\theta$  and to the file "cuts.f" a check on them. Alternatively one can exclude the events not respecting the angular separation requirement at the analysis level (at the cost of losing some events). In what follows we chose to limit  $\Delta R_{\gamma\gamma}$  from below

in the run card.

One should also note that a photon impressing more than one cell gives more information and can be reconstructed with an angular resolution possibly smaller than the cell size of 48 mrad in each direction. Indeed in the final plots we use angular resolutions of 24, 48 and 96 mrad (1,2,4 cells of 24 mrad) to display the effect of changing experimental resolution.

### 9.3.2 The dataset

Signal runs are repeated over different ALP masses. Each run counts  $10^4$  events. We use  $c_{B,W} = 1$ ,  $f_a = 10^4$  GeV, from which follow  $g_{a\gamma\gamma} = 10^{-4}\text{GeV}^{-1}$ ,  $g_{aZ\gamma} = 0$ , see eq. (1.27).

The background is made of 3 groups of unweighted runs, meaning that in each run all the events have the same weight, i.e. if in the run the computed cross section is  $\sigma$  and there are  $N$  events, each event has weight  $\frac{\sigma}{N}$ . Each group of runs spans the full phase space as follows:

- One group made by a single run counting  $10^5$  events.
- Two other groups in which each run has a bounded  $m_{\text{LOW}}$ , the smallest invariant mass of the three photons pairs invariant masses:
  - One group made of 2 runs that span respectively  $m_{\text{LOW}} \in [0.1 - 3\sigma_m, 1]$  GeV =  $[9.4 \cdot 10^{-2}, 1]$  GeV and  $m_{\text{LOW}} > 1$  GeV. Each of these runs counts  $10^4$  events.
  - One group made of 3 runs that span respectively  $m_{\text{LOW}} \in [9.4 \cdot 10^{-2}, 0.159]$  GeV,  $m_{\text{LOW}} \in [0.159, 0.4]$  GeV and  $m_{\text{LOW}} > 0.4$  GeV. Each of these runs counts  $10^4$  events.

In total there are 150k background events. This slicing was necessary to specifically populate those regions that go depleted after our selections. In our analysis we consider all the runs together, taking care of the different weighting of each simulation.

### 9.3.3 Reach

Say that after the event selection the signal has a total cross section  $\sigma_s \pm \Delta\sigma_s$ . With an assumed Belle II luminosity of  $\mathcal{L} = 50\text{ab}^{-1}$ , we expect  $E_s = \sigma_s \cdot \mathcal{L}$  signal events. The same definitions are valid for the background with  $s \rightarrow b$ .

The signal cross section is proportional to  $g_{a\gamma\gamma}^2$ . We want that  $g_{a\gamma\gamma}^{95\%}$  such that

$$\left(\frac{g_{a\gamma\gamma}^{95\%}}{g_{a\gamma\gamma}}\right)^2 \frac{E_s}{\sqrt{E_b}} = 2. \quad (9.17)$$

$g_{a\gamma\gamma}^{95\%}$  is computed with an error. We assume the luminosity to be an exact number and take the number of MG5\_aMC@NLO events in the bin ( $N_s, N_b$  respectively for the signal and the background) to have a Poissonian error  $\sqrt{N_{s,b}}$ . We propagate these errors for  $g_{a\gamma\gamma}^{95\%}$  and get

$$\sigma_{g_{a\gamma\gamma}} = \frac{g_{a\gamma\gamma}}{2} \left[ \frac{1}{4N_b} + \frac{1}{N_s} + \frac{\Delta\sigma_b^2}{\sigma_b^2} + \frac{\Delta\sigma_s^2}{4\sigma_s^2} \right]^{\frac{1}{2}}. \quad (9.18)$$

We depict our results for  $g_{a\gamma\gamma}^{95\%}$  in fig. 9.4: in fig. 9.4a we implement the *and cut* as defined in section 9.3.1, in fig. 9.4b we implement the *or cut*. In both pictures, the purple line corresponds to the yellow dashed line from the left panel in figure 7 in [72]. The blue line implements the high mass selection. You can see how it is best suited for  $M_a \gtrsim 5$  GeV. Apart from the joint around  $M_a \sim 5$  GeV with the low mass selection curves, the blue line has a nice agreement with the purple one.

Our yellow, green and red line implement the low mass selection, asking respectively for a 24, 48, 96 mrad angular separation. They are best suited for  $M_a < 5$  GeV. Both for the *and* and the *or cut*, at intermediate masses the number of cells separating photons is irrelevant and the accord with the purple line is almost perfect. The small discrepancies are to be attributed to the fact that we use a 95% CL while Dolan et al. use a 90% CL, that they generate their background using BABAYAGA.NLO rather than MG5\_aMC@NLO generation and to their choice of angular separation criterion. Angular separation manifests its importance way more for small  $M_a$ . We can deduce that there would be an important advantage if the ECL event analysis became sufficiently refined that only 48 or 24 mrad of separation were enough to tell photons apart.

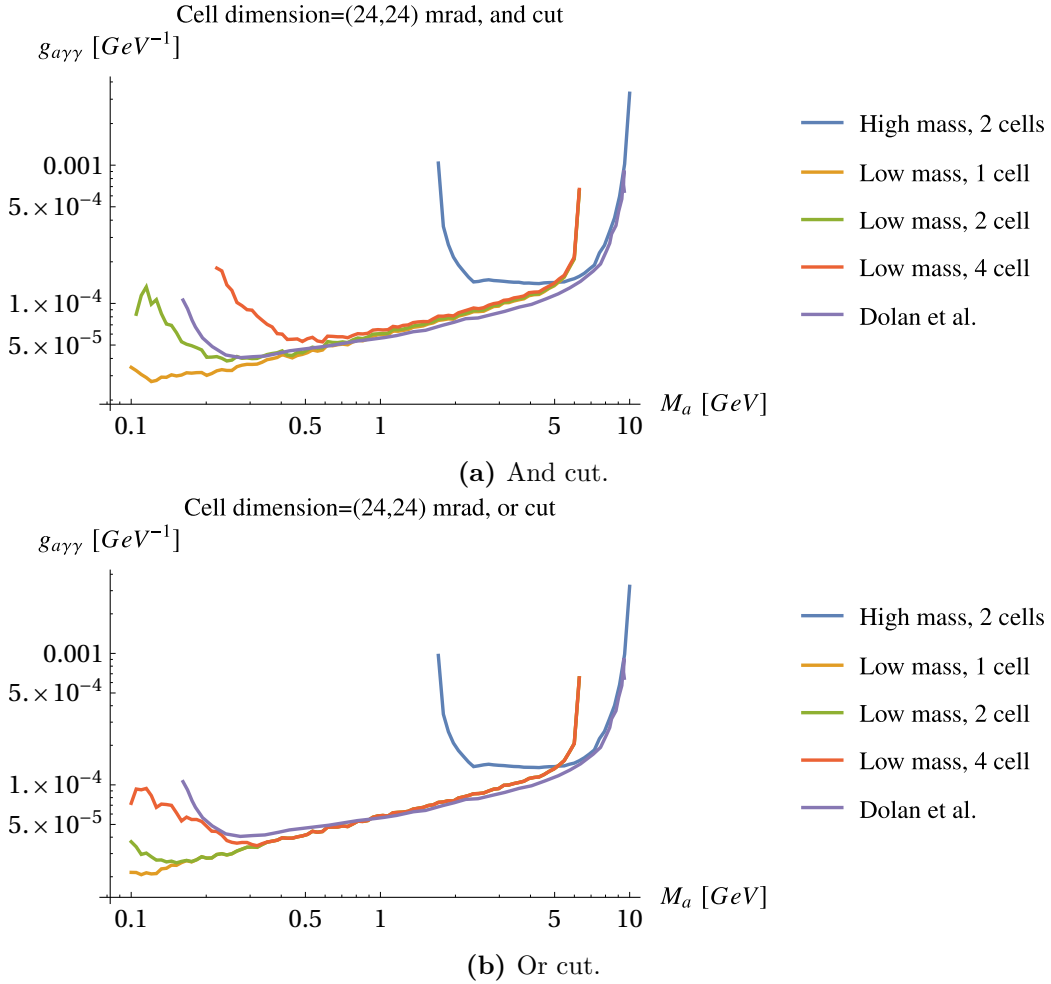


**Figure 9.4.** Belle II sensitivity to the ALP when ALP-strahlung is considered to be the only relevant channel. In both pictures, the purple line corresponds to the yellow dashed line from the left panel in figure 7 in [72]. The blue line implements the high mass selection. You can see how it is best suited for  $M_a \gtrsim 5$  GeV. Our yellow, green and red line implement the low mass selection, asking respectively for a 24, 48, 96 mrad angular separation. They are best suited for  $M_a < 5$  GeV.

## Chapter 10

# Visible reach: Belle II sensitivity to $e^-e^+ \rightarrow e^-e^+a, a \rightarrow \gamma\gamma$

In this chapter we want to test whether the VBF is negligible with respect to the ALP-strahlung when computing the Belle II sensitivity to a visible ALP or not. From our analytic computation we already know that most of the VBF cross section comes from the kinematic configuration with the final  $e^\pm$  flying along the beam pipe. Belle II can not detect them by construction, so we expect the VBF rate to be reduced. We can follow two strategies: one is sticking to the current polar angular aperture of the detector and searching for an optimising set of events selections, the other one is considering an improved  $e^\pm$  acceptance. This is possibly doable for example by the means of roman pots [129–131] and would not affect the  $e^+e^- \rightarrow 3\gamma$  sensitivity. So in section 10.1 we discuss the best possible aperture for a Belle II upgrade, that we call Belle III. In section 10.2 we explain how we picked the best events selections and in section 10.3 we show our results.

### 10.1 Belle III: what $e^\pm$ acceptance to choose?

At a quick glance, an unrefined Belle II sensitivity to the VBF channel is not very interesting. However we know from Part I that if the lepton acceptance was larger the VBF would overcome the ALP-strahlung, therefore we repeat all our computations for what we will be calling Belle III, i.e. Belle II with larger lepton acceptance. In this section I explain how we chose this new pseudorapidity boundary.

We generated signal and background with the Belle II geometric cuts for the photons and electrons as described in the previous section; on top of that we asked for  $\Delta R_{e^-e^+}, \Delta R_{e\gamma}, \Delta R_{\gamma\gamma} \geq x$ , with  $x = 48$  and 3 mrad, so to simulate a finite angular resolution of the ECL; ultimately we checked for different upper bounds  $\max \eta_l$  to the absolute final leptons pseudorapidity, in order to see how this change in acceptance affected the reach in  $g_{a\gamma\gamma}$ . The reach is computed with mass selection as only events refinement. The results are in fig. 10.1: the point in which VBF starts to overcome the strahlung is  $\max \eta_l \sim 4$  in the CoM; it is also notable that after a certain value of  $\eta \sim 10$  it is pointless to try and improve more and more the detector since the reach stabilises on a plateau.

We finally opt for  $\max \eta_l = 5$ , since it would give the best reach and still be

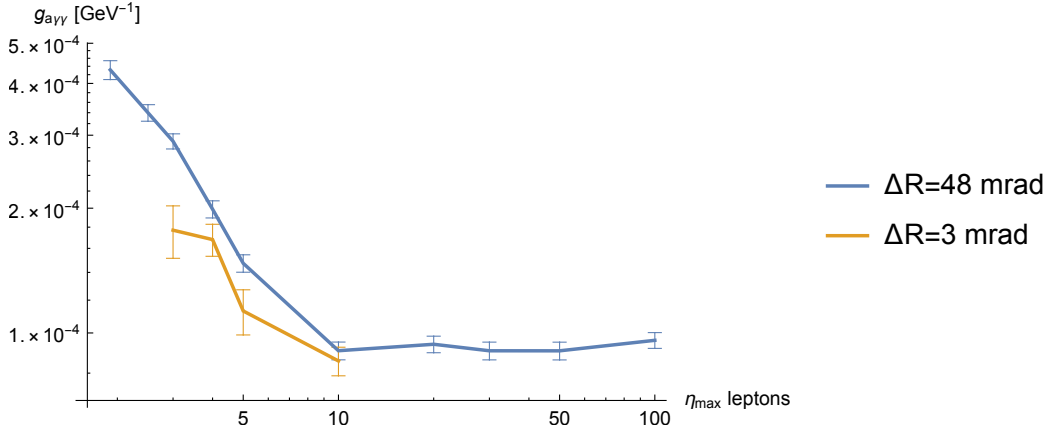


**Figure 10.1.** Reach for  $g_{a\gamma\gamma}$  obtained at different values of the maximum rapidity allowed to final  $e^\pm$ . In the signal, we used  $M_a = 8$  GeV; the luminosity is  $50 \text{ ab}^{-1}$ . The cut in  $\Delta R$  is intended on all possible couples of photons and electrons:  $(\gamma\gamma), (\gamma e), (ee)$ .

practically doable<sup>1</sup>. The photons acceptance, hence the ALP-strahlung only Belle III sensitivity, is unchanged. With these new detector parameters, we compare the two channels cross sections and see that the Belle III VBF signal is comparable to the ALP-strahlung signal, see fig. 10.2. As predicted in chapter 7, increasing the leptons forward acceptance increases the VBF cross section, which is now comparable to the strahlung for all ALP masses. This result shows how future colliders may see a more and more important VBF with respect to the ALP-strahlung.

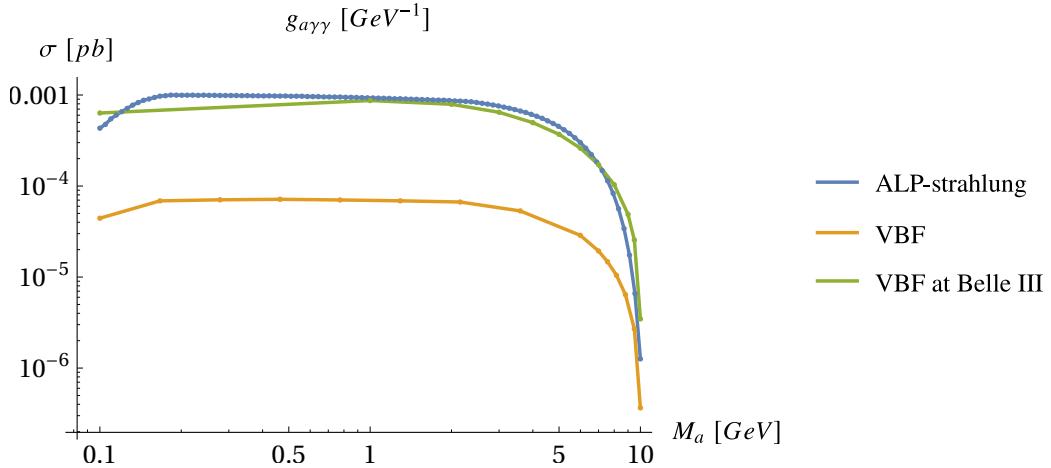


**Figure 10.2.** MG5\_aMC@NLO simulation of signal cross sections for different ALP masses. The blue line is the VBF channel with Belle II constraints ( $|\eta_l| \leq 1.5$ ), the green curve is the VBF channel with Belle III constraints ( $|\eta_l| \leq 5$ ), the yellow line is the ALP-strahlung; it is not sensitive to variations in final lepton angular acceptance.

<sup>1</sup>For example in [130] we read that for the ALPHA detector Roman Pots get down to millimetre distance from the LHC beams.

## 10.2 Event selection

First of all, for any ALP mass hypothesis we will always assume that the ALP is very close to its resonance. Therefore the invariant mass of the photons pair must be very similar to  $M_a$ . Concretely we ask for

$$m_{\gamma\gamma} \in M_a + \sigma_m[-3, 1.5]. \quad (10.1)$$

A further refinement is still necessary. To pick up the best set of event selections I explored different cuts and their combinations. I considered a vast set of kinematic variables and wrote down an algorithm that for each variable identified the phase space region that made the ratio  $\frac{\text{signal}}{\sqrt{\text{background}}}$  the biggest. Let me specify that this is not a Machine Learning algorithm (that we did not try but could improve our results even further) but just a tool for quickly finding the best interval to impose on many kinematic variables. You can find further details on its efficiency in appendix M. Some cuts proved little or no efficient and were discarded, some others were retained. I examined the combinations of the latter and finally opted for the simplest cuts having the biggest impact. I concluded that the optimal selection had to differentiate 4 ALP mass categories for both the Belle II and Belle III analysis, to which I will refer as light, medium, high and ultra-high regimes. I summarise the selections <sup>2</sup> in table 10.3.

Ma [GeV]	Variables	Intervals
(0, 1]	$\Delta R_{e^\pm\gamma}$	[2, 4.5]
	$ \eta_{\gamma_1} - \eta_{\gamma_2} $	[0, 0.7]
[1, 3]	$\Delta R_{e^\pm\gamma}$	[1.5, 4.5]
	$ \eta_{\gamma_1} - \eta_{\gamma_2} $	[0, 1.3]
[3, 7]	$\Delta R_{e^\pm\gamma}$	[1, 4.5]
	$\eta_{\gamma_1}^* \cdot \eta_{\gamma_2}^*$	[-0.3, 0.3]
[7, $\sqrt{s}$ ]	$\Delta R_{e^\pm\gamma}$	[0.5, 5]
	$\eta_{\gamma_1}^* \cdot \eta_{\gamma_2}^*$	[-0.3, 0.1]

**Table 10.1.** Belle II.

Ma [GeV]	Variables	Intervals
(0, 1]	$\Delta R_{e^\pm\gamma}$	[2.1, 6]
[1, 5]	$\Delta R_{e^\pm\gamma}$	[2.1, 6]
	$\eta_{\gamma_1}^* \cdot \eta_{\gamma_2}^*$	[-0.5, 0.5]
[5, 8]	$\Delta R_{e^\pm\gamma}$	[1, 6.5]
	$\eta_{\gamma_1}^* \cdot \eta_{\gamma_2}^*$	[-0.4, 0.3]
[8, $\sqrt{s}$ ]	$\eta_{\gamma_1}^* \cdot \eta_{\gamma_2}^*$	[-0.5, 0.1]
	$\Delta R_{\gamma\gamma}$	[3, 3.5]
	$\eta_\gamma^*$	[-1, 1]

**Table 10.2.** Belle III.

**Table 10.3.** Both for Belle II and the so called Belle III (Belle II with lepton rapidity  $|\eta_i^*| < 5$ ) we identify 4 regimes corresponding to an  $M_a$  interval. For example at Belle II, if  $M_a \in (0, 1]$  GeV, we choose to impose cuts on two Lorentz invariant variables: the angular separation between  $e^\pm$  and photons  $\Delta R_{e^\pm\gamma}$  and the photons rapidity difference  $|\eta_1 - \eta_2|$ , see eqs. (9.15) and (9.16) for their definitions. We keep events satisfying  $\Delta R_{e^\pm\gamma} \in [2, 4.5]$  and  $|\eta_1 - \eta_2| \in [0, 0.7]$ . Similarly for all other regimes.

We can see how the selections are mainly based on the photons behaviour, in fact the origin of photons is the main difference among signal and background. While imposing a tight constraint on their invariant mass affects all the kinematic variables in such a way that signal and background become very similar, the direction in which photons point still keeps some degree of freedom.

<sup>2</sup>Let me specify that by  $\Delta R_{e^\pm\gamma} \in [2, 4.5]$  I mean that both  $\Delta R_{e^-\gamma} \in [2, 4.5]$  and  $\Delta R_{e^+\gamma} \in [2, 4.5]$  must be true.

We propose here a short gallery depicting how our algorithm selected the kinematic boundaries to enforce on  $\Delta R_{e^\pm\gamma}$  for different  $M_a$  values, both for Belle II and Belle III. In figs. 10.3 and 10.4 the empty contours are the occurrence histogram for  $\Delta R_{e^\pm\gamma}$ , the coloured bins are the ones selected by the cuts in tables 10.1 and 10.2. You can see how the algorithm correctly selected the bins in which the  $\Delta R$  distribution is peaked.

Let us explain the histograms shape. We will derive it in the CoM as it is easier while we don't lose any generality as  $\Delta R$  is Lorentz invariant under boosts parallel to the beam pipe. From fig. 8.10b you can see that the ALP prefers to stay at rest in the CoM, producing back to back photons. If one assumes the ALP is at rest, the photons fourmomenta will look like

$$p_1 = \frac{M_a}{2} (1, \sin \theta_1 \cos \phi_1, \sin \theta_1 \sin \phi_1, \cos \theta_1), \quad (10.2)$$

$$p_2 = \frac{M_a}{2} (1, \sin \theta_2 \cos \phi_2, \sin \theta_2 \sin \phi_2, \cos \theta_2). \quad (10.3)$$

$$p_1 + p_2 = (M_a, \vec{0}) \quad (10.4)$$

The latter has two solutions:

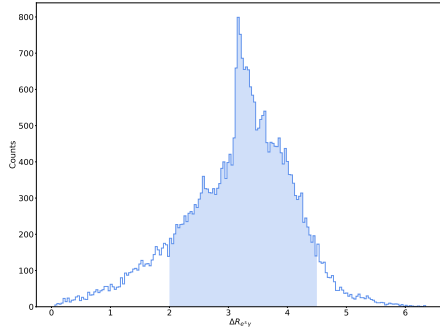
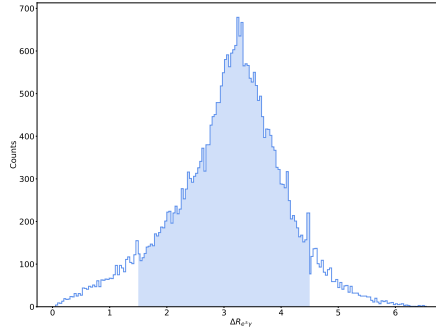
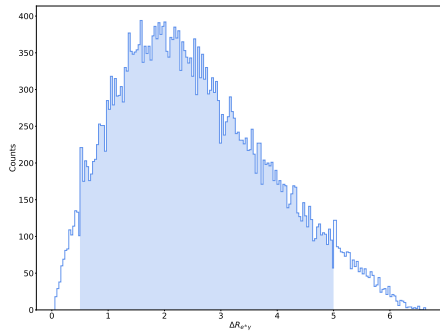
$$\theta_2 = \theta_1 + \pi, \quad \phi_2 = \phi_1, \quad (10.5)$$

$$\theta_2 = \pi - \theta_1, \quad \phi_2 = \phi_1 + \pi. \quad (10.6)$$

In both cases

$$(\eta_1 - \eta_2)^2 = 4 \log \left[ \tan \left( \frac{\theta_1}{2} \right) \right]^2. \quad (10.7)$$

Assuming a uniform  $\theta_1$  distribution, the distribution in eq. (10.7) is peaked around 0. Then the  $\Delta\eta$  contributes to the  $\Delta R_{e^\pm\gamma} \sim 3$  with a peak around 0. As to the azimuthal contribution, eq. (10.5) contributes nothing to  $\Delta R^2$  while eq. (10.6) provides a  $\pi^2$  shift. As from fig. 8.9, the ALP at rest approximation is less and less exact the more  $M_a$  increases, therefore the azimuthal and polar angles have more and more freedom to displace from eqs. (10.5) and (10.6). This explains why for small  $M_a$  there is a peak around  $\Delta R_{e^\pm\gamma} \sim 3$  and why it is diluted when  $M_a$  becomes bigger.

(a)  $M_a = 0.14$  GeV.(b)  $M_a = 1.53$  GeV.(c)  $M_a = 8.5$  GeV.

**Figure 10.3.** Values allowed to Belle II events for the variable  $\Delta R_{e\pm\gamma}$  at different ALP masses.

## 10.3 Reach

Figure 10.5 shows our optimised Belle II and Belle III sensitivity to the VBF ALP, following the selections from table 10.3. Let us describe our simulation dataset: for the Belle II simulations we used 5 background runs, each counting  $5 \cdot 10^4$  events. One run spans the whole phase space, the other 4 divide the photons invariant mass in the following slices:

$$m_{\gamma\gamma} \in [0, 1], [1, 3], [3, 7], [7, 10.58] \text{ GeV}, \quad (10.8)$$

for a total of 145.23 pb. In this case too it was necessary to cover the Phase Space twice since the mass selection is so strong that too few events would have survived otherwise.

For the Belle III simulations we used 7 background runs, each counting  $10^4$  events. For each run the photons invariant mass is in the following slices:

$$m_{\gamma\gamma} \in [0, 0.5], [0.5, 1], [1, 2], [2, 4], [4, 6], [6, 8], [8, 10.58] \text{ GeV}, \quad (10.9)$$

for a total of 219.00 pb.

For the signal we vary  $M_a \in [0, \sqrt{s}]$ , each run counts  $10^4$  events, both in the Belle II

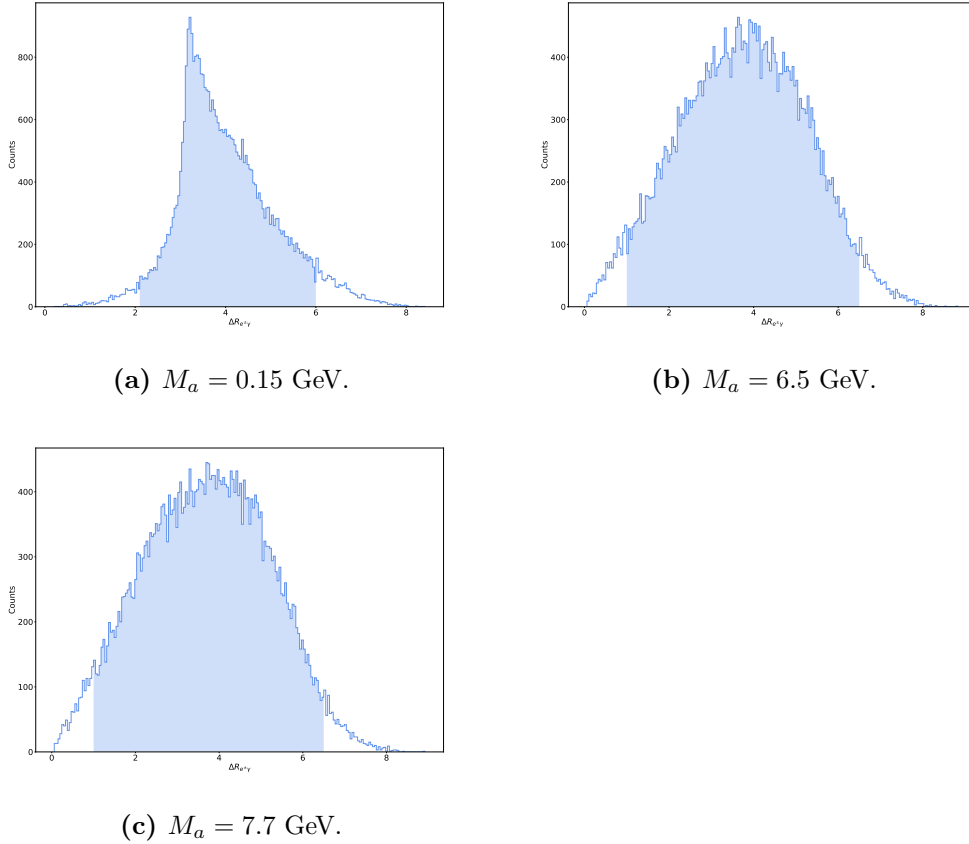
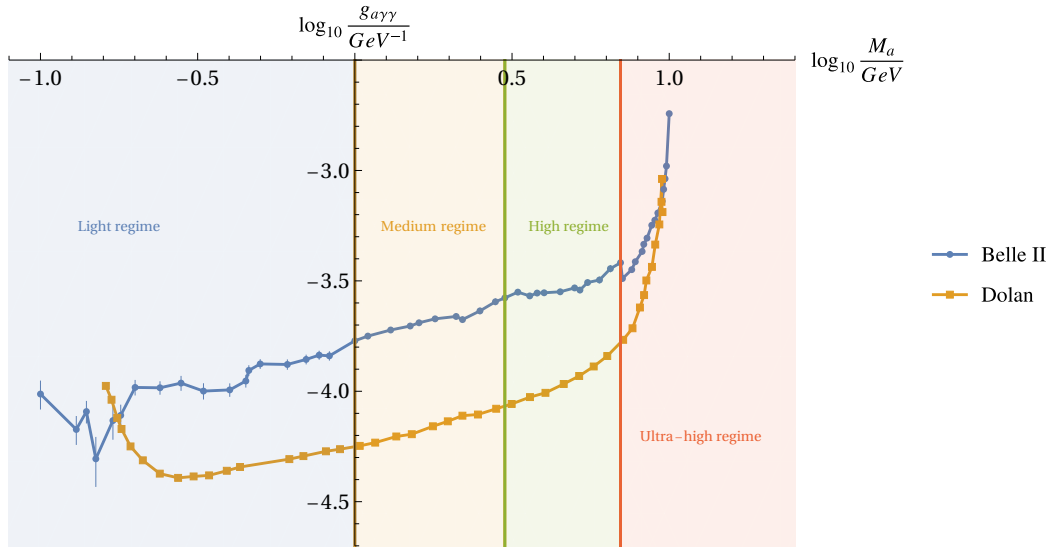


**Figure 10.4.** Values allowed to Belle III events for the variable  $\Delta R_{e\pm\gamma}$  at different ALP masses.

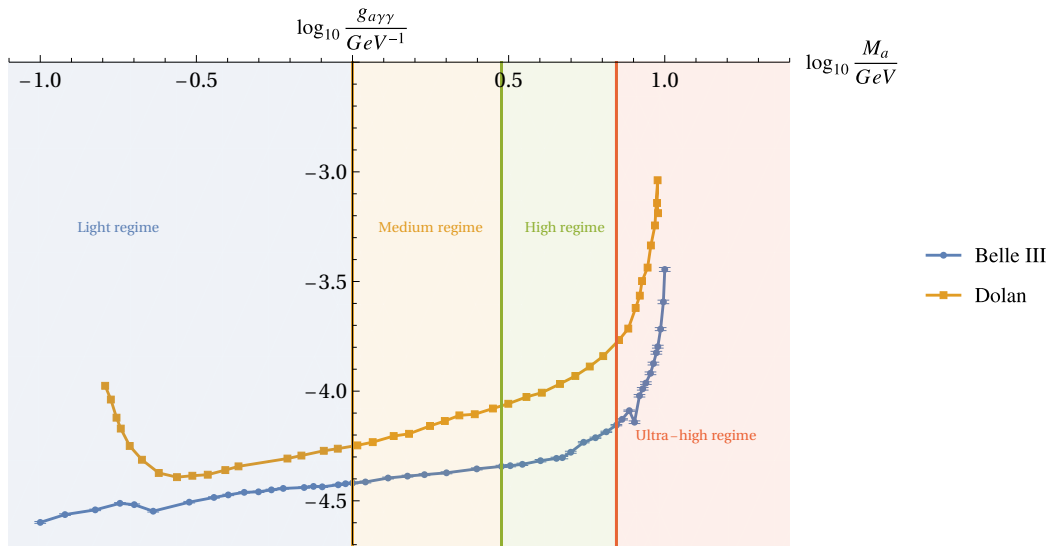
and Belle III case.

We conclude that in the visible case the VBF always deserves to be taken into account. At Belle II we manage to produce a comparable or better reach than the ALP-strahlung one when the ALP mass is extremely high or extremely low. Let us motivate it. First, in our signal we are sure that the two photons come from the ALP: on small  $M_a$  we have no combinatorial effects as it happens in the low mass algorithm, so we can thoroughly exploit the sharp ALP features. In the ALP-strahlung the pseudoscalar is very boosted, so photons coming from the ALP are very close to each other and get killed by photon separation constraints. In the VBF the opposite happens, with an ALP preferably at rest and back to back photons. At large  $M_a$  too having two photons only pays off, indeed we could design some more targeted selections such that, as one can see from table .4, even when we combine all the possible cuts we could think of, the signal efficiency is always around or above 0.5, while the high mass selection in figure 6 from [72] shows a signal efficiency always below 0.5.

Thanks to an incremented signal cross section, at Belle III the VBF proves always better than the ALP-strahlung.



(a) Belle II.



(b) Belle III.

**Figure 10.5.** In both panels, the yellow solid line corresponds to the yellow dashed line from the left panel in figure 7 in [72] and considers ALP-strahlung only; the blue solid line is the sensitivity to the ALP in the VBF channel only. The coloured bands signal different selection regimes, which we declared in table 10.3.



## Chapter 11

# Invisible reach: Belle II sensitivity to $e^-e^+ \rightarrow e^-e^+a, a \rightarrow \text{invisible}$

In this chapter we consider the process

$$e^+e^- \rightarrow e^+e^- + (\text{inv}). \quad (11.1)$$

The signal is  $e^+e^- \rightarrow e^+e^- + a$ , with an Axion-Like particle not decaying visibly at Belle II. This can either happen because the ALP is long-lived or because it mostly decays in invisible particles like DM (see appendix P).

There are two main kinds of backgrounds, what we call QED<sup>n</sup>

$$e^+e^- \rightarrow e^+e^-n\gamma_{\text{inv}} \quad (11.2)$$

with  $n$  invisible photons (see section 9.1 for the definition of an invisible photon at Belle II), and what we call  $\tau\tau$  background

$$e^+e^- \rightarrow \tau^+\tau^-, \tau \rightarrow \bar{\nu}\nu e. \quad (11.3)$$

All other backgrounds are negligible with respect to a signal for the value of  $g_{a\gamma\gamma} \sim 10^{-5} \text{ GeV}^{-1}$ . In later sections we will describe the analysis that we have invented for this search. Here we anticipate that the sensitivity for this process at Belle II depicted in fig. 11.1. It shows that for all ALP masses the invisible VBF channel must be taken in consideration because it provides a comparable or better sensitivity than that from the ALP-strahlung. Plus, for ALP masses beyond  $\sim 8.6 \text{ GeV}$ , the mono- $\gamma$  search is unfeasible due to photons triggers, while in our understanding there is no obstacle in probing such high masses for the VBF, because high energy electrons will be observable up to  $M_a \sim \sqrt{s}$ .

Figure 11.1 was obtained mainly via a high purity search, as opposed to a large background search such as the mono- $\gamma$ . The following sections are devoted to explaining how to achieve it. The first thing that we noticed about the invisible search was that experimental error due to detector effects can get so remarkable to completely was out the nice features we met in the previous chapters, like the ALP having a very narrow width. In section 11.1 we explain why this happens, how it

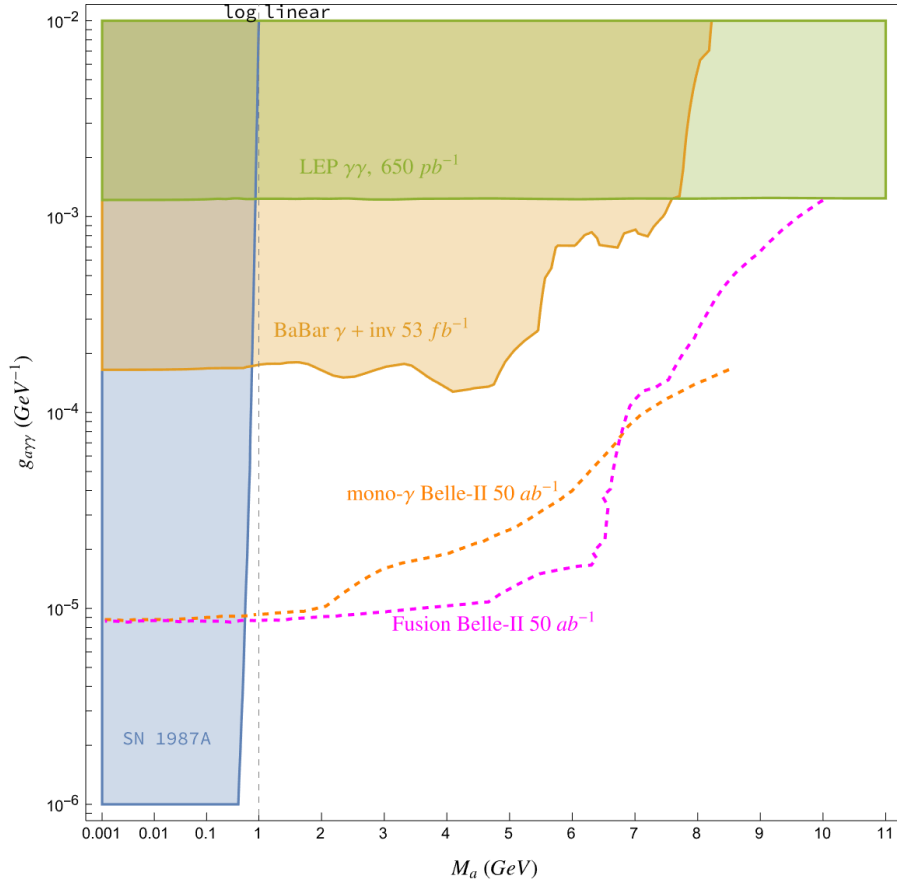


**Figure 11.1.** All boundaries in this exclusion plot constrain an Axion-Like particle decaying mainly into DM (invisible ALP). The yellow dashed line corresponds to the red dashed line from figure 4 in [72]. It is the so called mono- $\gamma$  signal, i.e.  $e^+e^- \rightarrow \gamma a, a \rightarrow \text{invisible}$ , in which we are only able to see one final photon. The magenta dashed line is the sensitivity to the ALP in the invisible VBF channel only:  $e^+e^- \rightarrow e^+e^-a, a \rightarrow \text{invisible}$ . The limits from heavy ions and  $pp$  collisions are taken from [132, 133].

affects our measurements and how it forced us to look for an alternative selection strategy. In section 11.2 we show how we managed to completely put the leading orders of  $\text{QED}^n$  to 0 up to  $m_{\text{miss}} \sim 6$  GeV. In section 11.6 we explain what selection made the  $\tau\tau$  vanish too.

## 11.1 Collider effects ask for original selections

One may think that the smallness of the ALP mass width may be exploited for discovery. Such a plan is undermined by the smearing that detectors induce on data. Our MC generator simulates the collisions at an ideal accelerator and output data as taken from an ideal detector. The biggest difference between MC data and the real one is the so called smearing. For example, due to smearing, the energy distribution of a monochromatic beam of particles would not be recorded with a Dirac  $\delta$  shape but rather as gaussian distributions, whose width is given by the quality of the

instrumentation (see appendix N for details on smearing implementation in our data analysis). Pure simulation based predictions are a good proxy of physical quantities as long as the measurement introduces a negligible uncertainty. While this can be true for most kinematic quantities of visible particles, the same cannot be said for the invisible ones: invisible kinematic variables are functions of visible kinematic variables and may be prone to major cancellations, while errors are always additive. Quantities that at the MC generator are very narrowly distributed may now become broader. This is exactly the case of the ALP mass: if it is invisible to Belle II because it did not decay inside the detector, its mass may only be recovered as the square of the missing momentum

$$M_a^2 = p_{\text{miss}}^2 = [p(e_{\text{in}}^-) + p(e_{\text{in}}^+) - p(e_{\text{fin}}^-) - p(e_{\text{fin}}^+)]^2. \quad (11.4)$$

$M_a^2$  has an extremely narrow distribution for all  $M_a \in [0, \sqrt{s}]$  before smearing but is sent to some distribution even a couple of GeVs broad for  $M_a \in [0, 1]$  GeV. This is depicted in figs. 11.2 and 11.3. As it may happen that the smeared missing energy is smaller than the smeared threemomentum, the squared ALP mass can be transformed into negative quantities too.

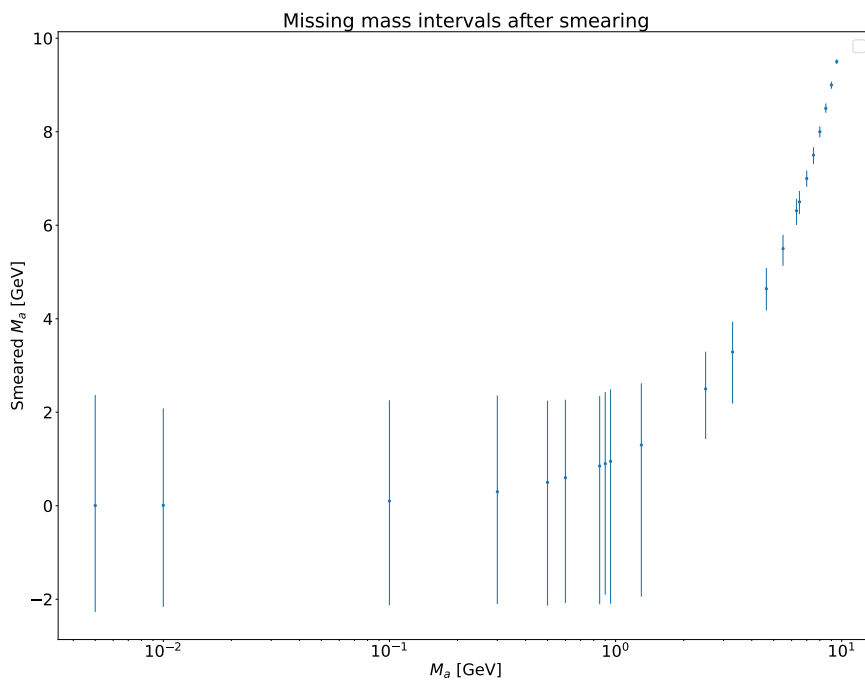


**Figure 11.2.** Each missing mass distribution is generated as an extremely narrow Breit-Wigner but is transformed into some broad bell-shaped curve by smearing. Left and right extrema of each distribution are shown as the bottom and top bar ends of each point respectively. Small masses are so severely smeared that the missing mass ceases to be a relevant quantity to consider in a signal detection. Big masses tend to keep a relatively narrow distribution.

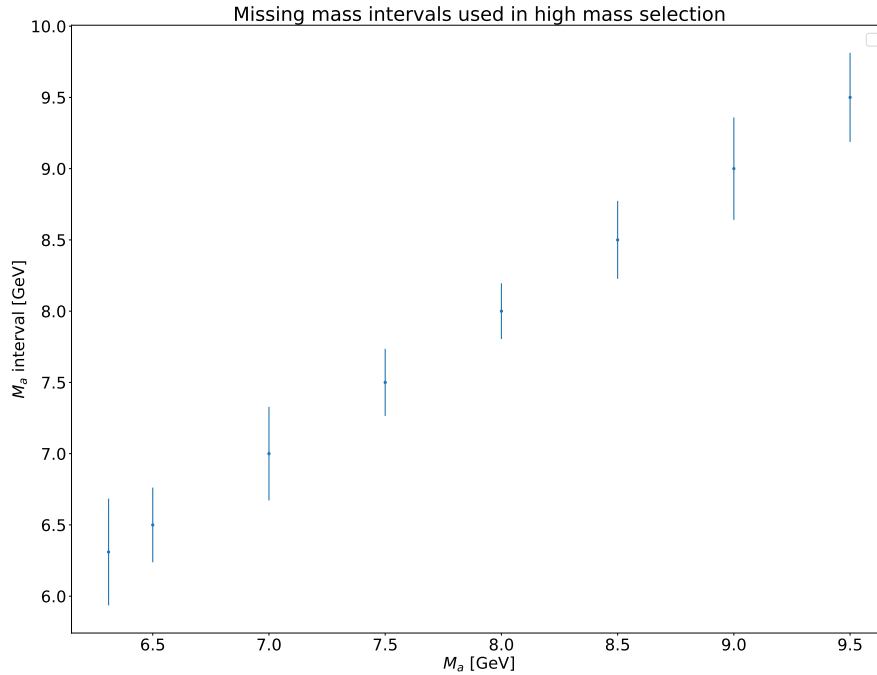


**Figure 11.3.** Zoom of fig. 11.2. Higher masses are enough well behaved that we will implement a selection on them (data in table 11.1).

We must conclude that the squared missing momentum is an unreliable quantity to base our reach upon.

The quantities to be analysed are those staying stable after the smearing. For example, a remarkable property that will always differentiate our signal from background is that the signal  $e^+e^- \rightarrow e^+e^-a$  has a single, on shell invisible body whose energy is preferably maximal and whose rapidity is preferably central, as discussed in section 11.2. At Belle II there is no other SM particle that can mimic the same properties. All other SM candidates can make up the invisible body only through multiple particles. On top of that, the fact that the signal is peaked around the maximal missing energy

$$\max E_a = \frac{s + M_a^2}{2\sqrt{s}} \quad (11.5)$$

is a stable property under smearing. Schematically, before the smearing the signal behaves as in fig. 11.4: the blue area is the maximal phase space allowed to  $E_{\text{miss}}$  and  $|\vec{p}_{\text{miss}}|$  when the missing momentum is due to more than one particle. The coloured isolines are the 1D *phase space* allowed to  $E_{\text{miss}}$  and  $|\vec{p}_{\text{miss}}|$  when the missing momentum is due to exactly one particle<sup>1</sup>:

<sup>1</sup>The (0,0) point is the 0D *phase space* allowed when there is no missing particle. This is worth

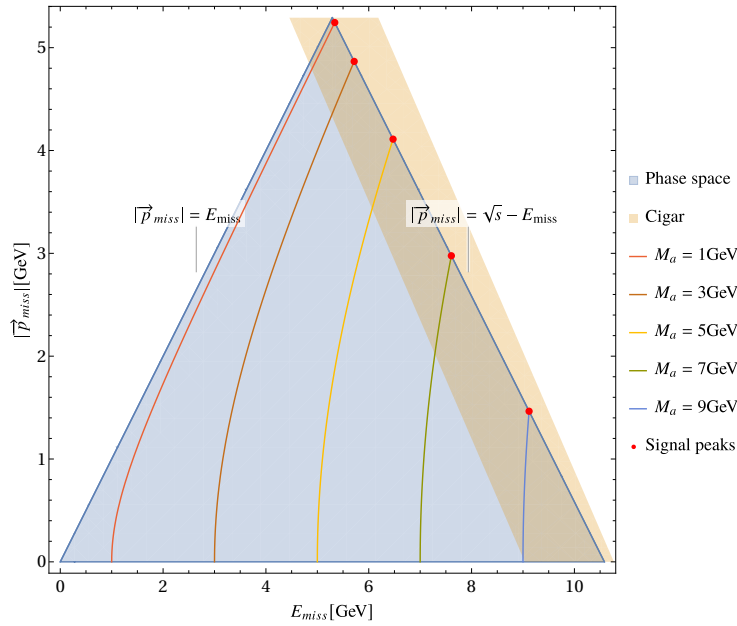


**Figure 11.4.** The blue area is the maximal phase space allowed to  $E_{\text{miss}}$  and  $|\vec{p}_{\text{miss}}|$  when the missing momentum is due to more than one particle. The coloured isolines are the 1D *phase space* allowed to  $E_{\text{miss}}$  and  $|\vec{p}_{\text{miss}}|$  when the missing momentum is due to exactly one particle. The red points indicate the peak of the ALP energy  $E_a$  distribution for different ALP masses. The yellow area, called *the signal region*, after the smearing encloses most part of the signal for every  $M_a$  while selecting a small, low intensity background area.

$$|\vec{p}_{\text{miss}}| = \sqrt{E_a^2 - M_a^2}. \quad (11.6)$$

The red points indicate the peak of the ALP energy  $E_a$  distribution for different ALP masses; their coordinates are

$$E_{\text{miss}} = \frac{s + M_a^2}{2\sqrt{s}}, \quad |\vec{p}_{\text{miss}}| = \frac{s - M_a^2}{2\sqrt{s}}. \quad (11.7)$$

Before the smearing, each signal distribution is slightly spread along the corresponding isoline, having an almost 0 width along the perpendicular direction to it. After the smearing, both the energy spread and the mass width get bigger.

After these considerations we decided to identify one signal rich region, the yellow area, that we call *cigar* for its elongated shape. The signal region wraps all of the spread signal for every  $M_a$  while selecting a small, low intensity background area. For this selection we had to use a dedicated background generation satisfying

**Definition 24** (signal region).

We say an event is in the *signal region* if its missing fourmomentum satisfies

$$10.437 - 1.155E_{\text{miss}} \leq |\vec{p}_{\text{miss}}| \leq 12.437 - 1.155E_{\text{miss}}. \quad (11.8)$$

mentioning as this is the Bhabha scattering configuration, which would have left no hope of detection otherwise. After smearing this point spreads around the origin, staying unharmed.

□

We specialised the background dataset to the signal region by the means of extra constraints at generation level implemented in the MG5\_aMC@NLO input file "cuts.f".

The signal region selection builds up with the other ones we describe in the following sections so that their joint action ends up with completely erasing both our backgrounds. We claim that this is not due to us having generated the background poorly, instead comes from deep, analytic reasons.

The action of the signal region cut is twofold as it affects both the  $\text{QED}^n$  and the  $\tau\tau$  backgrounds. As to the  $\tau\tau$  case, we will demonstrate that eq. (11.73) drastically empties the final  $e^\pm$  energies phase space. Although it may look like all regions of the  $(E(e^+), E(e^-))$  space are allowed, this background topology makes the energies very correlated so that in a big portion of the space the signal region constraint can not be satisfied.

For the  $\text{QED}^n$  case, a missing momentum due to invisible photons is not allowed to the phase space of a free particle but has a non trivial shape in energy, mass and rapidity. Let us define

**Definition 25** (Invisible phase space for  $n$  photons at Belle II  $\mathcal{P}_{\text{inv}}^{(n)}$ ).

An invisible photon at Belle II, following box 9.1, has some unaccessible phase space regions. However, an invisible body made of  $n$  invisible photons occupies the phase space  $\mathcal{P}_{\text{inv}}^{(n)}$  that grows with  $n$ . Depending on Belle II parameters, there will be some  $n$  for which  $\mathcal{P}_{\text{inv}}^{(n)}$  is indistinguishable from a visible particle phase space. We will parametrize  $\mathcal{P}_{\text{inv}}^{(n)}$  in terms of CoM variables: missing energy  $E_{\text{miss}}$ , missing rapidity  $\eta_{\text{miss}}$ , missing mass  $m_{\text{miss}}$  and number of photons  $n$ . Call the forbidden volume to  $n$  invisible photons  $\bar{\mathcal{P}}_{\text{inv}}^{(n)}$ .

□

In the following section we will demonstrate in which cases the volume of  $\bar{\mathcal{P}}_{\text{inv}}^{(n)}$  is non zero. We want to impose an event selection tailored around  $\bar{\mathcal{P}}_{\text{inv}}^{(n)}$  so to kill the  $\text{QED}^n$  background. The demonstration will be carried on without the signal region selection, however using it can only make  $\bar{\mathcal{P}}_{\text{inv}}^{(n)}$  larger. Performing an analytic demonstration with eq. (11.73) would be unnecessarily complicated, so we limit ourselves to perform a numeric simulation that you can look up in appendix O. One could either be satisfied with the simulation and view our selections as its direct consequence or want to deepen the analytical reasons behind it. This is what we will do in next sections.

In conclusion let us stress that the analytic studies on the  $2 \rightarrow 3$  scatterings in general triggered this original selection that opened an ALP discovery channel where traditional methods confirmed that the VBF should have been negligible. We find this very powerful and believe that many other processes may benefit from similar analyses.

## 11.2 QED background

The first ingredient of our proof is identifying the kinds of photons that can make up the invisible fourmomentum in the QED<sup>*n*</sup> case. For the following discussion it is useful to categorize invisible photons as “hard” or “soft” comparing their energy to the ECL threshold energy:

**Definition 26** (Soft and hard photons).

A soft photon is a photon having whatever rapidity and below threshold energy. At Belle II  $E_\gamma^* < E_0 = 0.25$  GeV.

A hard photon has an above threshold energy but a rapidity outside the collider aperture:  $|\eta_\gamma^*| > \eta_{\text{thresh}} = 1.6$  at Belle II. If a hard photon rapidity is positive, we say it belongs to the forward cone around the beam pipe of semiaperture 22° (in the CoM); if the rapidity is negative, the photon flies in the backward cone.

In a QED<sup>*n*</sup> process we say there are  $n$  photons, of which  $n_S$  are soft and  $n_H$  are hard.

□

The most relevant “soft” photons for our considerations are those close to, but still below, the ECL threshold. Therefore we stress that, even if we name them “soft” photons, there is no large logarithmic enhancement to alter the convergence of the perturbative series, thus we expect to be able to carry out reliable analyses based on fixed order kinematics at each order  $n = n_S + n_H$ .

At this point we can identify two macro-configurations of final photons that stem from the fact that using a *signal region selection* (eq. (11.73)) also implies that  $E_{\text{miss}} > 4.5$  GeV. In fact, as from fig. 11.4, the smallest missing energy allowed at the same time within the yellow and the blue area is  $\sim 4.5$  GeV. For the sake of simplicity from now on we will always assume the lower bound

$$E_{\text{miss}} > 4.5 \text{ GeV}, \quad (11.9)$$

knowing that the *signal region cut* will further refine it.

First the required missing energy can be recovered by considering  $n$  soft photons. Small masses and central rapidities will be allowed, but  $n$  will be so large that this kind of background will be negligible with respect to a signal with  $g_{a\gamma\gamma} \sim 10^{-5} \text{ GeV}^{-1}$ . In fact, assuming that all soft photons have threshold energy,

$$nE_0 \geq 4.5 \text{ GeV if } n \geq 18. \quad (11.10)$$

Second one can allow for one or more hard photons. But since hard photons have limited angles, the volume of  $\tilde{\mathcal{P}}_{\text{inv}}^{(n)}$  will be non zero. This is the case of interest for us. In turn this configuration splits in

1. Only one hard photon and  $(n - 1)$  soft photons.
2. Two hard photons
  - (a) In the same cone,

(b) In opposite cones.

3.  $k$  hard photons,  $(n - k)$  soft photons,  $k \in [3, n]$ .

This classification covers the whole set of possibilities. We will now examine every case one by one. In each configuration we want to show that the volume of  $\bar{\mathcal{P}}_{\text{inv}}^{(n)}$  is non zero. It would be ideal to analytically compute the boundary of the forbidden region  $\partial\bar{\mathcal{P}}_{\text{inv}}^{(n)}$  so that we could use it for event selection, but this is too complicated of a task. However we can give ourselves a much simpler task: we project  $\bar{\mathcal{P}}_{\text{inv}}^{(n)}$  in the  $(m_{\text{miss}}, \eta_{\text{miss}})$  phase space and look the circumscribed rectangle to the forbidden area. In section 11.2.1 we will explicitly define this rectangle. We then proceed with an analysis by categories: the one hard photon case (section 11.3.1), the (trivial) two had photons in the same cone case, the two hard photons in different cones configuration. We first approach the latter with an explicit computation (section 11.3.3), in order to prepare us to a more general proof (section 11.4).

### 11.2.1 Boundaries of the forbidden region from its circumscribed rectangle

Consider  $\bar{\mathcal{P}}_{\text{inv}}^{(n)}$  and project it in the  $(m_{\text{miss}}, \eta_{\text{miss}})$  space. The forbidden region is bounded by a curve  $\partial\bar{\mathcal{P}}_{\text{inv}}^{(n)}$ . Necessarily one branch of  $\partial\bar{\mathcal{P}}_{\text{inv}}^{(n)}$  must be  $m_{\text{miss}} = 0$  since we know that we can always make the photons invariant mass vanish by taking of all them aligned. That  $m_{\text{miss}}$  is on the boundary of the region is understood because the mass is semi-positive definite. It is sufficient for all photons to be aligned. For aligned photons, independently from  $n$ , the minimal positive allowed rapidity is attained onto the detector forward acceptance limit  $\eta_w$ , the maximal negative allowed rapidity is attained onto the backward acceptance limit  $-\eta_w$ . With this, we recovered 3 sides of the circumscribed rectangle to the forbidden area in the  $(m_{\text{miss}}, \eta_{\text{miss}})$  space. Allowing for bigger masses means allowing for bigger angular separations among photons. Therefore the minimal positive allowed rapidity will be smaller than  $\eta_w$ . There will be some missing mass such that this rapidity limit is pushed to 0. We conclude that the last side of the rectangle is  $m_{\text{miss}} = \max m_{\text{miss}}$  and is tangent to  $\partial\bar{\mathcal{P}}_{\text{inv}}^{(n)}$  on  $\eta_{\text{miss}} = 0$ . To recap, the sides are:

1. One horizontal side  $m_{\text{miss}} = 0$ .
2. The other horizontal side  $m_{\text{miss}} = \max m_{\text{miss}}$ . It is tangent to  $\partial\bar{\mathcal{P}}_{\text{inv}}^{(n)}$  in  $\eta_{\text{miss}} = 0$ .
3. A vertical side  $\eta_{\text{miss}} = \eta_w^{(n)} > 0$ , with  $\eta_w^{(n)}$  the smallest positive rapidity that can be reached.
4. The other, symmetrical vertical  $\eta_{\text{miss}} = -\eta_w^{(n)}$ .

We plot them in fig. 11.5

Three sides of the rectangle are fixed while the upper horizontal side depends on  $n$ . We will devote the following sections to its characterizations. Since we know that the point  $(m_{\text{miss}}, \eta_{\text{miss}}) = (\max m_{\text{miss}}, 0)$  does belong to  $\partial\bar{\mathcal{P}}_{\text{inv}}^{(n)}$ , we will have to

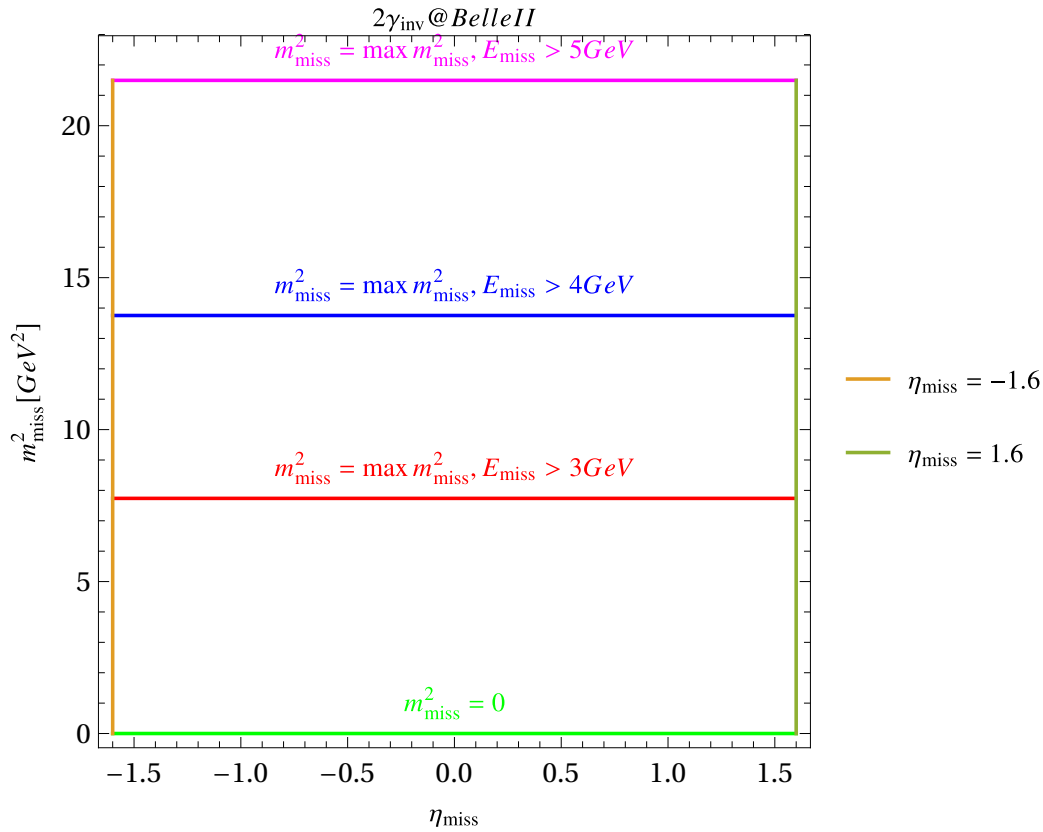


**Figure 11.5.** In this scheme we consider QED<sup>2</sup> i.e. the scattering  $e^+e^- \rightarrow e^+e^-2\gamma_{\text{inv}}$  with two final invisible photons at Belle II. The inside of the rectangles corresponds to the forbidden area in the  $(\eta_{\text{miss}}, m_{\text{miss}})$  plane. The position of the top side varies with the missing energy lower bound (here you can see  $E_{\text{miss}} > 3, 4, 5$  GeV), the other three sides are fixed and. One is  $m_{\text{miss}} = 0$ , the other two depend on Belle II characteristics: in the CoM the Belle II polar aperture corresponds to rapidities in  $[-1.6, 1.6]$ , then the vertical sides are  $\eta_{\text{miss}} = \pm 1.6$ .

impose  $\eta_{\text{miss}} = 0$ . This exercise could be repeated imposing some other values of the missing rapidity so to find other points of the region boundary, but  $(\max m_{\text{miss}}, 0)$  is the most interesting one because if  $\max m_{\text{miss}} = 0$  there will be no high purity signal region to exploit.

When does this happen? Consider that the pseudorapidity is defined as

$$\eta = \frac{1}{2} \log a, \quad (11.11)$$

with

$$a := \frac{\|\vec{p}_{\text{miss}}\| - p_{\text{miss}}^{(z)}}{\|\vec{p}_{\text{miss}}\| + p_{\text{miss}}^{(z)}} =: \frac{1 - q}{1 + q}, \quad q := \frac{p_{\text{miss}}^{(z)}}{\|\vec{p}_{\text{miss}}\|}. \quad (11.12)$$

If we only consider half of  $p_{\text{miss}}^{(z)}$  domain,  $p_{\text{miss}}^{(z)} \in [0, \|\vec{p}_{\text{miss}}\|]$ ,  $q \in [0, 1]$ , the other half can be recovered by symmetry. Here  $\eta$  will be negative. To build our rectangle sides, we will want the maximal  $\eta$ . Differentiating

$$\frac{d\eta}{dq} = -\frac{1}{1-q^2}, \quad (11.13)$$

which is always negative, therefore the  $\eta_w$  is attained for  $q = 0$ . Hence in what follows our aim will be making  $p_{\text{miss}}^{(z)}$  much smaller than  $\|\vec{p}_{\text{miss}}\|$ .

Another remark to be done on the rectangle sides is about  $m_{\text{miss}}$ . Let  $p_{\text{miss}}$  be the sum of  $n$  massless fourmomenta  $p_i$ . Then in general

$$m_{\text{miss}}^2 = \left( \sum_{i=1}^n p_i \right)^2 = \sum_{i=1}^n \sum_{j \neq i}^n 2E_i E_j (1 - \cos \theta_{ij}), \quad (11.14)$$

with  $\theta_{ij}$  the angle among  $\vec{p}_i$  and  $\vec{p}_j$ . It also holds

$$m_{\text{miss}}^2 = \sum_{i=1}^n \sum_{j \neq i}^n (p_i + p_j)^2 =: \sum_{i=1}^n \sum_{j \neq i}^n m_{ij}^2, \quad m_{ij} = 2E_i E_j (1 - \cos \theta_{ij}) \geq 0 \forall i, j, \quad (11.15)$$

i.e. it is a sum of semipositive definite monomials. Each monomial can vanish onto  $E_i = 0$  or  $E_j = 0$ , which only is the case for soft photons. Otherwise  $m_{ij}$  can vanish on  $\theta_{ij} = 0$ , which is the case of aligned photons, hence hard photons in different cones will have a positive lower bound to their invariant mass. Finally, the only way for the total missing mass to vanish is if all of its  $m_{ij}$  vanish.

### 11.3 Simultaneous missing mass and rapidity minimization: analysis by categories for $n \lesssim 10$ invisible photons

We proceed to recover the rectangle sides of section 11.2.1 for different  $n_{S,H}$ . We will use  $n_S + n_H \leq 10$  so that hard photons will always be necessary and provide the most important contribution to all kinematic variables, according to eq. (11.10).

#### 11.3.1 $n_H = 1$

The biggest contribution to the rapidity  $\eta_{\text{miss}}$  is given by the hard photon, that we call  $h_1$ . For the rapidity to be central,  $\theta_1 = \alpha_1$ . Soft photons need to be the hardest they can in order to pull the  $\eta_{\text{miss}}$  as much as they can towards 0. In other words, if  $E_i, i \in [2, n]$  are the soft photons energies, then we demand for  $E_i = E_0$ . Consequently the hard photon energy is  $E_1 = E_{\text{miss}} - (n-1)E_0$ . If soft photons are aligned, their total invariant mass is 0. Let  $\alpha_s$  be the soft photons angle. Soft photons can make  $\eta_{\text{miss}}$  central if they fly in the opposite direction with respect to  $h_1$ . Therefore we must take the hard photon fourmomentum

$$p_1 = E_1(1, \sin \alpha_1, 0, \cos \alpha_1), \quad (11.16)$$

and each soft photon

$$p_s = E_0(1, \sin \alpha_s, 0, \cos \alpha_s), \quad (11.17)$$

so that

$$p_{\text{miss}} = p_1 + (n-1)p_s = (E_{\text{miss}}, E_1 \sin \alpha_1 + E_0(n-1) \sin \alpha_s, 0, E_1 \cos \alpha_1 + E_0(n-1) \cos \alpha_s). \quad (11.18)$$

With two fourmomenta only,  $p_{\text{miss}}$  and  $p_s$ , we had the freedom to rotate away the azimuthal component. The solution to  $\eta_{\text{miss}} = 0$  is

$$\cos \alpha_s = \cos \alpha_1 \left( 1 - \frac{E_{\text{miss}}}{E_0(n-1)} \right). \quad (11.19)$$

If the solving  $\cos \alpha_s$  of eq. (11.19) is in  $[-1, 1]$  then the missing rapidity can be 0, otherwise the best that can be done is putting  $\cos \alpha_s = -1$ . Now

$$\cos \alpha_s \in [-1, 1] \text{ if } n \geq 1 + \frac{cE_{\text{miss}}}{E_0(1 + \cos \alpha_1)}. \quad (11.20)$$

In fig. 11.6 we plot  $m_{\text{miss}}$  and  $\eta_{\text{miss}}$  against  $n$  for different  $E_{\text{miss}}$  values. From the right panels we can see that increasing  $E_{\text{miss}}$  implies that it takes more soft photons to reach  $\eta_{\text{miss}} \sim 0$ , but on the other hand the corresponding missing mass will be larger.

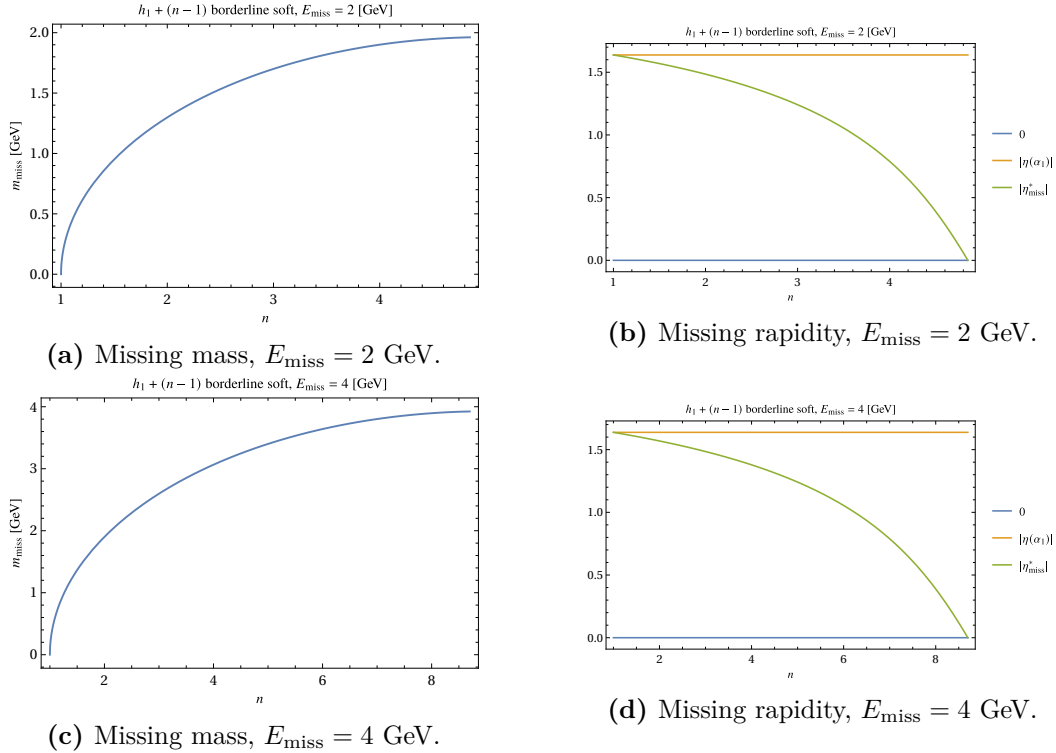


**Figure 11.6.** The two left panels depict the missing mass of an invisible body made of  $(n-1)$  aligned soft photons flying backward along the beam pipe and with borderline energy  $E_0$  and one forward hard photon  $h_1$ . The two right panels depict the missing rapidity for the same body.

### 11.3.2 Two hard photons in the same cone

The smallest achievable  $\eta_{\text{miss}}$  is obtained if both of the hard photons have  $\theta_1 = \theta_2 = \alpha_1$ . But then this case is identical to that of one hard photon, in that a number of soft photons must be used to bring  $\eta_{\text{miss}} \rightarrow 0$ .

### 11.3.3 Two hard photons in different cones

Consider the case of two invisible hard photons. Name the fourmomenta

$$\begin{aligned} p_1 &= E_1(1, s_1, 0, c_1), & s_1 &:= \sin \theta_1, c_1 := \cos \theta_1, \theta_1 \in [0, \alpha_1], \\ p_2 &= E_2(1, s_2 c_f, s_2 s_f, c_2), & \theta_2 &\in [\alpha_2, \pi], \\ p_{\text{miss}} &= p_1 + p_2, & p_{\text{miss}}^2 &=: m_2^2. \end{aligned} \quad (11.21)$$

To achieve null rapidity we are forced to take one photon in the forward cone and one in the backward one, so that  $p_{\text{miss}}^z = 0$ . This configuration has a non zero lower bound on the missing mass:

$$(m_{\text{miss}})_{n_H=2}^2 = 2E_1 E_2 (1 - c_{12}) \geq \min m_2^2 = 2 \left( \frac{E_{\text{miss}}}{2} \right)^2 [1 - \cos(\alpha_2 - \alpha_1)], \quad (11.22)$$

where  $\alpha_1$  and  $\alpha_2$  are the limiting angles from box 9.1. Let us demonstrate this statement.  $m_2^2$  is a function of energies and angles. From the missing energy definition

$$E_2 = E_{\text{miss}} - E_1. \quad (11.23)$$

From  $\eta_{\text{miss}} = 0$ :

$$E_1 = -E_2 \frac{\cos \theta_2}{\cos \theta_1}. \quad (11.24)$$

On eqs. (11.23) and (11.24) the missing mass becomes:

$$\begin{aligned} m_2^2 &= m_2^2(\theta_1, \theta_2, \phi, E_{\text{miss}}) \\ &= \frac{2E_{\text{miss}}^2 \cos \theta_1 \cos \theta_2 (\sin \theta_1 \sin \theta_2 \cos \phi + \cos \theta_1 \cos \theta_2 - 1)}{(\cos \theta_1 - \cos \theta_2)^2}, \end{aligned} \quad (11.25)$$

which is symmetric in  $\theta_1 \leftrightarrow \theta_2$ . Let us find its extremal points.  $m_2^2$  derivative with respect to  $\phi$  is always negative so we can fix  $\phi = 0$ . The hessian on  $\phi = 0$  is

$$\begin{aligned} \begin{vmatrix} \frac{d^2 m_2^2}{d\theta_1^2} & \frac{d^2 m_2^2}{d\theta_1 d\theta_2} & \frac{d^2 m_2^2}{d\theta_1 d\phi} \\ \frac{d^2 m_2^2}{d\theta_2 d\theta_1} & \frac{d^2 m_2^2}{d\theta_2^2} & \frac{d^2 m_2^2}{d\theta_2 d\phi} \\ \frac{d^2 m_2^2}{d\phi d\theta_1} & \frac{d^2 m_2^2}{d\phi d\theta_2} & \frac{d^2 m_2^2}{d\phi^2} \end{vmatrix}_{\phi=0} &= \frac{1}{8} \left[ E_{\text{miss}}^3 \frac{\cot\left(\frac{\theta_1 - \theta_2}{2}\right)}{\sin^4\left(\frac{\theta_1 + \theta_2}{2}\right)} \right]^2 (1 + 2 \cos \theta_1 \cos \theta_2) \sin(2\theta_1) \sin(2\theta_2). \end{aligned} \quad (11.26)$$

Due to the  $\theta_{1,2}$  domain, the hessian is negative semi-definite, then every point on which the gradient vanishes will be a maximum and not the minimum that we search, so it is not worth to try and find the solutions to

$$\left( \frac{d}{d\theta_1}, \frac{d}{d\theta_2}, \frac{d}{d\phi} \right) m_2^2 = \vec{0}. \quad (11.27)$$

Instead we can perform the change of variables

$$\theta_1 =: x_1, \quad \theta_2 = \pi - x_2, \quad x_{1,2} \in [0, \bar{x}], \quad (11.28)$$

and series expand in  $x_{1,2}$  since  $\bar{x}$  is small at Belle II ( $\frac{\bar{x}}{\pi} = 0.12$ ). Then

$$\left( \frac{d}{dx_1}, \frac{d}{dx_2}, \frac{d}{d\phi} \right) m_2^2 = -\frac{E_{\text{miss}}^2}{2} (x_1 + x_2 \cos \phi, x_2 + x_1 \cos \phi, -x_1 x_2 \sin \phi) + \mathcal{O}(x^2). \quad (11.29)$$

On  $\phi = 0$  the derivatives with respect to  $x_1$  and  $x_2$  are always negative so the absolute minimum is reached onto  $x_1 = x_2 = \bar{x}$ .

### 11.3.4 Larger $n$ rectangles have smaller $\bar{\mathcal{P}}_{\text{inv}}^{(n)}$

I will now demonstrate that  $\bar{\mathcal{P}}_{\text{inv}}^{(n)}$  in the  $(m_{\text{miss}}, \eta_{\text{miss}})$  space has smaller volume because the top side of the circumscribed rectangle is lower. Consider the case of three invisible photons. Let us name the fourmomenta

$$p_1^{(3)} = E_1^{(3)}(1, s_1^{(3)}, 0, c_1^{(3)}), \quad (11.30)$$

$$p_2^{(3)} = E_2^{(3)}(1, s_2^{(3)} \cos \phi_{12}, s_2^{(3)} \sin \phi_{12}, c_2^{(3)}), \quad (11.31)$$

$$p_3^{(3)} = E_3^{(3)}(1, s_3^{(3)} \cos \phi_{13}, s_3^{(3)} \sin \phi_{13}, c_3^{(3)}), \quad (11.32)$$

$$p_{\text{miss}}^{(3)} = (p_1 + p_2 + p_3)^{(3)}, \quad (11.33)$$

$$(p_{\text{miss}}^{(3)})^2 := m_3^2, \quad (11.34)$$

where I used the superscript (3) to distinguish this three photons case from the previous two photons case. We want to study how the phase space allowed to three such bodies is different with respect to the one allowed to two bodies. Specifically, on  $\eta_{\text{miss}} = 0$  the minimal missing mass is smaller. We show now why. Modulo relabellings, fourmomenta can have the following kinematics:

- $p_{1,2,3}$  soft. We exclude this configuration a priori.
- $p_{2,3}$  soft. We considered this configuration in section 11.3.1.
- $p_3$  soft.
- $p_{1,2,3}$  hard.

We will consider the all hard photons case in the following section. Here instead we consider the  $p_3$  soft case. Exploiting the fact that  $p_3$  is a perturbation with respect to  $p_1$  and  $p_2$ , we can give to  $p_{1,2}$  the same kinematic configuration they had in the previous section and derive  $p_3$  kinematics. First, one can compute the invariant mass of  $p_{1,2,3}$  on  $\phi_{12} = 0$ , derive with respect to  $\phi_{13}$  and find that mass minimization

happens on  $\phi_{13} = 0$ .

The whole polar angle range should be allowed to the soft photon but without loss of generality we can take the forward direction to be the one in which one hard and one soft photon are pointing to and name the forward hard photon  $p_1$ , the backward hard photon  $p_2$  and the soft photon  $p_3$ . In this setup we can write the three photons invariant squared mass  $m_3^2$  as a sum of the two photons invariant squared mass from previous section ( $m_2^2$  eq. (11.25)) and a term:

$$m_3^2(\phi_{12} = \phi_{13} = 0, \eta_{\text{miss}} = 0) = m_2^2 + \frac{8E_3E_m \sin\left(\frac{1}{2}(\theta_1 - \theta_2)\right) \sin(\theta_1 - \theta_2) \sin\left(\frac{1}{2}(\theta_1 - \theta_3)\right) \sin\left(\frac{1}{2}(\theta_2 - \theta_3)\right)}{(\cos(\theta_1) - \cos(\theta_3))^2} - \frac{4E_3^2 \sin^2\left(\frac{1}{2}(\theta_1 - \theta_3)\right) \sin^2\left(\frac{1}{2}(\theta_2 - \theta_3)\right)}{\sin^2\left(\frac{1}{2}(\theta_1 + \theta_2)\right)}. \quad (11.35)$$

The last term is a negative square. For the second term we need more discussion. We remark that

$$\sin\frac{\theta_1 - \theta_2}{2}, \sin\theta_1 - \theta_2, \sin\frac{\theta_1 - \theta_3}{2} \leq 0, \quad (11.36)$$

$$\sin\frac{\theta_2 - \theta_3}{2} \geq 0 \quad (11.37)$$

if  $\theta_1 < \theta_3 < \theta_2$ ; all  $|\sin \dots|$  depending on  $\theta_3$  are maximized onto  $\theta_3 = \frac{\pi}{2}$ . Moreover the mass difference  $m_3^2 - m_2^2$  is proportional to  $E_3$  hence it is largest in modulus when  $E_3 = E_0$ ; however, since  $E_0$  is negligible with respect to  $E_{\text{miss}}$ , this correction is  $\mathcal{O}(\%)$ . In fact, plugging in the Belle II parameters and selecting  $E_{\text{miss}} = 5 \text{ GeV}$

$$\min m_2^2 = 21.5 \text{ GeV}^2 \quad \min m_3^2 = 20.9 \text{ GeV}^2. \quad (11.38)$$

Let me remark that at this point we proved that the volume of  $\bar{\mathcal{P}}_{\text{inv}}^{(n)}$ ,  $n = 2, 3$  is non zero. This is enough for our purpose as QED $^{n \geq 4}$  is negligible with respect to the signal onto  $g_{a\gamma\gamma} \sim 10^{-5} \text{ GeV}^{-1}$ . Nonetheless, in the following section I provide a generalised proof of the previous cases.

## 11.4 Many hard photons, the generic case

An arbitrary number of hard photons can only be divided into backward and forward ones. What  $m_{\text{miss}}$  and  $\eta_{\text{miss}}$  can hard photons reach? Let me recall that

$$m_{\text{miss}}^2 = \left( \sum_{i=1}^n p_i \right)^2 = 2 \sum_{i=1}^n \sum_{i < j} E_i E_j (1 - c_{ij}) =: \sum_{i=1}^n \sum_{i < j} \mu_{ij}, \quad (11.39)$$

where I used

$$c_{ij} := c_i c_j + s_i s_j c\phi_{ij}, \quad c_i := \cos\theta_i, \quad s_i := \sin\theta_i, \quad (11.40)$$

$$c_{ij}^\phi := \cos(\phi_i - \phi_j). \quad (11.41)$$

If all the photons go in the same direction, each  $\mu_{ij}$  can be 0 because we can choose each  $c_{ij} = 1$ . This is attained when all photons are collinear. See fig. 11.7.

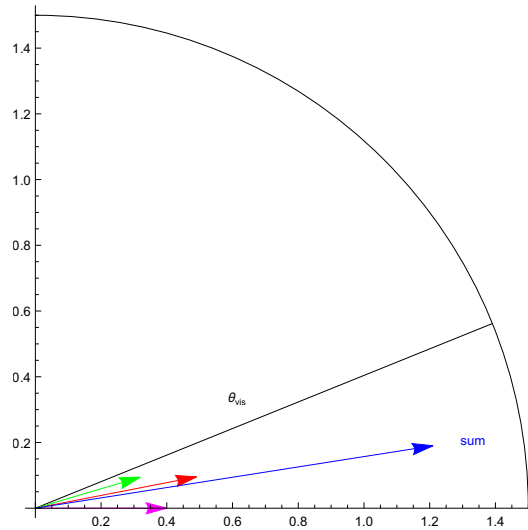


**Figure 11.7.** Example of all forward missed photons. For simplicity we reduced the problem to 2 dimensions. Photons are allowed to polar angles within  $[0, \theta_{\text{vis}}]$ . Their three-momenta are represented with coloured arrows. Their sum is the blue arrow. Its angle too is bound to be within  $[0, \theta_{\text{vis}}]$ .

In this configuration the smallest  $\eta_{\text{miss}}$  will be the one of the largest allowed angle:  $\eta_{\text{miss}}(\theta_{\text{vis}}) = 1.6$ , thus a configuration with all photons in the same hemisphere is not suitable.

If photons are both forward and backward the missing rapidity can be small but the missing mass can not. In fact, recalling that

$$\eta_{\text{miss}} = \frac{1}{2} \log \frac{|\vec{p}_{\text{miss}}| - p_{\text{miss}}^{(z)}}{|\vec{p}_{\text{miss}}| + p_{\text{miss}}^{(z)}}, \quad (11.42)$$

$$p_{\text{miss}}^{(z)} = \sum_{i=1}^n E_i c_i \rightarrow \sum_{i \in \text{forw}} E_i |c_i| - \sum_{j \in \text{back}} E_j |c_j|, \quad (11.43)$$

we find that  $p_{\text{miss}}^{(z)}$  from eq. (11.43) can vanish but  $m_{\text{miss}}^2 = 0$  is no longer allowed because some  $c_{ij}$  from eq. (11.39) can no longer be 1. We depict this configuration in fig. 11.8.

I remind that

11.4.1

#### Problem definition

Our objective is minimising the missing mass of a composite body made of  $n < 10$  invisible hard photons, with the constraints that the missing energy has a lower bound and the missing rapidity is zero.

Energy and rapidity requests can be solved with the energies of two invisible photons, all other variables remaining unconstrained. Specifically azimuthal angles

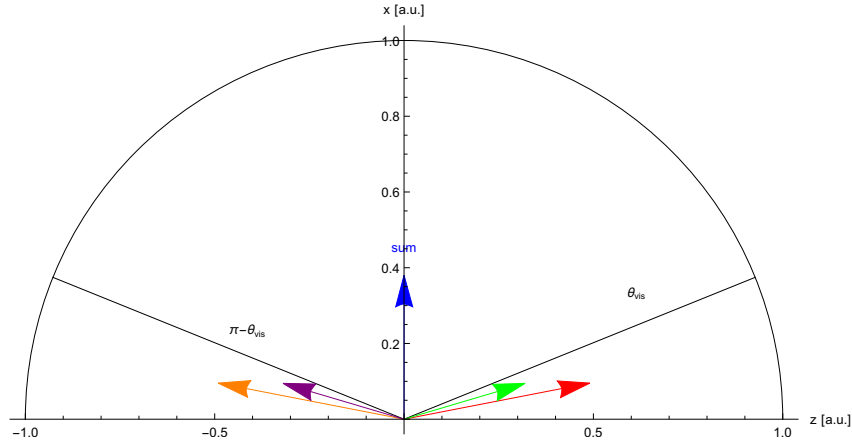


**Figure 11.8.** Example of forward and backward missed photons. For simplicity we reduced the problem to 2 dimensions. Photons are allowed to polar angles within  $[0, \theta_{\text{vis}}]$  or  $[\pi - \theta_{\text{vis}}, \pi]$ . Their three-momenta are represented with coloured arrows. Their sum is the blue arrow. We chose a set of vectors such that the sum has 0 rapidity. However there is a big angular distance among forward and backward photons, therefore the missing mass is big.

are unconstrained, therefore we can learn the best values of the  $\phi_i$  from the easier, unconstrained mass minimization problem.

#### 11.4.1 Unconstrained missing mass minimisation

In this subsection I will demonstrate that the absolute minimum of the mass of a composite body whose components have no constraint is attained when the components three-momenta are coplanar. This will be obtained by making the missing mass gradient vanish.

Consider the missing mass minimization problem without any restriction on missing energy nor angular acceptance. The missing mass is a sum of monomia

$$\mu_{ij} := 2E_i E_j (1 - c_{ij}). \quad (11.44)$$

They are all positive definite and in general their absolute minimum is 0, therefore the absolute minimum of  $m_{\text{miss}}^2$  is 0 and is attained when all of the monomia are null.  $\mu_{ij} = 0$  if at least one of the following is true

$$E_i = 0 \vee E_j = 0 \vee [(\theta_i = \theta_j) \wedge (\phi_i = \phi_j)]. \quad (11.45)$$

From now on we will not be considering the trival cases  $E_{i,j} = 0$ .

Let us now see where the function gradient will point us to. We just write the derivative with respect to one energy, one polar angle and one azimuthal angle, all the others being the same. Since  $m_{\text{miss}}^2$  is invariant under  $p_i \leftrightarrow p_j \forall i, j \in [1, n]$ , we can consider the derivatives with respect to  $E_1, \theta_1, \phi_1$ , and study them:

$$\frac{dm_{\text{miss}}^2}{dE_1} = 2 \sum_{j=2}^n E_j (1 - c_{1j}) \geq 0, \quad (11.46)$$

$$\frac{dm_{\text{miss}}^2}{d\theta_1} = -2 \sum_{j=2}^n E_1 E_j \frac{dc_{1j}}{d\theta_1}, \quad \frac{dc_{1j}}{d\theta_1} = -s_1 c_j + c_1 s_j \cos \phi_{ij}, \quad (11.47)$$

$$\frac{dm_{\text{miss}}^2}{d\phi_1} = -2 \sum_{j=2}^n E_1 E_j \frac{dc_{1j}}{d\phi_1}, \quad \frac{dc_{1j}}{d\phi_1} = -s_1 s_j \sin \phi_{ij}. \quad (11.48)$$

Is there a point such that  $\nabla m_{\text{miss}}^2 = \vec{0}$ ? Yes! Let us consider where each derivative goes to zero.

The sign of the summands of eq. (11.47) is not defined and the summands of eq. (11.48) are positive if  $\phi_1 - \phi_j \in [0, \pi]$  and negative if  $\phi_1 - \phi_j \in [\pi, 2\pi]$ , therefore eqs. (11.46) to (11.48) may go to zero thanks to cancellations.

At variance with eqs. 11.47, 11.48, each summand in eq. (11.46) is positive defined, hence to put their sum to 0 we would need for each of them to be 0. In particular  $\frac{d\mu_{1j}}{dE_1} = 0$  if  $c_{ij} = 1$ . This can either be attained onto

- $\theta_1 = \theta_j = 0 \forall j$ , meaning that all photons fly along the beampipe. This case is uninteresting as it won't be able to satisfy the missing rapidity constraint.
- $\theta_1 = \theta_j$  and  $\phi_1 = \phi_j \forall j$ , i.e. all particles travel along the same direction of  $\gamma_1$ .

The latter case annihilates eqs. 11.47, 11.48 too. This shows that there is a subspace of points satisfying  $\nabla m_{\text{miss}}^2 = \vec{0}$ . Therefore in what follows our minimization strategy will always use  $\phi_1 = \phi_j \forall j$  and  $\theta_1 = \theta_j$  every time it will be possible.

### 11.4.2 Constrained missing mass minimisation

We showed that for the constrained minimisation we can safely assume

$$\phi_i = \phi_j \forall i, j. \quad (11.49)$$

This provides great simplification as there are fewer variables to deal with and the 11.47 no longer change sign. The gradient of

$$m_{\text{miss}}^2 = 2 \sum_{i=1}^n \sum_{i < j} E_i E_j [1 - \cos(\theta_i - \theta_j)] \quad (11.50)$$

has components

$$\begin{aligned} \frac{dm_{\text{miss}}^2}{dE_1} &= 2 \sum_{j=2}^n E_j [1 - \cos(\theta_1 - \theta_j)], \\ \frac{dm_{\text{miss}}^2}{d\theta_1} &= 2 \sum_{j=2}^n E_1 E_j \sin(\theta_1 - \theta_j), \\ \frac{dm_{\text{miss}}^2}{d\phi_1} &= 0. \end{aligned} \quad (11.51)$$

The sign of all the summands in the derivatives is always positive definite, hence it is evident that the minimization is attained onto minimal  $|\theta_i - \theta_j|$ , independently from the energies.

We explained how the central rapidity forces some photons to be forward and some photons to be backward, hence not all  $|\theta_i - \theta_j|$  can be 0. Say we have  $n_F$  forward and  $n_B$  backward photons,  $n_F + n_B = n$ . We will demonstrate that the minimising configuration has  $n_f$  aligned forward photons and  $n_B$  aligned backward photons; the forward and the backward body must be aligned to the edges of the detector-blind region and equally split the missing energy.

Let us write the mass as:

$$m_{\text{miss}}^2 = \left( \sum_{i=1}^{n_F} p_i \right)^2 + \left( \sum_{j=1}^{n_B} p_j \right)^2 + 2 \sum_{i=1}^{n_F} \sum_{j=1}^{n_B} p_i \cdot p_j =: m_F^2 + m_B^2 + m_{BF}^2. \quad (11.52)$$

Is there a point that can make all our  $|\theta_i - \theta_j|$  the smallest at once? Yes. In fact  $m_F^2$  attains its absolute minimum by aligning all polar angles along some direction  $\theta_F$  for forward photons;  $m_B^2$  attains its absolute minimum by aligning all polar angles along some direction  $\theta_B$  for backward photons. At this stage any value of  $\theta_F$  ( $\theta_B$ ) in the forward (backward) cone is as good as the others and gives  $m_{F,B} = 0$ , thus the first two terms in eq. (11.52) are at their absolute minimum. For this choice of angles the third piece of eq. (11.52) reads:

$$m_{BF}^2 = 2 \sum_{i=1}^{n_F} \sum_{j=1}^{n_B} E_i E_j [1 - \cos(\theta_i - \theta_j)] \rightarrow 2[1 - \cos(\theta_B - \theta_F)] \sum_{i,j} E_i E_j. \quad (11.53)$$

It is minimized onto minimal  $|\theta_B - \theta_F|$  which here is  $\theta_F = \alpha_1, \theta_B = \alpha_2$ .

Let us now find the energy configuration that makes  $m_{FB}$  minimal. That's quickly found, as we are basically dealing with two bodies:

$$p_{F,B} = E_{F,B}(1, \sin \alpha_1, 0, \pm \cos \alpha_1), \quad E_{F,B} = \sum_{i=1}^{n_{F,B}} E_i, \quad (11.54)$$

where we used  $\alpha_1 + \alpha_2 = \pi$ . In other words, due to the peculiar configuration of angles that corresponds to the absolute minimum of  $m_F^2$  and  $m_B^2$ ,  $m_{BF}^2$  no longer depends separately on every single energy, but only depends on the sum of forward energies and the sum of backward energies. This means that for minimising we used angles and  $E_{B,F}$  while showing that the missing mass is flat along all other energies combinations. In fact we can rewrite the missing energy constraint as

$$E_{\text{miss}} = E_F + E_B, \quad (11.55)$$

and the central missing rapidity constraint as

$$\cos \alpha_1 (E_F - E_B) = 0, \quad (11.56)$$

which are solved by  $E_F = E_B = \frac{E_{\text{miss}}}{2}$ . Incidentally

$$m_{\text{miss}}^2 \rightarrow 2E_F(E_{\text{miss}} - E_F)[1 - \cos(\alpha_1 - \alpha_2)] \quad (11.57)$$

$$\frac{dm_{\text{miss}}^2}{dE_F} = 0 \text{ if } E_F = \frac{E_{\text{miss}}}{2} \quad (11.58)$$

i.e. the bounds are solved onto the minimizing energy configuration. The value of this lower bound is

$$\min m_{\text{miss}}^2 = E_{\text{miss}}^2 \cos^2 \alpha_1. \quad (11.59)$$

## 11.5 Allowing for one soft photon onto boundaries

We finally show that if we have  $n_F$  forward hard photons,  $n_B = n_H - n_F$  backward hard photons and  $n_s$  soft photons we can get a smaller mass than eq. (11.59) by placing hard photons as above and letting the soft ones stripping the biggest energy they can ( $n_s E_0$ ) while flying perpendicularly to the beam axis.

First, consider that the missing energy and missing rapidity bounds are solved for some energies, say  $E_{1,2}$ , therefore  $m_{\text{miss}}^2$  is a parabola in  $E_{\text{miss}}$ :

$$m_{\text{miss}}^2|_{\text{bounds}} = a_2 E_{\text{miss}}^2 + a_1 E_{\text{miss}} + a_0, \quad a_2 \geq 0. \quad (11.60)$$

This means that the smaller the  $E_{\text{miss}}$  the smaller the  $m_{\text{miss}}^2$ . The energy and rapidity bounds respectively become

$$\left\{ \begin{array}{l} \sum_{i=1}^{n_H} E_i + \sum_{j=1}^{n_s} E_j = E_{\text{miss}}, \\ \sum_{i=1}^{n_H} E_i c_i + \sum_{j=1}^{n_s} E_j c_j = 0. \end{array} \right. \quad (11.61)$$

If all soft polar angles are  $\frac{\pi}{2}$  we fall in the same configuration as before but with a reduced missing energy:

$$\left\{ \begin{array}{l} \sum_{i=1}^{n_H} E_i = E'_{\text{miss}} := E_{\text{miss}} - \sum_{j=1}^{n_s} E_j, \\ \sum_{i=1}^{n_H} E_i c_i = 0. \end{array} \right. \quad (11.62)$$

This demonstrates how by adding an extra soft photon we can produce smaller masses than the full hard case onto  $\eta_{\text{miss}} = 0$ . The minimal mass is now

$$\min m_{\text{miss}}^2 = E_{\text{miss}}^2 c_1^2 - E_s^2 (1 - s_1)^2 - 2E_s E_{\text{miss}} s_1 (1 - s_1), \quad (11.63)$$

where

$$E_s = n_s E_0, \quad c_1 := \cos \alpha_1, \quad s_1 := \sin \alpha_1. \quad (11.64)$$

Equation (11.63) is manifestly smaller than eq. (11.59).

In conclusion we demonstrated that the QED<sup>n</sup> background does have a forbidden ( $m_{\text{miss}}, \eta_{\text{miss}}$ ) region, that it shrinks when  $n$  increases, widens when the missing

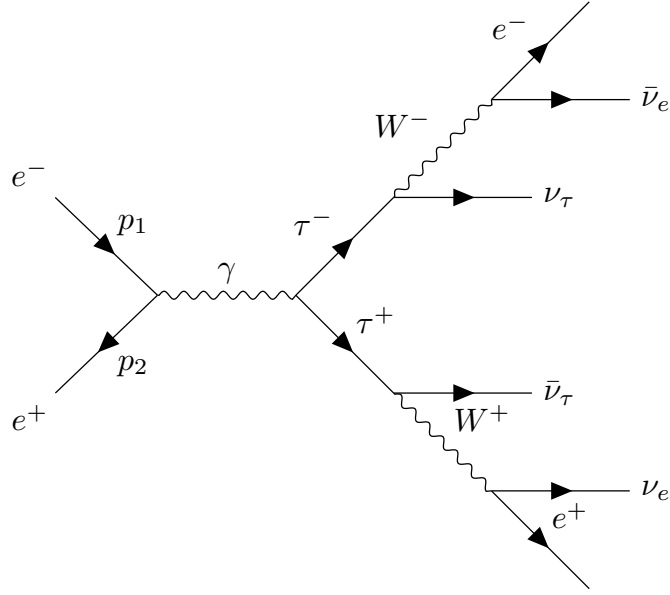


**Figure 11.9.** Feynman diagram for the process  $e^+e^- \rightarrow \tau^+\tau^-$ ,  $\tau \rightarrow \nu\bar{\nu}e$ , i.e. the  $\tau\tau$  background.

energy lower bound is increased and vanishes for a sufficiently large  $n$ . In the following sections we will show how we will exploit this property. Let me remark that this proof is valid not only for photons, but for any particle undergoing the same invisibility requirements.

## 11.6 Background from $\tau\tau$

In this section we describe some remarkable features of the  $\tau\tau$  background (fig. 11.9) that allow us to neatly discard it most of the times. Specifically this scattering can be factorised in three simpler processes whose kinematics is principally driven by the smallness of the  $\tau$  mass with respect to the beam energy.

I will first show how we managed to go background free in the low mass selection. A key observation is  $\tau$  leptons being produced on shell; it follows that the final  $e^\pm$  energies are correlated between themselves. The  $e^+e^- \rightarrow \tau^+\tau^-$  scattering can be considered separately from each of the  $\tau^\pm$  decays. The  $2 \rightarrow 2$  scattering has a simple kinematics: in the center of mass (CoM) the  $\tau$  leptons are back to back, with polar angle  $\theta$ , and have energy  $E_\tau^* = \frac{\sqrt{s}}{2}$ . Define  $\mathcal{F}$  the CoM frame rotated such that the  $\tau$  leptons fly along the  $z$  axis. In the  $\tau^-$  rest frame a body of mass  $m_\tau$  decays in two back to back bodies, one  $e^-$  of mass  $M_e$  and one  $N^- = (\bar{\nu}_e\nu_\tau)$  of mass  $\mu^- \in [0, m_\tau - M_e]$ . They fly along a line of angle  $\theta_-$  and their energies are respectively

$$E_{e^-}^{(\tau^-)} = \frac{M_e^2 - \mu_-^2 + m_\tau^2}{2m_\tau}, \quad E_{N^-}^{(\tau^-)} = \frac{-M_e^2 + \mu_-^2 + m_\tau^2}{2m_\tau}. \quad (11.65)$$

These results are identically valid for the  $\tau^+$ . Since our analysis relies on topology way more than on the matrix element, we do not lose generality when considering:

- $M_e \rightarrow 0$  because the  $e^\pm$  energy has a large enough lower bound  $E^\pm \geq E_0 = 0.25 \text{ GeV} \gg M_e$ ;
- A double antler decay (as in [134]) instead of the full process:  $p_0 \rightarrow \tau^+\tau^-, \tau^\pm \rightarrow e^\pm N^\pm$ , where we neglect the initial  $e^\pm$  and simply consider the initial particles as a single body of fourmomentum  $p_0$  and mass  $\sqrt{s}$  decaying at rest in the CoM, and do not consider that neutral bodies are composite; in other words a  $1 \rightarrow 2 \rightarrow 4$  decay rather than a  $2 \rightarrow 6$  scattering;
- The mass of the composite systems  $\mu_- = \mu_+ = 0$ : as is evident from eq. (11.65), the final electrons are allowed to a bigger phase space in this configuration, while the missing momentum phase space is not shrunk. Therefore if we can find selections that kill  $\tau\tau$  for  $\mu^\pm = 0$  we are guaranteed that  $\mu^\pm \geq 0$  will not populate the regions of the phase space. This will serve our aim of setting lower/upper bounds on the observable kinematic quantities.

In this framework we are left with 3 degrees of freedom: the angles of the  $e^\pm$  with respect to the direction of flight of the  $\tau$  leptons and  $\phi$ , the angle among the planes of the decay products of the  $\tau^\pm$ . Hence in the CoM of Belle II:

$$\begin{aligned}
 p(e^-) &= \frac{m_\tau}{2} \Lambda_-(1, s_-, 0, c_-), \\
 p(N^-) &= \frac{m_\tau}{2} \Lambda_-(1, -s_-, 0, -c_-), \\
 p(e^+) &= \frac{m_\tau}{2} \Lambda_+(1, s_+ c_\phi, s_+ s_\phi, c_+), \\
 p(N^+) &= \frac{m_\tau}{2} \Lambda_+(1, -s_+ c_\phi, -s_+ s_\phi, -c_+), \\
 p_{\text{miss}} &= p(N^-) + p(N^+).
 \end{aligned} \tag{11.66}$$

where  $\Lambda_\pm$  is the Lorentz matrix that boosts from the  $\tau^\pm$  rest frame to the CoM and  $s_x = \sin \theta_x, c_x = \cos \theta_x, x = +, -, \phi$ . Two properties spawn from eq. (11.66), one affecting the low mass selection and one affecting high mass selection. As to low missing masses, eq. (11.66) show that the final electrons energies are correlated. Then in most cases they can not satisfy the signal region cut. We depict this in figs. 11.10 and 11.11: in fig. 11.10 we show the  $\tau$  background before the signal region cut. In fig. 11.11 we show how the  $\tau$  background loses events with big final  $e^\pm$  CoM energy.

The edge of the empty space is parameterized by a hyperbole which we describe in section 11.7.1 and will use to our advantage to kill this background.

As to high masses, we exploit the fact that the  $\tau$  leptons are considerably boosted in the CoM frame, implying that they carry their decays products within a narrow cone along their direction of flight. In a numeric simulations we could reproduce that the distribution of the cosine of the angle among  $e^\pm$  in the CoM,  $c_{ee}$ , always starts from -1 regardless of the  $m_{\text{miss}}$  selection; if small and intermediate masses are selected, the distribution is peaked around -1 and has a tail toward  $c_{ee} \rightarrow 1$ . The bigger the selected mass, the further this tail manages to reach. We claim this behaviour can

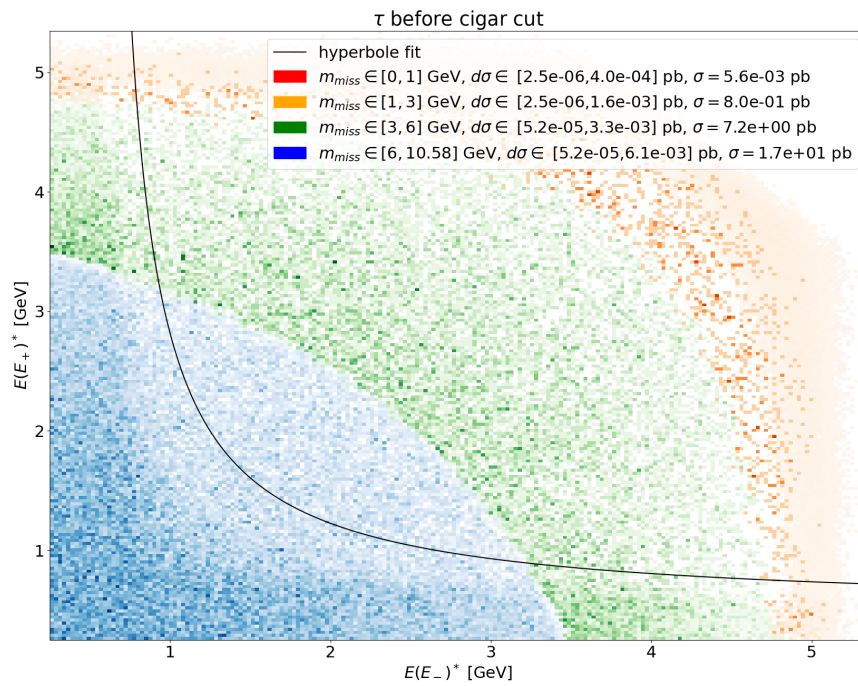


**Figure 11.10.**  $\tau$  background distribution with respect to the final electrons energies (in the CoM). Events were categorized in 4 missing mass groups. Darker bins correspond to higher cross section. No cut applied. The black line is eq. (11.74).

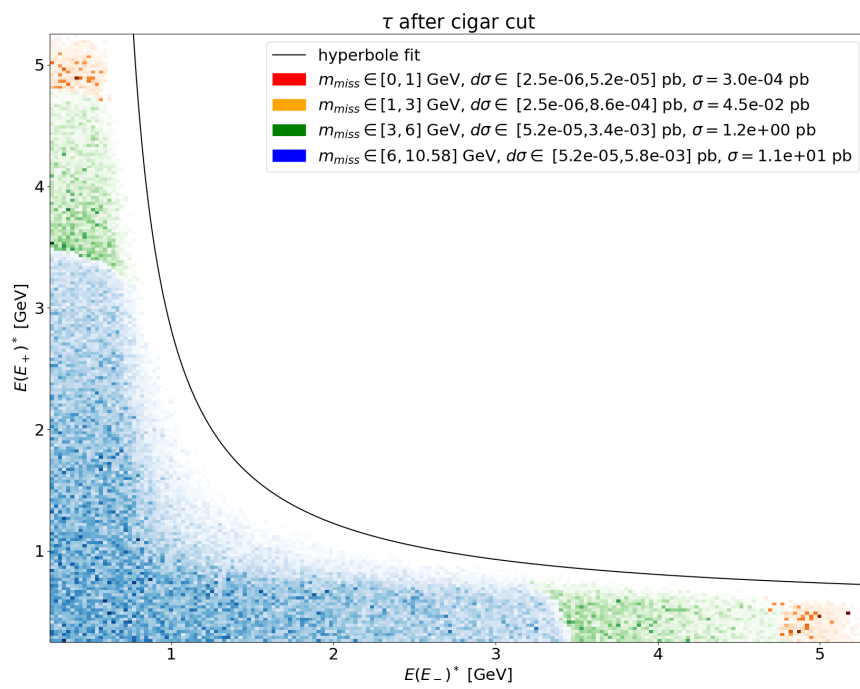


**Figure 11.11.** As in fig. 11.10 but the signal region cut was applied. Only events below the hyperbole could survive.

be explained through this simplified  $e^+e^- \rightarrow \tau^+\tau^-, \tau^\pm \rightarrow e^\pm N^\pm$  scattering we are considering; we depicted it in fig. 11.12. The boost on  $e^\pm$  projects the  $[0, \pi]$  domain of their angles in  $\tau^\pm$  rest frame non linearly in a  $[0, \pi]$  image, such that  $e^\pm$  and  $N^\pm$  tend to be emitted close to the  $\tau^\pm$  axis; hence, the cosine of the angle among  $e^+$  and  $e^-$  in the CoM tends to be close to -1, see fig. 11.13. To read this picture, take the  $z$  axis as the line of flight of  $\tau^\pm$ .  $\mathcal{F}^\pm$  is the rest frame of  $\tau^\pm$  (centre and bottom panel of fig. 11.12). Following eq. (11.66),  $\cos \theta_-^{\mathcal{F}^-}$ , for example, is the cosine of the  $e^-$  polar angle in the  $\tau^-$  rest frame.  $\cos \theta_-^*$  is the cosine of the  $e^-$  polar angle in the CoM frame (top panel of fig. 11.12). In both cases the polar angle is computed from the  $\tau$  leptons line of flight. To go from one rest frame to the other we perform a boost along the  $z$  axis, for the  $e^-$  along the positive direction, for the  $e^+$  along the negative direction. In both cases the Lorentz  $\beta = 0.94$ . The blue solid line is the transformation of  $\cos \theta_-^{\mathcal{F}^-}$  into  $\cos \theta_-^*$ . In formulas

$$\cos \theta_-^* = \frac{\cos \theta_-^{\mathcal{F}^-} + \beta}{\cos \theta_-^{\mathcal{F}^-} \beta + 1}. \quad (11.67)$$

Analogously for  $\cos \theta_+^*$ , represented in the solid yellow line.

Since we are neglecting the  $\tau^- \rightarrow e^- \nu_e \bar{\nu}_\tau$  matrix element for this section, we can pretend  $\cos \theta_-^{\mathcal{F}^-}$  is uniformly distributed. It follows that the mean  $\cos \theta_-^*$  is

$$\langle \cos \theta_-^* \rangle = \frac{\beta_- - \epsilon^2 \operatorname{arctanh} \beta_-}{\beta_-^2} \quad (11.68)$$

$$= 1 + \epsilon^2 \left( \frac{1}{2} + \log \frac{\epsilon}{2} \right) + \mathcal{O}(\epsilon^4 \log(\epsilon)) \quad (11.69)$$

$$\epsilon^2 := \frac{4m_\tau^2}{s} = 0.11 \quad (11.70)$$

$$\beta_- := \sqrt{1 - \epsilon^2} \quad (11.71)$$

In numbers  $\langle \cos \theta_\pm^* \rangle = \pm 0.84$ , i.e. the final electrons are aligned to their parent  $\tau$ . If the  $\tau$  leptons are back to back, then also  $\langle c_{ee} \rangle \sim -1$ .

The missing mass is

$$m_{\text{miss}}^2 = (p(N^-) + p(N^+))^2 = (\mu^-)^2 + (\mu^+)^2 + 2p(N^-) \cdot p(N^+) = 2p(N^-) \cdot p(N^+) = 2E(N^-)E(N^+)(1 - c_{NN}) \quad (11.72)$$

It is maximal when the neutral bodies energies  $E(N^\pm)$  are big and they fly in opposite directions ( $c_{NN} \rightarrow -1$ ). Both of these properties can be obtained if we align each  $N^\pm$  to the parent  $\tau^\pm$  direction of flight: in this way the boost from the  $\tau$  rest frame to the CoM keeps them back to back and maps their energies onto their CoM maximum. Consequently,  $e^\pm$  fly oppositely with respect to their parent  $\tau$  and the boost will make their energy small in the CoM. Although small angle windows in the  $\mathcal{F}^\pm$  frames are allowed to  $e^\pm$  in order to get a big mass, the big boost projects them onto almost all the  $[0, \pi]$  domain. This explains why bigger  $c_{ee}$  are reached when we ask for larger masses and why the peak on  $c_{ee} \sim -1$  broadens. Our simulations show that the said effects are enhanced by the SM matrix element, therefore in next section we will use  $c_{ee} > 0.4$  as a selection.

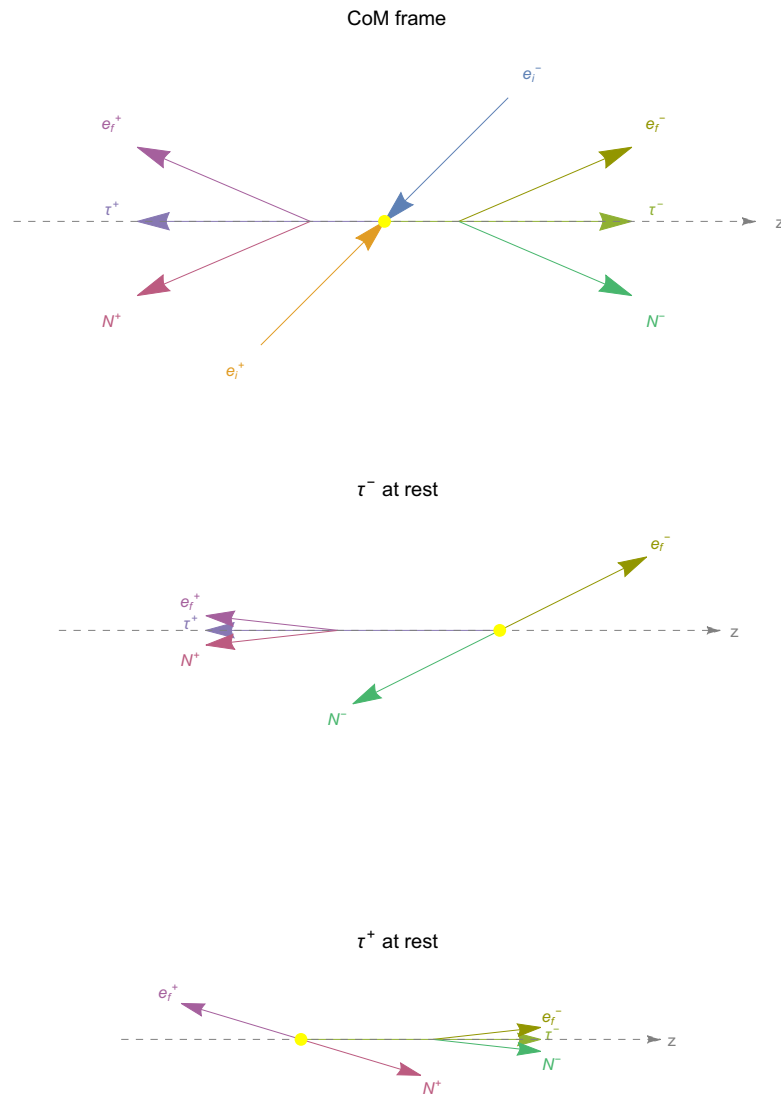


**Figure 11.12.** Cartoon for the process  $e^+e^- \rightarrow \tau^+\tau^-$ ,  $\tau^\pm \rightarrow e^\pm N^\pm$  in three reference frames, from top to bottom: CoM,  $\tau^-$  rest frame,  $\tau^+$  rest frame.

## 11.7 Cuts and regimes

We will be dividing our analysis in three regimes, one for *small* masses (below 6 GeV), one for high masses ( $m_{\text{miss}} \in (6, 8)$  GeV) and one for ultra high masses ( $m_{\text{miss}} > 8$  GeV). This comes from the fact that our backgrounds prefer to produce small missing masses and its cross section greatly overcomes that of the signal, imposing us to go search for an ALP signal only in the Belle II blinded kinematic region. However  $\sim 6$  GeV define the threshold where this region closes, making a different approach necessary. On the other hand, the bigger the  $m_{\text{miss}}$  the more similar the signal becomes to the background: if for high masses the missing rapidity and the angle among the final electrons can distinguish the signal from the background, at ultra high masses the  $m_{\text{miss}}$  selection is the only thing that is left to do.

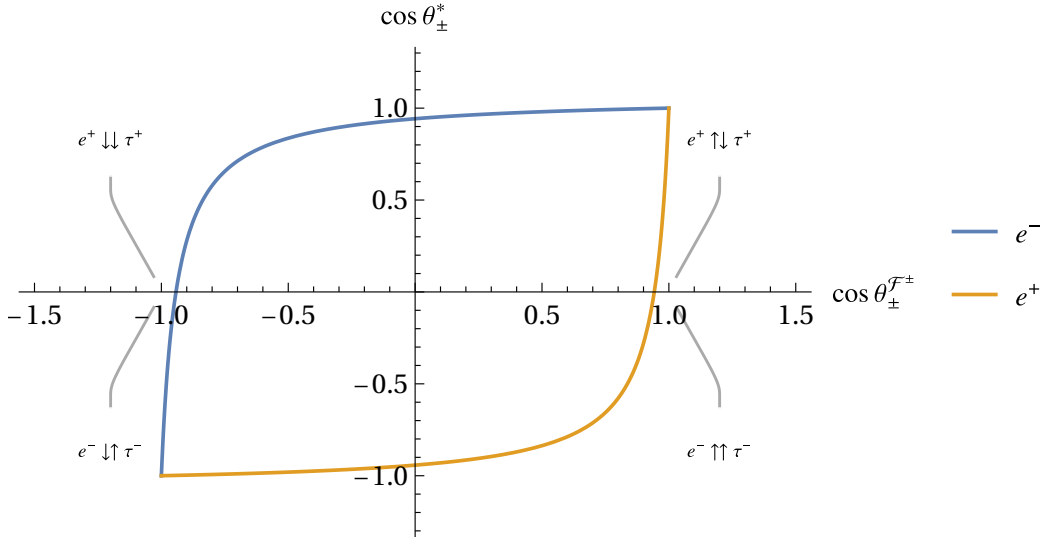


**Figure 11.13.** Representation of eq. (11.67). See text for definitions.

In what follows all pictures show smeared events except when differently specified.

### 11.7.1 Cuts used in the small mass analysis

#### signal region

Numerically the signal region cut means we will select events with

$$10.437 \text{ GeV} - 1.155E_{\text{miss}} \leq |\vec{p}_{\text{miss}}| \leq 12.437 \text{ GeV} - 1.155E_{\text{miss}}. \quad (11.73)$$

#### Hyperbole cut

This cut is implemented to select the  $\tau\tau$  background ( $E(e^+), E(e^-)$ ) area that is depleted after the signal region cut:

$$E_+^* > 0.50 \text{ GeV} + \frac{1.06 \text{ GeV}^2}{-0.54 \text{ GeV} + E_-^*}. \quad (11.74)$$

No event will be taken below the positive branch.

Figure 11.10 shows that the area around the sharp edge induced by the signal region cut is satisfactorily populated so that when we will consider events above the hyperbole we can be sure that we are not going background free thanks to any poor MC area exploration.

#### Parabola cut

Figure 11.14 shows the forbidden area to the QED background when the signal region selection is applied.

The edge of the empty space is parametrized by a parabola. Numerically:

$$m_{\text{miss}}^2 < -20.41(\eta_{\text{miss}}^* - 1.4)(\eta_{\text{miss}}^* + 1.4) \text{ GeV}^2. \quad (11.75)$$

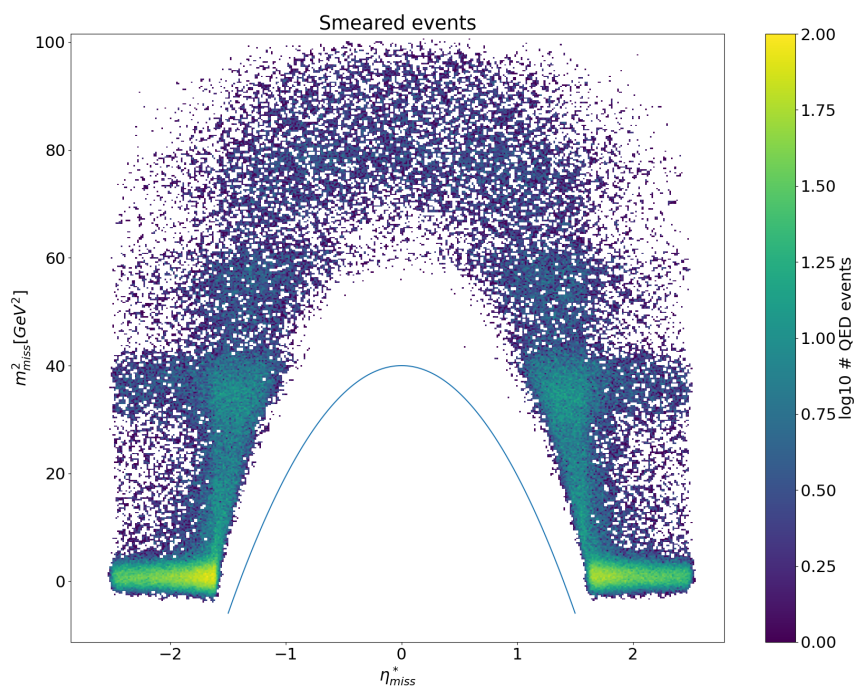


Figure 11.14.  $e^+e^- \rightarrow e^+e^-2\gamma_{\text{inv}}$  smeared events in the  $(m_{\text{miss}}, \eta_{\text{miss}})$  plane.

$M_a$ [GeV]	$m_0$ [GeV]	$m_1$ [GeV]
6.31	5.94	6.68
8.50	8.24	8.76
7.50	7.17	7.83
9.00	8.76	9.24
9.50	9.30	9.70
8.00	7.73	8.27
6.50	6.14	6.86
7.00	6.69	7.31

**Table 11.1.** Optimizing mass interval for high and ultra-high mass search: both on signal and background we impose  $m_0 \leq m_{\text{miss}} \leq m_1$ .

### 11.7.2 Cuts in the high mass analysis

#### $m_{\text{miss}}$ cut

For each nominal ALP mass we measured the interval  $[m_0, m_1]$  such that

$$m_0 \leq m_{\text{miss}} \leq m_1. \quad (11.76)$$

In fig. 11.2 we can see why it is not convenient to use large ranges, while for bigger masses this is more suitable. We report them in fig. 11.3 and table 11.1.

The efficiency of this cut depends on the fact that at high missing masses the background distribution in  $m_{\text{miss}}$  is uniform while that of the signal is peaked around  $M_a$ .

#### Angle between final electrons

In the high mass regime we will consider only those events having

$$c_{\pm} := \cos \theta(e^-, e^+)^* \geq 0.4 \quad (11.77)$$

In fact the signal has two comparably contributing  $s$  and  $t$ -channels. This allows for a prominent  $c_{\pm} \sim 1$  peak in the signal, as can be seen in fig. 11.17. On the other hand a big portion of the QED background (fig. 11.15) and most of the  $\tau\tau$  background (fig. 11.16) can be cut away, as we motivated in section 11.6.

#### $\eta_{\text{miss}}^*$

The background missing rapidity distribution does not exhibit any remarkable feature while the signal tends to prefer central missing particles hence selecting rapidities around 0

$$-0.5 \leq \eta_{\text{miss}}^* \leq 0.5 \quad (11.78)$$

will rule out a lot of background, see figs. 11.18 to 11.20

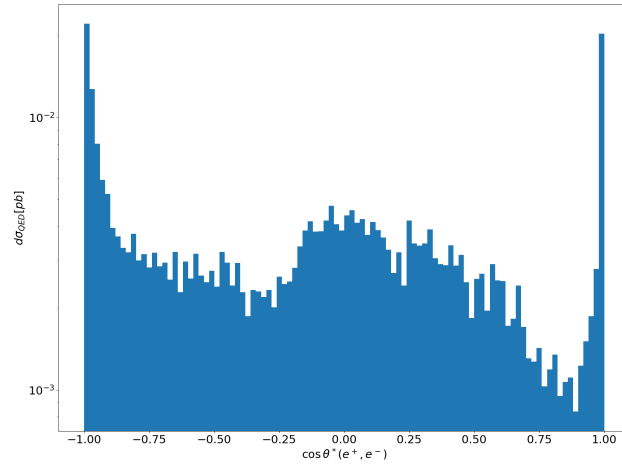


**Figure 11.15.** QED cross section distribution with respect to the cosine of the Centre of Mass angle among final electrons.  $c_{\pm} < 0$  values are preferred. We imposed  $6.3 \text{ GeV} \leq m_{\text{miss}} \leq 6.7 \text{ GeV}$ .

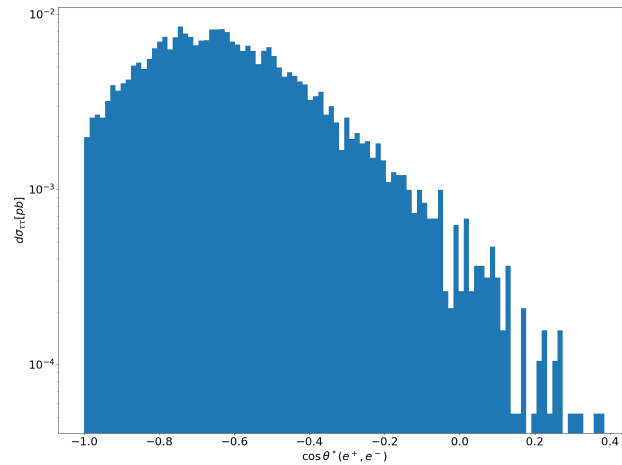


**Figure 11.16.**  $\tau$  cross section distribution with respect to the cosine of the Centre of Mass angle among final electrons.  $c_{\pm} < 0$  values are preferred. We imposed  $6.3 \text{ GeV} \leq m_{\text{miss}} \leq 6.7 \text{ GeV}$ .

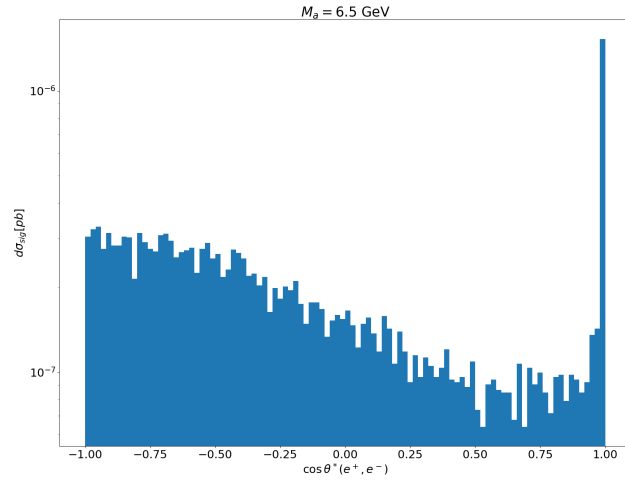


**Figure 11.17.** Signal cross section distribution with respect to the cosine of the Centre of Mass angle among final electrons. Two features are evident: a narrow preference for  $c_{\pm} \sim 1$  and some broader enhancement around  $c_{\pm} \sim -1$  which becomes more evident when  $M_a \rightarrow \sqrt{s}$ . The MC mass is  $M_a = 6.5$  GeV.

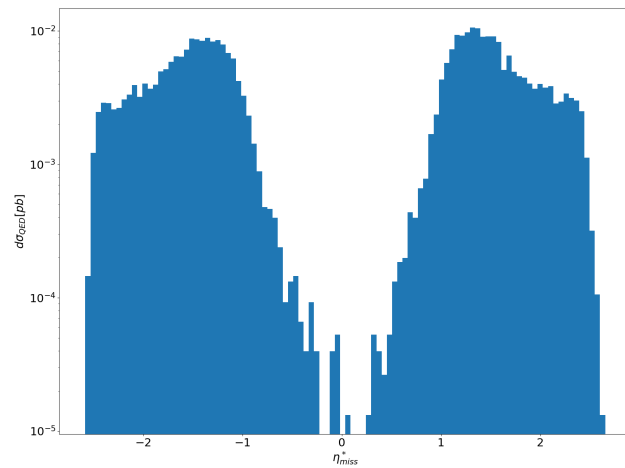


**Figure 11.18.** QED cross section distribution with respect to the Centre of Mass missing rapidity. We imposed  $6.3 \text{ GeV} \leq m_{\text{miss}} \leq 6.7 \text{ GeV}$ .

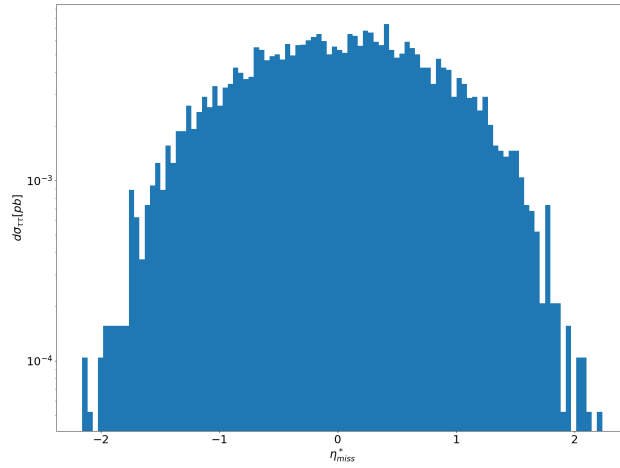


**Figure 11.19.**  $\tau$  cross section distribution with respect to the Centre of Mass missing rapidity. We imposed  $6.3 \text{ GeV} \leq m_{\text{miss}} \leq 6.7 \text{ GeV}$ .

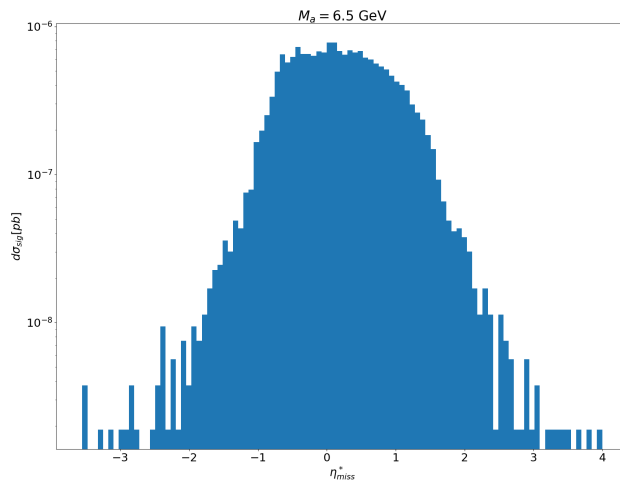


**Figure 11.20.** Signal cross section distribution with respect to the Centre of Mass missing rapidity. The MC mass is  $M_a = 6.5 \text{ GeV}$ .

### Ultra high mass

Phase space closure makes most of the signal characteristics fade away so that the mass selection could be the only effective selection to apply.

In conclusion we summarise our search strategy. We identify three mass ranges: low and intermediate, high masses and ultra high masses. For low and intermediate masses up to  $M_a \sim 6$  GeV we exploit two aspects, the detector blind spot in the  $(m_{\text{miss}}, \eta_{\text{miss}})$  space in which the QED background vanishes, and the  $(E_{\text{miss}}, |\vec{p}_{\text{miss}}|)$  space in which the signal rate is concentrated. Selecting events only in the latter area has a positive effect as the  $(m_{\text{miss}}, \eta_{\text{miss}})$  QED forbidden space widens; plus, the  $\tau\tau$  background obtains a large empty area in the  $(E(e^-), E(e^+))$  space. Finally the low and intermediate analysis consists in three selections, the so called signal region cut, the parabola cut in the  $(m_{\text{miss}}, \eta_{\text{miss}})$  space and the hyperbole cut in the  $(E(e^-), E(e^+))$  space.

For high masses constraining the missing mass becomes efficient again since the smearing has a smaller impact; we also apply selections on the missing rapidity and the cosine of the angle between the final electrons.

On ultra high masses we only constrain the missing mass.

## Chapter 12

# Conclusions

In this dissertation we considered the production of an Axion-Like Particle from an electron-positron scattering. In particular we addressed the Vector Boson Fusion  $e^+e^- \rightarrow e^+e^-a$ , since it appeared to us that this kind of process got unfairly neglected in the literature. Some analytic demonstration was needed to prove our point. In chapter 2 I showed that taming the VBF analytic integration is not a task to take naïvely. But as you know, whenever there is a problem, there always is someone from the 70s who already solved it. This was (almost) my case: [93] addresses the  $2 \rightarrow 3$  pure Phase Space distribution problem.

Their language is Mandelstam variables and Gram Determinants, which we learned in chapters 3 and 4. If one is convinced as she should be of the necessity of pursuing this as the only viable route for analytically describing the VBF, one's next necessity will be orienting oneself in the 70s jargon. I hope that chapters 3 and 4 will serve the community as an Ariadne's thread through this literature and that the reader could not only appreciate my (*per se* relevant) archaeological work, but also my modern contributions: in those sections I tried to work in full generality such that many results are provided for a generic  $m \rightarrow n$  process, some other for a generic  $2 \rightarrow 3$  scattering and the results specific to the  $e^+e^- \rightarrow e^+e^-a$  fusion were provided when necessary, so that there will be no difficulty to consider other processes. I tied the GD concept to known functions like the triangular  $\lambda$  (section 3.2) or the Dalitz plots (section 4.2.2); I explained how to convert from the usual polar coordinates to GDs and showed how easily the Phase Space boundary is expressed in terms of them (sections 3.3 and 3.4).

All this allowed us to finally characterise the  $2 \rightarrow 3$  phase space (section 4.2.2): one of the most important results of the dissertation is that we can build increasingly more complex but increasingly smaller and more precise Phase Space volume if we consider higher orders of  $(-1)^{n+1}\Delta_n \geq 0$  (verified onto all possible arguments, see corollary 5). This means that the Phase Space problem can become as easy as finding the roots to an order 2 polynomial. It did not happen to me to come across any literature stating <sup>1</sup> that the GD formalism has such an inbuilt characteristic, neither it happened to me to find an equivalently straightforward method to approximate a generic Phase Space within other formalisms. Moreover, this statement is constructive as it allowed us to perform all of the computations appearing in

---

<sup>1</sup>At least not as explicitly as I did.

chapters 5 to 7. These are original results as I did not limit myself to the Phase Space integration but considered a non constant matrix element.

If in this dissertation I limited myself to some spin blind matrix elements, I leave for future work considering more complicated integrands, although I was able to demonstrate that spin blindness is a completely valid approximation in many cases (section 7.3).

It was not necessary to actually compute all the distributions we provided as for half of them it was sufficient to rely on the symmetries of the problem: in chapter 6 we reflected upon the fact that the GD formalism makes it blatant that the phase space is symmetric under whatever fourmomenta permutation you may think of. Depending on your matrix element you will be able to keep some of those symmetries and to get some cross section distributions for free.

With this, we could thoroughly characterized the  $e^+e^- \rightarrow e^+e^-a$  scattering and declare it suitable for the Equivalent Photon Approximation (section 8.2): we recovered the the right approximation for a fully scalar theory, applied it to both our vectors (photons) fusing into our boson (ALP) and retrieved a simplified cross section, peaking just where the GD method predicted, onto resting ALP.

These theoretical considerations helped us to move to some more phenomenological aspects. In both chapters 10 and 11 we deliver some solid results as they add up to the fundamental BSM research the whole community is addressing to in these years. If on the one hand simplicity and simplification are principles without whom science simply could not exist, oversimplification can mean being blind to groundbreaking discoveries. We hope that this work was sufficiently general and complete to help our readers to address their difficulties with  $2 \rightarrow 3$  Vector Boson Fusion, both under a theoretical and phenomenological point of view.

The most important results of this channels are the Belle II sensitivities figs. 10.5 and 11.1. Their value not only comes from proving the importance of the VBF as a complementary and independent way to search for ALPs at high intensity  $e^+e^-$  colliders, but also from the strategies we adopted for obtaining them, mostly in the invisible case. Our original selection gained us the possibility of a high purity search of great importance for the present scattering but also for other ones. In fact, the search strategy we propose can be extended to other possible BSM production of invisible particles, such as  $\gamma'$  production. We leave the investigation of the reach on this type of signal to future work.

Another layer of generality of our work comes from it depending only on few characteristics of Belle II: we only used the leptonic nature of the beams and the blindness of the detector for some energies and angles; for example we did not use the most remarkable peculiarity of Belle II, that of having a boosted CoM with the energy of the  $\Upsilon(4S)$ .

The importance of fusion production mechanism for invisible ALP signatures that we highlight at Belle II, can be carried over many other experimental setups, including other present high-intensity  $e^+e^-$  colliders as well as future colliders. Significant differences can arise in the latter case, as new backgrounds due to electroweak bosons arise, hence we defer this extension of our investigation to a future work.

# Appendices

## A Shortcuts

## B Acronyms

**SM** Standard Model.

**SSM** Scalar Standard Model (see its rules in section 2.2).

**BSM** Beyond the Standard Model.

**ALP** Axion-Like Particle.

**gMv** Generalized Mandelstam Variable.

**CoM** Centre of Mass (frame).

**GD** Gram Determinant.

**PGD** Principal Gram Determinant (given a set of fourmomenta, the PGD is the symmetric GD computed onto the largest set of independent fourmomenta).

**LC** Levi-Civita symbol (full asymmetric  $\epsilon_{\alpha_1\alpha_2\dots}$ ).

**LS** Lepton Swap

**EPA** Equivalent Photon Approximation

**PS** Phase Space

**VBF** Vector Boson Fusion, in this dissertation always used to refer to  $e^+e^- \rightarrow e^+e^-a$ .

**ALP-strahlung**  $e^+e^- \rightarrow \gamma a$ , also referred to as mono- $\gamma$ .

## C Polar coordinates

- $m_i$  = mass of the  $i$ th particle. For  $e^+e^- \rightarrow e^+e^-a$  we used  $m_i = M_e \forall i \neq 4, m_4 = M_a$ .
- $\epsilon := \frac{M_e}{\sqrt{s}}$

- $E_i$  = energy of the  $i$ th particle.
- $\theta_i$  = polar angle of the  $i$ th particle.
- $c_i, s_i$  = cosine and sine of the  $i$ th particle polar angle respectively.
- $c_{ij}$  = cosine among the  $i$ th and  $j$ th particle.
- $\phi_i$  = azimuthal angle of the  $i$ th particle.
- $c_i^\phi, s_i^\phi$  = cosine and sine of the  $i$ th particle azimuthal angle respectively.

## D Belle II parameters

- $\sqrt{s}$  = CoM energy=10.58 GeV
- $p_1 = e^-$  fourmomentum. In Lab

$$p_1^{\text{Lab}} = (E_1, 0, 0, \sqrt{E_1^2 - M_e^2}), \quad E_1 = 7 \text{ GeV}. \quad (\text{D.1})$$

In CoM

$$p_1^{\text{CoM}} = \left( \frac{\sqrt{s}}{2}, 0, 0, \sqrt{\frac{s}{4} - M_e^2} \right). \quad (\text{D.2})$$

- $p_2 = e^+$  fourmomentum. In Lab

$$p_2^{\text{Lab}} = (E_2, 0, 0, -\sqrt{E_2^2 - M_e^2}), \quad E_2 = 4 \text{ GeV}. \quad (\text{D.3})$$

In CoM

$$p_2^{\text{CoM}} = \left( \frac{\sqrt{s}}{2}, 0, 0, -\sqrt{\frac{s}{4} - M_e^2} \right). \quad (\text{D.4})$$

- $p_0$  = initial fourmomentum. In Lab

$$p_0^{\text{Lab}} = (E_1 + E_2, 0, 0, \sqrt{E_1^2 - M_e^2} - \sqrt{E_2^2 - M_e^2}) \simeq (11, 0, 0, 3) \text{ GeV}. \quad (\text{D.5})$$

In CoM

$$p_0^{\text{CoM}} = (\sqrt{s}, 0, 0, 0). \quad (\text{D.6})$$

- $E_0$  = CoM energy threshold that leptons and photons have to overcome to be detected by the calorimeter.  $E_0 = 0.25 \text{ GeV}$ .
- $\theta_{\text{vis}}$  = In the CoM frame, leptons and photons must have polar angle in  $[\theta_{\text{vis}}, \pi - \theta_{\text{vis}}]$  to be detected by the calorimeter.  $\theta_{\text{vis}} = 22^\circ$ .

## E The 2 → 3 scattering

**Convention 3.**

$$p_1 + p_2 \rightarrow p_3 + p_4 + p_5, \quad (\text{E.7})$$

$$p_i^2 = m_i^2, \quad (\text{E.8})$$

$$\vec{m} := (m_1, m_2, m_3, m_4, m_5). \quad (\text{E.9})$$

□

**Definition 27.**

$\mathcal{P}_5 = 2 \rightarrow 3$  scattering or  $1 \rightarrow 4$  decay phase space.

□

**Definition 28** (gMVs  $(s_1, s_2, t_1, t_2)$  and auxiliary variables  $(u_{1,5})$ ).

$$\begin{aligned} s &:= (p_1 + p_2)^2, & u_1 &:= (p_3 + p_5)^2, \\ s_1 &:= (p_3 + p_4)^2, & u_2 &:= (p_1 - p_5)^2, \\ s_2 &:= (p_4 + p_5)^2, & u_3 &:= (p_2 - p_3)^2, \\ t_1 &:= (p_1 - p_3)^2, & u_4 &:= (p_2 - p_4)^2, \\ t_2 &:= (p_2 - p_5)^2, & u_5 &:= (p_1 - p_4)^2. \end{aligned} \quad (\text{E.10})$$

□

**Property 1** (From scalar products to gMVs).

$$\begin{aligned} p_{12} &= \frac{s - m_1^2 - m_2^2}{2}, & p_{23} &= \frac{s - s_2 + t_1 - m_1^2}{2}, \\ p_{34} &= \frac{s_1 - m_3^2 - m_4^2}{2}, & p_{24} &= \frac{s_2 - t_1 + t_2 - m_5^2}{2}, \\ p_{45} &= \frac{s_2 - m_4^2 - m_5^2}{2}, & p_{14} &= \frac{s_1 + t_1 - t_2 - m_3^2}{2}, \\ p_{13} &= -\frac{t_1 - m_1^2 - m_3^2}{2}, & p_{15} &= \frac{s - s_1 + t_2 - m_2^2}{2}, \\ p_{25} &= -\frac{t_2 - m_2^2 - m_5^2}{2}, & p_{35} &= \frac{s - t_1 + t_2 - m_5^2}{2}. \end{aligned} \quad (\text{E.11})$$

□

**Property 2** (From gMVs to auxiliary and vice versa).

$$\begin{aligned} u_1 &= m_3^2 + m_4^2 + m_5^2 + s - s_1 - s_2, & s &= u_1 - u_4 - u_5 + m_1^2 + m_2^2 + m_4^2, \\ u_2 &= m_1^2 + m_2^2 + m_5^2 - s + s_1 - t_2, & s_1 &= u_2 - u_3 - u_4 + m_2^2 + m_3^2 + m_4^2, \\ u_3 &= m_1^2 + m_2^2 + m_3^2 - s + s_2 - t_1, & s_2 &= -u_2 + u_3 - u_5 + m_1^2 + m_4^2 + m_5^2, \\ u_4 &= m_2^2 + m_4^2 + m_5^2 - s_2 + t_1 - t_2, & t_1 &= -u_1 - u_2 + u_4 + m_1^2 + m_3^2 + m_5^2, \\ u_5 &= m_1^2 + m_3^2 + m_4^2 - s_1 - t_1 + t_2, & t_2 &= -u_1 - u_3 + u_5 + m_2^2 + m_3^2 + m_5^2. \end{aligned} \quad (\text{E.12})$$

□

**Property 3** (SSM Matrix element).

$$\mathcal{M}_s \rightarrow \frac{1}{su_1}, \quad \mathcal{M}_t \rightarrow \frac{1}{t_1 t_2}. \quad (\text{E.13})$$

□

**Theorem 23** (Permutation from s to t channel).

$$\sigma_s^t \mathcal{S}_0 = (-3, 1, 5, 4, -2), \quad (\text{E.14})$$

$$\sigma_s^t \mathcal{M}(\mathcal{S}_0) = (t_1, s_2, u_4, u_1, s, t_2, u_3, u_2, u_5, s_1). \quad (\text{E.15})$$

□

**Definition 29** (Lepton Swap permutation).

$$\sigma_{\text{LS}} \mathcal{S}_0 = (2, 1, 5, 4, 3), \quad (\text{E.16})$$

$$\mathcal{M}(\mathcal{S}_{\text{LS}}) := (s, s_2, s_1, t_2, t_1, u_1, u_3, u_2, u_5, u_4). \quad (\text{E.17})$$

□

**Definition 30** (Big  $M_a$  parametrization).

$$M_a = \sqrt{s} - 2(1 + \alpha)M_e. \quad (\text{E.18})$$

□

**Definition 31** ( $\mathcal{G}_{1,2}$ ).

$$\mathcal{G}_1 = \frac{M_e^2 s_1^2}{2} - s_1 \left( \frac{st_2}{2} + M_e^4 \right) + \frac{1}{2} (M_e^6 - 3M_e^2 st_2 + st_2(s + t_2)) \quad (\text{E.19})$$

$$\begin{aligned} \mathcal{G}_2 &= \frac{t_1 s_1^2}{2} - \frac{1}{2} s_1 (M_a^2 + 2M_e^2 + t_2 - t_1) \\ &+ \frac{1}{2} (M_a^4 M_e^2 + M_e^4 t_1 + M_e^2 t_2 (t_2 - t_1) + M_a^2 (t_1 t_2 - M_e^2 (t_1 + 2t_2))) \end{aligned} \quad (\text{E.20})$$

□

**Definition 32.**

In a scattering where the two incoming fourmomenta are  $p_{1,2}$ , the collision flux will always depend on a triangular lambda like

$$\lambda_{\text{in}} := \lambda(s, m_1^2, m_2^2). \quad (\text{E.21})$$

□

### E.1 Dimensionality of frequently occurring quantities

- Gram determinants of dimension  $n$  can be thought as  $\prod_{i=1}^n \lambda_i$ , each  $\lambda_i$  having dimension  $s$ . Then

$$[\Delta_n(\cdot)] = s^n. \tag{E.22}$$

Consequently  $[\mathcal{D}] = s^{-2}$ .

- In general the 3 entries of the triangular  $\lambda$ s need to have the same dimensionality; since they all come from Gram determinants of dimension 2, all arguments have the same dimension of  $s$ . As the  $\lambda$ s linearly combine products of 2 of their entries, it will always be  $[\lambda(\cdot, \cdot, \cdot)] = s^2$ .
- The couplings dimensionality depends on the theory. As we will be using a full scalar theory we can anticipate that  $[c_{ee\gamma}] = [c_{a\gamma\gamma}] = \sqrt{s}$  and  $|\mathcal{M}|^2 = \frac{1}{t_1^2 t_2^2} \rightarrow [|\mathcal{M}|^2] = s^{-4}$ .
- $[f] = s$ .
- $[\sigma_0] = s$ .
- $[s_1] = [s_2] = [t_1] = [t_2] = s$  then  $[d\mu_L] = s^4$ .
- A proper cross section is expected to have the same dimension as  $s^{-1}$ , which is the case.

## F Gram determinants and Levi-Civita symbols

In section 2.1 we stopped at eq. (2.6) claiming that the Levi-Civita symbols (LCs) contraction makes the difficulty of the square amplitude numerator blow up. In this section we will show that GDs can be handy for at least write down a more compact numerator. First, I will demonstrate that contractions of 2 Levi-Civita symbols and a set of  $2n, n \in [0, 4]$  4momenta will generate a Gram determinant of dimension  $n$  (appendix F.1). Then I will use this property in a simple rewriting of the complete ALP theory square amplitude.

### F.1 From the product of two Levi-Civita symbols to the determinant of a matrix of metric tensors

At school we are thought that [106]

**Theorem 24** (Two Levi-Civita symbols and the metric tensor).

$$\epsilon^{\mu_1 \mu_2 \mu_3 \mu_4} \epsilon^{\alpha_1 \alpha_2 \alpha_3 \alpha_4} = -\det A(\vec{\mu}, \vec{\alpha}), \tag{F.23}$$

with

$$A_{ij}(\vec{\mu}, \vec{\alpha}) := g^{\mu_i \alpha_j}. \tag{F.24}$$

□

Let's show why. We will need lemmas 12 and 13.

**Lemma 12** (Levi-Civita symbols and Determinants).

The determinant of an  $n \times n$  matrix can be expressed in terms of  $n$  Levi-Civita symbols of dimension  $n$ :

$$\det A = \frac{1}{n!} \sum_{i_1=1}^n \cdots \sum_{i_n=1}^n \sum_{j_1=1}^n \cdots \sum_{j_n=1}^n \epsilon_{i_1 \dots i_n} \epsilon_{j_1 \dots j_n} A_{i_1 j_1} \cdots A_{i_n j_n}. \quad (\text{F.25})$$

□

As an example take

$$\begin{aligned} \det M &= \begin{vmatrix} a & b \\ c & d \end{vmatrix} = ad - bc = \\ &= \frac{1}{2!} \sum_{i_1=1}^2 \sum_{i_2=1}^2 \sum_{j_1=1}^2 \sum_{j_2=1}^2 \epsilon_{i_1 i_2} \epsilon_{j_1 j_2} M_{i_1 j_1} M_{i_1 j_2} M_{i_2 j_1} M_{i_2 j_2} = \\ &= \frac{1}{2} [\epsilon_{12} \epsilon_{12} M_{11} M_{22} + \epsilon_{21} \epsilon_{12} M_{21} M_{12} + \epsilon_{21} \epsilon_{21} M_{21} M_{12} + \epsilon_{21} \epsilon_{21} M_{22} M_{11}] = \\ &= M_{11} M_{22} - M_{21} M_{12}. \end{aligned} \quad (\text{F.26})$$

**Lemma 13** (Levi-Civita full contraction).

$$\epsilon^{\mu_1 \mu_2 \mu_3 \mu_4} \epsilon_{\mu_1 \mu_2 \mu_3 \mu_4} = 24. \quad (\text{F.27})$$

□

In fact every time  $\epsilon^{\mu_1 \mu_2 \mu_3 \mu_4}$  is 0,  $\epsilon_{\mu_1 \mu_2 \mu_3 \mu_4}$  too is 0; every time  $\epsilon^{\mu_1 \mu_2 \mu_3 \mu_4}$  is  $\pm 1$ ,  $\epsilon_{\mu_1 \mu_2 \mu_3 \mu_4}$  too is  $\pm 1$ , with the same sign, so the contribution to the sum is always 1. Since the non 0 entries of  $\epsilon^{\mu_1 \mu_2 \mu_3 \mu_4}$  are 24, eq. (F.27) is proved.

We are now ready for proving theorem 24. In fact

$$\epsilon^{\mu_1 \mu_2 \mu_3 \mu_4} = \epsilon_{\alpha_1 \alpha_2 \alpha_3 \alpha_4} g^{\mu_1 \alpha_1} g^{\mu_2 \alpha_2} g^{\mu_3 \alpha_3} g^{\mu_4 \alpha_4}. \quad (\text{F.28})$$

From lemma 13, if I contract by  $\epsilon_{\mu_1 \mu_2 \mu_3 \mu_4}$  on the left hand side I get 24, while on the right hand side

$$\begin{aligned} 24 &= \epsilon_{\mu_1 \mu_2 \mu_3 \mu_4} \epsilon^{\mu_1 \mu_2 \mu_3 \mu_4} \\ &= \epsilon_{\mu_1 \mu_2 \mu_3 \mu_4} \epsilon_{\alpha_1 \alpha_2 \alpha_3 \alpha_4} g^{\mu_1 \alpha_1} g^{\mu_2 \alpha_2} g^{\mu_3 \alpha_3} g^{\mu_4 \alpha_4}. \end{aligned} \quad (\text{F.29})$$

By inverting the last equation, theorem 24 is proven.

**Corollary 12.**

$$\epsilon^{\mu_1\mu_2\mu_3\mu_4}\epsilon^{\alpha_1\alpha_2\alpha_3\alpha_4} = -\det A(\{\mu_1, \dots, \mu_4\}, \{\alpha_1, \dots, \alpha_4\}), \quad (\text{F.30a})$$

$$\epsilon^{\mu_1\mu_2\mu_3\mu_4}\epsilon_{\mu_1}^{\alpha_2\alpha_3\alpha_4} = -\det A(\{\mu_2, \dots, \mu_4\}, \{\alpha_2, \dots, \alpha_4\}), \quad (\text{F.30b})$$

$$\epsilon^{\mu_1\mu_2\mu_3\mu_4}\epsilon_{\mu_1\mu_2}^{\alpha_3\alpha_4} = -2\det A(\{\mu_3, \mu_4\}, \{\alpha_3, \alpha_4\}), \quad (\text{F.30c})$$

$$\epsilon^{\mu_1\mu_2\mu_3\mu_4}\epsilon_{\mu_1\mu_2\mu_3}^{\alpha_4} = -6\det A(\mu_4, \alpha_4) = -6g^{\mu_4\alpha_4}, \quad (\text{F.30d})$$

$$\epsilon^{\mu_1\mu_2\mu_3\mu_4}\epsilon_{\mu_1\mu_2\mu_3\mu_4} = -24. \quad (\text{F.30e})$$

□

**Theorem 25** (From Levi-Civita with 4momenta contraction to Gram determinants). Given two sets of linearly independent fourmomenta  $p_{1\dots 4}$  and  $p_{5\dots 8}$ , the following are true

$$\epsilon^{\mu_1\mu_2\mu_3\mu_4}\epsilon^{\alpha_5\alpha_6\alpha_7\alpha_8}p_1^{\mu_1}p_2^{\mu_2}p_3^{\mu_3}p_4^{\mu_4}p_5^{\alpha_5}p_6^{\alpha_6}p_7^{\alpha_7}p_8^{\alpha_8} = G\left(\begin{matrix} \{p_1, \dots, p_4\} \\ \{p_5, \dots, p_8\} \end{matrix}\right), \quad (\text{F.31a})$$

$$\epsilon^{\mu\mu_1\mu_2\mu_3}\epsilon_{\mu}^{\alpha_4\alpha_5\alpha_6}p_1^{\mu_1}p_2^{\mu_2}p_3^{\mu_3}p_4^{\alpha_4}p_5^{\alpha_5}p_6^{\alpha_6} = G\left(\begin{matrix} \{p_1, \dots, p_3\} \\ \{p_4, \dots, p_6\} \end{matrix}\right), \quad (\text{F.31b})$$

$$\epsilon^{\mu\nu\mu_1\mu_2}\epsilon_{\mu\nu}^{\alpha_3\alpha_4} = p_1^{\mu_1}p_2^{\mu_2}p_3^{\alpha_3}p_4^{\alpha_4} = G\left(\begin{matrix} \{p_1, p_2\} \\ \{p_3, p_4\} \end{matrix}\right). \quad (\text{F.31c})$$

□

As an example, consider

$$\begin{aligned} \det A(\{\mu_1, \mu_2\}, \{\alpha_3, \alpha_4\})p_1^{\mu_1}p_2^{\mu_2}p_3^{\alpha_3}p_4^{\alpha_4} &= \begin{vmatrix} g^{\mu_1\alpha_3} & g^{\mu_1\alpha_4} \\ g^{\mu_2\alpha_3} & g^{\mu_2\alpha_4} \end{vmatrix} p_1^{\mu_1}p_2^{\mu_2}p_3^{\alpha_3}p_4^{\alpha_4} \\ &= (g^{\mu_1\alpha_3}g^{\mu_2\alpha_4} - g^{\mu_1\alpha_4}g^{\mu_2\alpha_3})p_1^{\mu_1}p_2^{\mu_2}p_3^{\alpha_3}p_4^{\alpha_4} \\ &= (p_1 \cdot p_3)(p_2 \cdot p_4) - (p_1 \cdot p_4)(p_2 \cdot p_3) \\ &= \begin{vmatrix} p_1 \cdot p_3 & p_1 \cdot p_4 \\ p_2 \cdot p_3 & p_2 \cdot p_4 \end{vmatrix} = G\left(\begin{matrix} \{p_1, p_2\} \\ \{p_3, p_4\} \end{matrix}\right). \end{aligned} \quad (\text{F.32})$$

In (other) words, the string of 4momenta corresponding to the first (second) entry of  $A$  entered as the first (second) argument of a 2 dimensional  $G$ . This reasoning can be repeated for all the cases in theorem 25.

## F.2 Matrix element in terms of GDs

In eq. (2.3) we chose to contract the LCs with  $p_a$  and  $p_2 - p_5$ . This means that  $|\mathcal{M}_t|^2$  will revolve around these momenta in the sense that it is proportional to

$$\epsilon_{\mu\nu\rho\sigma}\epsilon_{\alpha\beta\gamma\delta}p_a^\sigma p_a^\delta (p_2 - p_5)^\rho (p_2 - p_5)^\gamma. \quad (\text{F.33})$$

We say  $p_a$  is a double pivot and  $p_{2,5}$  are single pivots meaning that  $p_a$  will always be in our GDs while  $p_2$  or  $p_5$  many not. Exploiting the symmetries of this problem and the fourmomentum conservation, other trios can be reached.

Consider the numerator only

$$\mathcal{N}_t := \mathcal{N}_t^{(0)}(p_1 - p_3)^4(p_2 - p_5)^4|\mathcal{M}_t|^2 = \mathcal{N}_t^{(2)} + \mathcal{N}_t^{(3)} + \mathcal{N}_t^{(4)}, \quad (\text{F.34})$$

where in  $\mathcal{N}_t^{(0)}$  we collected all the unuseful constants. The mass dimension of  $\mathcal{N}_t$  is 8. It can be written in terms of  $G_{2,3,4}$ . When considering the  $G_2$  part, dimensional analysis requires for the  $G_2$  to be multiplied by 2 scalar products. Given the pivots, they can only be

$$(p_1 - p_3)^2(p_2 - p_5)^2. \quad (\text{F.35})$$

The  $G_2$  themselves must have a combination of  $p_2$  and  $p_5$  in their arguments:

$$\mathcal{N}_t^{(2)} = (p_1 - p_3)^2(p_2 - p_5)^2 \left[ G \begin{pmatrix} 2, a \\ 2, a \end{pmatrix} + G \begin{pmatrix} 5, a \\ 5, a \end{pmatrix} + G \begin{pmatrix} 2, a \\ 5, a \end{pmatrix} \right]. \quad (\text{F.36})$$

Let us now work out the  $G_3$  part. Given the pivots, the fourmomenta of the antiparticles appear twice, those of the particles once, either inside  $G_3$  or as the multiplying scalar product:

$$\frac{\mathcal{N}_t^{(3)}}{2} = (p_1 - p_3)^2 G \begin{pmatrix} 2, 5, a \\ 2, 5, a \end{pmatrix} + (p_2 - p_5)^2 \left[ -G \begin{pmatrix} 1, 2, a \\ 2, 3, a \end{pmatrix} + G \begin{pmatrix} 1, 2, a \\ 3, 5, a \end{pmatrix} + (2 \leftrightarrow 5) \right]. \quad (\text{F.37})$$

Same reasoning for  $G_4$ , where, however, we only have the choice

$$\mathcal{N}_t^{(4)} = 4G \begin{pmatrix} 1, 2, 5, a \\ 3, 2, 5, a \end{pmatrix}. \quad (\text{F.38})$$

## G Special functions

### Hypergeometric function

$${}_2F_1(a, b, c, z) = \sum_{n=0}^{\infty} \frac{(a)_n (b)_n}{(c)_n} \frac{z^n}{n!}, \quad (\text{G.39})$$

with  $(q)_n$  the rising Pochhammer symbol

$$(q)_n = \begin{cases} 1 & n = 0, \\ q(q+1)\dots(q+n-1) & n > 0. \end{cases} \quad (\text{G.40})$$

### Incomplete elliptic integral of the second kind

$$E(x; k) = \int_0^x dt \frac{\sqrt{1 - k^2 t^2}}{\sqrt{1 - t^2}}. \quad (\text{G.41})$$

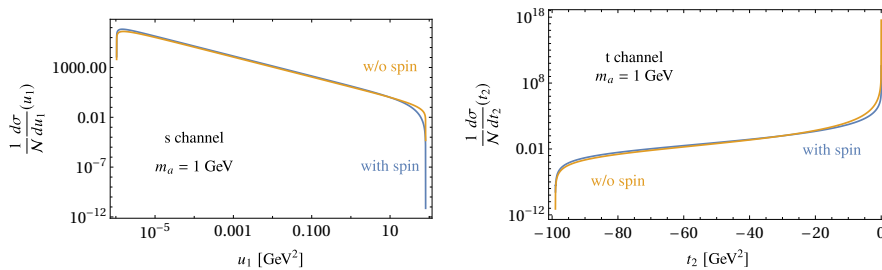


**Figure .1.** On the left panel we plot the s channel cross section distributions with respect to the gMv  $u_1$  for both the (SM+ALP) theory (blue line, *with spin*) and the SSM theory (yellow line, *without spin*). Both curves are normalised by  $\mathcal{N}(x_0 = 10 \text{ GeV}^2)$  as in eq. (H.44). The right panel has same colour coding for the t channel cross section distributions with respect to  $t_2$ . Here the normalization is  $\mathcal{N}(x_0 = -30 \text{ GeV}^2)$ .

### Incomplete elliptic integral of the third kind

$$\Pi(n; \phi|m) = \int_0^{\sin \phi} \frac{dt}{1 - nt^2} \frac{1}{\sqrt{(1-t^2)(1-mt^2)}}. \quad (\text{G.42})$$

### Complete elliptic integral of the first kind

$$K(x) = \int_0^1 \frac{1}{\sqrt{(1-t^2)(1-x^2t^2)}}. \quad (\text{G.43})$$

## H Cross sections from theories with or without spins

In section 2.2 I identified two difficulties in finding the cross section from the theory in eq. (1.25), the matrix element and the phase space. Fortunately they can be tackled separately: the whole first part of this thesis is devoted to explain how to deal with the  $2 \rightarrow 3$  scattering phase space when integrating the first non trivial matrix element (SSM). In this appendix I will complete my analysis by presenting the full matrix element results. It would be unnecessarily verbose to copy here the full cross section distributions. Rather, let us analyse figs. .1 and .2. In order not to have to deal with the conversion between the coupling of the different theories, we just show normalised cross sections and distributions. In particular the distributions  $\frac{d\sigma}{dx}$  will be normalised by

$$\mathcal{N}(x_0) := \left. \frac{d\sigma}{dx} \right|_{x=x_0}. \quad (\text{H.44})$$

In general we can not expect cross section distributions to be the same when considering particles spins or not. However variables appearing in propagators lead the matrix element behaviour independently from the selected theory, causing cross section distribution to vary very little when the theory is varied fig. .1. In turn, the cross section itself is dominated by close to divergence phase space regions, which the (SM+ALP) and the SSM theory share. This explains the similarity between the curves in fig. .2.

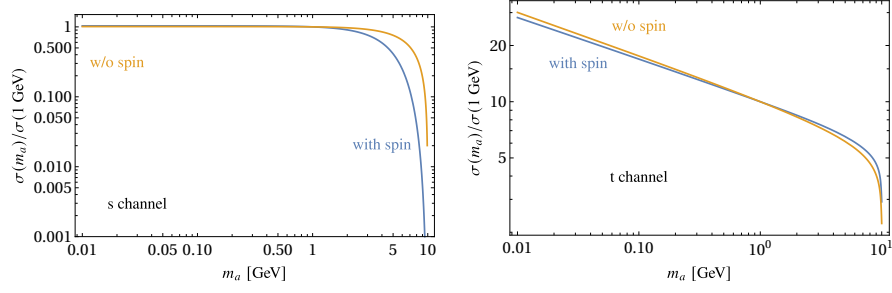


**Figure .2.** On the left panel we plot the s channel cross section for both the (SM+ALP) theory (blue line, *with spin*) and the SSM theory (yellow line, *without spin*). The right panel has same colour coding for the t channel cross section.

At this point one may wonder whether to pick on theory or the other: on the one hand, using the SSM theory provides results that compare quite good to the full theory and are easier and more readable, to the point that I could compute the s-channel cross section and t channel single differential distributions in an analytic closed form; on the other hand the (SM+ALP) theory is our ultimate goal and s and t channel single differential distributions are calculable too. In conclusion, the GD method does not fail when the matrix element complexity is increased and picking one theory or the other does not depend on it.

## I Proof of eq. (4.48)

We need to prove that, given the  $n \times n$  symmetric matrix  $M$  with

$$M_{lm} = M_{ml} = x, \quad (\text{I.45})$$

$$\det M = ax^2 + bx + c, \quad (\text{I.46})$$

$$a = -\Delta^{(lm)} = -\Delta^{(ml)}, \quad (\text{I.47})$$

$$b = \frac{V_{lm0}}{2} = \frac{V_{ml0}}{2}, \quad (\text{I.48})$$

$$c = \det M|_{x=0} =: D_0 \quad (\text{I.49})$$

it holds

$$\det M = 0 \quad \text{onto} \quad x = \frac{V_{ij0} \pm \sqrt{\Delta^{(l)} \Delta^{(m)}}}{\Delta^{(ij)}}, \quad (\text{I.50})$$

or equivalently

$$V_{lm0}^2 - \Delta^{(l)} \Delta^{(m)} - D_0 \Delta^{(lm)} = 0. \quad (\text{I.51})$$

The idea is using recursively Laplace expansion on eq. (I.51). We already know how to apply it once (eq. (4.39)) and twice (eq. (4.40)), but to express  $\Delta^{(lm)}$  we need it thrice, so

**Lemma 14** (Laplace expansion thrice).

Pick three distinct rows  $i, k, q$  and define

$$\det A = \sum_{j=1}^n \sum_{r \neq j} \sum_{v \neq j, r} (-1)^\delta a_i^j a_k^r a_q^v A_{i, k, q}^{j, r, v}, \quad (\text{I.52})$$

$$\delta = i + j + \phi(i, k) + \phi(j, r) + \phi_2(i, k, q) + \phi_2(j, r, v) \quad (\text{I.53})$$

$$\phi_2(a, b, c) = \begin{cases} c & \text{if } (c < a \wedge c < b) \vee (c > a \wedge c > b) \\ c - 1 & \text{if } c < a \vee c < b \\ \text{error value} & \text{if } a = b \vee a = c \vee b = c \end{cases} \quad (\text{I.54})$$

whit  $\vee$  = exclusive or and  $\phi_2$  following the same philosophy of  $\phi$

□

To put  $V_{lm0}^2, \Delta^{(l)} \Delta^{(m)}$  and  $D_0 \Delta^{(lm)}$  on the same footage we apply lemma 14 on all of them:

$$\begin{aligned} D_0 \Delta^{(lm)} &= \sum_{j \neq m} \sum_{r \neq l, m} \sum_{k \neq j, l} (-1)^{\delta_1} a_i^r a_l^j a_m^k A_{l, r, i}^{j, k} A_{l, r, i}^{l, r, j} \\ \delta_1 &= j + l + \phi(l, m) + \phi(j, k) + \phi_2(l, m, i) + \phi_2(l, m, r) \\ \Delta^{(l)} \Delta^{(m)} &= \sum_{k \neq l} \sum_{j \neq m} \sum_{r \neq j, m} (-1)^{\delta_2} a_i^r a_l^j a_m^k A_{l, r, i}^{j, k} A_{l, r, i}^{r, j, i} \\ \delta_2 &= m + l + \phi(l, k) + \phi(m, j) + \phi_2(l, m, i) + \phi_2(m, j, r) \\ V_{lm0}^2 &= \sum_{k \neq l, m} \sum_{j \neq l, m} \sum_{r \neq k, m} (-1)^{\delta_3} a_i^r a_l^j a_m^k A_{l, r, i}^{j, k} A_{l, r, i}^{r, k, j} \\ \delta_3 &= m + j + \phi(j, l) + \phi(m, k) + \phi_2(l, m, i) + \phi_2(m, k, r) \end{aligned} \quad (\text{I.55})$$

The effort of writing these expansions is worth because it never really depends on  $n$ : once  $l, m, i$  are given and eq. (I.51) holds for those  $j, k, r$  that have the same value of  $l, m, i$ , there is no restriction on all other values and they cycle equally among the sums. Therefore it is sufficient to show it for the easiest non trivial case  $n = 3$ . This can be done by the means of you favourite maths manipulator (paper and pen too if you want). I can provide a Mathematica Notebook that in principle works for generic  $n, l, m, r$ , in practice we all know that determinants of big matrices are computationally costly (the proof for  $n = 7$  took 92 seconds on my laptop). However having the proof verified at least up to  $n = 7$  in full generality is more than enough if one wants to work in  $7d$  or less. One last remark is that [93] seem to assume that  $M$  being symmetric is necessary for eq. (I.51) to hold but in my notebook I never assumed it and still obtained my result. In our special case there is still nothing to worry about as we actually deal with symmetric matrices.

## J Allowed permutations in the $e^+e^- \rightarrow e^+e^-a$ process

#	$\mathcal{S}_i$	4mom indices
0	$(s, s_1, s_2, t_1, t_2, u_1, u_2, u_3, u_4, u_5)$	$(1, 2, 3, 4, 5)$
1	$(s, s_2, s_1, u_2, u_3, u_1, t_1, t_2, u_4, u_5)$	$(1, 2, 5, 4, 3)$
2	$(t_1, u_4, s_2, s, u_1, t_2, u_2, u_3, s_1, u_5)$	$(1, -3, -2, 4, 5)$
3	$(t_1, s_2, u_4, u_2, u_3, t_2, s, u_1, s_1, u_5)$	$(1, -3, 5, 4, -2)$
4	$(u_2, u_4, s_1, s, u_1, u_3, t_1, t_2, s_2, u_5)$	$(1, -5, -2, 4, 3)$
5	$(u_2, s_1, u_4, t_1, t_2, u_3, s, u_1, s_2, u_5)$	$(1, -5, 3, 4, -2)$
6	$(s, s_1, s_2, u_3, u_2, u_1, t_2, t_1, u_5, u_4)$	$(2, 1, 3, 4, 5)$
7	$(s, s_2, s_1, t_2, t_1, u_1, u_3, u_2, u_5, u_4)$	$(2, 1, 5, 4, 3)$
8	$(u_3, u_5, s_2, s, u_1, u_2, t_2, t_1, s_1, u_4)$	$(2, -3, -1, 4, 5)$
9	$(u_3, s_2, u_5, t_2, t_1, u_2, s, u_1, s_1, u_4)$	$(2, -3, 5, 4, -1)$
10	$(t_2, u_5, s_1, s, u_1, t_1, u_3, u_2, s_2, u_4)$	$(2, -5, -1, 4, 3)$
11	$(t_2, s_1, u_5, u_3, u_2, t_1, s, u_1, s_2, u_4)$	$(2, -5, 3, 4, -1)$
12	$(t_1, u_4, s_2, u_3, u_2, t_2, u_1, s, u_5, s_1)$	$(-3, 1, -2, 4, 5)$
13	$(t_1, s_2, u_4, u_1, s, t_2, u_3, u_2, u_5, s_1)$	$(-3, 1, 5, 4, -2)$
14	$(u_3, u_5, s_2, t_1, t_2, u_2, u_1, s, u_4, s_1)$	$(-3, 2, -1, 4, 5)$
15	$(u_3, s_2, u_5, u_1, s, u_2, t_1, t_2, u_4, s_1)$	$(-3, 2, 5, 4, -1)$
16	$(u_1, u_5, u_4, t_1, t_2, s, u_3, u_2, s_2, s_1)$	$(-3, -5, -1, 4, -2)$
17	$(u_1, u_4, u_5, u_3, u_2, s, t_1, t_2, s_2, s_1)$	$(-3, -5, -2, 4, -1)$
18	$(u_2, u_4, s_1, t_2, t_1, u_3, u_1, s, u_5, s_2)$	$(-5, 1, -2, 4, 3)$
19	$(u_2, s_1, u_4, u_1, s, u_3, t_2, t_1, u_5, s_2)$	$(-5, 1, 3, 4, -2)$
20	$(t_2, u_5, s_1, u_2, u_3, t_1, u_1, s, u_4, s_2)$	$(-5, 2, -1, 4, 3)$
21	$(t_2, s_1, u_5, u_1, s, t_1, u_2, u_3, u_4, s_2)$	$(-5, 2, 3, 4, -1)$
22	$(u_1, u_5, u_4, u_2, u_3, s, t_2, t_1, s_1, s_2)$	$(-5, -3, -1, 4, -2)$
23	$(u_1, u_4, u_5, t_2, t_1, s, u_2, u_3, s_1, s_2)$	$(-5, -3, -2, 4, -1)$

**Table .1.** Permutations of fourmomenta indices sending  $s$  in  $s$  and the fourth fourmomentum in itself. In the first column, the number with which we will refer to the Mandelstam string appearing in the second column; in the second column the Mandelstam string; in the last one, the corresponding ordered list of fourmomenta indices.

## K $\mathcal{G}_{12}$ roots ordering

This appendix serves section 7.1 for depicting in what cases we can obtain  $\mathcal{G}_1 \leq 0$  and  $\mathcal{G}_2 \leq 0$  at the same time. Figure .3 provides a gallery for all possible orderings of the  $\mathcal{G}_{12}$  roots.

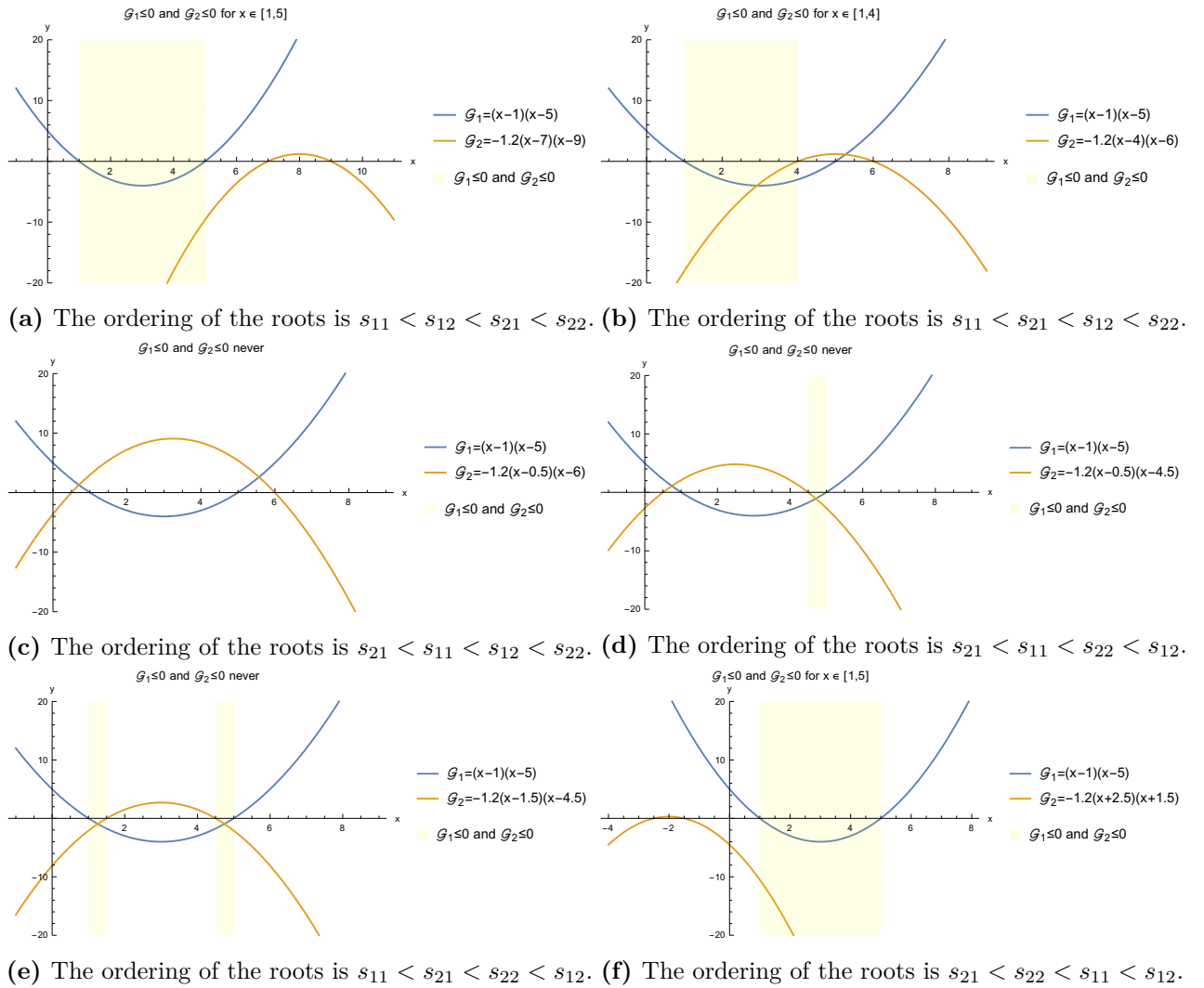


**Figure .3.** From the text we know that  $\mathcal{G}_1 \leq 0$  and  $\mathcal{G}_2 \leq 0$  at the same time.  $\mathcal{G}_1$  is a parabola in  $s_1$  with roots  $s_{11}$  and  $s_{12}$  and is negative if  $s_{11} < s_1 < s_{12}$ .  $\mathcal{G}_2$  is a parabola in  $s_1$  with roots  $s_{21}$  and  $s_{22}$  and is negative if  $s_1 > s_{22}$  or  $s_1 < s_{12}$ . All the possible ways in which the roots  $s_{11}, s_{1,2}, s_{21}, s_{22}$  can be ordered are depicted in the above panels. In all panels  $x, y$  are mock variables, the solid blue line is  $\mathcal{G}_1$ , the solid orange line is  $\mathcal{G}_2$  and the yellow area is the region in which  $\mathcal{G}_1 \leq 0$  and  $\mathcal{G}_2 \leq 0$  at the same time.

## L $\frac{d^2\sigma_t}{dt_1 dt_2}$ gallery

This section serves as a gallery to section 7.2. Let us remind that by  $\Phi$  we indicate the pure  $2 \rightarrow 3$  scattering phase space, so in the following pictures we will be plotting eq. (7.18) with constant matrix element. All of the plots have the third (colour) axis in arbitrary units since we are only interested in the overall trend rather than on the exact function value. Specifically we want to give a flavour of the anisotropy of both  $\frac{d^2\sigma_t}{dt_1 dt_2}$  and  $\frac{d^2\Phi}{dt_1 dt_2}$ . This anisotropy is such that some massage was needed for the plots, for example in figs. .4 to .7 we plot the log of the distributions or in figs. .8 to .11 we trade  $t_{1,2}$  on the axes for  $\log(-t_{1,2})$  (in this sense they are log log plots). Therefore, when you will see something like  $\log_{10} \frac{d^2\sigma_t}{dt_1 dt_2}$  it is to be intended that the needed log argument rescaling was performed.

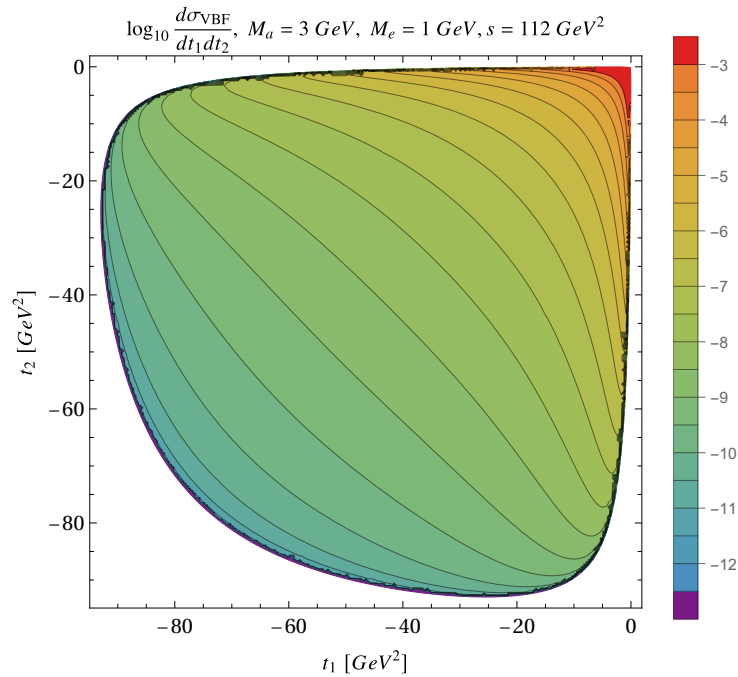


**Figure .4.**  $\log_{10} \frac{d^2\sigma_t}{dt_1 dt_2}, s = 112 \text{ GeV}^2, M_a = 3 \text{ GeV}, M_e = 1 \text{ GeV}.$

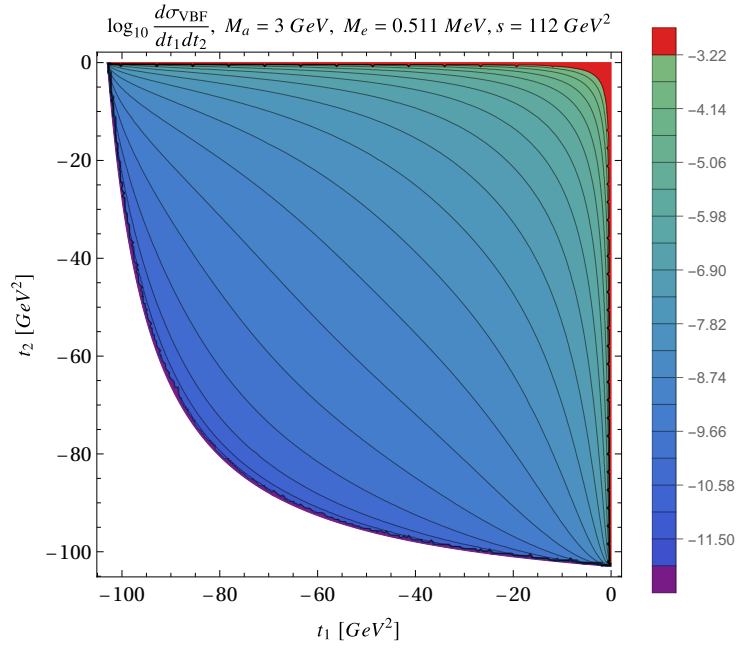


**Figure .5.**  $\log_{10} \frac{d^2\sigma_t}{dt_1 dt_2}, s = 112 \text{ GeV}^2, M_a = 3 \text{ GeV}, M_e = 5.11 \cdot 10^{-4} \text{ GeV}.$

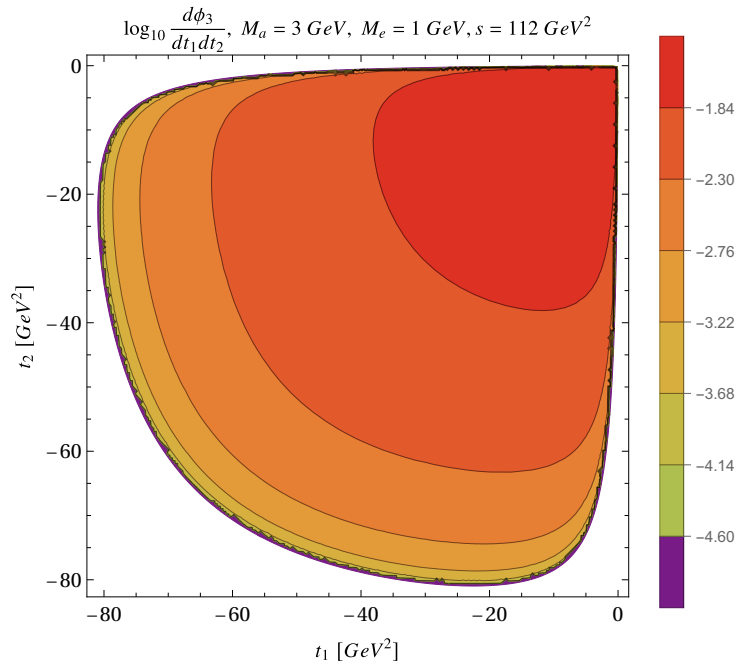


**Figure .6.**  $\log_{10} \frac{d^2\Phi}{dt_1 dt_2}, s = 112 \text{ GeV}^2, M_a = 3 \text{ GeV}, M_e = 1 \text{ GeV}.$

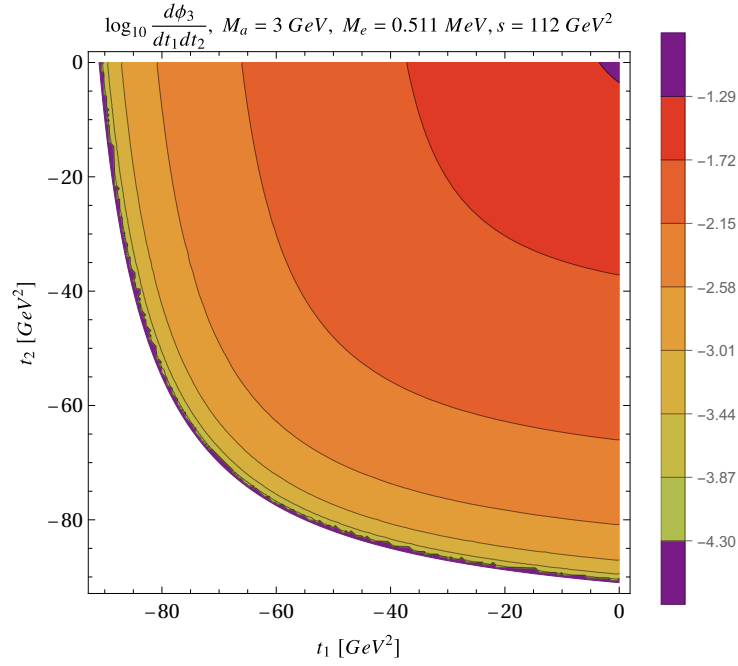


**Figure .7.**  $\log_{10} \frac{d^2 \Phi}{dt_1 dt_2}$ ,  $s = 112 \text{ GeV}^2$ ,  $M_a = 3 \text{ GeV}$ ,  $M_e = 5.11 \cdot 10^{-4} \text{ GeV}$ .

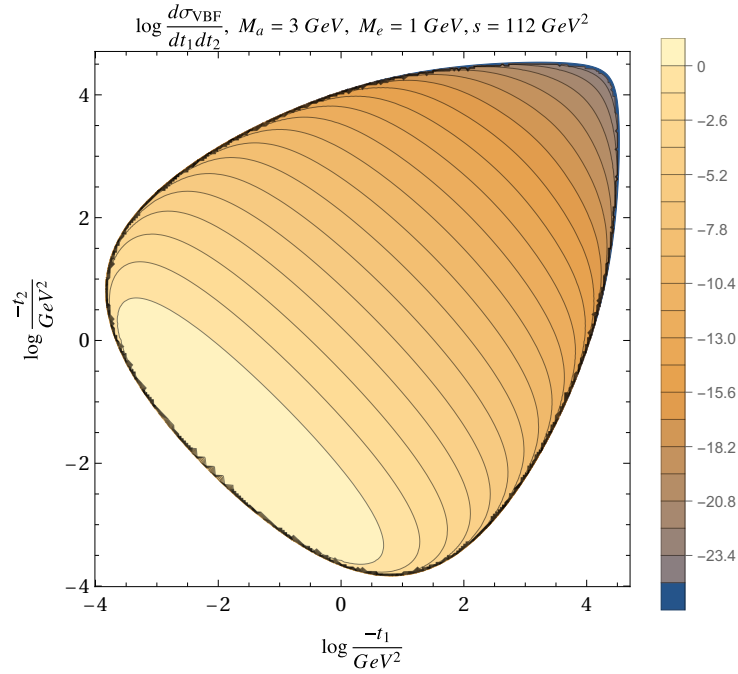


**Figure .8.** Same as fig. .4 ( $\log \frac{d^2 \sigma_t}{dt_1 dt_2}$ ,  $s = 112 \text{ GeV}^2$ ,  $M_a = 3 \text{ GeV}$ ,  $M_e = 1 \text{ GeV}$ ) but the axes are log scaled in the sense that we traded  $t_{1,2}$  on the axes for  $\log(-t_{1,2})$ .

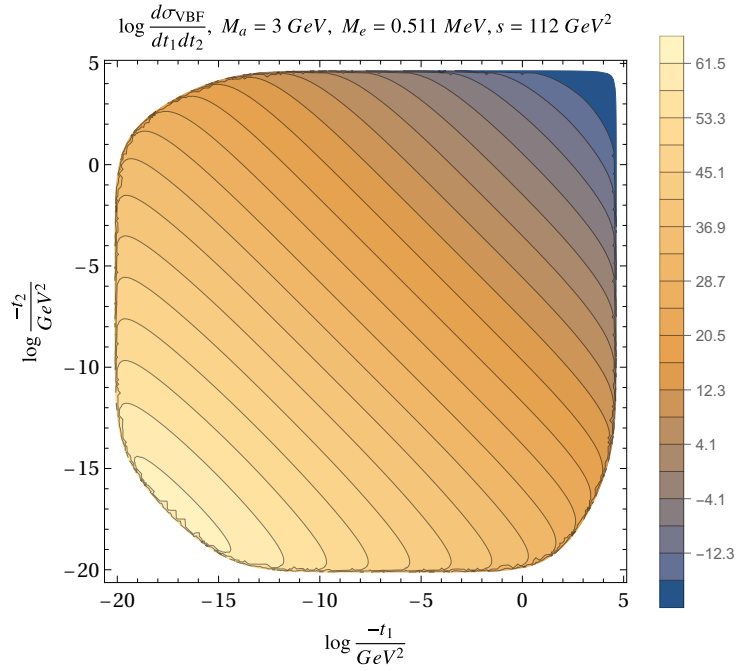


**Figure .9.** Same as fig. .5 ( $\log \frac{d^2\sigma_t}{dt_1 dt_2}$ ,  $s = 112 \text{ GeV}^2$ ,  $M_a = 3 \text{ GeV}$ ,  $M_e = 5.11 \cdot 10^{-4} \text{ GeV}$ ) but the axes are log scaled in the sense that we traded  $t_{1,2}$  on the axes for  $\log(-t_{1,2})$ .

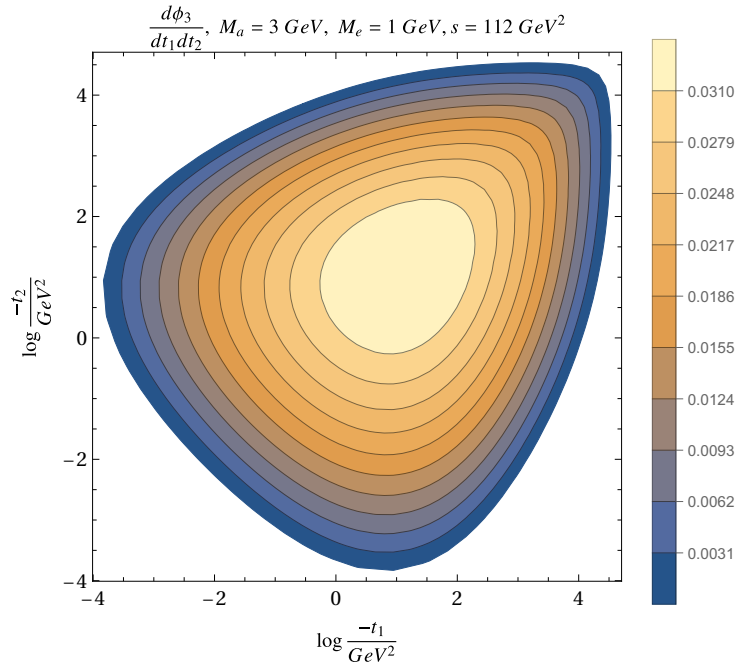


**Figure .10.** Same as fig. .6 ( $\frac{d^2\phi}{dt_1 dt_2}$ ,  $s = 112 \text{ GeV}^2$ ,  $M_a = 3 \text{ GeV}$ ,  $M_e = 1 \text{ GeV}$ ) but the axes are log scaled in the sense that we traded  $t_{1,2}$  on the axes for  $\log(-t_{1,2})$ .

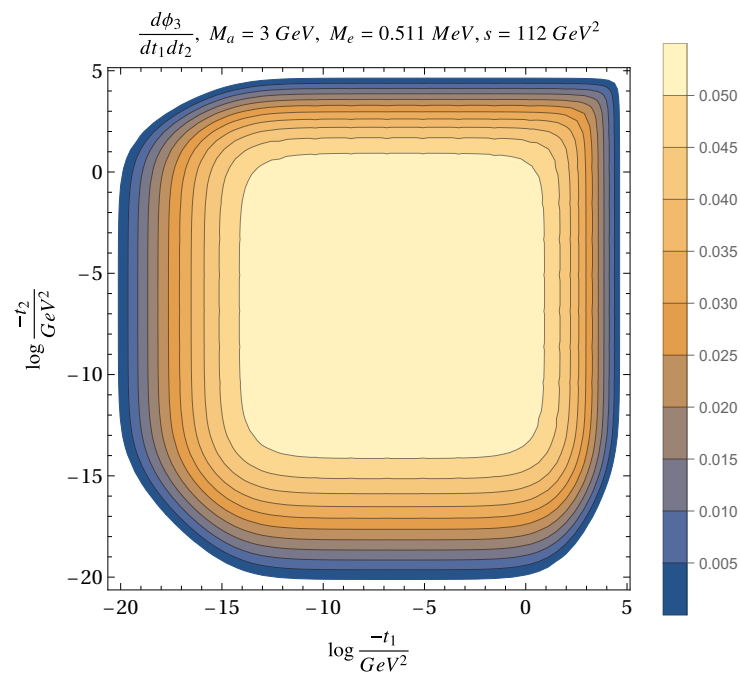


**Figure .11.** Same as fig. .7 ( $\frac{d^2\Phi}{dt_1 dt_2}$ ,  $s = 112 \text{ GeV}^2$ ,  $M_a = 3 \text{ GeV}$ ,  $M_e = 5.11 \cdot 10^{-4} \text{ GeV}$ ) but the axes are log scaled in the sense that we traded  $t_{1,2}$  on the axes for  $\log(-t_{1,2})$ .

## M VBF selections efficiency

In this appendix we show the effect of our events selections at Belle II for two ALP masses,  $M_a = 0.2$  and 9 GeV. We will always be applying  $m_{\gamma\gamma} \in M_a + \sigma_m[-3, 1.5]$  (see eq. (10.1)). On top of that, we also considered selections on the following kinematic variables:

- *mass bin* indicates that we limit ourselves to the mass selection and there is no further selection.
- $\beta_z^*(\text{ALP})$ , the longitudinal component of the ALP Lorentz parameter.
- $\beta^*(\text{ALP})$ , the norm of the ALP Lorentz parameter.
- $E_{e^\pm}^*$ , the final  $e^\pm$  energy in the CoM frame.
- $E_\gamma^*$ , the final photons energy in the CoM frame.
- $h_i$ , the cos of the helicity angles of the photons computed as in section 9.2.1.
- $\eta_{e^-}^* \cdot \eta_{e^+}^*$ , the product of the  $e^\pm$  rapidities in the CoM (see eq. (9.15)).
- $\eta_{\gamma_1}^* \cdot \eta_{\gamma_2}^*$ , the product of the photons rapidities in the CoM.
- $|\eta_{\gamma_1} - \eta_{\gamma_2}|$ , the difference of rapidity of the photons.
- $\eta_\gamma^*$ , the photons rapidities in the CoM.
- $\Delta R_{\gamma\gamma}$ , the photons angular separation (see eq. (9.16)).
- $\Delta R_{e^\pm\gamma}$ , the angular separation among photons and  $e^\pm$ .
- $\Delta R_{e^+e^-}$ , the angular separation among photons and  $e^+$  and  $e^-$ .

Table .2 is to be read as follows: for one selection we compute the total signal and bg cross section surviving, we multiply it by the Belle II luminosity  $\mathcal{L} = 50\text{ab}^{-1}$  and obtain the surviving signal and background events  $N_s$  and  $N_b$ . The significance  $r$  is

$$r := \frac{N_s}{\sqrt{N_b}} \quad (\text{M.56})$$

and its error  $\delta r$  is computed from the MC error<sup>2</sup> on signal and background cross sections. The third column of the table shows the significance of a single selection. The fifth column shows the significance  $R$  of all selections up to the current row and its error is called  $\delta R$ . The mass selection alone is not a sufficient selection. Some cuts can be neglected as they leave the same set of events that is left from the mass selection, for example for  $M_a = 0.2$  GeV, all cuts from  $\beta_z^*(\text{ALP})$  to  $\eta_{e^-}^* \cdot \eta_{e^+}^*$ . Some other cuts can importantly improve the significance, for example, again for  $M_a = 0.2\text{GeV}$ , the  $\Delta R_{e^\pm\gamma}$  selection. Nonetheless, cumulating too many selections can lead to exclude all of the signal events and make the significance smaller, as is clear from the last row for  $M_a = 0.2$  GeV. From this kind of tables we learned that

<sup>2</sup>Typically if a MC simulation counts  $N$  events, the error is  $\sqrt{N}$ .

some cuts could be excluded and iteratively refined our set of selections until we reached table 10.3.

What we noticed for table .2 is reinforced in tables .3 and .4. Let us explain how to read them: masses and selections are the same as in table .2. In the third column  $\epsilon_1$  is the ratio of the number of events surviving the current cut over the total number of events (that simply satisfy Belle II requirements). In the fourth column  $\epsilon_c$  is the ratio of the number of events surviving all the selections up to the current row over the total number of events. In the last column  $\epsilon_r$  is the relative efficiency, i.e. the ratio of the current cumulative efficiency over the previous one. The best cuts (and cuts combinations) are those making the background efficiency very small while keeping the signal efficiency close to 1.

### M.1 Significance with systematics at Belle II

Mass [GeV]	Cut	$r \cdot 10^3$	$\delta r \cdot 10^3$	$R \cdot 10^3$	$\delta R \cdot 10^3$	
0.2	mass bin	278.17	0.03			
	$\beta_z^*$ (ALP)	278.17	0.03	278.17	0.03	
	$E_{e^\pm}^*$	278.17	0.03	278.17	0.03	
	$\cos \theta_{ij}^0$	278.17	0.03	278.17	0.03	
	$E_\gamma^*$	278.17	0.03	278.17	0.03	
	$\eta_{e^-}^* \cdot \eta_{e^+}^*$	278.17	0.03	278.17	0.03	
	$ \eta_{\gamma_1} - \eta_{\gamma_2} $	395.81	0.06	395.81	0.06	
	$\eta_\gamma^*$	419.06	0.07	548.50	0.14	
	$\Delta R_{\gamma\gamma}$	587.41	0.12	765.76	0.27	
	$\beta^*$ (ALP)	545.51	0.14	937.89	0.58	
	$\eta_{\gamma_1}^* \cdot \eta_{\gamma_2}^*$	416.35	0.11	917.24	0.88	
	$\Delta R_{e^\pm\gamma}$	1759.40	1.47	902.60	1.04	
	$\Delta R_{e^+e^-}$	825.67	0.95	245.90	0.28	
	9	mass bin	50.22	0.01		
		$E_{e^\pm}^*$	50.22	0.01	50.22	0.01
		$\cos \theta_{ij}^0$	50.22	0.01	50.22	0.01
		$\Delta R_{e^+e^-}$	50.22	0.01	50.22	0.01
$\beta^*$ (ALP)		50.00	0.01	50.00	0.01	
$\eta_{e^-}^* \cdot \eta_{e^+}^*$		51.99	0.01	52.09	0.01	
$\beta_z^*$ (ALP)		53.62	0.01	53.26	0.01	
$E_\gamma^*$		60.42	0.02	62.24	0.02	
$\Delta R_{e^\pm\gamma}$		59.83	0.02	75.87	0.03	
$\Delta R_{\gamma\gamma}$		55.97	0.02	83.97	0.05	
$ \eta_{\gamma_1} - \eta_{\gamma_2} $		58.65	0.02	90.66	0.06	
$\eta_\gamma^*$		59.68	0.02	94.79	0.07	
$\eta_{\gamma_1}^* \cdot \eta_{\gamma_2}^*$		59.93	0.02	97.77	0.08	

**Table .2**

## M.2 Belle II bg efficiencies

Mass [GeV]	Cuts	$\epsilon_1$	$\epsilon_c$	$\epsilon_r$	
0.2	$\beta_z^*(\text{ALP})$	1.000	1.000	1.000	
	$E_{e^\pm}^*$	1.000	1.000	1.000	
	$h_i$	1.000	1.000	1.000	
	$E_\gamma^*$	1.000	1.000	1.000	
	$\eta_{e^-}^* \cdot \eta_{e^+}^*$	1.000	1.000	1.000	
	$ \eta_{\gamma_1} - \eta_{\gamma_2} $	0.367	0.367	0.367	
	$\eta_\gamma^*$	0.271	0.127	0.346	
	$\Delta R_{\gamma\gamma}$	0.199	0.065	0.511	
	$\beta^*(\text{ALP})$	0.120	0.022	0.337	
	$\eta_{\gamma_1}^* \cdot \eta_{\gamma_2}^*$	0.110	0.009	0.406	
	$\Delta R_{e^\pm\gamma}$	0.010	0.001	0.154	
	$\Delta R_{e^+e^-}$	0.004	0.001	0.500	
	9	$E_{e^\pm}^*$	1.000	1.000	1.000
		$h_i$	1.000	1.000	1.000
		$\Delta R_{e^+e^-}$	1.000	1.000	1.000
$\beta^*(\text{ALP})$		0.925	0.925	0.925	
$\eta_{e^-}^* \cdot \eta_{e^+}^*$		0.797	0.731	0.791	
$\beta_z^*(\text{ALP})$		0.793	0.680	0.930	
$E_\gamma^*$		0.693	0.498	0.733	
$\Delta R_{e^\pm\gamma}$		0.606	0.305	0.612	
$\Delta R_{\gamma\gamma}$		0.421	0.127	0.416	
$ \eta_{\gamma_1} - \eta_{\gamma_2} $		0.414	0.099	0.778	
$\eta_\gamma^*$		0.340	0.079	0.797	
$\eta_{\gamma_1}^* \cdot \eta_{\gamma_2}^*$		0.309	0.070	0.895	

Table .3

### M.3 Belle II sig efficiencies

Mass [GeV]	Cuts	$\epsilon_1$	$\epsilon_c$	$\epsilon_r$	
0.2	$\beta_z^*(\text{ALP})$	1.000	1.000	1.000	
	$E_{e^\pm}^*$	1.000	1.000	1.000	
	$h_i$	1.000	1.000	1.000	
	$E_\gamma^*$	1.000	1.000	1.000	
	$\eta_{e^-}^* \cdot \eta_{e^+}^*$	1.000	1.000	1.000	
	$ \eta_{\gamma_1} - \eta_{\gamma_2} $	0.858	0.858	0.858	
	$\eta_\gamma^*$	0.797	0.718	0.836	
	$\Delta R_{\gamma\gamma}$	0.935	0.698	0.973	
	$\beta^*(\text{ALP})$	0.688	0.496	0.710	
	$\eta_{\gamma_1}^* \cdot \eta_{\gamma_2}^*$	0.517	0.314	0.633	
	$\Delta R_{e^\pm\gamma}$	0.689	0.256	0.815	
	$\Delta R_{e^+e^-}$	0.234	0.070	0.272	
	9	$E_{e^\pm}^*$	1.000	1.000	1.000
		$h_i$	1.000	1.000	1.000
$\Delta R_{e^+e^-}$		1.000	1.000	1.000	
$\beta^*(\text{ALP})$		0.963	0.963	0.963	
$\eta_{e^-}^* \cdot \eta_{e^+}^*$		0.921	0.888	0.922	
$\beta_z^*(\text{ALP})$		0.945	0.875	0.985	
$E_\gamma^*$		0.954	0.838	0.958	
$\Delta R_{e^\pm\gamma}$		0.880	0.742	0.885	
$\Delta R_{\gamma\gamma}$		0.779	0.572	0.771	
$ \eta_{\gamma_1} - \eta_{\gamma_2} $		0.802	0.541	0.945	
$\eta_\gamma^*$		0.741	0.509	0.942	
$\eta_{\gamma_1}^* \cdot \eta_{\gamma_2}^*$		0.703	0.485	0.953	

Table .4

## N The smearing algorithm

If we still want to base our analysis onto missing particle quantities we must include some detection simulation too into our computations. After MC data generation we apply to our data the following algorithm

- Only final leptons are smeared in energy, polar angle and azimuthal angle. Each quantity  $x$  is sent into a smeared quantity  $x^s$  randomly extracted from a gaussian distribution of mean  $x$  and a standard deviation  $\sigma(x)$ .
- We assume angles to have a constant standard deviation,  $\sigma_\theta = 10^{-3}$ . The error on the energy is given from the ECL:

$$\frac{\sigma_E}{E} = \sqrt{\left(\frac{0.066\%}{E}\right)^2 + \left(\frac{0.81\%}{\sqrt{E}}\right)^2 + (1.34\%)^2}. \quad (\text{N.57})$$

Acronym	# hard forward $\gamma$	# hard backward $\gamma$	# soft $\gamma$	# points
2hf1s	2	0	1	35662
1hf1hb1s	1	1	1	70288
2hb1hf	0	2	0	1013
3hf	3	0	0	788
1hb2s	0	1	2	7330

Table .5

- A new, invisible event is created using the same incoming momenta as the real event and smeared outgoing visible particles, assuming total 4-momentum conservation:

$$p_{inv} = p_{in} - p_{out}^s \quad (\text{N.58})$$

- The only check we enforce on the smeared event is lepton visibility at Belle II.
- Consider a kinematic point in a region which lays slightly outside our run card cuts. Smearing can make them fluctuate inside the acceptance region, therefore in generating the background we do not use the real cuts  $x_0$  but some broader cuts  $x_0^s := x_0 + \text{sgn}(x_0)\sigma(x_0)$ :
  - We still accept as real events those events respecting the original cuts for both visible and invisible particles.
  - We will accept as smeared events those respecting visible particle cuts, not being able to recover single invisible particles information.

## O Python simulation of forbidden region to 3 invisible photons

I run a python simulation of 3 final invisible photons made of  $\sim 10^5$  data points. I specialised the generation to all the possible configurations, modulo  $\mathbb{Z}_2$  flips. In total we have 5 non redundant categories, that I list in table .5 with their acronym, their content in terms of hard and soft photons, and the number of simulated points in python. I finally plot them in fig. .12. Data points respect all the selections that we require in our MC simulation.

## P Long Lived ALP

In our model the ALP decay rate is

$$\Gamma = \frac{g_{a\gamma\gamma}^2 M_a^3}{64\pi}. \quad (\text{P.59})$$

With a branching ratio to photons equal to 1, the ALP lifetime at rest is  $\tau_0 = 1/\Gamma$ . The actual lifespan of the particle  $\tau$  is extracted from the pdf of the exponential

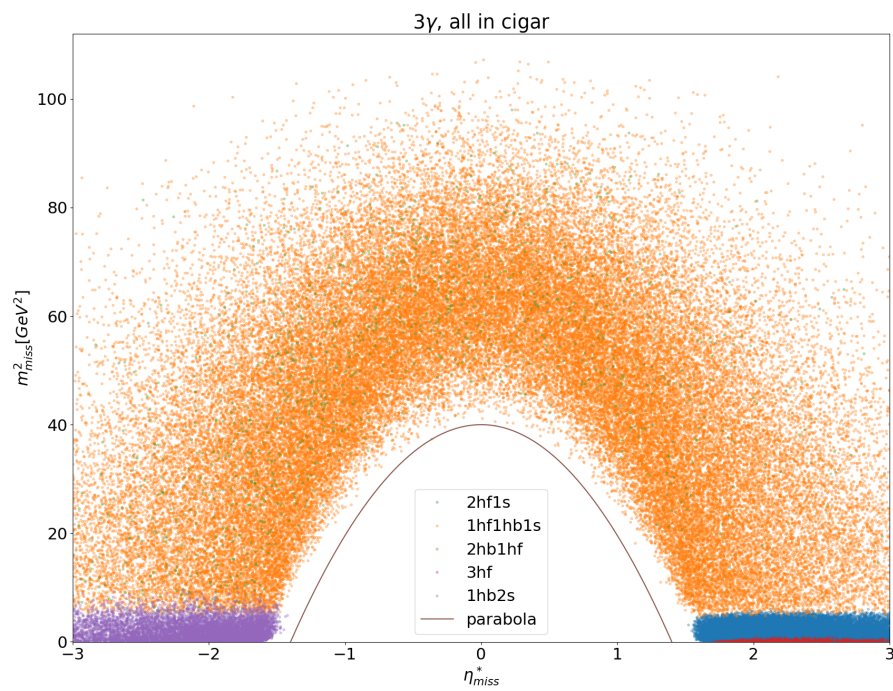


**Figure .12.** Python simulation of missing mass and rapidity allowed to three invisible photons at Belle II. See text for the labels. *parabola* corresponds to eq. (11.75).

decay with mean life  $\tau_0$ . Correspondingly, the ALP will be able to travel in out laboratory a distance

$$d_{\text{LAB}} = \gamma\beta c\tau. \quad (\text{P.60})$$

$d_{\text{LAB}}$  is crescent in  $\beta$ , then the worst case scenario is depicted in fig. .13 and is realised when  $\beta = \beta_{\text{max}}$  with

$$\beta_{\text{max}} = \sqrt{1 - \left(\frac{M_a}{E_{\text{max}}^a}\right)^2}, \quad E_{\text{max}}^a = \frac{s + M_a^2 - 4M_e^2}{\sqrt{s}}. \quad (\text{P.61})$$

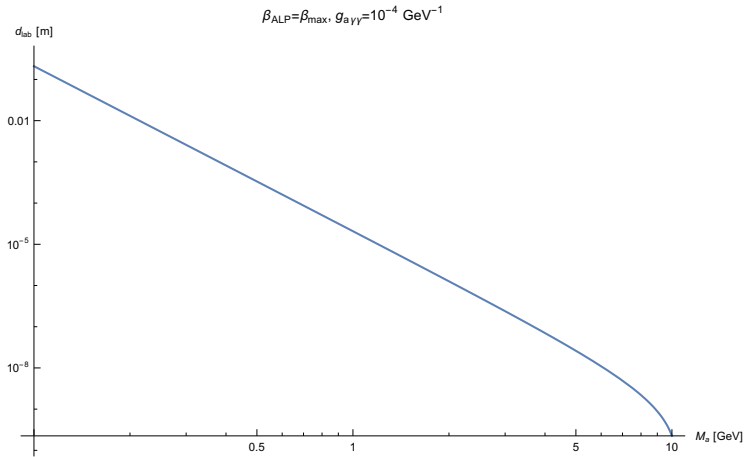


**Figure .13.** Largest distance that an ALP of mass M can go before decaying in the lab frame.

If the detector is 1 m long we can predict that massive ALPs have very little chance to decay outside of it. In our MC simulations we verified that for all ALP masses the number of pseudoscalars that manage to escape Belle II before decaying into photons is negligible. This is why we opt for an ALP decaying into DM.



# Bibliography

- [1] W. J. G. de Blok. The Core-Cusp Problem. *Adv. Astron.*, 2010:789293, 2010.
- [2] V. C. Rubin and W.K. Ford, Jr. Rotation of the Andromeda Nebula from a Spectroscopic Survey of Emission Regions. *apj*, 159:379, February 1970.
- [3] Fritz Zwicky. On the masses of nebulae and of clusters of nebulae. *The Astrophysical Journal*, 86:217, 1937.
- [4] Douglas Clowe, Maruša Bradač, Anthony H Gonzalez, Maxim Markevitch, Scott W Randall, Christine Jones, and Dennis Zaritsky. A direct empirical proof of the existence of dark matter. *The Astrophysical Journal Letters*, 648(2):L109, 2006.
- [5] R.D. Peccei and Helen Quinn. Cp conservation in the presence of pseudoparticles. *Physical Review Letters - PHYS REV LETT*, 38:1440–1443, 06 1977.
- [6] Frank Wilczek. Problem of Strong  $P$  and  $T$  Invariance in the Presence of Instantons. *Phys. Rev. Lett.*, 40:279–282, 1978.
- [7] Steven Weinberg. A New Light Boson? *Phys. Rev. Lett.*, 40:223–226, 1978.
- [8] Anson Hook. TASI Lectures on the Strong CP Problem and Axions. *PoS, TASI2018:004*, 2019.
- [9] A. Ringwald. Axions and Axion-Like Particles. In *49th Rencontres de Moriond on Electroweak Interactions and Unified Theories*, pages 223–230, 2014.
- [10] Maurizio Giannotti. Aspects of Axions and ALPs Phenomenology. In *10th Symposium on Large TPCs for Low-Energy Rare Event Detection*, 5 2022.
- [11] V. Anastassopoulos et al. New CAST Limit on the Axion-Photon Interaction. *Nature Phys.*, 13:584–590, 2017.
- [12] Biljana Lakić. International Axion Observatory (IAXO) status and prospects. *J. Phys. Conf. Ser.*, 1342(1):012070, 2020.
- [13] M. J. Jewell et al. New Results from HAYSTAC’s Phase II Operation with a Squeezed State Receiver. 1 2023.
- [14] Simon Knapen and Andrea Thamm. Direct discovery of new light states at the FCCee. *Eur. Phys. J. Plus*, 136(9):936, 2021.

- [15] Csaba Csáki, Salvator Lombardo, and Ofri Telem. *TASI Lectures on Non-supersymmetric BSM Models*, pages 501–570. WSP, 2018.
- [16] R. D. Peccei and Helen R. Quinn. Constraints Imposed by CP Conservation in the Presence of Instantons. *Phys. Rev. D*, 16:1791–1797, 1977.
- [17] Steven Weinberg and John C Taylor. The quantum theory of fields volume 2: Modern applications. *Nature*, 385(6614):310–310, 1997.
- [18] Lisa Randall and Raman Sundrum. A Large mass hierarchy from a small extra dimension. *Phys. Rev. Lett.*, 83:3370–3373, 1999.
- [19] Paul Langacker. Grand Unified Theories and Proton Decay. *Phys. Rept.*, 72:185, 1981.
- [20] S. Dimopoulos, S. Raby, and Frank Wilczek. Supersymmetry and the Scale of Unification. *Phys. Rev. D*, 24:1681–1683, 1981.
- [21] Tsutomu Yanagida. Horizontal gauge symmetry and masses of neutrinos. *Conf. Proc. C*, 7902131:95–99, 1979.
- [22] Jihn E. Kim. Light Pseudoscalars, Particle Physics and Cosmology. *Phys. Rept.*, 150:1–177, 1987.
- [23] Apostolos Pilaftsis. Astrophysical and terrestrial constraints on singlet Majoron models. *Phys. Rev. D*, 49:2398–2404, 1994.
- [24] Frank Wilczek. Axions and Family Symmetry Breaking. *Phys. Rev. Lett.*, 49:1549–1552, 1982.
- [25] Michael Dine and Willy Fischler. The Not So Harmless Axion. *Phys. Lett. B*, 120:137–141, 1983.
- [26] L. F. Abbott and P. Sikivie. A Cosmological Bound on the Invisible Axion. *Phys. Lett. B*, 120:133–136, 1983.
- [27] John Preskill, Mark B. Wise, and Frank Wilczek. Cosmology of the Invisible Axion. *Phys. Lett. B*, 120:127–132, 1983.
- [28] Luca Di Luzio, Maurizio Giannotti, Enrico Nardi, and Luca Visinelli. The landscape of QCD axion models. *Phys. Rept.*, 870:1–117, 2020.
- [29] M. Srednicki. *Quantum field theory*. Cambridge University Press, 1 2007.
- [30] Kazuo Fujikawa. Path Integral Measure for Gauge Invariant Fermion Theories. *Phys. Rev. Lett.*, 42:1195–1198, 1979.
- [31] R. J. Crewther, P. Di Vecchia, G. Veneziano, and Edward Witten. Chiral Estimate of the Electric Dipole Moment of the Neutron in Quantum Chromodynamics. *Phys. Lett. B*, 88:123, 1979. [Erratum: *Phys.Lett.B* 91, 487 (1980)].

- [32] C. Abel et al. Measurement of the Permanent Electric Dipole Moment of the Neutron. *Phys. Rev. Lett.*, 124(8):081803, 2020.
- [33] Howard M. Georgi, Lawrence J. Hall, and Mark B. Wise. Grand Unified Models With an Automatic Peccei-Quinn Symmetry. *Nucl. Phys. B*, 192:409–416, 1981.
- [34] Richard Holman, Stephen D. H. Hsu, Thomas W. Kephart, Edward W. Kolb, Richard Watkins, and Lawrence M. Widrow. Solutions to the strong CP problem in a world with gravity. *Phys. Lett. B*, 282:132–136, 1992.
- [35] Marc Kamionkowski and John March-Russell. Planck scale physics and the Peccei-Quinn mechanism. *Phys. Lett. B*, 282:137–141, 1992.
- [36] Giovanni Grilli di Cortona, Edward Hardy, Javier Pardo Vega, and Giovanni Villadoro. The QCD axion, precisely. *JHEP*, 01:034, 2016.
- [37] P. Di Vecchia and G. Veneziano. Chiral Dynamics in the Large  $n$  Limit. *Nucl. Phys. B*, 171:253–272, 1980.
- [38] Michael Dine, Willy Fischler, and Mark Srednicki. A Simple Solution to the Strong CP Problem with a Harmless Axion. *Phys. Lett. B*, 104:199–202, 1981.
- [39] A. R. Zhitnitsky. On Possible Suppression of the Axion Hadron Interactions. (In Russian). *Sov. J. Nucl. Phys.*, 31:260, 1980.
- [40] Jihn E. Kim. Weak Interaction Singlet and Strong CP Invariance. *Phys. Rev. Lett.*, 43:103, 1979.
- [41] Mikhail A. Shifman, A. I. Vainshtein, and Valentin I. Zakharov. Can Confinement Ensure Natural CP Invariance of Strong Interactions? *Nucl. Phys. B*, 166:493–506, 1980.
- [42] I.G Irastorza, F.T Avignone, S Caspi, J.M Carmona, T Dafni, M Davenport, A Dudarev, G Fanourakis, E Ferrer-Ribas, J Galá n, J.A García, T Gerasis, I Giomataris, H Gómez, D.H.H Hoffmann, F.J Iguaz, K Jakovčić, M Krčmar, B Lakić, G Luzón, M Pivovarov, T Papaevangelou, G Raffelt, J Redondo, A Rodríguez, S Russenschuck, J Ruz, I Shilon, H. Ten Kate, A Tomás, S Troitsky, K. van Bibber, J.A Villar, J Vogel, L Walckiers, and K Zioutas. Towards a new generation axion helioscope. *Journal of Cosmology and Astroparticle Physics*, 2011(06):013–013, jun 2011.
- [43] Francesca Chadha-Day, John Ellis, and David J. E. Marsh. Axion dark matter: What is it and why now? *Sci. Adv.*, 8(8):abj3618, 2022.
- [44] Matthew J. Dolan, Felix Kahlhoefer, Christopher McCabe, and Kai Schmidt-Hoberg. A taste of dark matter: flavour constraints on pseudoscalar mediators. *Journal of High Energy Physics*, 2015(3), mar 2015.
- [45] Céline Boehm, Matthew J. Dolan, Christopher McCabe, Michael Spannowsky, and Chris J. Wallace. Extended gamma-ray emission from coy dark matter. *Journal of Cosmology and Astroparticle Physics*, 2014(05):009–009, may 2014.

- [46] Yasunori Nomura and Jesse Thaler. Dark matter through the axion portal. *Physical Review D*, 79(7), apr 2009.
- [47] Marius Millea, Lloyd Knox, and Brian Fields. New Bounds for Axions and Axion-Like Particles with keV-GeV Masses. *Phys. Rev. D*, 92(2):023010, 2015.
- [48] Manuel Meyer, Dieter Horns, and Martin Raue. First lower limits on the photon-axion-like particle coupling from very high energy gamma-ray observations. *Phys. Rev. D*, 87(3):035027, 2013.
- [49] Maurizio Giannotti, Igor Irastorza, Javier Redondo, and Andreas Ringwald. Cool WISPs for stellar cooling excesses. *JCAP*, 05:057, 2016.
- [50] J. Beacham et al. Physics Beyond Colliders at CERN: Beyond the Standard Model Working Group Report. *J. Phys. G*, 47(1):010501, 2020.
- [51] Asimina Arvanitaki, Savvas Dimopoulos, Sergei Dubovsky, Nemanja Kaloper, and John March-Russell. String Axiverse. *Phys. Rev. D*, 81:123530, 2010.
- [52] Michele Cicoli, Mark Goodsell, and Andreas Ringwald. The type IIB string axiverse and its low-energy phenomenology. *JHEP*, 10:146, 2012.
- [53] Kenneth A. Intriligator and Nathan Seiberg. Lectures on Supersymmetry Breaking. *Class. Quant. Grav.*, 24:S741–S772, 2007.
- [54] Ann E. Nelson and Nathan Seiberg. R symmetry breaking versus supersymmetry breaking. *Nucl. Phys. B*, 416:46–62, 1994.
- [55] Jonathan Bagger, Erich Poppitz, and Lisa Randall. The R axion from dynamical supersymmetry breaking. *Nucl. Phys. B*, 426:3–18, 1994.
- [56] Bogdan A. Dobrescu and Konstantin T. Matchev. Light axion within the next-to-minimal supersymmetric standard model. *JHEP*, 09:031, 2000.
- [57] Brando Bellazzini, Alberto Mariotti, Diego Redigolo, Filippo Sala, and Javi Serra. R-axion at colliders. *Phys. Rev. Lett.*, 119(14):141804, 2017.
- [58] Ken Mimasu and Verónica Sanz. Alps at colliders, 2015.
- [59] Joerg Jaeckel and Michael Spannowsky. Probing MeV to 90 GeV axion-like particles with LEP and LHC. *Physics Letters B*, 753:482–487, feb 2016.
- [60] Babette Döbrich, Joerg Jaeckel, Felix Kahlhoefer, Andreas Ringwald, and Kai Schmidt-Hoberg. ALPtraum: ALP production in proton beam dump experiments. *Journal of High Energy Physics*, 2016(2), feb 2016.
- [61] I. Brivio, M. B. Gavela, L. Merlo, K. Mimasu, J. M. No, R. del Rey, and V. Sanz. ALPs effective field theory and collider signatures. *The European Physical Journal C*, 77(8), aug 2017.
- [62] Martin Bauer, Matthias Neubert, and Andrea Thamm. LHC as an axion factory: Probing an axion explanation for  $(g - 2)_\mu$  with exotic higgs decays. *Physical Review Letters*, 119(3), jul 2017.

- [63] Kiwoon Choi, Sang Hui Im, Chan Beom Park, and Seokhoon Yun. Minimal flavor violation with axion-like particles. *Journal of High Energy Physics*, 2017(11), nov 2017.
- [64] Martin Bauer, Matthias Neubert, and Andrea Thamm. Collider probes of axion-like particles. *Journal of High Energy Physics*, 2017(12), dec 2017.
- [65] Brando Bellazzini, Csaba Csáki, and Javi Serra. Composite higgses. *The European Physical Journal C*, 74(5), may 2014.
- [66] Ben Gripaios, Alex Pomarol, Francesco Riva, and Javi Serra. Beyond the minimal composite higgs model. *Journal of High Energy Physics*, 2009(04):070–070, apr 2009.
- [67] Darwin Chang, We-Fu Chang, Chung-Hsien Chou, and Wai-Yee Keung. Large two-loop contributions to  $g-2$  from a generic pseudoscalar boson. *Physical Review D*, 63(9), apr 2001.
- [68] W. J. Marciano, A. Masiero, P. Paradisi, and M. Passera. Contributions of axionlike particles to lepton dipole moments. *Physical Review D*, 94(11), dec 2016.
- [69] Ulrich Ellwanger and Stefano Moretti. Possible explanation of the electron positron anomaly at 17 meV in  $^8\text{Be}$  transitions through a light pseudoscalar, 2016.
- [70] Thomas Flacke, Claudia Frugiuele, Elina Fuchs, Rick S. Gupta, and Gilad Perez. Phenomenology of relaxion-higgs mixing. *Journal of High Energy Physics*, 2017(6), jun 2017.
- [71] Peter W. Graham, David E. Kaplan, and Surjeet Rajendran. Cosmological relaxation of the electroweak scale. *Physical Review Letters*, 115(22), nov 2015.
- [72] Matthew J. Dolan, Torben Ferber, Christopher Hearty, Felix Kahlhoefer, and Kai Schmidt-Hoberg. Revised constraints and Belle II sensitivity for visible and invisible axion-like particles. *JHEP*, 12:094, 2017. [Erratum: *JHEP* 03, 190 (2021)].
- [73] Martin Bauer, Matthias Neubert, Sophie Renner, Marvin Schnubel, and Andrea Thamm. The low-energy effective theory of axions and ALPs. *Journal of High Energy Physics*, 2021(4), apr 2021.
- [74] Jonathan L. Ouellet et al. First Results from ABRACADABRA-10 cm: A Search for Sub- $\mu\text{eV}$  Axion Dark Matter. *Phys. Rev. Lett.*, 122(12):121802, 2019.
- [75] L. Zhong et al. Results from phase 1 of the HAYSTAC microwave cavity axion experiment. *Phys. Rev. D*, 97(9):092001, 2018.
- [76] Dmitry Budker, Peter W. Graham, Micah Ledbetter, Surjeet Rajendran, and Alex Sushkov. Proposal for a Cosmic Axion Spin Precession Experiment (CASPER). *Phys. Rev. X*, 4(2):021030, 2014.

- [77] Béla Majorovits. The search of Axion Dark Matter with a dielectric halo-scope: MADMAX. *EPJ Web Conf.*, 282:01008, 2023.
- [78] D. Alesini et al. Search for Galactic axions with a high-Q dielectric cavity. *Phys. Rev. D*, 106(5):052007, 2022.
- [79] A. Abeln et al. Conceptual design of BabyIAXO, the intermediate stage towards the International Axion Observatory. *JHEP*, 05:137, 2021.
- [80] K. Zioutas et al. First results from the CERN Axion Solar Telescope (CAST). *Phys. Rev. Lett.*, 94:121301, 2005.
- [81] E. Aprile et al. The XENON1T Dark Matter Experiment. *Eur. Phys. J. C*, 77(12):881, 2017.
- [82] R Bähre, B Döbrich, J Dreyling-Eschweiler, S Ghazaryan, R Hodajerdi, D Horns, F Januschek, E A Knabbe, A Lindner, D Notz, A Ringwald, J E von Seggern, R Stromhagen, D Trines, and B Willke. Any light particle search ii — technical design report. *Journal of Instrumentation*, 8(09):T09001, sep 2013.
- [83] P. Sikivie. Experimental Tests of the Invisible Axion. *Phys. Rev. Lett.*, 51:1415–1417, 1983. [Erratum: *Phys.Rev.Lett.* 52, 695 (1984)].
- [84] Alexander J. Millar, Georg G. Raffelt, Javier Redondo, and Frank D. Steffen. Dielectric Haloscopes to Search for Axion Dark Matter: Theoretical Foundations. *JCAP*, 01:061, 2017.
- [85] Anton V. Sokolov and Andreas Ringwald. Generic axion Maxwell equations: path integral approach. 3 2023.
- [86] Dario Buttazzo, Roberto Franceschini, and Andrea Wulzer. Two Paths Towards Precision at a Very High Energy Lepton Collider. *JHEP*, 05:219, 2021.
- [87] Antonio Costantini, Federico De Lillo, Fabio Maltoni, Luca Mantani, Olivier Mattelaer, Richard Ruiz, and Xiaoran Zhao. Vector boson fusion at multi-TeV muon colliders. *JHEP*, 09:080, 2020.
- [88] R. H. Dalitz. On the analysis of tau-meson data and the nature of the tau-meson. *Phil. Mag. Ser. 7*, 44:1068–1080, 1953.
- [89] E. Fabri. A study of tau-meson decay. *Nuovo Cim.*, 11:479–491, 1954.
- [90] N. Byers and C. N. Yang. Physical Regions in Invariant Variables for n Particles and the Phase-Space Volume Element. *Rev. Mod. Phys.*, 36(2):595–609, 1964.
- [91] P. Nyborg, H. S. Song, W. Kernan, and R. H. Good. Phase-Space Considerations for Four-Particle Final States. *Phys. Rev.*, 140:B914–B920, 1965.
- [92] Richard A. Morrow. The Physical Regions of Many-Particle Processes. *Journal of Mathematical Physics*, 7(5):844–848, 05 2005.

- [93] K. Kajantie and P. Lindblom. Physical region on the plane of two invariant momentum transfers for a reaction with three particles in the final state. *Phys. Rev.*, 175:2203–2213, 1968.
- [94] C. H. Poon. Kinematics of many-particle processes in invariant variables - physical regions, phase space and all that. *Nucl. Phys. B*, 20:509–552, 1970.
- [95] B. C. Allanach, C. G. Lester, Michael Andrew Parker, and B. R. Webber. Measuring sparticle masses in nonuniversal string inspired models at the LHC. *JHEP*, 09:004, 2000.
- [96] B. K. Gjelsten, D. J. Miller, and P. Osland. Measurement of SUSY masses via cascade decays for SPS 1a. *JHEP*, 12:003, 2004.
- [97] B. K. Gjelsten, D. J. Miller, and P. Osland. Measurement of the gluino mass via cascade decays for SPS 1a. *JHEP*, 06:015, 2005.
- [98] D. J. Miller, P. Osland, and A. R. Raklev. Invariant mass distributions in cascade decays. *JHEP*, 03:034, 2006.
- [99] Konstantin T. Matchev, Filip Moortgat, Luc Pape, and Myeonghun Park. Precise reconstruction of sparticle masses without ambiguities. *JHEP*, 08:104, 2009.
- [100] Michael Burns, Konstantin T. Matchev, and Myeonghun Park. Using kinematic boundary lines for particle mass measurements and disambiguation in SUSY-like events with missing energy. *JHEP*, 05:094, 2009.
- [101] Prateek Agrawal, Can Kilic, Craig White, and Jiang-Hao Yu. Improved Mass Measurement Using the Boundary of Many-Body Phase Space. *Phys. Rev. D*, 89(1):015021, 2014.
- [102] Dipsikha Debnath, James S. Gainer, Can Kilic, Doojin Kim, Konstantin T. Matchev, and Yuan-Pao Yang. Identifying Phase Space Boundaries with Voronoi Tessellations. *Eur. Phys. J. C*, 76(11):645, 2016.
- [103] Dipsikha Debnath, James S. Gainer, Can Kilic, Doojin Kim, Konstantin T. Matchev, and Yuan-Pao Yang. Enhancing the discovery prospects for SUSY-like decays with a forgotten kinematic variable. *JHEP*, 05:008, 2019.
- [104] Guido Altarelli, B. Mele, and F. Pitolli. Heavy Higgs Production at Future Colliders. *Nucl. Phys. B*, 287:205–224, 1987.
- [105] Franz Mandl and Graham Shaw. *Quantum field theory*. John Wiley & Sons, 2010.
- [106] C. Itzykson and J. B. Zuber. *Quantum Field Theory*. International Series In Pure and Applied Physics. McGraw-Hill, New York, 1980.
- [107] Izrail Solomonovich Gradshteyn and Iosif Moiseevich Ryzhik. *Table of integrals, series, and products*. Academic press, 2014.

- [108] Tao Han. Collider phenomenology: Basic knowledge and techniques. In *Theoretical Advanced Study Institute in Elementary Particle Physics: Physics in  $D \geq 4$* , pages 407–454, 8 2005.
- [109] Eero Byckling and K. Kajantie. *Particle Kinematics*. University of Jyvaskyla, Jyvaskyla, Finland, 1971.
- [110] Giovanni Costa. *Kinematics and Symmetries*, volume 2. Institut national de physique nucléaire et de physique des particules, 1979.
- [111] Michael E. Peskin and Daniel V. Schroeder. *An Introduction to quantum field theory*. Addison-Wesley, Reading, USA, 1995.
- [112] Wolfram Research, Inc. System Modeler, Version 12.3.1. Champaign, IL, 2021.
- [113] V. M. Budnev, I. F. Ginzburg, G. V. Meledin, and V. G. Serbo. The Two photon particle production mechanism. Physical problems. Applications. Equivalent photon approximation. *Phys. Rept.*, 15:181–281, 1975.
- [114] Enrico Fermi. On the theory of collisions between atoms and electrically charged particles. *Nuovo Cim.*, 2:143–158, 1925.
- [115] E Lifshitz and L Landau. The classical theory of fields, vol. 2. *Course of Theoretical Physics Series, Butterworth-Heinemann*, 1980.
- [116] E. J. Williams. Correlation of certain collision problems with radiation theory. *Kong. Dan. Vid. Sel. Mat. Fys. Med.*, 13N4(4):1–50, 1935.
- [117] C. F. von Weizsacker. Radiation emitted in collisions of very fast electrons. *Z. Phys.*, 88:612–625, 1934.
- [118] Stefano Frixione, Michelangelo L. Mangano, Paolo Nason, and Giovanni Ridolfi. Improving the Weizsacker-Williams approximation in electron - proton collisions. *Phys. Lett. B*, 319:339–345, 1993.
- [119] W. Altmannshofer et al. The Belle II Physics Book. *PTEP*, 2019(12):123C01, 2019. [Erratum: PTEP 2020, 029201 (2020)].
- [120] T. Abe et al. Belle II Technical Design Report. 11 2010.
- [121] von F. Zernike. Beugungstheorie des schneidenver-fahrens und seiner verbesserten form, der phasenkontrastmethode. *Physica*, 1(7):689–704, 1934.
- [122] T. Ferber, C. Hearty, and M. Roney. Design of the ECL Software for Belle II. 2016.
- [123] R. M. Brown and D. J. A. Cockerill. Electromagnetic calorimetry. *Nucl. Instrum. Meth. A*, 666:47–79, 2012.
- [124] H. Ikeda et al. A detailed test of the CsI(Tl) calorimeter for BELLE with photon beams of energy between 20-MeV and 5.4-GeV. *Nucl. Instrum. Meth. A*, 441:401–426, 2000.

- [125] J. Alwall, R. Frederix, S. Frixione, V. Hirschi, F. Maltoni, O. Mattelaer, H. S. Shao, T. Stelzer, P. Torrielli, and M. Zaro. The automated computation of tree-level and next-to-leading order differential cross sections, and their matching to parton shower simulations. *JHEP*, 07:079, 2014.
- [126] Adam Alloul, Neil D. Christensen, Céline Degrande, Claude Duhr, and Benjamin Fuks. FeynRules 2.0 - A complete toolbox for tree-level phenomenology. *Comput. Phys. Commun.*, 185:2250–2300, 2014.
- [127] Celine Degrande, Claude Duhr, Benjamin Fuks, David Grellscheid, Olivier Mattelaer, and Thomas Reiter. UFO - The Universal FeynRules Output. *Comput. Phys. Commun.*, 183:1201–1214, 2012.
- [128] Jeffrey D. Richman. An Experimenter’s Guide to the Helicity Formalism. 6 1984.
- [129] U. Amaldi, R. Biancastelli, C. Bosio, G. Matthiae, J.V. Allaby, W. Bartel, M.M. Block, G. Cocconi, A.N. Diddens, R.W. Dobinson, J. Litt, and A.M. Wetherell. Measurements of the proton-proton total cross section by means of coulomb scattering at the cern intersecting storage rings. *Physics Letters B*, 43(3):231–236, 1973.
- [130] S. Abdel Khalek et al. The ALFA Roman Pot Detectors of ATLAS. *JINST*, 11(11):P11013, 2016.
- [131] K. Akiba et al. LHC Forward Physics. *J. Phys. G*, 43:110201, 2016.
- [132] Albert M Sirunyan et al. Evidence for light-by-light scattering and searches for axion-like particles in ultraperipheral PbPb collisions at  $\sqrt{s_{NN}} = 5.02$  TeV. *Phys. Lett. B*, 797:134826, 2019.
- [133] Georges Aad et al. Measurement of light-by-light scattering and search for axion-like particles with  $2.2 \text{ nb}^{-1}$  of Pb+Pb data with the ATLAS detector. *JHEP*, 03:243, 2021. [Erratum: *JHEP* 11, 050 (2021)].
- [134] Tao Han, Ian-Woo Kim, and Jeonghyeon Song. Kinematic Cusps: Determining the Missing Particle Mass at Colliders. *Phys. Lett. B*, 693:575–579, 2010.